frontiers | Research Topics

Application of molecular genetics for the diagnosis and classification of rare cancers in surgical pathology

Edited by
Jinping Lai, Ming Zhou, Dengfeng Cao, Ming Zhao and Minghua Ge

Published in
Frontiers in Oncology

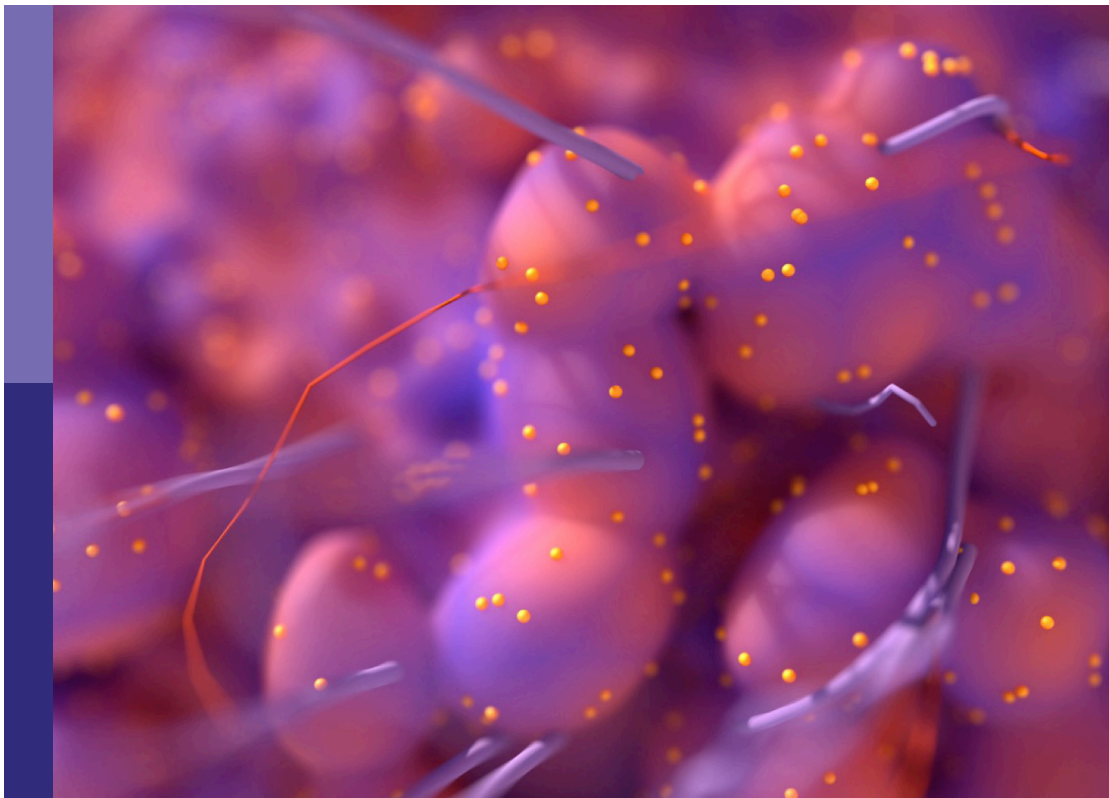

ISSN 1664-8714
ISBN 978-2-8325-3273-7
DOI 10.3389/978-2-8325-3273-7

About Frontiers

Frontiers is more than just an open access publisher of scholarly articles: it is a pioneering approach to the world of academia, radically improving the way scholarly research is managed. The grand vision of Frontiers is a world where all people have an equal opportunity to seek, share and generate knowledge. Frontiers provides immediate and permanent online open access to all its publications, but this alone is not enough to realize our grand goals.

Frontiers journal series

The Frontiers journal series is a multi-tier and interdisciplinary set of open-access, online journals, promising a paradigm shift from the current review, selection and dissemination processes in academic publishing. All Frontiers journals are driven by researchers for researchers; therefore, they constitute a service to the scholarly community. At the same time, the *Frontiers journal series* operates on a revolutionary invention, the tiered publishing system, initially addressing specific communities of scholars, and gradually climbing up to broader public understanding, thus serving the interests of the lay society, too.

Dedication to quality

Each Frontiers article is a landmark of the highest quality, thanks to genuinely collaborative interactions between authors and review editors, who include some of the world's best academicians. Research must be certified by peers before entering a stream of knowledge that may eventually reach the public - and shape society; therefore, Frontiers only applies the most rigorous and unbiased reviews. Frontiers revolutionizes research publishing by freely delivering the most outstanding research, evaluated with no bias from both the academic and social point of view. By applying the most advanced information technologies, Frontiers is catapulting scholarly publishing into a new generation.

What are Frontiers Research Topics?

Frontiers Research Topics are very popular trademarks of the *Frontiers journals series*: they are collections of at least ten articles, all centered on a particular subject. With their unique mix of varied contributions from Original Research to Review Articles, Frontiers Research Topics unify the most influential researchers, the latest key findings and historical advances in a hot research area.

Find out more on how to host your own Frontiers Research Topic or contribute to one as an author by contacting the Frontiers editorial office: frontiersin.org/about/contact

Application of molecular genetics for the diagnosis and classification of rare cancers in surgical pathology

Topic editors

Jinping Lai — Kaiser Permanente Sacramento Medical Center, United States
Ming Zhou — Tufts Medical Center, United States
Dengfeng Cao — Washington University in St. Louis, United States
Ming Zhao — Ningbo Diagnostic Pathology Center, China
Minghua Ge — Zhejiang Provincial People's Hospital, China

Citation

Lai, J., Zhou, M., Cao, D., Zhao, M., Ge, M., eds. (2023). *Application of molecular genetics for the diagnosis and classification of rare cancers in surgical pathology*. Lausanne: Frontiers Media SA. doi: 10.3389/978-2-8325-3273-7

Table of contents

05 Papillary renal neoplasm with reverse polarity: A clinicopathological and molecular genetic characterization of 16 cases with expanding the morphologic spectrum and further support for a novel entity
Miaomiao Shen, Xiaona Yin, Yanfeng Bai, Huizhi Zhang, Guoqing Ru, Xianglei He, Xiaodong Teng, Guorong Chen and Ming Zhao

20 Primary intrathoracic liposarcomas: A clinicopathologic and molecular study of 43 cases in one of the largest medical centers of China
You Xie, Wenyi Jing, Wei Zhao, Ran Peng, Min Chen, Ting Lan, Heng Peng, Xin He, Huijiao Chen, Zhang Zhang and Hongying Zhang

39 Primary intraosseous Rosai–Dorfman disease: An analysis of clinicopathologic characteristics, molecular genetics, and prognostic features
Xin Weng, Yajie Yang, Meng Zhang, Chang Cai, Yanhua Sun, Xikang Wu, Rongrong Zhang, Huihui Gui, Wei Li, Qizhong Xu and Xia Liu

50 Metanephric stromal tumor with *BRAF* V600E mutation in an adult patient: Case report and literature review
Yuqian Fan, Jingjing Yu and Ming Zhao

57 Atypical metanephric adenoma: Shares similar histopathological features and molecular changes of metanephric adenoma and epithelial-predominant Wilms' tumor
Xiaoxue Yin, Xingming Zhang, Xiuyi Pan, Junya Tan, Linmao Zheng, Qiao Zhou and Ni Chen

70 Case report: *ALK*-rearranged spindle and epithelioid cell neoplasms with S100 and CD34 co-expression: Additional evidence of kinase fusion–positive soft tissue tumors
Shao-Jie Sheng, Ju-Ming Li, Qin-He Fan, Yang Liu, Shao-Yu Chen, Ming Zhao and Qi-Xing Gong

79 Case report: Atypical spindle cell/pleomorphic lipomatous tumor masquerading as a myxoid liposarcoma or intramuscular myxoma
Jiro Ichikawa, Tomonori Kawasaki, Hiroki Imada, Satoshi Kanno, Naofumi Taniguchi, Tomoyuki Ashizawa and Hirotaka Haro

86 Epithelioid glioblastoma exhibits a heterogeneous molecular feature: A targeted next-generation sequencing study
Rui Pan, Xiaotong Wang, Ru Fang, Qiuyuan Xia, Nan Wu and Qiu Rao

96 *USP6*-associated soft tissue tumors with bone metaplasia: Clinicopathologic and genetic analysis and the identification of novel *USP6* fusion partners
Yahan Zhang, Yan Qiu, Xianliang Zhang, Xin He, Chen Chen, Min Chen and Hongying Zhang

110 Pediatric dermatofibrosarcoma protuberans: A clinicopathologic and genetic analysis of 66 cases in the largest institution in Southwest China
Zhang Zhang, Yang Lu, Changle Shi, Min Chen, Xin He and Hongying Zhang

123 Expression and significance of m6A-RNA-methylation in oral cancer and precancerous lesion
Zhiming Qin, Jiaying Bai, Huiying He and Binbin Li

134 Case Report: An NTRK1 fusion-positive embryonal rhabdomyosarcoma: clinical presentations, pathological characteristics and genotypic analyses
Na-Mei Li, Shi-He Jiang, Peng Zhou and Xiao-Hong Li

142 Primary pulmonary hyalinizing clear cell carcinoma with fusions of both EWSR1::CREM and IRF2::NTRK3: report of a case with an aggressive behavior
You-Li Wu, Feng Wu, Mian-Fu Cao, Yang Lan, Ming-Shan Du, Song-Tao Yu, Yan Wang, Xiao-Chu Yan, Xiu-Wu Bian and Guang-Jie Duan

frontiers | Frontiers in Oncology

TYPE Original Research
PUBLISHED 22 July 2022
DOI 10.3389/fonc.2022.930296

OPEN ACCESS

EDITED BY
Rocco Cappellesso,
University Hospital of Padua, Italy

REVIEWED BY
Sabahattin Cömertpay,
Kahramanmaras Sütçülmam University, Turkey
João Lobo,
Portuguese Oncology Institute, Portugal

*CORRESPONDENCE
Ming Zhao
zhaomingpathol@163.com

†These authors have contributed equally to this work and share first authorship

SPECIALTY SECTION
This article was submitted to Surgical Oncology, a section of the journal Frontiers in Oncology

RECEIVED 27 April 2022
ACCEPTED 24 June 2022
PUBLISHED 22 July 2022

CITATION
Shen M, Yin X, Bai Y, Zhang H, Ru G, He X, Teng X, Chen G and Zhao M (2022) Papillary renal neoplasm with reverse polarity: A clinicopathological and molecular genetic characterization of 16 cases with expanding the morphologic spectrum and further support for a novel entity. *Front. Oncol.* 12:930296. doi: 10.3389/fonc.2022.930296

Papillary renal neoplasm with reverse polarity: A clinicopathological and molecular genetic characterization of 16 cases with expanding the morphologic spectrum and further support for a novel entity

Miaomiao Shen[1†], Xiaona Yin[2†], Yanfeng Bai[3], Huizhi Zhang[4], Guoqing Ru[1], Xianglei He[1], Xiaodong Teng[4], Guorong Chen[5] and Ming Zhao[1*]

[1]Cancer Center, Department of Pathology, Zhejiang Provincial People's Hospital, Affiliated People's Hospital, Hangzhou Medical College, Hangzhou, China, [2]Department of Pathology, Hangzhou Women's Hospital, Hangzhou, China, [3]Department of Pathology, The First Affiliated Hospital, Zhejiang University School of Medicine, Hangzhou, China, [4]Department of Pathology, Ningbo Diagnostic Pathology Center, Ningbo, China, [5]Department of Pathology, The First Affiliated Hospital, Wenzhou Medical University, Wenzhou, China

Papillary renal neoplasm with reverse polarity (PRNRP) is a recently described, rare renal tumor that differs clinically, morphologically, and molecularly from papillary renal cell carcinoma (RCC). To further characterize the pathological spectrum of this rare tumor, in this study, we retrospectively identified 16 cases of PRNRP from three institutions to comprehensively investigate the clinicopathological and molecular genetic features, using immunohistochemistry (IHC), fluorescence *in-situ* hybridization (FISH), and targeted next-generation sequencing (NGS). The patients included nine men and seven women, with age ranging from 47 to 80 years (median = 67.5 years, mean = 65 years). The tumor size ranged from 0.4 to 9.5 cm in the greatest dimension (median = 1.8 cm, mean = 2.6 cm). Most tumors (12/16) were incidentally identified by imaging studies. By AJCC stage, 15 were categorized as pT1 and 1 was pT2. Follow-up showed no recurrences, metastases, or disease-related deaths in all the 16 patients. Grossly, 14 cases demonstrated at least a partially cystic appearance. Microscopically, all PRNRPs except 1 (case 13) were composed predominantly of thin, branching papillary architecture covered by a single layer of cuboidal cells with finely granular cytoplasm, and low-grade nuclei typically located toward the apical surface away from the basement. Case 13 consisted mostly of solid, densely packed tubules with only

a minor papillary component (5%). Other commonly seen histological features included hyalinized or edematous papillae (n = 11), lymphocyte aggregation in fibrovascular cores (n = 10), mast cell infiltration (n = 8), and intralesional hemorrhage (n = 7). Uncommonly seen histological features included lymphoid cuff (n = 4), hemosiderin deposition (n = 5), foci of clear cell change (n = 4), intracytoplasmic vacuoles (n = 4), eosinophilic hobnail cells (n = 2), and infarct-type necrosis (n = 1). Two PRNRPs were concurrent with ipsilateral clear cell papillary RCC and clear cell RCC, respectively. By IHC, the tumors were consistently positive for GATA3, CK7, and PAX8. Fourteen out of 16 tumors showed a basolateral-membranous E-cadherin expression pattern, and 12/16 cases were positive for 34βE12.The expression of AMACR, CD10, and vimentin was either absent or only weak and focal. By targeted NGS, 13/14 evaluated PRNRPs harbored *KRAS* missense mutations involving c.35G>T resulting in p.G12V (7/13), c.35G>A resulting in p.G12D (4/13), and c.34G>T resulting in p.G12C (2/13). By FISH, 1/15 had gains of chromosomes 7 and 17, and 2/8 male cases had deletion of chromosomes Y. In conclusion, our study confirms that PRNRP is an indolent renal cell neoplasm with unique morphology, consistent immunohistochemical profile, and recurrent *KRAS* mutation. Our study expands the morphologic spectrum of PRNRP and provides further evidence supporting it as a novel entity.

KEYWORDS

papillary renal neoplasm with reverse polarity, papillary renal cell carcinoma, GATA3, *KRAS* mutation, next-generation sequencing

Introduction

Papillary renal cell carcinoma (PRCC), the second prevalent subtype among RCCs, has been divided into types 1 and 2 for more than two decades (1). Histologically, PRCC type 1 is characterized by papillary architecture covered by a single layer of cuboidal cells with scant pale or basophilic cytoplasm and low-grade nuclei under the criterion made by the World Health Organization/International Society of Urological Pathology (WHO/ISUP), whereas PRCC type 2 usually exhibits large pseudostratified cells with abundant eosinophilic cytoplasm and high WHO/ISUP nuclear grade (1–3). PRCC type 2 has worse prognosis than type 1 (2). The Cancer Genome Atlas (TCGA) research group revealed that PRCC type 1 was associated with *MET* mutations, while PRCC type 2 was a heterogeneous tumor at the molecular level involving *CDKN2A* silencing, *SETD2* mutations, and *TFE3* fusions (4). Genetic differences further explained the morphologic discrimination between these two types (4). In practice, however, it may be challenging to dichotomize PRCC as such, since well-sampled tumors frequently harbor mixtures of type 1 and 2 areas (5). Currently, the 2022 WHO classification eliminated the PRCC type 1/2 subcategorization, given the recognition of frequent mixed tumor phenotypes and the existence of entities with a different molecular background within the PRCC type 2 category (6). A subset of PRCCs that had granular eosinophilic cytoplasm but favorable prognosis has been designated as oncocytoid-type or oncocytic PRCC (7, 8). Subsequently, several studies that referred to varied inclusion criteria were performed and proposed various terminologies such as oncocytic PRCC with an inverted nuclear pattern and oncocytic low-grade variant of PRCC (9, 10). In 2016, WHO designated PRCC with voluminous granular eosinophilic cytoplasm and a monotonous layer of cells with low WHO/ISUP nuclear grade as oncocytic PRCC (3). However, emerging evidence suggests that oncocytic PRCC may not be an independent tumor entity, as oncocytic change can be noted in otherwise typical type 1 or 2 PRCC (11). In 2017, Saleeb et al. (12) subdivided PRCC into four types, of which PRCC type 4 showed morphology similar to that of oncocytic PRCC and was characterized by specific GATA3 immunoreactivity. In 2019, Al-Obaidy et al. (13) used the term "papillary renal neoplasm with reverse polarity" (PRNRP) for the first time and proposed that it should be distinguished from both PRCC types 1 and 2. Subsequently, the term "papillary renal neoplasm" not "papillary RCC" was widely adopted based on its extremely indolent behavior.

PRNRPs are composed of papillary or rarely tubular architectures with a single layer of uniform cuboidal cells with finely granular cytoplasm and apically located, low WHO/ISUP grade nuclei with inconspicuous nucleoli. Immunohistochemical staining for GATA3 and L1CAM along with the lack of vimentin expression is characteristic (13). The same group subsequently discovered that recurrent *KRAS* missense mutations at codon 12 of exon 2 may be a molecular hallmark for PRNRP, verifying the distinction from other renal cell neoplasms (14). More recently, several studies have also been published on this entity, reinforcing our understanding of its histologic and molecular genetic characteristics (15–19). In 2021, in its update on existing renal neoplasms, the Genitourinary Pathology Society (GUPS) has considered PRNRP to represent a distinct pattern/variant within the spectrum of PRCC (20). Most recently, type D papillary adenoma (PA) has been suggested to represent an analogue or a small-sized, clinically undetected PRNRP on the basis of their identical morphology, immunophenotype, and molecular genetics, broadening the concept of PRNRP (21–23).

In the current study, we identified 16 cases of PRNRP to further analyze the clinicopathological, immunohistochemical, and molecular features, expanding the morphologic spectrum of PRNRP and providing further evidence to support it as a novel entity.

Materials and methods

Case selection

Sixteen cases of PRNRP diagnosed between 2016 and 2021 from the files of three departments of pathology in China (The First Affiliated Hospital of Zhejiang University School of Medicine, Hangzhou; Ningbo Diagnostic Pathology Center, Ningbo; and Zhejiang Provincial People's Hospital, Hangzhou) were retrieved. The clinical details and follow-up data were obtained from a review of the patients' electronic records and from the physicians' offices. For all cases, the hematoxylin–eosin (HE)-stained and immunohistochemical slides were reviewed and the diagnosis of PRNRP was further confirmed according to the diagnostic criteria proposed by Al-Obaidy et al. (13) in 2019. All tumors were graded according to the WHO/ISUP nuclear grading system (10) and staged on the basis of the eighth edition TNM staging system of renal neoplasms (24). This study was approved by the institutional ethics committee of Zhejiang Provincial People's Hospital.

Immunohistochemistry

All specimens were formalin-fixed and paraffin-embedded (FFPE). Tissues were sliced into 3-μm sections. Immunohistochemistry (IHC) was performed at a single laboratory (Zhejiang Provincial People's Hospital, Hangzhou, China) using a Ventana Benchmark autostainer (Ventana Medical Systems, Tucson, USA). The following primary antibodies were used: PAX8 (Clone EP298, ZSGB-BIO, Beijing, China), GATA3 (Clone EP368, ZSGB-BIO, China), cytokeratin 7 (CK7, Clone EP16, ZSGB-BIO, China), 34βE12 (Clone 34βE12, ZSGB-BIO, China), E-cadherin (Clone EP6, ZSGB-BIO, China), alpha-methylacyl-CoA-racemase (AMACR, Clone 13H4, ZSGB-BIO, China), CD10 (Clone SP67, ZSGB-BIO, China), vimentin (Clone EP21, ZSGB-BIO, China), and CD117 (Clone YR145, Roche, China). The staining process was performed in accordance with the instructions and established positive and negative controls. We regarded the result as positive findings if the intensity was more than mild and evaluated the proportional score as follows: 0 negative, focal <50%; diffuse ≥50%.

Fluorescence *in-situ* hybridization

Fluorescence *in-situ* hybridization (FISH) analysis was performed to identify the presence of chromosomal abnormalities including gains of 7 and 17, or losses of Y, as described previously (25, 26). The centromere-specific probe (CEP) 7, CEP17, CEP X, and CEP Y were all from Anbiping™ (Anbiping, Guangzhou, China). Only individual and well-delineated cells were scored. Overlapping cells were excluded from the analysis. Approximately 100 tumor cells were analyzed in the targeted region. Using established criteria, chromosomal gains were considered significant if present in greater than 20% of tumor cells (25), and chromosomal losses were considered significant if present in >45% of tumor cells (26). Gains or losses were considered artifactual if seen in less than 20% of cells and 45% of tumors, respectively.

Targeted next-generation sequencing

For next-generation sequencing (NGS), 10 FFPE sections 5 μm thin containing >20% tumor cells confirmed by HE staining were used for genomic DNA and total RNA isolation. Genomic DNA and total RNA were extracted using a QIAamp Mini Kit (QIAGEN, Hilden, Germany). The DNA concentration was measured using a Qubit 4.0 Fluorometer (Thermo Fisher, Waltham, USA). A library was generated using RingCap™ loop-mediated amplification technology for the 13-gene panel (SpaceGen, Xiamen, China). This panel targeted the hotspot regions of *EGFR*, *KRAS*, *BRAF*, *PIK3CA*, *NRAS*, *HER2*, *MET*, *AKT1*, *KIT*, and *PDGFRA* with more than 500 hotspot mutations and 52 fusion variants of *ALK*, *ROS1*, and *RET* genes. Reads were generated on a MiniSeq platform (Illumina, San Diego, USA). Single-nucleotide variants (SNVs) and small insertions and deletions (InDels) with variant allele frequency

more than 5% and gene fusions were annotated using a commercial mutation-reporting system (SpaceGen, Xiamen, China) and identified manually by Integrative Genomics Viewer.

Results

Clinicopathological characteristics

The clinicopathological data of the 16 cases were tabulated in Table 1. The patients included nine men and seven women, with age ranging from 47 to 80 years (median = 67.5 years, mean = 65 years). Most tumors (12/16) were incidentally identified by imaging studies while three presented with symptoms including back pain and hematuria; the remaining one (case 4, the smallest one) was incidentally identified in the radical nephrectomy specimen for end-stage renal disease (ESRD). Ten neoplasms affected the left kidney, and six the right. Except for case 4, all neoplasms were treated by partial nephrectomy. All tumors were confined to the kidney; hence, 15 were categorized as pT1 and 1 (case 3) was pT2, according to the eighth edition TNM staging system (24). With a median follow-up of 15 months (range, 1–62 months), no tumor recurrences, metastases, or disease-related deaths were identified for all the 16 patients.

Grossly, most tumors (13/16) were small tumors, less than 3 cm in size (median = 1.8 cm, mean = 2.6 cm; range, 0.4–9.5 cm). All tumors were well-demarcated or encapsulated and most (14/16) demonstrated at least a partially cystic appearance. Five cases with larger size were predominantly cystic, frequently with intracystic polypoid or papillary masses protruding into the cystic spaces (Figure 1); nine were predominantly solid with minor areas of cystic change; and two were completely solid. The tumors were typically soft and friable in texture and tan to light brown in color. Microscopically, at low power, the tumors were frequently mixed solid and cystic (Figure 2A). All tumors were circumscribed, and seven had a thick fibrous capsule, four of which had peri-capsule lymphoid cuff (Figure 2B). In all PRNRPs, except in one (case 13), the solid areas were composed predominantly of thin, branching papillary architecture (Figures 2A–C), with variable amounts of hyalinized or edematous papillae noted in 11 cases (Figures 2D, E); in case 13, the tumor consisted mostly of solid, densely packed tubules with only a minor papillary component (5%) (Figure 2F). The papillae and tubules were covered by a single layer of cuboidal cells with moderate, eosinophilic, or finely granular/oncocytic cytoplasm, indistinct cell membrane, and round, WHO/ISUP grade 1–2 nuclei typically located toward the apical surface away from the basement (Figures 2G, H). Foci of clear cell change and intracytoplasmic vacuoles were each observed in four cases (Figures 3A, B). In addition, eosinophilic hobnail cells were focally present in two cases (cases 4 and 12) (Figure 3C). Lymphocyte aggregation and scattered mast cell infiltration in the fibrovascular cores were notable in 10 and 8 PRNRP cases, respectively (Figure 3D). The cystic areas when noted were frequently filled with eosinophilic proteinaceous material or blood clots (Figures 2A, 3E). Intralesional hemorrhage was identified in seven cases, and hemosiderin deposition was occasionally noted in five cases (intracellular in three and extracellular in two) (Figure 3F). In case 12, areas of infarct-type necrosis, due (putatively) to extensive intralesional hemorrhage, were identified (Figure 3G). Pseudostratification, psammoma bodies, foam cell clusters, coagulative-type tumor necrosis, or mitotic figures were absent in all tumors. All PRNRP cases were confined to the kidney, and none had microscopic lymphovascular invasion, perinephric fat invasion, or pelvicalyceal system involvement. A separate clear cell RCC (4.8 cm, WHO/ISUP grade 2) was observed in case 15, whereas a clear cell papillary RCC (1.4 cm) was present in case 2 (Figure 3H).

Immunohistochemical results

The immunohistochemical results for PRNRPs are summarized in Table 2. All PRNRPs showed strong and diffuse immunoreactivity to GATA3 (Figure 4A), CK7, and PAX8. Fourteen of the 16 tumors showed E-cadherin expression, with a diffuse, basolateral-membranous/"cup-like" staining pattern (Figure 4B), and 12/16 cases were strongly positive for 34βE12 (Figure 4C), with staining being diffusely in 11 and focally in 1. AMACR was weakly positive in 11 cases and negative in the remaining 5 cases (Figure 4D), and CD10 was focally and weakly positive in 3 cases and negative in the remaining 13 cases (Figure 4E). Vimentin was negative in 15 tumors and only focally positive in the remaining one (Figure 4F). All PRNRPs were completely negative for CAIX and CD117, while CD117 highlighted the mast cell infiltration in the fibrovascular cores of the papillae. The concurrent clear cell papillary RCC in case 2 showed a diffuse and strong expression of GATA3, 34βE12, CK7, and "cup-like" CAIX (Figure 3H).

Targeted NGS and FISH findings

The targeted NGS and FISH findings are summarized in Tables 3 and 4. The targeted NGS was performed in 14 out of 16 PRNRP cases. The targeted NGS was not performed in the remaining two cases, because their quality was not suitable for targeted sequencing. PRNRP tumors exhibited *KRAS* missense mutations in 13 out of the 14 cases (93%) by targeted NGS. These mutations were due to a c.35 G>T (7/13, 54%), c.35G>A (4/13, 31%), and c.34G>T(2/13, 15%) substitution, resulting in p.G12V, p.G12D, and p.G12C alterations, respectively (Figure 5). The allele frequency (AF) ranged from 9.2% to

TABLE 1 Clinicopathological characteristics of PRNRP.

Case no.	Sex/ age (y)	Clinical manifestation	Laterality	Size (cm)	Stage	Follow-up (months)	Concurrent RCC	WHO/ ISUP grade	Fibrous-capsule	Cystic change	Edematous/ hyalinized papillae	Intracytoplasmic vacuoles	Clear cell change	Hobnail cells	Hemosiderin	Hemorrhage	Lymphocytes aggregation	Mast cells infiltration
1	F/76	Incidentally identified	Right	2.5	pT1a	NED (3)	N	1	N	Y, prominent	N	Y	Y	N	N	N	N	N
2	M/ 80	Incidentally identified	Right	2.8	pT1a	NED (3)	Y, CCPRCC	1	Y, lymphoid cuff	Y, prominent	Y	N	N	N	Y, extracellular	Y	N	N
3	M/ 67	Incidentally identified	Left	9.5	pT2a	NED (9)	N	2	Y, lymphoid cuff	Y, prominent	Y	N	N	N	N	N	Y	N
4	M/ 79	Incidentally identified	Right	0.4	pT1a	NED (1)	N	2	N	Y	N	Y	Y	Y	N	N	Y	N
5	M/ 54	Incidentally identified	Left	2.1	pT1a	NED (4)	N	2	Y	Y	Y	Y	Y	N	Y, extracellular	Y	Y	N
6	M/ 67	Back pain	Right	1.9	pT1a	NED (8)	N	1	N	Y	Y	Y	N	N	Y, intracellular	Y	Y	Y
7	M/ 55	Hematuria	Left	4.5	pT1b	NED (16)	N	2	N	Y, prominent	Y	N	Y	N	Y, intracellular	Y	Y	N
8	F/57	Incidentally identified	Right	1.2	pT1a	NED (39)	N	2	N	Y	Y	N	N	N	N	N	Y	Y
9	F/47	Incidentally identified	Left	2.6	pT1a	NED (62)	N	1	Y, lymphoid cuff	Y	Y	N	N	N	N	Y	Y	N
10	F/50	Incidentally identified	Right	1.0	pT1a	NED (15)	N	1	N	N	N	N	N	N	N	N	N	Y
11	F/76	Incidentally identified	Left	1.2	pT1a	NED (14)	N	1	N	Y	Y	N	N	N	N	N	Y	Y
12	M/ 70	Back pain, fever and hematuria	Left	6.0	pT1b	NED (7)	N	2	Y, lymphoid cuff	Y, prominent	Y	N	N	Y	N	Y, with infarct-type necrosis	N	Y
13	M/ 73	Incidentally identified	Right	1.0	pT1a	NED (42)	N	2	Y	N	N	N	N	N	N	N	N	N
14	M/ 70	Incidentally identified	Right	1.5	pT1a	NED (4)	N	2	N	Y	N	N	N	N	N	N	N	Y
15	F/68	Incidentally identified	Right	1.7	pT1a	NED (11)	Y, CCRCC	2	N	Y	Y	N	N	N	Y, intracellular	Y	Y	Y
16	F/51	Incidentally identified	Right	1.2	pT1a	NED (8)	N	2	Y	Y	Y	N	N	N	N	N	Y	Y

CCPRCC, clear cell papillary renal cell carcinoma; CCRCC, clear cell renal cell carcinoma; F, female; M, male; N, not; NED, no evidence of disease; WHO/ISUP, World Health Organization/International Society of Urological Pathology; Y, yes.

10.3389/fonc.2022.930296

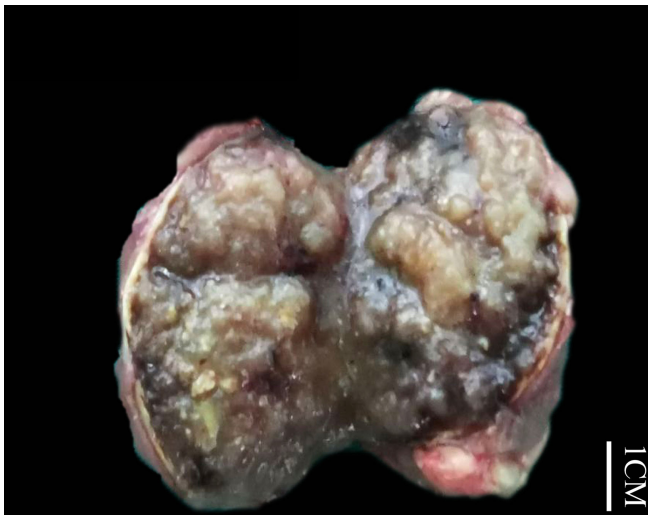

FIGURE 1
Gross examination showing an encapsulated and cystic PRNRP with a soft and friable, intracystic polypoid mass.

33%. No mutations of other genes in the panel were identified in any of the PRNRPs. No fusion genes were detected. No *KRAS* mutations were found in either concurrent clear cell RCC or clear cell papillary RCC. By FISH analysis, one of the 15 PRNRP cases analyzed (case 1) demonstrated trisomy 7 and 17 (**Figures 6A, B**). Chromosome Y deletion was present in two of eight male cases examined (case 13 and 14)(**Figure 6C**).

Discussion

RCC featuring papillary architecture and eosinophilic or oncocytic cytoplasm represents a heterogeneous disease, encompassing an increasing number of tumor variants, such as PRNRP, PRCC type 2, MiT family translocation RCC, biphasic hyalinizing psammomatous RCC, acquired cystic disease-associated RCC, and fumarate hydratase (FH)-deficient RCC. PRNRP was firstly designated as its current name in 2019 by Al-Obaidy and colleagues (13). It accounts for 1.3% to 9.1% of all PRCCs according to the previous reports (13, 17, 18, 22, 27), and to date there are a total of approximately 160 cases of PRNRP that have been published in the English-language literature. In the current study, we were able to identify 16 cases of PRNRP from three tertiary medical institutions between 5 years during which more than 350 PRCCs have been diagnosed, further indicating the rarity of this tumor type.

In agreement with previous studies, the 16 PRNRPs in our cohort presented mostly with an incidentally identified mass during the imaging study and showed a slight male predilection, and had small tumor size, low TNM stage, low WHO/ISUP nuclear grade, and a favorable prognosis at follow-up, without any recurrence, metastasis, or tumor-related death after surgical excision (13–19, 22, 23). Although most are solitary tumors, previous studies have demonstrated that a subset of PRNRPs may have multiple tumors as defined by presence of ≥2 unilateral or bilateral tumors, particularly for those with small size which are usually clinically undetectable (13, 22, 23). A recently published paper by Wei et al. (19) comprehensively reviewed the 100 reported cases of PRNRP and emphasized that this tumor was frequently a cystic tumor and at least a partially cystic change can be noted in 62% cases. Additionally, Al-Obaidy et al. (23) documented cystic expansion with intracystic papillary proliferation in 7 of their 16 clinically detected (≥5 mm) neoplasms. In line with these results, in our cohort, 14 cases displayed at least a partially cystic appearance and 5 larger tumors were predominantly cystic, frequently with intracystic polypoid or papillary masses protruding into the cystic spaces. Chang et al. (22) demonstrated that PRNRP showed a significantly higher association with ESRD compared with PRCC type 2. Similarly, Al-Obaidy et al. (23) showed that 12 of 35 clinically undetected (<5 mm) neoplasms were discovered on nephrectomy specimens performed for ESRD. In the current study, the smallest one (case 4, 0.4 cm) was clinically undetected and was incidentally identified in the nephrectomy specimen for ESRD. Concurrent ipsilateral renal tumor is not uncommon in PRNRP, and Lee et al. (28) reported a PRNRP with a *KRAS* mutation and a co-occurring clear cell RCC with a *PIK3CA* mutation in 2020. Most recently, Al-Obaidy and colleagues (23) found that 26 of 50 PRNRPs had other concurrent tumors of different histologic subtypes in the ipsilateral kidney, particularly for those with diameters less than 5 mm. In their study, the concurrent renal tumors included PRCCs, clear cell RCCs, acquired cystic disease-associated RCCs, chromophobe RCCs, and oncocytomas. In

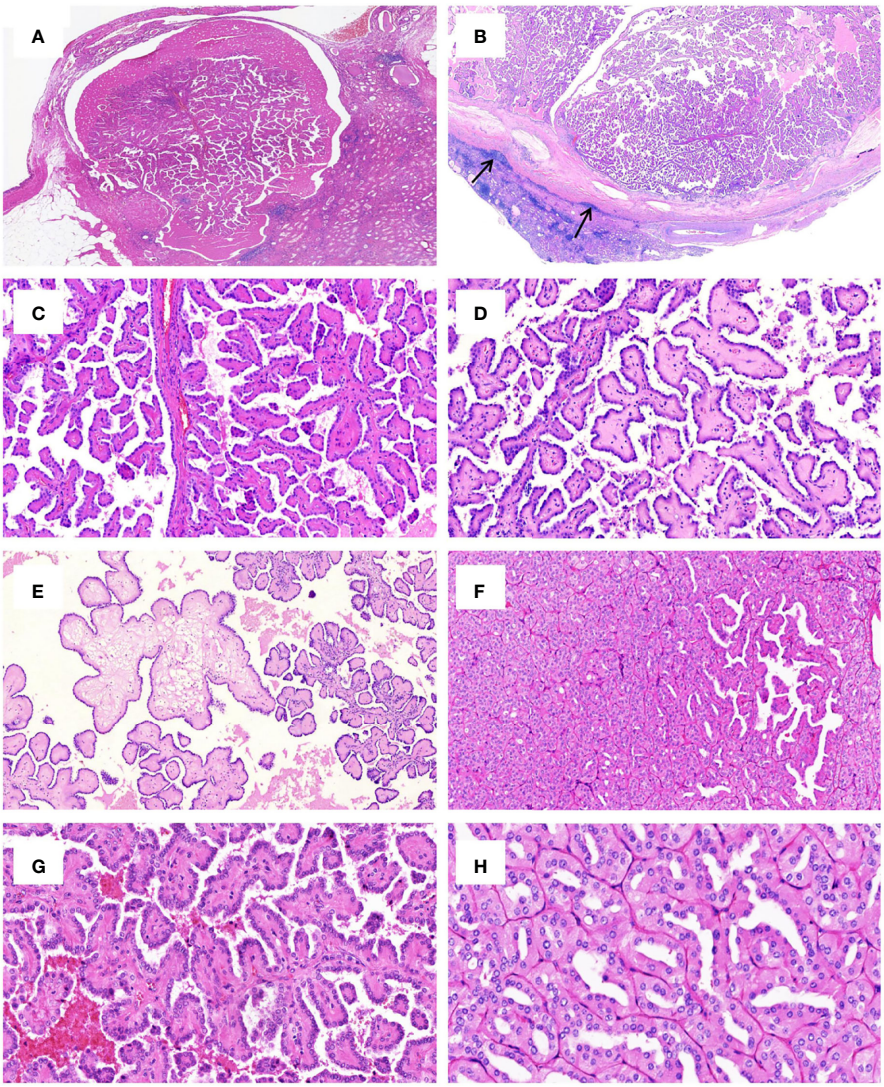

FIGURE 2
Histologic features of PRNRP. **(A)** Mixed solid and cystic tumor with eosinophilic proteinaceous material (HE, low magnification). **(B)** Thick fibrous capsule with peri-capsule lymphoid cuff (arrows, HE, low magnification). **(C)** Branching papillary architecture with delicate fibrovascular cores (HE, medium magnification). **(D)** Hyalinized papillae (HE, medium magnification). **(E)** Foci of edematous papillae (HE, medium magnification). **(F)** PRNRP consisting mostly of solid, densely packed tubules with only a minor papillary component (HE, medium magnification). The papillae (**G**, HE, high magnification) and tubules (**H**, HE, high magnification) are covered by oncocytic cells with inverted low-grade nuclei.

our cases, two PRNRPs coexisted with clear cell RCC and clear cell papillary RCC, respectively. To our knowledge, the latter tumor type was the first time to be reported to co-occur with PRNRP.

Histologically, PRNRP was originally documented by Al-Obaidy and colleagues (13) as a well-demarcated or encapsulated neoplasm displaying delicate and thin, arborizing papillary patterns or predominantly solid tubular growth in occasional cases. In that study, a minority of tumors showed thicker and hyalinized papillary cores or edematous papillae with cystically dilated tips filled with clear to eosinophilic fluid containing floating foamy macrophages. However, subsequent multiple studies reported that hyalinized or edematous papillae could be observed in the majority of PRNRP cases (26/30 in Kim et al. (15), 7/10 cases in Tong et al. (16), 9/14 in Kiyozawa et al. (18), and 11/16 in our cohort). The lining epithelium typically consisted of a monolayer of cuboidal to columnar cells with moderate to abundant, finely granular eosinophilic cytoplasm frequently with intracytoplasmic clear vacuoles or lumens, and apically located round, bland-appearing nuclei with inconspicuous nucleoli. Rare areas of nuclear clearing, wrinkled nuclear contours, and mild nuclear enlargement were also observed. Al-Obaidy et al. (13) did not identify psammoma bodies, intracellular hemosiderin, tumor necrosis, tight clusters

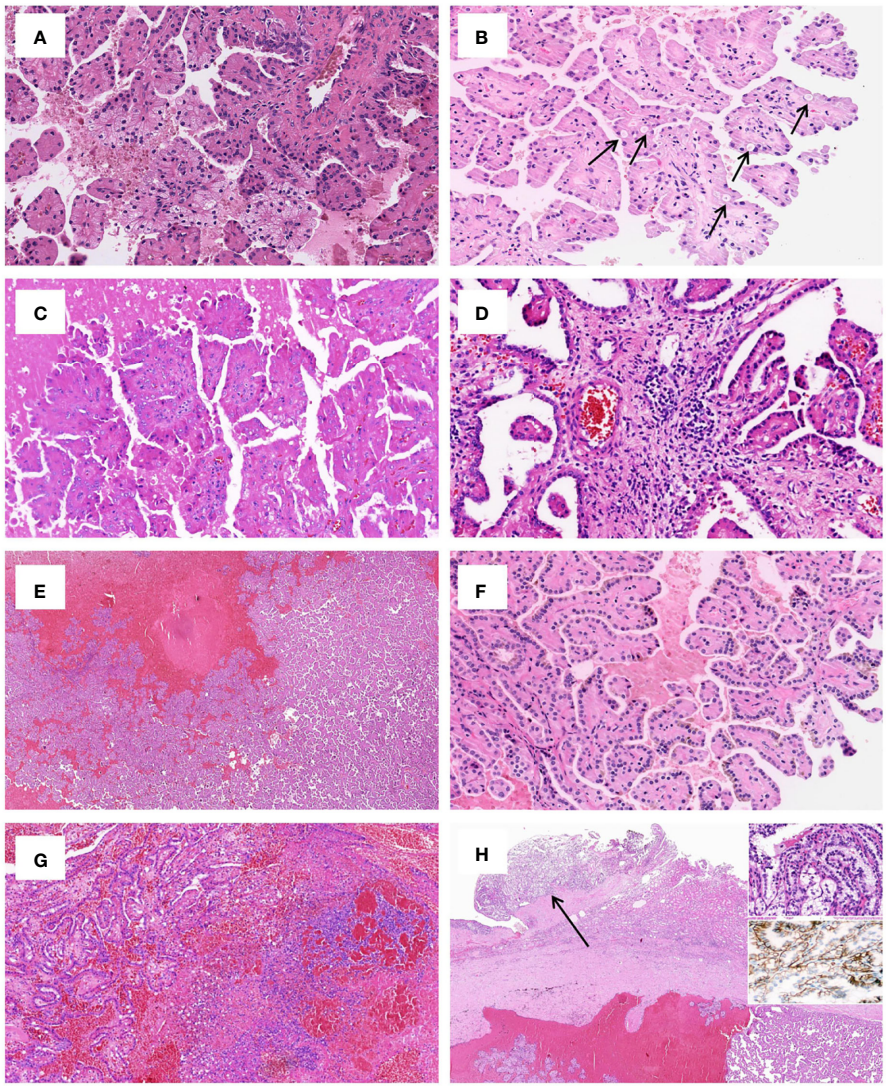

FIGURE 3
Uncommonly seen histologic features of PRNRP. **(A)** Clear cell change (HE, high magnification). **(B)** Intracytoplasmic vacuoles (arrows, HE, high magnification). **(C)** Eosinophilic hobnail cells (HE, high magnification). **(D)** Lymphocyte aggregation and scattered mast cell infiltration in the fibrovascular cores (HE, high magnification). **(E)** Cystic change with blood clots (HE, low magnification). **(F)** Intracellular hemosiderin deposition (HE, high magnification). **(G)** Infarct-type necrosis (HE, medium magnification). **(H)** PRNRP coexisting with an adjacent clear cell papillary renal cell carcinoma (arrow, HE, low magnification). ***Inserts*** showing clear cells with nuclei aligned circumferentially (right upper, HE, high magnification) and "cup-like" CAIX expression (right middle, high magnification).

of foamy macrophages, and mitoses in all tumors. Subsequent studies expanded the morphological spectrum of PRNRP to include eosinophilic hobnail cells (16, 22, 23), clear cell change on the tumor cells (18, 22, 23), peritumoral lymphoid cuff (15, 22), foamy histiocyte aggregation (15, 16, 18, 22), intracellular hemosiderin (22, 23), and lymphocyte or mast cell infiltration in the stroma (15, 16, 22, 23). These morphologies are typically focal and only present in a small subset of cases. The cases in our cohort had comparable findings except for foamy histiocyte aggregation, which were not identified. Tong et al. (16) reported that 8/10 cases had focal areas showing hobnail cells with abundant eosinophilic cytoplasm. Chang et al. (22) demonstrated that 60% (6/10) of their cases had focal hobnail features. In the most recently published to date study on the largest series of PRNRPs, Al-Obaidy et al. (23) found that hobnail conformation was present in only 3 out of the 50 cases. We found eosinophilic hobnail features in 2 of the 16 cases. Despite the presence of hobnail features, all of these reported cases had non-overlapping and WHO/ISUP low-grade nuclei. Although Kim et al. (15) reported 4/30 (13%) of their cases with WHO/ISUP grade 3 nuclei, our cases and other studies only found WHO/ISUP grade 1 or 2 nuclei in PRNRPs.

TABLE 2 Immunohistochemistry staining features of PRNRP.

Case no.	GATA3	34βE12	AMACR	E-cadherin*	PAX8	CK7	CD10	CD117	Vimentin	CAIX
1	+	+	+ (weak)	+	+	+	–	–	–	–
2	+	+	+ (weak)	+	+	+	–	–	–	–
3	+	+	+ (weak)	+	+	+	–	–	–	–
4	+	+	–	–	+	+	–	–	–	–
5	+	+	+ (weak)	+	+	+	–	–	–	–
6	+	+	+ (weak)	+	+	+	–	–	–	–
7	+	+	–	+	+	+	–	–	–	–
8	+	+	–	–	+	+	+(focal and weak)	–	–	–
9	+	+	+ (weak)	+	+	+	–	–	+ (focal)	–
10	+	+	+ (weak)	+	+	+	–	–	–	–
11	+	+ (focal)	+ (weak)	+	+	+	+ (focal and weak)	–	–	–
12	+	–	–	+	+	+	–	–	–	–
13	+	–	+ (weak)	+	+	+	–	–	–	–
14	+	+	+ (weak)	+	+	+	+ (focal and weak)	–	–	–
15	+	–	+ (weak)	+	+	+	–	–	–	–
16	+	–	–	+	+	+	–	–	–	–

*basolateral-membranous staining pattern.

Foamy histiocytes are uncommonly seen in PRNRPs; when present, they typically appeared as loose, scattered macrophages floating within the edematous cores (13), contrasting sharply to the tight clusters in papillary RCC. We identified foci of infarct-type necrosis in our case 12, which is exceptional for PRNRP, as tumor necrosis was consistently absent in previously documented cases. We speculate that infarct formation in this case is related to intralesional hemorrhage and cystic degeneration, which leads to the increased pressure in the cystic cavity, further resulting in ischemic infarction of the tumor. However, it should be mentioned that the cysts are commonly filled with proteinaceous fluid or blood clots and may contain floating degenerated cell debris with hemosiderin deposition, which may be confused with necrosis; however, true tumor type coagulative necrosis is never present in PRNRPs (23).

In the current study, all PRNRP cases exhibited a diffuse and strong expression of PAX8, CK7, and GATA3, whereas the expression of AMACR, CD10, and vimentin was either absent or only weak and focal, and the tumor cells were completely negative for CD117 and CAIX. The immunohistochemical profiles of PRNRP in our cohort are in line with the results in a recent meta-analysis by Wei and colleagues (19). In three previous reports, it was disclosed that PRNRP usually displayed a diffuse L1CAM expression typically in a basolateral and lateral membrane pattern, leading to a "cup-like" staining appearance (13, 15, 23). As L1CAM is not available in our laboratory, we performed immunostaining for E-cadherin and found that it was expressed in 14/16 (87.5%) of our PRNRP cases and all the 14 cases showed a "cup-like" staining pattern identical to that of L1CAM. Only one previous study has investigated the expression of E-cadherin in PRNRP. Kim et al. (15) found that 23/30 (77%) of their cases showed positive reactivity to E-cadherin with the expression being significantly higher than both PRCC types 1 and 2; however, they did not specify the staining pattern in their study. In the present study, we found that 12/16 (75%) PRNRPs were strongly positive for 34βE12, with staining being diffusely in 11 and focally in 1, consistent with the results reported by Zhou et al. (17), who found that all the seven cases of PRNRP in their study strongly expressed 34βE12. These data suggest that 34βE12 may serve as a sensitive marker for the diagnosis of PRNRP. Co-expression of GATA3 and 34βE12 is relatively rare in renal cell tumors and is often seen in tumors of distal nephron or collecting duct origin, such as collecting duct carcinoma (29, 30) and clear cell papillary RCC (31, 32). For the latter, studies have demonstrated that both GATA3 and 34βE12 can be used as sensitive and specific markers for its diagnosis and differential diagnosis (31, 32). With regard to the cell origin, the co-expression of GATA3 and 34βE12 in PRNRP may also point to its distal nephron origin. Using public data sets, Tong et al. (16) found that PRNRP shared similar gene expression profiles with cortical collecting duct, suggesting that PRNRP may potentially originate from the distal renal tubule. In addition, a negative or focal/weak expression of proximal renal tubule markers, such as vimentin, CD10, CD15, and AMACR (33), also supports this speculation. In a most recently published abstract, using unsupervised clustering analysis, Park and colleagues (34) found that PRNRPs formed a tight group on tSNE and were distant from PRCCs while close to clear cell papillary RCCs, further supporting this hypothesis.

At the molecular genetic level, NGS revealed in our cohort that PRNRP contained *KRAS* mutation at a high frequency (13/

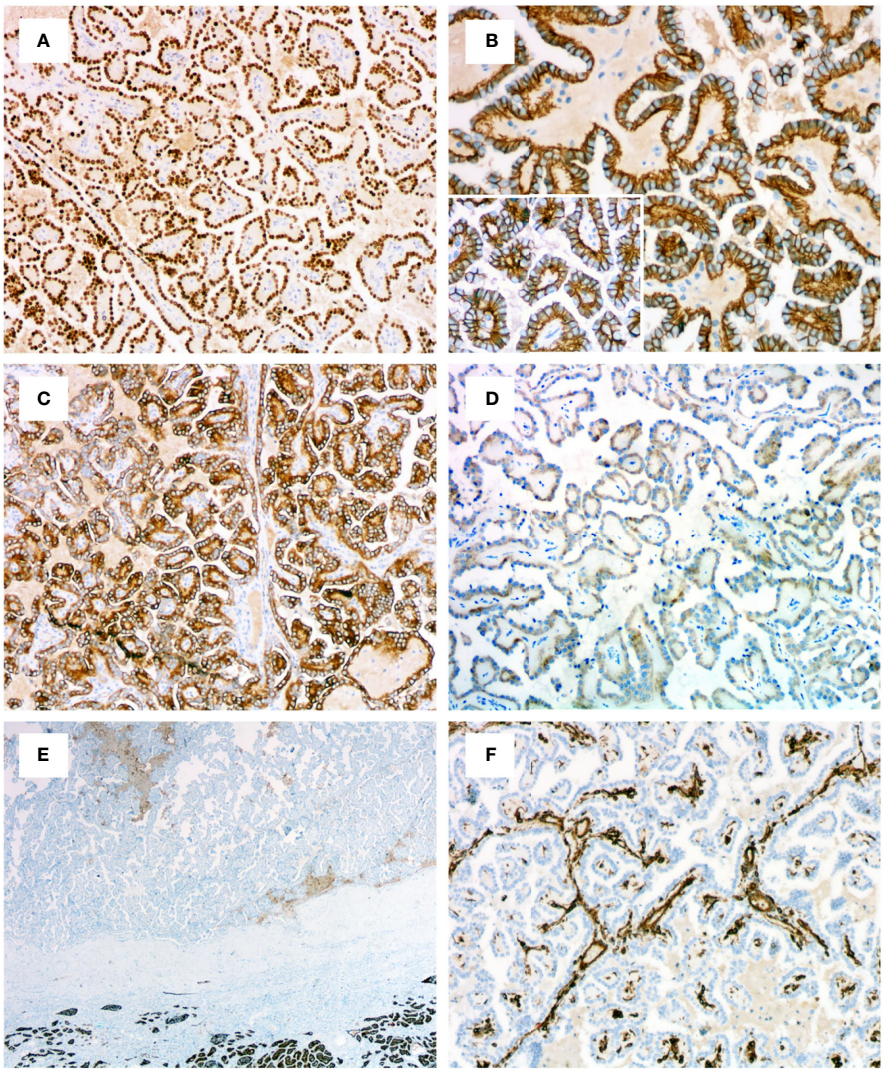

FIGURE 4
Immunohistochemical profiles of PRNRP. **(A)** Diffusely and strongly positive for GATA3 (medium magnification). **(B)** Basolateral-membranous/"cup-like" staining pattern of E-cadherin (high magnification). **(C)** Positive for 34βE12 (medium magnification). **(D)** Weakly positive for AMACR (medium magnification). Negative for CD10 (**E**, low magnification) and vimentin (**F**, medium magnification).

14, 93%). The one without *KRAS* mutation (case 14) showed typical morphological and immunohistochemical features consistent with PRNRP. *KRAS* missense mutations clustered in codon 12 in exon 2, with c.35G>T (p.G12V, 54%), c.35G>A (p.G12D, 31%), and c.34G>T (p.G12C, 15%). The AF ranged from 9.2% to 33%, supporting the somatic origin. There was no correlation between histologic phenotype and *KRAS* mutant genotype. Case 13 showed a predominantly tubular growth pattern which had immunohistochemical features identical to those with prominent papillary morphology. This case harbored a *KRAS* mutation with c.35G>T (p.G12V). *KRAS* mutation was identified in 57%–93% of PRNRPs in previous studies (14–16, 18, 19, 22, 23), with an overall frequency of 85% and the most common *KRAS* mutation being p.G12V (54%), as documented by Wei et al. (19). One *KRAS*-mutated PRNRP was reported to harbor a G12A/V/D complex mutation (23). In the past research, other somatic mutations detected by NGS in PRNRP included mutations in *BRCA2*, *BRIP1*, *RAD50*, *TP53*, and *BRAF* (14, 15, 18). Chang et al. (22) demonstrated recurrent activating *KRAS* mutation in six of eight cases of type D PA, which shows identical morphology and immunophenotype to PRNRP (21). Additionally, Al-Obaidy et al. (23) found *KRAS* mutation in 44% (15/34) of the microscopic (<5 mm) PRNRPs, and in 88% (14/16) of the clinically detected (≥5 mm) ones. These findings indicate that *KRAS* mutation may be an early molecular event in the tumorigenesis or progression of PRNRP, and type D PA may represent an analogue or a small-sized PRNRP (22, 23). *KRAS* missense mutation rarely appeared in other types of RCC, and

TABLE 3 Targeted next-generation sequencing findings of PRNRP.

Case no.	SNV	Amino acid changes	AF (%)
1	c.35G>T	p.G12V	32.61%
2	c.35G>T	p.G12V	32.98%
3	c.34G>T	p.G12C	29.66%
4	ND	——	——
5	ND	——	——
6	c.35G>T	p.G12V	9.17%
7	c.35G>A	p.G12D	14.28%
8	c.35G>T	p.G12V	13.29%
9	c.35G>A	p.G12D	25.66%
10	c.34G>T	p.G12C	30.97%
11	c.35G>A	p.G12D	18.14%
12	c.35G>A	p.G12D	10.31%
13	c.35G>T	p.G12V	9.72%
14	Negative	Negative	Negative
15	c.35G>T	p.G12V	20.39%
16	c.35G>T	p.G12V	20.63%

AF, allele frequency; ND, not done; SNV, single-nucleotide variant.

only Raspollini et al. (35) reported a case of clear cell RCC harboring *KRAS* mutation. Several previous studies have documented that *KRAS* mutation was absent in clear cell RCC, PRCC (both types 1 and 2), chromophobe RCC, and clear cell papillary RCC (14, 15, 23). According to TCGA database, mutation of *KRAS* occurred in 0.7% (2/279) of PRCCs and 0.2% (1/451) of clear cell RCCs (14–16). Five tumors harboring a *KRAS* mutation have been registered as PRCC in the TCGA database; however, different groups have reviewed these tumors independently and concluded that three of these tumors in fact represented PRNRP (14–16). These above findings suggest that *KRAS* mutation is a consistent and unique finding in PRNRP and can serve as a powerful molecular tool for the accurate diagnosis of PRNRP when at challenging settings. Bioinformatics analysis has shown that a prominent *KRAS* signature is associated with activation of several important

TABLE 4 Fluorescence *in-situ* hybridization findings of PRNRP.

	Chromosome 7			Chromosome 17			Chromosome Y	
Case no.	1G(%)	2G(%)	3G(%)	1G(%)	2G(%)	3G(%)	1G(%)	1R1G(%)
1	6	71	23	4	76	20	——	——
2	4	91	5	4	92	4	5	95
3	15	83	2	14	84	2	2	98
4	ND	ND	ND	ND	ND	ND	ND	ND
5	22	75	3	39	58	3	3	99
6	28	66	6	35	63	2	2	98
7	21	67	2	31	63	5	1	99
8	24	76	0	31	65	4	——	——
9	18	77	5	21	78	1	——	——
10	5	92	3	68	21	11	——	——
11	10	87	3	40	58	2	——	——
12	33	64	3	31	66	3	25	75
13	5	92	3	55	34	11	68	32
14	41	56	3	49	47	4	76	24
15	45	49	6	39	54	7	——	——
16	7	89	4	37	56	7	——	——

G, green; ND, not done; R, red.

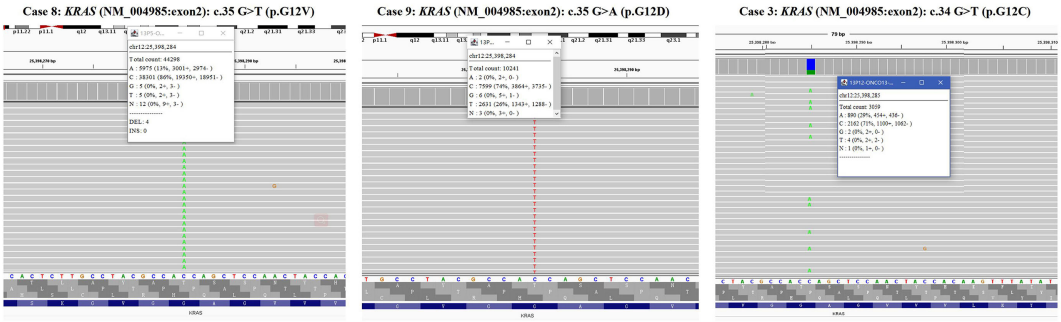

FIGURE 5
KRAS mutations in PRNRP. Integrative Genomics Viewer screenshot of the representative *KRAS* mutation hotspot, including c.35 G>T (p.G12V) (case 8), c.35G>A (p.G12D)(case 9), and c.34G>T(p.G12C)(case 3).

transcription factor networks, including GATA3 (36). In addition, overexpression of GATA3 was found in *KRAS*-driven lung cancer cells and further promoted the oncogenesis *via* microRNAs (37). These aforementioned evidence may explain the potential link between the genotype and immunophenotype of PRNRP; however, the function of mutated *KRAS* in the pathogenesis or progression of PRNRP requires further investigations. Trisomy of chromosome 7 and/or 17 and/or deletion of Y chromosome have been shown to be chromosomal abnormalities characteristic of PRCC (38). Prior studies using FISH analysis demonstrated that a subset of PRNRPs shared these specific chromosomal abnormalities with PRCCs (13, 17). However, Kiyozawa et al. (18) and Wei et al. (19) found that no cases of PRNRP had gains of chromosome 7 and/or 17, or loss of the Y chromosome, using copy number alteration analysis and chromosomal microarray analysis, respectively. In the present study, FISH study revealed trisomy 7 and 17 in only one of the 15 PRNRP cases analyzed. Chromosome Y deletion was identified in two of the eight male cases examined. These above findings suggest that the presence of trisomy 7 and/or 17 and loss of Y chromosome in PRNRP is likely to represent a random rather than a recurrent event, contrasting to those in PRCC.

A potential limitation of our study is the relatively short follow-up time for these tumors, although the vast majority of tumors were in the pT1 stage with 1 in the pT2 stage. The current data seem to be inadequate to make a conclusion about the long-term outcomes of this emerging neoplasm entity. Because PRNRP is overall a low-stage tumor with an indolent biological behavior, it is important to differentiate PRNRP from other renal tumors featuring papillary architecture and oncocytic cytoplasm. Differentiation of PRNRP from PRCC type 2 is sometimes difficult, as both of them may display similar histologic appearances. Although reverse polarity of nuclei is one of the characteristic features of PRNRP, it can be focally observed in a subset cases of PRCC type 2 (15). In addition, pseudostratification, a commonly seen feature in PRCC type 2, has also been reported in a few PRNRPs (13, 22). In cases with overlapping histology, immunohistochemical staining and *KRAS* mutation analysis can help for making a correct diagnosis. Positivity for GATA3 and 34βE12 along with negativity for CD10 and vimentin could be useful for supporting PRNRP, while detection of *KRAS* mutation by molecular genetics can further confirm the diagnosis. Since a few RCCs with MiT family alterations may demonstrate oncocytic and papillary RCC-like morphology with reverse polarity of nuclei, it

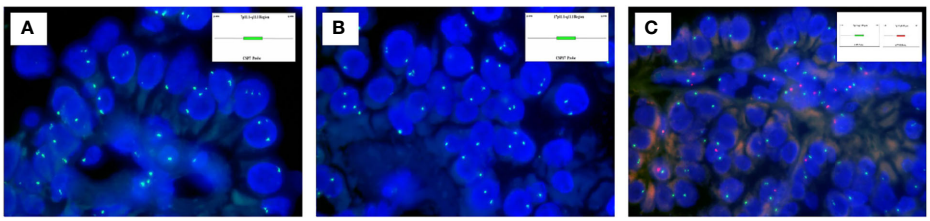

FIGURE 6
Fluorescence *in-situ* hybridization findings of PRNRP. **(A)** Trisomy 7 (case 1). ***Inset*** indicating the schematic diagram of the centromere-specific probe of chromosome 7. **(B)** Trisomy 17 (case 1). ***Inset*** indicating the schematic diagram of the centromere-specific probe of chromosome 7. **(C)** Deletion of chromosome Y (case 13). ***Insets*** indicating schematic diagrams of the centromere-specific probe of chromosome X (green) and chromosome Y(red).

is necessary to exclude these tumors by FISH assays (39). As mentioned above, a diffuse and strong expression of both GATA3 and 34βE12 can also be noted in clear cell papillary RCC (31, 32), which may be confused with PRNRP with focal clear cell change. However, clear cell papillary RCC is characterized by a papillary growth of low-grade clear cells with circumferentially aligned nuclei and lack of the oncocytic cytoplasm and inverted nuclei characteristic of PRNRP. FH-deficient RCC is a highly aggressive renal cancer and shows quite variable morphology; it can have prominent papillary architecture and oncocytic cytoplasm mimicking PRNRP. However, FH-deficient RCC usually has nuclear features of large reddish inclusion-like nucleoli surrounded by a clear halo that can suggest the diagnosis. Loss of FH and 2 succinyl cysteine positivity by IHC and/or detection of *FH* mutation (either germline or somatic) can further confirm the diagnosis (20, 40). Lastly, PRNRP with a prominent tubular pattern may be confused with recently characterized low-grade oncocytic tumor or eosinophilic vacuolated tumor; however, these tumors are frequently associated with mutations involving TSC/MTOR pathways and typically lack the inverted nuclei and GATA3 positivity in PRNRP (41–43).

Conclusions

In summary, PRNRP is a rare renal tumor with an indolent clinical course. We confirm the previous reports that PRNRP is pathologically characterized by papillary or tubulopapillary architecture with frequently cystic change, low-grade tumor cells with oncocytic cytoplasm and inverted nuclear location, diffuse and strong expression of GATA3 and 34βE12, and recurrent *KRAS* mutation. We further expand the histologic spectrum of PRNRP to include the presence of infarct-type necrosis, concurrent with clear cell papillary PRCC, and basolateral and lateral membrane expression of E-cadherin by IHC. Our study further supports that PRNRP should be considered as a novel renal cell tumor entity.

Data availability statement

The original contributions presented in the study are included in the article/supplementary material. Further inquiries can be directed to the corresponding author.

Ethics statement

The studies involving human participants were reviewed and approved by the Institutional Review Board Committee of Zhejiang Provincial People's Hospital, Affiliated People's Hospital, Hangzhou Medical College. Written informed consent for participation was not required for this study in accordance with the institutional requirements.

Author contributions

MS, XY, and MZ conceptualized the study concept and design. MS, YB, and HZ provided the follow-up information and analyzed the clinical data. MS, XY, YB, HZ, XH, XT, and MZ were in charge of the histologic diagnosis and interpretation of immunohistochemistry and analysis of the results of the targeted next-generation sequencing. MS and XY drafted the manuscript. GR, GC, and MZ revised the manuscript. All authors contributed to the article and approved the submitted version.

Funding

This work was supported by Zhejiang Provincial Natural Science Foundation (LY21H160052) and Zhejiang Provincial Medicine and Health Research Foundation (2019KY020, 2019KY029, and WKJ-ZJ-1929). The funders did not have any role in the design and conduct of the study, the analysis and interpretation of the data, and preparation of the manuscript.

Acknowledgments

The authors are grateful to SpaceGen, Xiamen, China, for the NGS service, and Anbiping Laboratory, Guangzhou, China, for FISH analysis.

Conflict of interest

The authors declare that the research was conducted in the absence of any commercial or financial relationships that could be construed as a potential conflict of interest.

Publisher's note

References

1. Delahunt B, Eble JN. Papillary renal cell carcinoma: a clinicopathologic and immunohistochemical study of 105 tumors. *Mod Pathol* (1997) 10(6):537–44.

2. Delahunt B, Eble JN, McCredie MR, Bethwaite PB, Stewart JH, Bilous AM. Morphologic typing of papillary renal cell carcinoma: comparison of growth kinetics and patient survival in 66 cases. *Hum Pathol* (2001) 32(6):590–5. doi: 10.1053/hupa.2001.24984

3. H Moch, PA Humphrey, TM Ulbright and VE Reuter eds. *World health organization classification of tumours of the urinary system and male genital organs. 4th ed*. Lyon: IARC Press (2016).

4. Cancer Genome Atlas Research Network, Linehan WM, Spellman PT, Ricketts CJ, Creighton CJ, Fei SS, et al. Comprehensive molecular characterization of papillary renal-cell carcinoma. *N Engl J Med* (2016) 374 (2):135–45. doi: 10.1056/NEJMoa1505917

5. Chevarie-Davis M, Riazalhosseini Y, Arseneault M, Aprikian A, Kassouf W, Tanguay S, et al. The morphologic and immunohistochemical spectrum of papillary renal cell carcinoma: study including 132 cases with pure type 1 and type 2 morphology as well as tumors with overlapping features. *Am J Surg Pathol* (2014) 38(7):887–94. doi: 10.1097/PAS.0000000000000247

6. Lobo J, Ohashi R, Amin MB, Berney DM, Compérat EM, Cree IA, et al. WHO 2022 landscape of papillary and chromophobe renal cell carcinoma. *Histopathology* (2022). doi: 10.1111/his.14700.

7. Allory Y, Ouazana D, Boucher E, Thiounn N, Vieillefond A. Papillary renal cell carcinoma. prognostic value of morphological subtypes in a clinicopathologic study of 43 cases. *Virchows Arch* (2003) 442(4):336–42. doi: 10.1007/s00428-003-0787-1

8. Lefèvre M, Couturier J, Sibony M, Bazille C, Boyer K, Callard P, et al. Adult papillary renal tumor with oncocytic cells: clinicopathologic, immunohistochemical, and cytogenetic features of 10 cases. *Am J Surg Pathol* (2005) 29(12):1576–81. doi: 10.1097/01.pas.0000184821.09871.ec

9. Kunju LP, Wojno K, Wolf JSJr, Cheng L, Shah RB. Papillary renal cell carcinoma with oncocytic cells and nonoverlapping low grade nuclei: expanding the morphologic spectrum with emphasis on clinicopathologic, immunohistochemical and molecular features. *Hum Pathol* (2008) 39(1):96–101. doi: 10.1016/j.humpath.2007.05.016

10. Xia QY, Rao Q, Shen Q, Shi SS, Li L, Liu B, et al. Oncocytic papillary renal cell carcinoma: a clinicopathological study emphasizing distinct morphology, extended immunohistochemical profile and cytogenetic features. *Int J Clin Exp Pathol* (2013) 6(7):1392–9.

11. Angori S, Lobo J, Moch H. Papillary renal cell carcinoma: current and controversial issues. *Curr Opin Urol* (2022) 32(4):344–51. doi: 10.1097/MOU.0000000000001000

12. Saleeb RM, Brimo F, Farag M, Rompré-Brodeur A, Rotondo F, Beharry V, et al. Toward biological subtyping of papillary renal cell carcinoma with clinical implications through histologic, immunohistochemical, and molecular analysis. *Am J Surg Pathol* (2017) 41(12):1618–29. doi: 10.1097/PAS.0000000000000962

13. Al-Obaidy KI, Eble JN, Cheng L, Williamson SR, Sakr WA, Gupta N, et al. Papillary renal neoplasm with reverse polarity: a morphologic, immunohistochemical, and molecular study. *Am J Surg Pathol* (2019) 43(8):1099–111. doi: 10.1097/PAS.0000000000001288

14. Al-Obaidy KI, Eble JN, Nassiri M, Cheng L, Eldomery MK, Williamson SR, et al. Recurrent KRAS mutations in papillary renal neoplasm with reverse polarity. *Mod Pathol* (2020) 33(6):1157–64. doi: 10.1038/s41379-019-0362-1

15. Kim SS, Cho YM, Kim GH, Kee KH, Kim HS, Kim KM, et al. Recurrent KRAS mutations identified in papillary renal neoplasm with reverse polarity-a comparative study with papillary renal cell carcinoma. *Mod Pathol* (2020) 33 (4):690–9. doi: 10.1038/s41379-019-0420-8

16. Tong K, Zhu W, Fu H, Cao F, Wang S, Zhou W, et al. Frequent KRAS mutations in oncocytic papillary renal neoplasm with inverted nuclei. *Histopathology* (2020) 76(7):1070–83. doi: 10.1111/his.14084

17. Zhou L, Xu J, Wang S, Yang X, Li C, Zhou J, et al. Papillary renal neoplasm with reverse polarity: a clinicopathologic study of 7 cases. *Int J Surg Pathol* (2020) 28(7):728–34. doi: 10.1177/1066896920918289

18. Kiyozawa D, Kohashi K, Takamatsu D, Yamamoto T, Eto M, Iwasaki T, et al. Morphological, immunohistochemical, and genomic analyses of papillary renal neoplasm with reverse polarity. *Hum Pathol* (2021) 112:48–58. doi: 10.1016/j.humpath.2021.03.009

19. Wei S, Kutikov A, Patchefsky AS, Flieder DB, Talarchek JN, Al-Saleem T, et al. Papillary renal neoplasm with reverse polarity is often cystic: report of 7 cases and review of 93 cases in the literature. *Am J Surg Pathol* (2022) 46(3):336–43. doi: 10.1097/PAS.0000000000001773

20. Trpkov K, Hes O, Williamson SR, Adeniran AJ, Agaimy A, Alaghehbandan R, et al. New developments in existing WHO entities and evolving molecular concepts: The genitourinary pathology society (GUPS) update on renal neoplasia. *Mod Pathol* (2021) 34(7):1392–424. doi: 10.1038/s41379-021-00779-w

21. Caliò A, Warfel KA, Eble JN. Papillary adenomas and other small epithelial tumors in the kidney: an autopsy study. *Am J Surg Pathol* (2019) 43(2):277–87. doi: 10.1097/PAS.0000000000001189

22. Chang HY, Hang JF, Wu CY, Lin TP, Chung HJ, Chang YH, et al. Clinicopathological and molecular characterisation of papillary renal neoplasm with reverse polarity and its renal papillary adenoma analogue. *Histopathology* (2021) 78(7):1019–31. doi: 10.1111/his.14320

23. Al-Obaidy KI, Saleeb RM, Trpkov K, Williamson SR, Sangoi AR, Nassiri M, et al. Recurrent KRAS mutations are early events in the development of papillary renal neoplasm with reverse polarity. *Mod Pathol* (2022). doi: 10.1038/s41379-022-01018-6

24. Amin MB, Edge SB, Greene FL, Byrd DR, Brookland RK, Washington MK, et al. AJCC cancer staging manual. *8th ed*. Chicago, IL: Springer (2017).

25. Argani P, Netto GJ, Parwani AV. Papillary renal cell carcinoma with low-grade spindle cell foci: a mimic of mucinous tubular and spindle cell carcinoma. *Am J Surg Pathol* (2008) 32(9):1353–9. doi: 10.1097/PAS.0b013e31816a1c34

26. Wang G, Amin MB, Grossmann P, Ptáková N, Hayes M, Hartmann A, et al. Renal cell tumor with sex-cord/gonadoblastoma-like features: analysis of 6 cases. *Virchows Arch* (2022) 480(2):349–58. doi: 10.1007/s00428-021-03235-x

27. Lobo J, Ohashi R, Helmchen BM, Rupp NJ, Rüschoff JH, Moch H. The morphological spectrum of papillary renal cell carcinoma and prevalence of Provisional/Emerging renal tumor entities with papillary growth. *Biomedicines* (2021) 9(10):1418. doi: 10.3390/biomedicines9101418

28. Lee HJ, Shin DH, Park JY, Kim SY, Hwang CS, Lee JH, et al. Unilateral synchronous papillary renal neoplasm with reverse polarity and clear cell renal cell carcinoma: a case report with KRAS and PIK3CA mutations. *Diagn Pathol* (2020) 15(1):123. doi: 10.1186/s13000-020-01042-7

29. Gonzalez-Roibon N, Faraj SF, Munari E, Bezerra SM, Albadine R, Sharma R, et al. Comprehensive profile of GATA binding protein 3 immunohistochemical expression in primary and metastatic renal neoplasms. *Hum Pathol* (2014) 45 (2):244–8. doi: 10.1016/j.humpath.2013.08.020

30. Qian X, Wang Z, Zhang J, Wang Q, Zhou P, Wang S, et al. Clinical features and prognostic outcome of renal collecting duct carcinoma: 12 cases from a single institution. *Cancer Manag Res* (2020) 12:3589–95. doi: 10.2147/CMAR.S244094

31. Mantilla JG, Antic T, Tretiakova M. GATA3 as a valuable marker to distinguish clear cell papillary renal cell carcinomas from morphologic mimics. *Hum Pathol* (2017) 66:152–8. doi: 10.1016/j.humpath.2017.06.016

32. Martignoni G, Brunelli M, Segala D, Munari E, Gobbo S, Cima L, et al. Validation of 34betaE12 immunoexpression in clear cell papillary renal cell carcinoma as a sensitive biomarker. *Pathology* (2017) 49(1):10–8. doi: 10.1016/j.pathol.2016.05.014

33. Truong LD, Shen SS. Immunohistochemical diagnosis of renal neoplasms. *Arch Pathol Lab Med* (2011) 135(1):92–109. doi: 10.5858/2010-0478-RAR.1

34. Park K, Serrano J, Tran I, Feng X, Chen F, Vasudevaraja V, et al. Methylation profiling of papillary renal neoplasm with reverse polarity. *Mod Pathol* (2022) 35(SUPPL 2):655–6.

35. Raspollini MR, Castiglione F, Martignoni G, Lapini A, Cheng L, Montironi R, et al. Multiple and bilateral kidney tumors with clear cells of three different histotypes: A case report with clinicopathologic and molecular study. *APMIS* (2016) 124(7):619–23. doi: 10.1111/apm.12536

36. Peng D, Guo Y, Chen H, Zhao S, Washington K, Hu T, et al. Integrated molecular analysis reveals complex interactions between genomic and epigenomic alterations in esophageal adenocarcinomas. *Sci Rep* (2017) 7:40729. doi: 10.1038/srep40729

37. Valencia K, Erice O, Kostyrko K, Hausmann S, Guruceaga E, Tathireddy A, et al. The Mir181ab1 cluster promotes KRAS-driven oncogenesis and progression in lung and pancreas. *J Clin Invest* (2020) 130(4):1879–95. doi: 10.1172/JCI129012

38. Jiang F, Richter J, Schraml P, Bubendorf L, Gasser T, Sauter G, et al. Chromosomal imbalances in papillary renal cell carcinoma: genetic differences between histological subtypes. *Am J Pathol* (1998) 153(5):1467–73. doi: 10.1016/S0002-9440(10)65734-3

39. Skala SL, Xiao H, Udager AM, Dhanasekaran SM, Shukla S, Zhang Y, et al. Detection of 6 TFEB-amplified renal cell carcinomas and 25 renal cell carcinomas with MITF translocations: systematic morphologic analysis of 85 cases evaluated by clinical TFE3 and TFEB FISH assays. *Mod Pathol* (2018) 31(1):179–97. doi: 10.1038/modpathol.2017.99

40. Lau HD, Chan E, Fan AC, Kunder CA, Williamson SR, Zhou M, et al. A clinicopathologic and molecular analysis of fumarate hydratase-deficient renal cell carcinoma in 32 patients. *Am J Surg Pathol* (2020) 44(1):98–110. doi: 10.1097/PAS.0000000000001372

41. Argani P, Mehra R. Renal cell carcinoma associated with tuberous sclerosis complex (TSC)/mammalian target of rapamycin (MTOR) genetic alterations. *Mod Pathol* (2022) 35(3):296–7. doi: 10.1038/s41379-021-00971-y

42. Kapur P, Gao M, Zhong H, Chintalapati S, Mitui M, Barnes SD, et al. Germline and sporadic mTOR pathway mutations in low-grade oncocytic tumor of the kidney. *Mod Pathol* (2022) 35(3):333–43. doi: 10.1038/s41379-021-00896-6

43. Farcaş M, Gatalica Z, Trpkov K, Swensen J, Zhou M, Alaghehbandan R, et al. Eosinophilic vacuolated tumor (EVT) of kidney demonstrates sporadic TSC/MTOR mutations: next-generation sequencing multi-institutional study of 19 cases. *Mod Pathol* (2022) 35(3):344–51. doi: 10.1038/s41379-021-00923-6

frontiers | Frontiers in Oncology

TYPE Original Research
PUBLISHED 17 August 2022
DOI 10.3389/fonc.2022.949962

OPEN ACCESS

EDITED BY
Ming Zhao,
Zhejiang Provincial People's Hospital, China

REVIEWED BY
Joon Hyuk Choi,
Yeungnam University, South Korea
Anjia Han,
The First Affiliated Hospital of Sun Yat-sen University, China

*CORRESPONDENCE
Hongying Zhang
hy_zhang@scu.edu.cn

†These authors have contributed equally to this work

SPECIALTY SECTION
This article was submitted to Surgical Oncology, a section of the journal Frontiers in Oncology

RECEIVED 22 May 2022
ACCEPTED 27 July 2022
PUBLISHED 17 August 2022

CITATION
Xie Y, Jing W, Zhao W, Peng R, Chen M, Lan T, Peng H, He X, Chen H, Zhang Z and Zhang H (2022) Primary intrathoracic liposarcomas: A clinicopathologic and molecular study of 43 cases in one of the largest medical centers of China. *Front. Oncol.* 12:949962. doi: 10.3389/fonc.2022.949962

Primary intrathoracic liposarcomas: A clinicopathologic and molecular study of 43 cases in one of the largest medical centers of China

You Xie[1†], Wenyi Jing[1†], Wei Zhao[1], Ran Peng[1], Min Chen[1], Ting Lan[2], Heng Peng[1], Xin He[1], Huijiao Chen[1], Zhang Zhang[1] and Hongying Zhang[1*]

[1]Department of Pathology, West China Hospital, Sichuan University, Chengdu, China, [2]Department of Pathology, Sichuan Cancer Hospital and Institute, Sichuan Cancer Center, Cancer Hospital Affiliate to School of Medicine, University of Electronic Science and Technology of China, Chengdu, China

Introduction: Primary intrathoracic liposarcoma is extremely rare, and most published series lack genetic analyses. The aim of our study is to better understand the clinicopathologic and genetic features of these rare lesions.

Materials and methods: Forty-three primary intrathoracic liposarcomas were identified and most cases were analyzed by systematic genetic studies, including fluorescence *in situ* hybridization (FISH), whole-exome sequencing (WES), and Sanger sequencing.

Results: This series included 27 males and 16 females (ratios, 1.68:1) aged 24-73 years (median, 53 years). Tumors mainly occurred in the mediastinum (n=23, 53.5%), followed by pleural cavity (n=16, 37.2%) and lung (n=4, 9.3%). The study included 21 well-differentiated liposarcomas (WDLs), 19 dedifferentiated liposarcomas (DDLs), 2 myxoid pleomorphic liposarcomas (MPLs) and 1 pleomorphic liposarcoma (PL), without identification of myxoid liposarcoma. FISH analysis identified *MDM2* amplification in 17 of 18 WDLs (94.4%) and all DDLs (16/16, 100.0%). The *MDM2*-nonamplified WDL was *CDK4*-nonamplified but *FRS2*-amplified. WES and Sanger sequencing found somatic *TP53* mutation in the 2 MPLs. Follow-up information was available for 33 of 38 cases (86.8%). Thirteen patients (39.4%) showed no evidence of disease, 10 patients (30.3%) were alive with disease, and 8 patients (24.2%) died of disease. Fourteen cases developed recurrence and 1 with metastasis.

Conclusions: WDL/DDL was the overwhelming subtype in this location, followed by MPL and PL. Analysis of the *FRS2* gene, in combination with *MDM2* and other genes of 12q13-15, may more precisely characterize WDL/

DDLs. MPL is the most fatal subtype of this site. Further studies are needed to explore the role of *TP53* in the pathogenesis of MPL.

KEYWORDS

liposarcoma, thorax, molecular analysis, well-differentiated liposarcoma, dedifferentiated liposarcoma, myxoid pleomorphic liposarcoma

Introduction

Liposarcoma is one of the most common soft tissue malignancies. The recent fifth World Health Organization (WHO) Classification of Tumors of Soft Tissue and Bone divided liposarcoma into 4 major clinicopathologic and genetic subtypes: atypical lipomatous tumor (ALT)/well-differentiated liposarcoma (WDL)/dedifferentiated liposarcoma (DDL), myxoid liposarcoma (ML), pleomorphic liposarcoma (PL), and myxoid pleomorphic liposarcoma (MPL) (1–5). ALT/WDL/DDL accounts for 50-60% of all liposarcomas and is characterized by the amplification of 12q13-15, including several oncogenes, such as *MDM2*, *CDK4*, *FRS2*, *HMGA2*, and *CPM*. The term "ALT" is used for tumors located in the site where surgical excision can be carried out and is curative, and the term "WDL" is used for lesions arising in sites such as the retroperitoneum, spermatic cord, and mediastinum, where tumors have a greater possibility for progression (1, 2). Nearly 20-30% of liposarcomas are MLs, most of which are characterized by the *FUS-DDIT3* fusion gene and a subset of tumors harboring the *EWSR1-DDIT3* fusion gene (3). PL represents less than 5% of liposarcoma with complex chromosomal aberrations (4). The newly proposed subtype, MPL, is an extremely rare and highly aggressive tumor (5).

Most liposarcomas occur in deep soft tissue of the extremities, followed by the retroperitoneum and trunk, although the location of liposarcomas depends on their subtype. Primary intrathoracic liposarcoma is very rare, accounting for only 1-2% of all liposarcomas (6). To the best of our knowledge, there were only 7 relatively large series of primary intrathoracic liposarcoma in the English literature, with clinical and pathologic information (7–13). However, the majority of previous series studies only reported mediastinal liposarcoma, without pleural and pulmonary tumors. Moreover, most series lacked systematic genetic studies, and only two previous large series explored genetic changes by fluorescence *in situ* hybridization (FISH) in 2/18 (11.1%) and 10/24 (41.7%) of their cases, respectively (10, 12).

Therefore, to better understand the clinicopathologic and genetic features of these rare lesions, we report a large series of 43 cases of primary intrathoracic liposarcomas from one of the largest medical centers in China. To the best of our knowledge, this is the largest population-based analysis with the highest rate for molecular testing in the English literature. Genetic analyses, including FISH, whole-exome sequencing (WES), and Sanger sequencing, were carried out in most cases (>90%).

Materials and methods

Case identification

This study was approved by the West China Hospital Institutional Review Board. A SNOMED search of hospital surgical pathology files from January 2007 to June 2021 identified 1386 liposarcoma cases. Seventy-eight liposarcomas were identified as intrathoracic liposarcomas, of which 35 tumors were metastatic or extended from other locations. All metastatic intrathoracic liposarcomas, primary cardiac liposarcomas, and intimal sarcomas arising in large blood vessels were excluded from the study. Finally, forty-three (43/1386, 3.1%) were included as primary intrathoracic liposarcomas in this study.

Radiology methods

All available images of the cases were reviewed by one radiologist with thoracic tumor imaging expertise. Several parameters were evaluated, consisting of tumor margin and heterogeneity, pleural effusion, calcification, necrosis, cystic change and the involvement of other organs.

Histologic evaluation

All cases were reviewed by 2 pathologists (H.Z., H.C.) with soft tissue tumor pathology expertise and 3 general surgical pathologists (Y.X., W.J., W.Z.) according to well-described criteria. Grading was evaluated following the 'modified' French Federation of Cancer Centers (FNCLCC) grading system (14).

Immunohistochemistry (IHC)

Immunohistochemical analysis was performed on formalin-fixed, paraffin-embedded tissue using the Dako Envision Plus detection system (Dako, Carpinteria, CA, USA) with controls. The antibodies used included MDM2 (clone SMP14, ready-to-use; Abcam, Cambridge, UK), CDK4 (clone EP180, 1:100; Santa Cruz Biotechnology, Santa Cruz, CA, USA), S-100 protein (clone 4C49, 1:100; Abcam, Cambridge, UK), CD34 (clone QBEnd 10, 1:100; Abcam, Cambridge, UK), desmin (clone D33, 1:100; Dako, Carpinteria, CA, USA), smooth muscle actin (SMA) (clone 1A4, 1:100; Dako, Carpinteria, CA, USA), H-caldesmon (clone h-CD, 1:100; Dako, Carpinteria, CA, USA), and p53 (clone Do-7, ready-to-use; Dako, Carpinteria, CA, USA).

Fluorescence *in situ* hybridization (FISH)

FISH analysis was conducted on formalin-fixed, paraffin-embedded 4-μm-thick tissue sections of 41 cases that had material available for further study. Additionally, FISH for the *CDK4* and *FRS2* was performed on the *MDM2* nonamplified case but with a potential diagnosis of WDL. *MDM2*, *CDK4*, *FRS2*, *DDIT3*, *HMGA2*, and *RB1* FISH analyses were performed using the commercially available Vysis *MDM2* Dual Color Probe (Abbott Molecular, Des Plaines, IL, USA), GSP *CDK4* (12q14) Gene Amplification Probe (Anbiping, Guangzhou, China), GSP *FRS2* (12q15) Gene Amplification Probe (Anbiping, Guangzhou, China), Vysis LSI *DDIT3* Dual Color Break Apart Probe (Abbott Molecular, Des Plaines, IL, USA) and Vysis LSI 13 (*RB1*) 13q14 Spectrum Orange Probe (Abbott Molecular, Des Plaines, IL, USA). All FISH analyses were performed according to a previously established laboratory protocol (15–17). Each case was examined and evaluated by counting a minimum of 100 nuclei by two independent investigators (H.Z. and M.C.). *MDM2*, *CDK4* or *FRS2* amplification was defined as an *MDM2*/CEP12, *CDK4*/CEP12 or *FRS2*/CEP12 ratio ≥2.0, and a ratio <2.0 was considered nonamplified. *DDIT3* gene rearrangement was defined as ≥ 10% cells exhibiting the split signal pattern, that is, the distance between the green and red signals was greater than the diameter of two signals. Cells containing *RB1* deletion displayed only one orange signal pattern. *RB1* deletion was defined as more than 25% of the cells exhibiting the deletion pattern.

Whole exome sequencing (WES)

WES was performed on one MPL case (case 42) by Genomic OE Biotech Co., Ltd. (Shanghai, China). Genomic DNA was extracted using a QIAamp DNA Mini Kit (Qiagen, Valencia, CA, USA), and the quantification and integrity of DNA were identified by a Nanodrop spectrophotometer (Thermo Fisher Scientific, Inc., Wilmington, DE, USA). Genomic DNA samples were captured on an Agilent SureSelect whole exome library following the manufacturer's protocol. In brief, genomic DNA was sheared, purified immediately and ligated with adapters. The amplification of the libraries was conducted by polymerase chain reaction (PCR) and then hybridized with custom probes. The bound DNA fragments were washed and eluted; then, these libraries were sequenced on the Illumina sequencing platform (HiSeq X-10, Illumina, Inc., San Diego, CA, USA), and 150 bp paired-end reads were generated.

TP53 mutation analysis

TP53 mutation analysis was performed on the 2 MPL cases (including tumors and their adjacent normal tissues) by PCR and Sanger sequencing according to a previously reported method (15). Primers were used as follows: *TP53*-F: TCCCAAGCAATGGATGATTT, *TP53*-R: TTCTGGGAAGGG ACAGAAGA. Sanger sequencing was performed by Tsingke Biological Technology Co., Ltd. (Chengdu, China).

Statistical analysis

For survival analysis, overall survival (OS) was defined as time from disease diagnosis to death from tumor. DFS (disease-free survival) was defined as time from complete resection until local recurrence or metastasis. OS and DFS were analyzed using the Kaplan-Meier method followed with log- rank test. Data were analyzed using SPSS version 20.0 (IBM Corp, Armonk, NY, USA). $P < 0.05$ indicates the statistical significance between different groups.

Results

Clinical findings

The clinicopathologic findings of the 43 patients are summarized in Table 1. This study comprised 27 males and 16 females (ratios, 1.68:1) with a median age of 53 years (range, 24 to 73 years). The tumors involved the mediastinum (23/43, 53.5%), pleura space (16/43, 37.2%), and lung (4/43, 9.3%). Among the 23 mediastinal cases, 6 tumors involved anterior mediastinum (6/23, 26.1%), 4 in the posterior mediastinum (4/23, 17.3%), 3 in the superior mediastinum (3/23, 13.1%), and 3 tumors (3/23, 13.1%) extensively involved multiple mediastinal compartments. The remaining 7 (7/23, 30.4%) stated no definite mediastinal location.

TABLE 1 Clinicopathologic features of 43 primary intrathoracic liposarcomas.

Case No.	Age/ sex	Symptoms	Size (cm)	Location	Histology	IHC results	Genetic results	Treatment	Outcome/ Follow-up duration
1	56/F	Cough, Short of breath	NA	Pleura space	WDL (lipoma-like)	ND	Failed	Marginal excision	AWD/113 mo
2	43/M	Cough	NA	Mediastinum	WDL (lipoma-like)	ND	*MDM2* +(FISH)	Biopsy only	Lost
3	65/M	Chest pain	6	Left pleura space	WDL (lipoma-like)	CDK4+	Failed	Complete excision	ANED/93 mo
4	57/F	Cough	20	Right pleura space	WDL (lipoma-like)	ND	*MDM2*-, *CDK4*-, *FRS2* + (FISH)	Complete excision	ANED/16 mo
5	70/F	Asymptomatic	26	Anterior mediastinum	WDL (lipoma-like) (original diagnosis: WDL)	MDM2+	*MDM2* +(FISH)	Marginal excision	Recurrence at 5 mo, 20 mo, and 53mo resected; DOD/70 mo
6	43/F	Chest tightness,	12	Middle and posterior mediastinum	WDL (lipoma-like)	MDM2+, CDK4+	*MDM2* +(FISH)	Complete excision	ANED/48 mo
7	64/M	Asymptomatic	22	Left pleura space	WDL (lipoma-like)	ND	*MDM2* +(FISH)	Complete excision	Recurrence at 31 mo, resected and RT; AWD/ 36 mo
8	42/M	Asymptomatic	18	Anterior mediastinum	WDL (lipoma-like) with myxoid change	MDM2+, CDK4+	*MDM2* +(FISH)	Complete excision	Lost
9	69/M	Asymptomatic	23	Posterior mediastinum	WDL (sclerosing and lipoma-like) with myxoid change	MDM2+, CDK4+	*MDM2* +(FISH)	Complete excision	ANED/35 mo
10	73/F	Cough	20	Right pleura space	WDL (inflammatory and lipoma-like) (original diagnosis: WDL)	MDM2+, CDK4+	*MDM2* +(FISH)	Marginal excision	Recurrence at 37 mo, 61 mo and 72 mo, resected; DOD/72 mo
11	50/M	Asymptomatic	12	Superior mediastinum (the right side)	WDL (lipoma-like) with myxoid change (original diagnosis: liposarcoma)	ND	*MDM2* +(FISH)	Marginal excision	Recurrence at 84 mo, resected and RT; AWD/ 161 mo
12	64/F	Asymptomatic	6.4	Anterior mediastinum	WDL (lipoma-like) (original diagnosis: DDL with myxofibrosarcoma-like differentiation)	MDM2+, CDK4+	*MDM2*+, no *RB1* loss (FISH)	Marginal excision	Recurrence at 22 mo, resected; NED/42 mo
13	46/F	Short of breath	NA	Pleura space (the whole)	WDL (lipoma-like) with myxoid change (original diagnosis spindle cell liposarcoma, spindle cell lipoma)	MDM2+, CDK4+	*MDM2*+, no *RB1* loss (FISH)	Marginal excision	Recurrence at 32 mo, resected; AWD/39 mo
14	38/F	Asymptomatic	NA	Anterior mediastinum	WDL (lipoma-like)	ND	*MDM2* +(FISH)	Marginal excision; CT, RT	Recurrence at 33 and 66 mo, resected; AWD/120 mo
15	65/M	Asymptomatic	11	Superior mediastinum (the right side)	WDL (inflammatory), with myxoid change	ND	ND	Complete excision	DFU/53 mo

(Continued)

TABLE 1 Continued

Case No.	Age/ sex	Symptoms	Size (cm)	Location	Histology	IHC results	Genetic results	Treatment	Outcome/ Follow-up duration
16	56/M	Asymptomatic	10.5	Left pleura space (involving to lung)	WDL (inflammatory) (original diagnosis inflammatory pseudotumor)	MDM2+, CDK4+	*MDM2* +(FISH)	Complete excision	ANED/37 mo
17	53/M	Cough, Expectoration	17	Posterior mediastinum	WDL (sclerosing and lipoma-like)	MDM2+, CDK4+	*MDM2* +(FISH)	Marginal excision	AWD/17 mo
18	37/F	Cough	12	Posterior mediastinum	WDL (sclerosing and lipoma-like)	MDM2+, CDK4+	*MDM2* +(FISH)	Marginal excision	Recurrence at 36 mo, RT+CT; AWD/43 mo
19	57/M	Asymptomatic	19.2	Right and posterior mediastinum	WDL (sclerosing and lipoma-like) with myxoid change	MDM2+, CDK4+	*MDM2* +(FISH)	Complete excision	ANED/42 mo
20	44/M	Short of breath	35	Posterior mediastinum	WDL (sclerosing and lipoma-like)	MDM2+, CDK4+	*MDM2* +(FISH)	Marginal excision; CT, RT	Recurrence at 16 and 28 mo, resected; DOD/36 mo
21	38/M	Cough	10	Mediastinum	WDL (lipoma-like)	MDM2+, CDK4+	*MDM2*+, *CDK4*+, *FRS2* + (FISH)	Complete excision	ANED/7 mo
22	62/M	Facial edema	16	Mediastinum	DDL, with undifferentiated pleomorphic sarcoma-like differentiation and myxoid change; well-differentiated liposarcoma area (lipoma-like) (original diagnosis: malignant tumor: 1.SFT 2. MFH 3. liposarcoma)	CDK4+	failed	Marginal excision	Lost
23	48/M	Asymptomatic	NA	Mediastinum	DDL, with undifferentiated pleomorphic sarcoma-like differentiation and myxoid change; (original diagnosis: DDL)	MDM2+, CDK4+	*MDM2* +(FISH)	Marginal excision; CT, RT	DOD/3 mo
24	56/M	Asymptomatic	18	Right pleura space	DDL, with high-grade myxofibrosarcoma- like differentiation; well-differentiated liposarcoma area (sclerotic); (original diagnosis: spindle cell tumor. 1. SFT with malignant transformation2. synovial sarcoma 3. thymoma (type A) 4. DDL need to be excluded)	MDM2+	*MDM2* +(FISH)	Complete excision	Lost
25	58/M	Chest tightness, Short of breath	20	Anterior mediastinum	DDL, with undifferentiated pleomorphic sarcoma-like differentiation; well-differentiated liposarcoma area (sclerotic)	ND	ND	Marginal excision	Lost
26	62/M	Cough, Expectoration, Chest pain	8	Inferior and anterior mediastinum	DDL, with undifferentiated pleomorphic sarcoma-like differentiation; well-differentiated liposarcoma area (sclerotic)	MDM2+, CDK4+	*MDM2* +(FISH)	Marginal excision; CT	Recurrence at 11 mo, resected; DOD/39 mo
27	65/M	Short of breath	5	mediastinum	DDL, with undifferentiated pleomorphic sarcoma-like differentiation; well-differentiated liposarcoma area (sclerotic); (original diagnosis poorly differentiated sarcoma)	MDM2+, CDK4+	*MDM2* +(FISH)	Marginal excision	DOD/4 mo
28	30/M	Chest pain	16	Left pleura space	DDL, with high-grade myxofibrosarcoma -like differentiation, well- differentiated liposarcoma area (lipoma-like and sclerotic)	MDM2+, CDK4+	*MDM2* +(FISH)	Complete excision, CT	ANED/24 mo

(Continued)

TABLE 1 Continued

Case No.	Age/ sex	Symptoms	Size (cm)	Location	Histology	IHC results	Genetic results	Treatment	Outcome/ Follow-up duration
29	53/M	Cough	24	mediastinum	DDL, with osteosarcoma/ chondrosarcomatous-like differentiation and myxoid change, well- differentiated liposarcoma area (lipoma-like and sclerotic)	MDM2+, CDK4+	*MDM2*+, *DDIT3*- (FISH)	Complete excision	ANED/23 mo
30	60/F	Asymptomatic	NA	Left lung tissue	DDL, with high-grade myxofibrosarcoma -like differentiation	MDM2+, CDK4+	*MDM2* +(FISH)	Biopsy; CT, RT	AWD/12 mo
31	53/F	Cough, Expectoration, Dorsagia	12	Left pleura space	DDL, with myxofibrosarcoma-like differentiation and myxoid change, well-differentiated liposarcoma area (lipoma-like)	ND	*MDM2* +(FISH)	Marginal excision; CT	Recurrence at 25 and 37 mo, resected; AWD/55 mo
32	43/M	Cough, Expectoration, Chest pain	20	Right pleura space	DDL, with myxofibrosarcoma-like differentiation and myxoid change, well-differentiated liposarcoma area (lipoma-like and sclerotic)	MDM2+,	*MDM2*+, *DDIT3*- (FISH)	Marginal excision, CT	Recurrence at 58 and 74 mo, Scalp metastasis at 70 mo, resected; AWD/91 mo
33	44/M	Short of breath	7	Right pleura space (involving to lung tissue)	DDL with leiomyosarcomatous differentiation, well- differentiated liposarcoma area (sclerotic)	MDM2+, CDK4+, SMA+, Desmin+	*MDM2* +(FISH)	Complete excision	Lost
34	62/M	Cough, Expectoration	1.2	Left lung tissue	DDL, with myxofibrosarcoma-like differentiation	CDK4+	*MDM2* +(FISH)	Complete excision	ANED/28 mo
35	31/F	Cough, Expectoration	26.4	Right pleura space	DDL, with IMT-like differentiation, and myxoid change, well-differentiated liposarcoma area (lipoma-like)	MDM2+, CDK4+	*MDM2* +(FISH)	Complete excision	ANED/30 mo
36	40/F	Cough, Chest pain	13	Left pleura space	DDL, with IMT-like differentiation, well-differentiated liposarcoma area (sclerotic)	ND	*MDM2* +(FISH)	Marginal excision; CT	DFU/17 mo
37	40/F	Cough	10.2	Right pleura space	DDL, with low-grade fibrosarcoma-like differentiation (desmoid-type fibromatosis-like); well-differentiated liposarcoma area (sclerotic)	ND	ND	Marginal excision	AWD/13 mo
38	72/F	Short of breath	NA	Right lung tissue	DDL, with IMT-like differentiation well-differentiated liposarcoma area (sclerotic); (original diagnosis: low-grade soft tissue tumor, with a tendency to histocytic tumor or hemanyiopericytoma)	ND	*MDM2* +(FISH)	Biopsy, CT	Lost
39	46/M	Cough, Short of breath	35	Right pleura space	DDL, with low-grade fibrosarcoma-like differentiation, well- differentiated liposarcoma area (inflammatory and sclerotic)	MDM2+, CDK4+	*MDM2* +(FISH)	Marginal excision	Recurrence at 65 mo, resected; AWD/105 mo
40	51/M	NA	NA	Lung	DDL with osteosarcomatous differentiation	ND	*MDM2* +(FISH)	Biopsy only	DOD/6 mo
41	24/M	Asymptomatic	15	Superior mediastinum	MPL, displaying myxoid stroma, and pleomorphic lipoblasts (original diagnosis: desmoid-type fibromatosis)	P53+, MDM2-, CDK4-, CD34-, S100-	*MDM2*-, *DDIT3*-, no *RB1* loss (FISH); *TP53* somatic mutation (PCR)	Marginal excision, CT, RT	Recurrence at 3 mo, unresected; DOD/9 mo

(Continued)

TABLE 1 Continued

Case No.	Age/ sex	Symptoms	Size (cm)	Location	Histology	IHC results	Genetic results	Treatment	Outcome/ Follow-up duration
42	49/F	Dizziness, Hemoptysis, Chest tightness	7.8	Anterior mediastinum	MPL, displaying myxoid stroma, and pleomorphic lipoblasts; (original diagnosis: malignant tumor with the tendency to soft tissue sarcoma)	P53+, MDM2-, CDK4-, CD34-, S100-	*MDM2*-, *DDIT3*-, no *RB1* loss (FISH); *TP53* somatic mutation (WES&PCR)	Marginal excision	DOD/7 mo
43	59/M	Short of breath	NA	mediastinum	PL, displaying spindle, pleomorphic tumors cells with pleomorphic lipoblasts	P53+, MDM2-	*MDM2*-, *CDK4*-, *FRS2*-(FISH)	Biopsy only	AWD/7 mo

M, male; F, female; NA, not available; WDL, well-differentiated liposarcoma; DDL, de-differentiated liposarcoma; M-PL, myxoid pleomorphic liposarcoma; SFT, solitary fibrous tumor; MFH, malignant fibrous histiocytoma; IMT, inflammatory myofibroblastic tumor; IHC, immunohistochemistry; "+" positive, "-" negative; FISH, fluorescence *in situ* hybridization; PCR, polymerase chain reaction; WES, whole exome sequencing; RT, radiotherapy; CT, chemotherapy; ANED, alive with no evidence of disease; AWD, alive with disease; DFU, died from unrelated reasons; DOD, died of disease; ND, not done; mo, month.

Radiologic findings

Computed tomography (CT) images were available in thirty-two patients (32/43, 74.4%). The tumor margins were well defined in 15 cases (15/32, 46.9%), ill-defined in 15 cases (15/32, 46.9%) and infiltrative in 2 cases (2/32,6.2%). Twenty-two cases had contrast-enhanced CT data, 16 of 22 (72.7%) cases displayed heterologous enhancement, and 6 cases (27.3%) showed homologous enhancement. Necrosis or cystic change was identified in 5 of 32 (15.6%) cases, and 1 of 32 cases (3.1%) had calcification. Seventeen cases (17/32, 53.1%) extensively involved or compressed the adjacent tissues and vital vessels, and pleural effusion was found in five cases (5/32, 15.6%). None of the 32 cases showed lymphadenopathy.

Clinical treatments

Surgical excisions were performed on 38 patients (38/43, 88.4%), including marginal excision (n=22) and complete excision (n=16), and 9 patients (23.7%) received chemotherapy and/or radiotherapy. Five patients (5/43, 11.6%) received biopsy only, and 2 were treated with chemotherapy and/or radiotherapy.

Pathologic and molecular findings

Gross findings

Macroscopic descriptions were available in 26 of the 38 (68.4%) resected specimens. Macroscopically, eighteen cases (18/26, 69.2%) were well-circumscribed masses, and the remaining 8 lesions (8/26, 30.8%) were poorly circumscribed with infiltration of adjacent organs or tissues. The cut surface of tumors showed a solid appearance from yellow to white.

Microscopic and molecular findings

WDL (N=21)

The 21 conventional WDLs comprised 13 lipoma-like (61.9%) (Figure 1A), 2 inflammatory (9.5%) (Figure 1B), and 6 mixed-subtype tumors (28.6%). Lipoma-like WDL tumors were mainly composed of atypical adipocytes of varying sizes, and inflammatory WDL was characterized by extensive chronic inflammatory infiltrate. The 6 mixed-type tumors included 5 cases with mixed lipoma-like and sclerosing subtypes, and 1 case was a mixture of lipoma-like and inflammatory variants. Atypical, hyperchromatic stromal cells were identified in all of the tumors. A small focal area with increased cellularity was found in 10 cases, consistent with the morphology of cellular WDL. Myxoid change (Figure 1C) was found in 6 of 21 (28.6%) cases.h

Immunohistochemically, MDM2 and CDK4 positivity was observed in 13/13 (100.0%) and 13/13 (100.0%) WDL cases, respectively. *MDM2* amplification was observed in 17/18 (94.5%) cases (Figure 1D). The *MDM2* FISH-negative case was *CDK4*-nonamplified but *FRS2*-amplified (case 4) (Figures 2A–D).

DDL (N=19)

Among the 19 DDLs, 15 cases (15/19, 79.0%) comprised WDL and DDL components simultaneously, and 4 cases only had DDL components. In the 15 cases with both components, 11 cases (11/15, 73.3%) showed an abrupt transition from WDL to

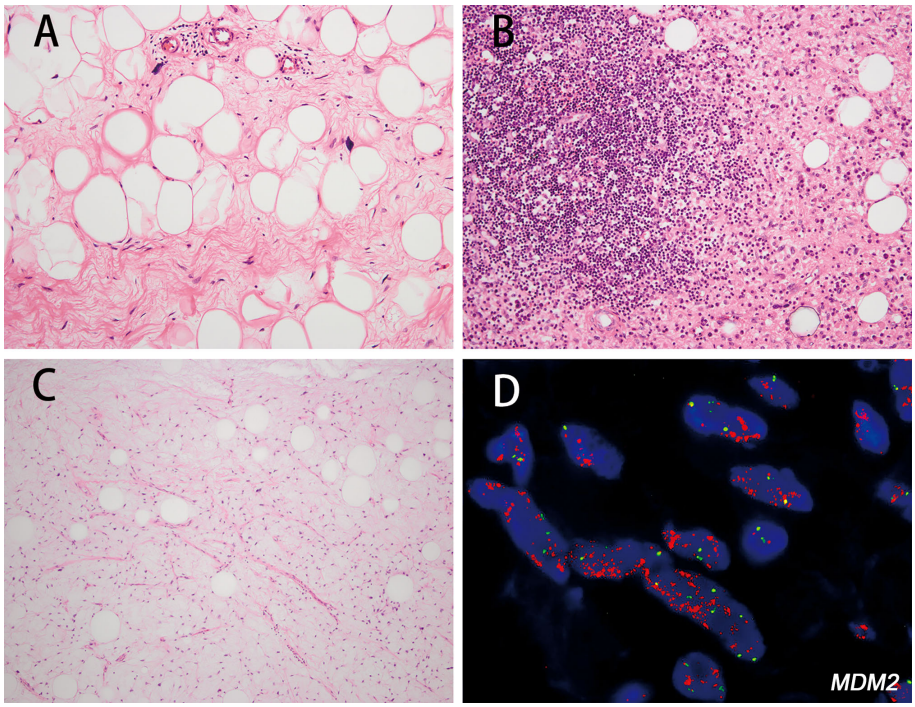

FIGURE 1
The histologic features of well-differentiated liposarcoma (WDL) and corresponding fluorescence *in situ* hybridization (FISH) images. Lipoma-like WDL showing variation in adipocyte size, with the presence of bizarre, hyperchromatic stromal cells (**A** hematoxylin and eosin staining [H&E]; magnification: 200×). Inflammatory WDL with predominant inflammatory cell arrogation and atypical, hyperchromatic cells can be identified in the stroma (**B** H&E; magnification: 200×). WDL with extensive myxoid change showing abundant myxoid stroma and containing small branching vessels (**C** H&E; magnification: 200×). FISH analysis identified *MDM2* amplification in the WDL (case 17) **(D)**.

DDL components, 3 cases (3/15, 20.0%) with gradual transition, and one case (1/15, 6.7%) with a mosaic transition pattern.

In 19 DDL cases, 13 (68.4%) tumors exhibited classic histologic patterns, including undifferentiated pleomorphic sarcoma-like (n=5, 26.4%) (Figure 3A) and intermediate- to high-grade myxofibrosarcoma/fibrosarcoma-like patterns (n=6, 31.6%) (Figure 3B), and 2 cases exhibited osteosarcomatous/chondrosarcomatous differentiation (Figure 3C). The other 6 cases (31.6%) manifested uncommon dedifferentiated components, including 3 with inflammatory myofibroblastic tumor (IMT)-like morphology (15.8%), 2 cases with low-grade dedifferentiation (10.5%), and one DDL with leiomyosarcomatous differentiation. The mitotic rate ranged from 1-30 per 10 high-power fields (HPFs). Necrosis was found in 6 of 19 cases (31.6%). Myxoid change was identified in 6 cases (31.6%). Thirteen DDLs were classified as FNCLCC 2, and 6 DDLs were graded as FNCLCC 3.

In IMT-like DDLs (cases 35, 36, 38), the spindled tumor cells ranged in a fascicular cluster set in a slight myxoid matrix with varying degrees of chronic inflammatory cell infiltration. The spindle cells had abundant, eosinophilic cytoplasm and vesicular nuclei with small nucleoli (Figure 3D). Two DDL cases showed low-grade dedifferentiation resembling low-grade fibrosarcoma or desmoid fibromatosis (cases 37, 39). The tumor cells organized in a fascicular pattern, exhibiting moderate cellularity. The spindle cells had abundant, eosinophilic cytoplasm with mild nuclear atypia (Figures 3E, F).

In one case (case 33), the tumor developed based on the pleura, involving the pleural cavity and lung parenchyma simultaneously. The pleural part was composed of a classic WDL component (Figure 4A). The lesion within the lung parenchyma exhibited more complexity and diversity. At low magnification, the growth of the spindle tumor cells under the bronchiolar epithelium caused cleft-like architecture, mimicking the pattern of pulmonary adenofibroma (Figure 4B). At high magnification, most areas displayed fascicular arrangement of spindle tumor cells, with hyperchromatic, cigar-shaped nuclei and mild to moderate atypia, mimicking low-grade smooth muscle tumors (Figure 4C). In the focal area of the lesion, the tumor cells exhibited increased nuclear atypia with obvious pleomorphism (Figure 4D). The mitotic activity increased to 12 per 10 HPF in this area, and atypical mitosis and necrosis could be identified.

Immunoreactivity for MDM2 and CDK4 was present in 11/11 (100%) and 11/11 (100%) DDL cases, respectively. The IHC results of DDL with well-differentiated leiomyosarcoma-like

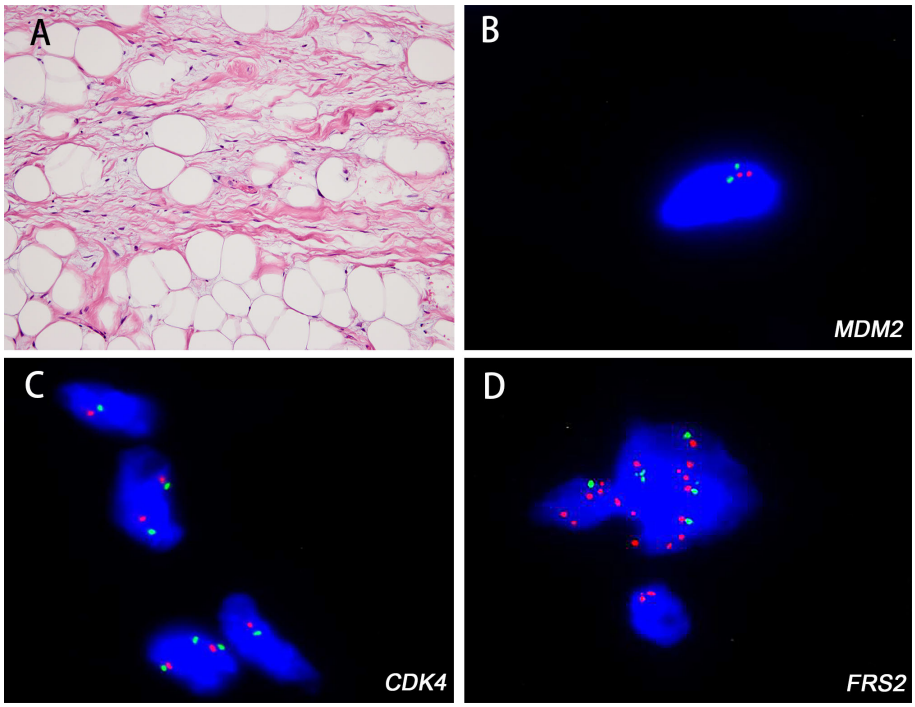

FIGURE 2
The histologic features of well-differentiated liposarcoma (WDL) with unusual genetic results and corresponding fluorescence *in situ* hybridization (FISH) images. The WDL (case 4) showing hyperchromatic bizarre stromal cells (**A** H&E; magnification: 200×). FISH analysis revealed that the tumor was negative for *MDM2* **(B)** and *CDK4* **(C)** gene amplification but with *FRS2* gene amplification **(D)**.

area (case 33) exhibited positivity for smooth muscle actin, desmin and h-caldesmon. In the dedifferentiated area, the tumor cells were negative for those myogenic markers (case 33; Figures 4E–G). High level *MDM2* amplification was identified in 16/16 cases (100%) (Figure 4H), including 2 cases with myxoid change, which were negative for *DDIT3* rearrangement (cases 29, 32).

MPL (N=2)

Two cases (cases 41, 42) showed mixed features of conventional PL and variable portions of myxoid background (Figure 5A). The tumor cells in the PL-like area exhibited marked atypia, and pleomorphic lipoblasts were also identified. The conspicuous ML-like areas ranged from 40-60% in each case, displaying a well-developed plexiform vasculature pattern, pulmonary edema-like mucous pool, and scattered small lipoblasts and bland round cells (Figure 5B). The mitotic rates varied from 22 to 27 mitoses per 10 HPF. Necrosis could be observed in both cases. The 2 MPLs were graded as FNCLCC 3.

Both of the cases were strongly positive for p53(Figure 5C) and negative for CD34, MDM2, CDK4, and S-100 protein. FISH analysis revealed that both MPLs were negative for *MDM2* amplification (Figure 5D), *DDIT3* rearrangement (Figure 5E), and *RB1* deletion.

WES was performed on 1 MPL (case 42) to find more detailed genetic change of this subtype. The structural variants (SV) analysis showed that the number of interchromosomal translocation was the most frequent variant, followed by intrachromosomal translocation, deletion, duplication and inversion. Copy number variation (CNV) result showed the loss locus of chromosomes were more than the gains. The most frequent loss loci were 8p23.1, 16p13.11 and 1q21.3, and gain loci of 14q11.2, 7q22.1 and 7q11.23 were found. Somatic *TP53* mutation in exon 4: c.215G>C, p.P72R. was detected in this MPL, which was verified by Sanger sequencing analysis. The same result was observed in another MPL (case 41), while the *TP53* mutation was not detected in the nontumorous tissues of either case (Figure 5F).

PL (N=1)

The lesion comprised spindle, epithelioid tumor cells with severe atypia. The bizarre lipoblasts can be identified in some areas within the tumor (Figures 6A, B). Myxoid change was identified in focal area, resembling the morphology of myxofibrosarcoma (Figure 6C). Tumor necrosis and atypical mitotic figure were seen in the tumor. Immunohistochemical analysis revealed that the tumor cells were diffusely positive for P53 (Figure 6D) and focally positive for S-100 but negative for

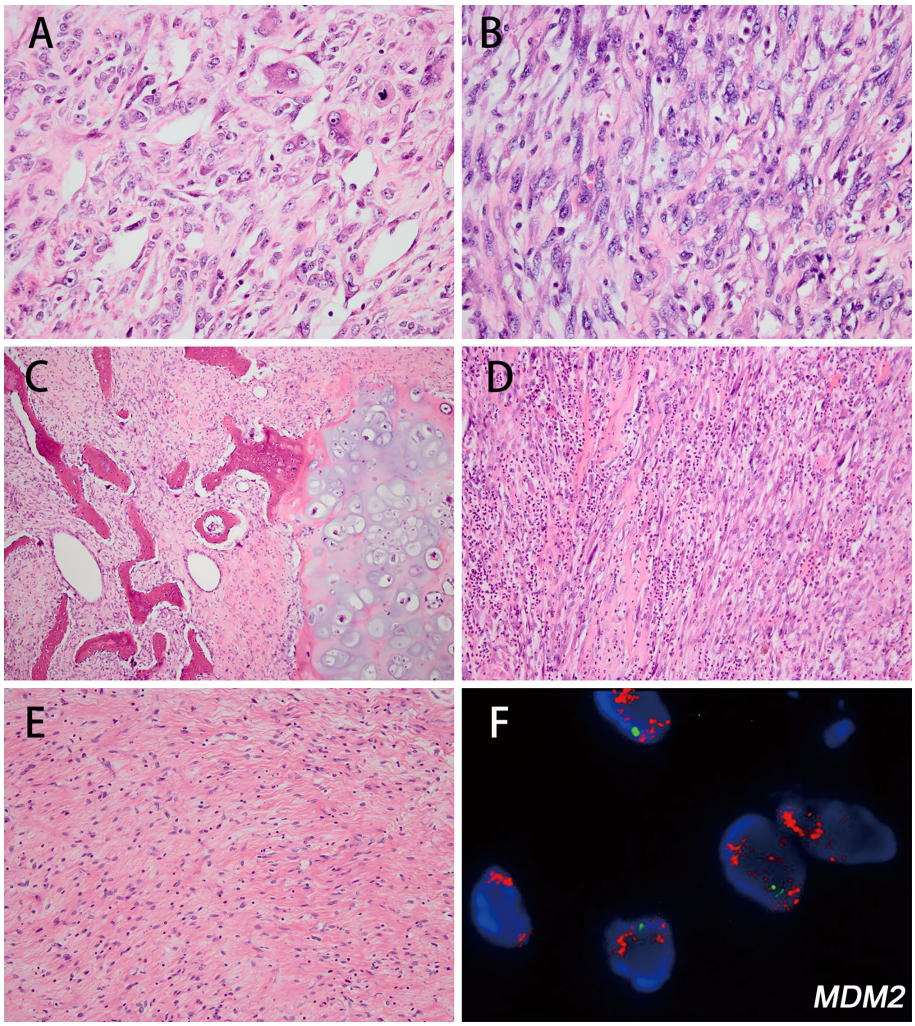

FIGURE 3
The histologic features of dedifferentiated liposarcoma (DDL) and corresponding fluorescence *in situ* hybridization (FISH) images. DDL with undifferentiated pleomorphic sarcoma-like differentiation; tumor cells exhibited moderate cytologic atypia with obvious nuclear pleomorphism (**A** H&E; magnification: 400×). DDL showed a fibrosarcoma-like pattern, exhibiting marked hypercellularity and cytologic atypia. (**B** H&E; magnification: 400×). DDL showing areas of osteosarcoma and chondrosarcoma-like differentiation (**C** H&E; magnification: 100×). DDL with IMT-like features with varying degrees of chronic inflammatory cell infiltration (**D** H&E; magnification: 200×). DDL with low-grade fibrosarcoma-like differentiation, exhibiting mild cytologic atypia (**E** H&E; magnification: 200×). FISH analysis identified *MDM2* amplification in the DDL (case 32) **(F)**.

MDM2 protein. FISH analysis revealed that the tumor was negative for *MDM2*/*CDK4*/*FRS2* amplification.

Clinical follow-up

Clinical follow-up data were available for 33 of 38 (86.8%) patients who received surgical intervention, with a median follow-up duration of 37 months (mean, 44.8 months; range 3 - 161 months). Local recurrence occurred in 14 cases (14/33, 42.4%) (median, 25 months; range 3- 84 months), including 9 WDLs, 4 DDLs and 1 MPL. Metastasis occurred in 1 patient with DDL. Thirteen patients (13/33, 39.4%) were alive with no evidence of disease (median, 35 months; range 7-105 months), including 8 WDLs and 5 DDLs. Ten patients (10/33, 30.3%) were alive with disease from 13 to 161 months after diagnosis (median, 49 months), including 7 WDL cases and 3 DDLs. Eight patients (8/33, 24.2%) died of disease, including 3 WDLs, 3 DDLs and 2 MPLs. Additionally, two cases (2/33, 6.1%) died from unrelated causes.

The results of Log-rank analyses of the clinical parameters are summarized in Table 2. The survival analysis found that tumor subtype ($\chi 2 = 16.118$, $p < 0.05$), necrosis ($\chi 2 = 6.174$, $p < 0.05$) and surgical resection (complete resection vs. marginal

10.3389/fonc.2022.949962

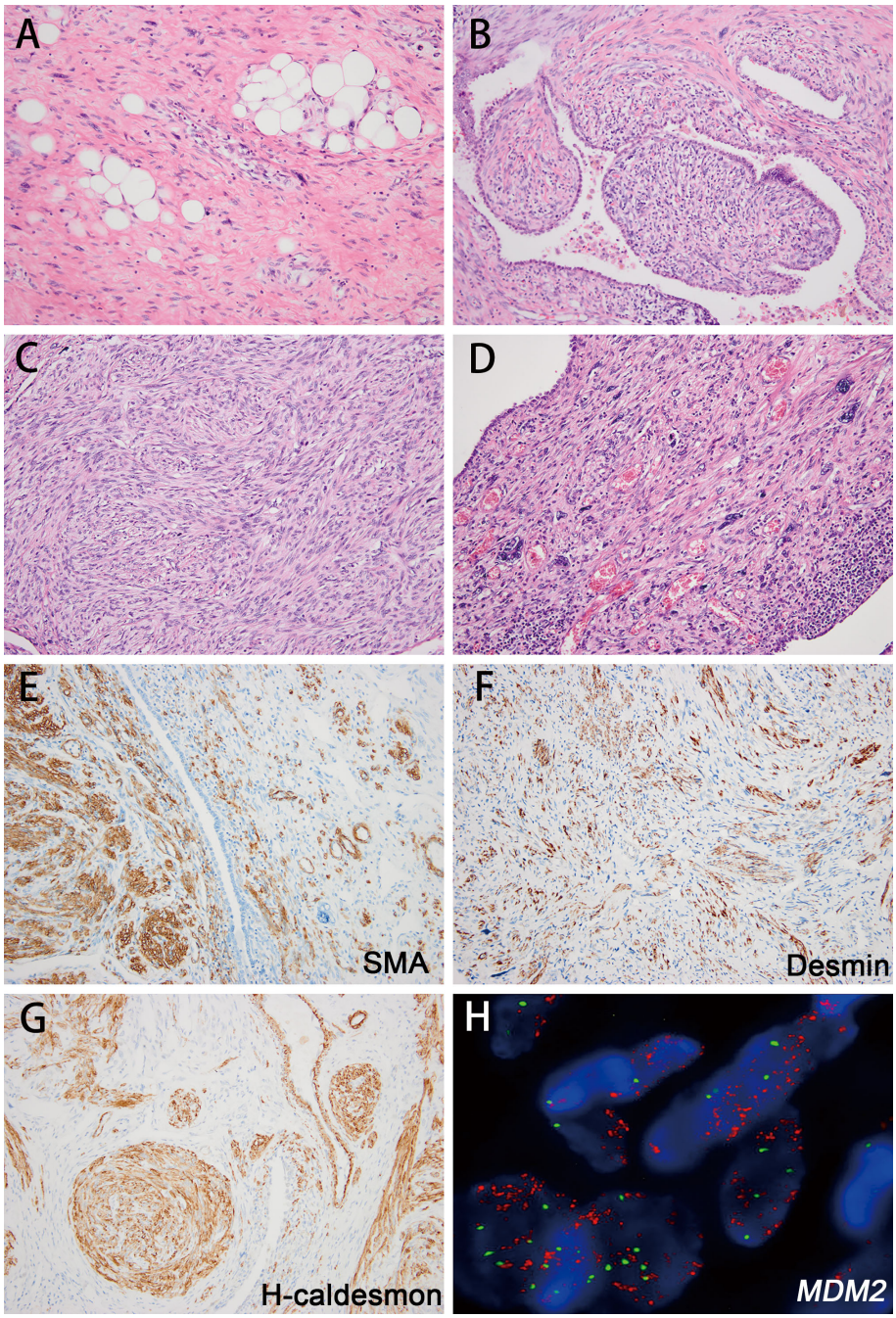

FIGURE 4
The histologic features of DDL with leiomyosarcomatous differentiation (case 33) and its corresponding immunohistochemical and fluorescence *in situ* hybridization (FISH) image. Sclerotic well-differentiated area outside the lung (**A** H&E; magnification: 200×). At low magnification, the growth of the spindle tumor cells showed cleft-like architecture, mimicking the pattern of pulmonary adenofibroma (**B** H&E; magnification: 200×). Spindle tumor cells display a fascicular arrangement, with hyperchromatic, cigar-shaped nuclei and mild to moderate atypia (**C** H&E; magnification: 200×). The tumor cells exhibited increased nuclear atypia with obvious pleomorphism (**D** H&E; magnification: 200×). The tumor cells showed SMA (**E** magnification: 200×), desmin (**F** magnification: 200×) and h-caldesmon (**G** magnification: 200×) positivity in well-differentiated areas and negativity in focal sarcoma-like areas. *MDM2* amplification was identified in this case **(H)**.

10.3389/fonc.2022.949962

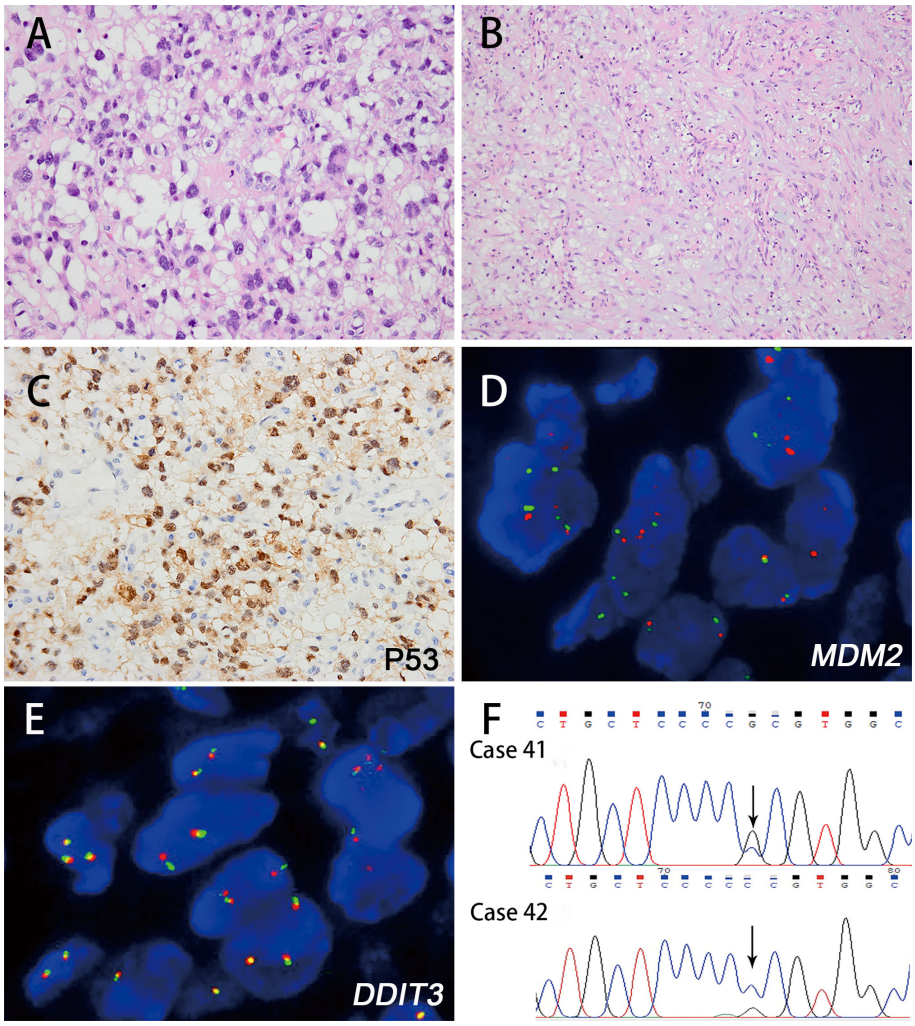

FIGURE 5
The histologic features of myxoid pleomorphic liposarcoma and corresponding immunohistochemical and genetic results. The tumor exhibited features of pleomorphic liposarcoma with myxoid matrix, and multivacuolated lipoblasts were found (**A** H&E; magnification: 400×) (case 42). Myxoid liposarcoma-like areas were also identified within the tumor, displaying a well-developed plexiform vasculature pattern (**B** H&E; magnification: 400×). The tumor cells (case 42) showed positivity for p53 immunostaining (**C** magnification: 400×). FISH analysis revealed negativity for *MDM2* amplification **(D)** or *DDIT3* rearrangement **(E)**. Sanger sequencing results showed *TP53* mutations in both tumors **(F)**.

resection; $\chi 2 = 4.156$, $p < 0.05$) were associated with overall survival (OS). DFS (disease-free survival) was related to tumor subtype ($\chi 2 = 9.526$, $p < 0.05$) and surgical resection (complete resection vs. marginal resection; $\chi 2 = 7.605$, $p < 0.05$). No significant difference was observed between the other survival factors with OS and DFS, including sex, age and tumor size.

Discussion

This study enrolled 43 primary intrathoracic liposarcomas, aged from 24 to 73 years (median, 53 years) with male predilection (M: F= 1.68:1). We reviewed previously reported primary intrathoracic liposarcoma (1990-2021) with available clinicopathological information in English literature(n=300), summarizing the series cases in Table 3 and the rest in Supplementary Table 1 (7–13). The majority of the historical cases were also older adults (median, 54 years) with a male predication (M: F= 1.46:1).

In this cohort, a preference for the mediastinum (23/43, 53.5%) was observed, which is in agreement with the tendency of previous cases (222/300, 74.0%). The percentage of our series (53.5%) was lower than that of previous studies (74.0%), which may be caused by our research analyzing all intrathoracic liposarcomas, whereas some large series studies focused on mediastinal tumors only (8, 9, 12). Only 4 cases in our cohort

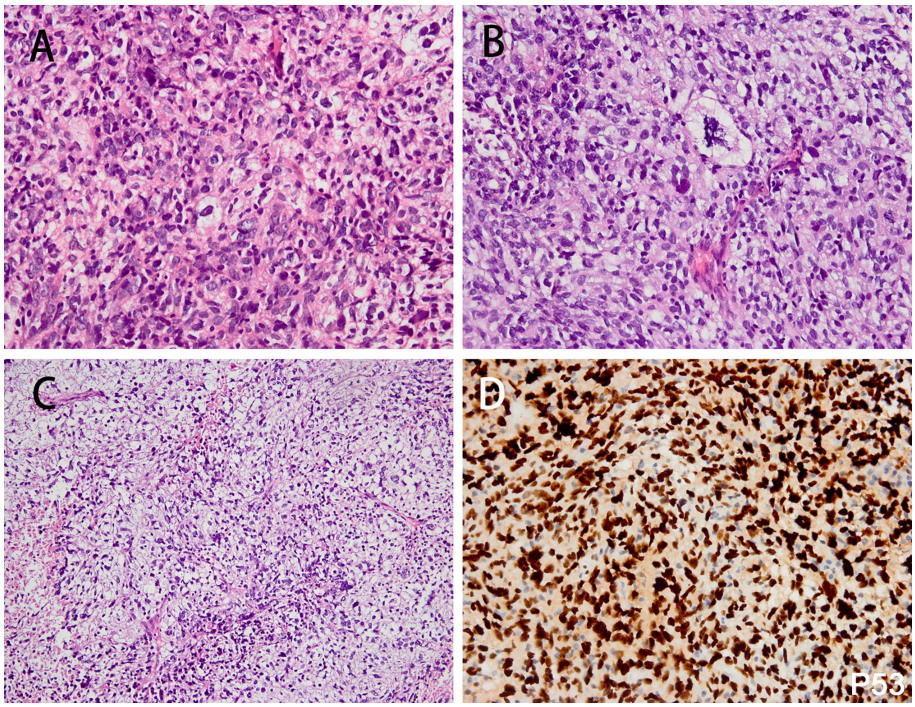

FIGURE 6
The histologic features of pleomorphic liposarcoma and corresponding immunohistochemical results. The spindled, epithelial tumor cells exhibited marked nuclear atypia (**A** H&E; magnification: 400×) (case 43). The bizarre lipoblasts can be identified within the lesion (**B** H&E; magnification: 400×). Myxoid change in focal area, resembling the morphology of myxofibrosarcoma (**C** H&E; magnification: 200×). The tumor cells were diffusely positive for P53 (**D** magnification: 400×).

were located within the lung parenchyma (4/43, 9.3%), and 18 pulmonary liposarcomas were reported previously (18/300, 6.0%) (11, 13, 18–29). These results indicated that primary pulmonary liposarcoma is exceedingly rare but does exist.

According to the results of this study, the most significant difference between our series and previous studies is the distribution spectrum of the subtype. In our study, WDL/DDL was the overwhelming subtype (40/43, 93.0%), followed by MPL (2/43, 4.7%) and PL (1/43, 2.3%). Notably, ML was not identified in our study. The distribution spectrum differed significantly from the overall distribution of liposarcoma subtypes, in which WDL/DDL, ML and PL accounted for approximately 65%, 30%, and 5% of cases, respectively, and MPL was exceptionally rare. Moreover, our result is also different from to that of historical intrathoracic cases, in which WDL/DDL, ML, PL and MPL accounted for 56.7% (170/300), 21.3% (64/300), 11.3% (34/300) and 2.7% (8/300), respectively. Notably, the subtype distribution of our thoracic liposarcoma is similar to that of primary retroperitoneal liposarcoma, in which WDL/DDL is the predominant subtype and ML and PL are vanishingly rare (30).

The 21 WDLs in our study comprised lipoma-like (61.9%), inflammatory (9.5%), and mixed subtype tumors (28.6%). Most historical WDLs with available subtype information (n=54), were also lipoma-like (12/54, 22.2%) and mixed-subtype (32/54, 59.3%). Conspicuous myxoid change was observed in 6 of our cases (28.6%) and appeared to be more common than in reported tumors with available descriptions (12/66, 18.2%) (9, 10, 12). Attention should be given to these cases, as some WDLs can show extensive myxoid changes mimicking ML.

It should be mentioned that only 8 historical WDLs (6.8%) were analyzed by FISH, including 6 *MDM2*-amplified cases, 1 case with equivocal *MDM2*-FISH results, and 1 *CPM*-nonamplified case (10, 12, 20, 31–34). In our study, all 18 tested WDLs were 12q13-15 amplified, including 17 *MDM2*-amplified cases and 1 *FRS2*-amplified/*MDM2*-nonamplified/*CDK4*-nonamplified tumor (case 4). We reported the first *FRS2*+/*MDM2*-/*CDK4*- WDL in English literature. The position of the *FRS2* gene is close to the *MDM2* and *CDK4* genes within the 12q13-15 chromosomal region. In 2011, Wang et al. identified consistent amplification of the *FRS2* gene in 57 WDL/DDLs (100%) (35).Subsequently, our research found a high amplification frequency of the *FRS2* gene in WDL/DDLs (136/146, 93.2%) and low-grade osteosarcoma (21/22, 95%), slightly lower than that of *MDM2* (100%). These results indicated that FISH analysis of the *FRS2* gene could also be a useful ancillary tool for the diagnosis of WDL/DDL (17, 36).

10.3389/fonc.2022.949962

TABLE 2 Survival data of the primary intrathoracic liposarcoma patients of the study.

Parameter	N (%)	Disease–free survival		Overall survival	
		Log–rank	*P*–value	Log–rank	*P*–value
Gender	33	0.891	0.345	0.267	0.605
Male	19 (57.6)				
Female	14 (42.4)				
Age	33	0.723	0.395	0.017	0.896
<=50y	16 (48.5)				
>50 y	17 (51.5)				
Size	29	0.110	0.740	2.321	0.128
<=10cm	7 (24.1)				
>10 cm	22 (75.9)				
Location	33	1.488	0.475	5.225	0.073
Mediastinum	18 (54.6)				
Pleura space	14 (42.4)				
Lung	1 (3.0)				
Subtype	33	9.526	<0.05	16.118	<0.001
Well-differentiated	19 (57.6)				
Dedifferentiated	12 (36.4)				
Myxoid pleomorphic	2 (6.0)				
Necrosis	33	2.795	0.095	6.174	<0.05
Yes	8 (24.2)				
No	25 (75.8)				
Surgical resection	33	7.605	<0.05	4.156	<0.05
Complete resection	14(42.4)				
Marginal resection	19(57.6)				

Moreover, in addition to *MDM2* and *CDK4*, aberrations of other genes at 12q13-15 may also participate in the pathogenesis of this entity, and comprehensive molecular analysis in challenging cases is valuable.

In the 19 DDLs, 13 tumors (68.4%) exhibited a conventional dedifferentiation pattern, and the other 6 cases showed uncommon morphology, including an IMT-like pattern (n=3, 15.8%), low-grade dedifferentiation (n=2, 10.5%) and DDL with leiomyosarcomatous differentiation (n=1, 5.3%). It should be mentioned that IMT-like features are a recently described histologic pattern of DDL, while none of the intrathoracic cases have been described in the English literature (37–39). In the 52 reported DDLs, 10 of them (10/52, 19.2%) exhibited low-grade dedifferentiation (9, 10, 12, 40–42). Notably, 1 case was DDL with leiomyosarcomatous differentiation, mimicking smooth muscle tumor and pulmonary adenofibroma histologically. However, typical areas of WDL were found after extensive sampling. Furthermore, the identification of *MDM2* amplification helped the final diagnosis. To the best of our knowledge, only 1 primary intrathoracic DDL with leiomyosarcomatous differentiation has been described (12). In the study cohort, all tested DDL tumors (16/16, 100%) exhibited *MDM2* amplification. However, only 11 of 52 (21.1%) historical cases were subjected to FISH analysis, and all of them displayed positive results (10, 18, 40, 42–47). We endorsed ancillary tests for cases in rare locations, such as the mediastinum, lung and/or ambiguous morphology.

Two MPLs were identified in this study. As an exceptionally rare subtype of liposarcoma, only 38 MPLs have been reported previously. Of the 37 reported cases with available information, MPLs have a predilection for the mediastinum (15/37, 40.6%), suggesting although MPL is an extremely rare subtype of liposarcoma, it is not the rarest liposarcoma variant in the mediastinum (10, 15, 48–55). The 2 MPL patients in our study were 24 and 49 years old. The median age of cases from case reports and series study was 17 years and 35 years, respectively (55). These result suggested MPL is more prone to occur in young age group.

The MPL tumors of this cohort simultaneously harbored pleomorphic liposarcoma-like areas and myxoid liposarcoma-like areas, with a plexiform vasculature pattern in a myxoid background, similar to previously reported cases. The MPLs in our study and historically tested MPL cases were all negative for *MDM2* amplification or *DDIT3* rearrangement, indicating the phenotype of MPL was different from that of WDL/DDL or ML (10, 48, 50–54). The WES results of our MPL case showed numerous chromosome gain and loss loci, similar to 2 previous aCGH studies of 2 MPLs, and 1 large series study of MPLs (50,

TABLE 3 Clinicopathologic features of previously reported primary mediastinal and intrathoracic liposarcomas of large series studies.

Published time	Case No.	Author	Gender (M:F)	Age (year)	Clinical Presentation	Size (cm)	Location	Histology	Molecular/IHC	Therapy	Follow-upInformation	Outcome
1964	8	Cicciarelli, F. E.,et al (7)	3:5	50 (13-70)	pain, cough, dyspnea, loss of weight	17.8 (14-22)	2 PM, 2 AM, 4 MC	8 Liposarcoma	NA	5 excision & RT, 2 excision,1 RT	6 recurrence	5 DOD, 3 AWD
1995	28	Klimstra DS, et al (8)	16:12	43 (14-72)	pain, cough, dyspnea,	15.7 (6-40)	28 AM	15 WDL,7 ML,3 PL, 3 mixed-type	NA	28 excision	7 (7/22) recurrence	11 ANED, 4 AWD, 7 DOD,
2007	24	Hahn HP, et al. (9)	13:11	58 (3-72)	Dyspnea and cough	16 (2.2-61)	9 AM,7 PM, 1 SM,7 mediastinum	10 WDL,8 DDL,2 ML,4 PL	NA	14 complete excision, 1 marginal excision +CT, 1 RT+CT	5 (5/15) recurrence 2 (2/15) metastasis	11 ANED, 1 AWD, 2 DOD, 1 DFU
2012	24	Boland JM, et al. (10)	13:11	53 (15-73)	NA	16 (8-30)	6 AM, 6PM, 2SM, 3 MM, 5MC, 1PS, 1AM/SM	8 WDL,6 DDL,2 ML, 4PL,3M-PL,1 Unclassifiable type	WDL:1/1*CPM*-(FISH), DDL:3/3 *CPM* +(FISH), ML:1/1*CPM*-, *DDIT3*-(FISH), PL:2/2 *CPM*-(FISH); MPL: 1/1 *DDIT3*-,1/1 *DDIT3*-, *EWS*-(FISH) Unclssifiable:1/1 *CPM*-, *FUS*- *DDIT3*-(FISH),	22 excision	8 (8/19) recurrence 5 (5/19) metastasis	6 ANED, 3 AWD, 9 DOD 3 Alive
2014	23	Chen M, et al. (11)	12:11	49 (16-72)	Chest pain, cough, dyspnea, shortness of breath	8 (4-39)	10mediastinum,9 PS, 4 lung	8 WDL, 4 DDL, 8 ML,3 PL	WDL:6/8 MDM2+, 6/8 CDK4+, 8/8 S100+(IHC) DDL: 3/4 MDM2+, 3/4 CDK4+, 4/4 S100+(IHC) ML:8/8 S100+(IHC)	17 complete excision,6 marginal excision	9(9/17) recurrence 6 (6/23) metastasis	10 DOD
2015	18	Ortega P, et al. (12)	11:7	57 (29-87)	Cough, dysphagia, and chest pain	15 (6-30)	18 PM	10 WDL,3 DDL, 3 ML,2 PL	WDL: 1/2 S100 +, 5/5 MDM2+(IHC); 2/2 *MDM2* +(FISH) DDL: 3/3 MDM2+, 0/3 S100+(IHC) ML: 3/3 S100+, 0/3 MDM2+(IHC)	12 complete excision, 4 marginal excesion+RT,1 RT	3 (3/13) recurrence 3 (3/13) metastasis	7 ANED, 3 AWD, 2 DOD, 1DFU
2019	31	Fu Z et al. (13)	19:12	45 (20-64)	Chest tightness	10 (1.8-32)	16 AM, 8PM, 5 PS, 2 lung	6 WDL,3 DDL,13 ML,4PL,5Mixed-type	NA	17excision,8 excision+RT,3 RT, 1 excision +CT, 2excision+RT +CT	20 (20/31) recurrence 11 (11/31) metastasis	18 DOD

M, male; F, female; NA, not available; AM, anterior mediastinum; PM, posterior mediastinum; SM, superior mediastinum; MM, middle mediastinum; MC, multiple compartments; PS, pleural space; WDL, well-differentiated liposarcoma; DDL, dedifferentiated liposarcoma; ML, myxoid liposarcoma; PL, pleomorphic liposarcoma; M-PL, myxoid pleomorphic liposarcoma; IHC, immunohistochemistry; "+" positive, "-" negative; FISH, fluorescence *in situ* hybridization; RT, radiotherapy; CT, chemotherapy, ANED, alive with no evidence of disease; AWD, alive with disease; DFU, died from unrelated reasons; DOD, died of disease.

10.3389/fonc.2022.949962

51, 55). Moreover, our results found losses are more frequent than gains in MPL case, which were in agreement with Creytens et al. but different from other studies, and more MPL cases are needed to verify the finding. Furthermore, both our research and previous studies found complex chromosomal aberrations in MPL. However, these results revealed MPL showed a simpler pattern of chromosome alterations than conventional PL, with focal copy number changes rather than whole chromosomal gains and losses.

MPL may be related to Li-Fraumeni syndrome (LFS) associated with germline *TP53* mutations. Both MPL tumors of our study harbored somatic *TP53* mutations, without association with LFS. Including our 2 cases, *TP53* mutation was found in 78% of MPLs (7/9) (15, 51–54). These findings reminded us *TP53* mutation might play a role in the pathogenesis of MPL. *RB1* gene deletion was found in 10 of 15 (66.7%) historical MPLs and 1 MPL was reported to have *KMT2D* gene mutation, while our 2 MPL cases were negative for such genetic changes (15, 51, 55). It should be pointed out that conventional PL also harbors frequent *TP53* and *RB1* mutations (56), implying that aberrant genes of conventional PL overlapped with those of MPL. Further study is needed to identify the relationship and difference between these two entities.

Only 1 conventional PL was found in our study with the identification of typical of bizarre, giant lipoblasts and without amplification of *MDM2*/*CDK4*/*FRS2* genes. In previous studies, PL was also rarely seen in this location and accounted for 11.3% (34/300) of reported cases. The majority of historical PLs were diagnosed based on morphology only, and only 2 cases were found to be *CPM* nonamplified (10). Therefore, PL in the thorax is scarce and the diagnosis of PL in this location is challenging. Molecular analysis is needed to rule out the possibility of other subtypes of liposarcoma.

Primary intrathoracic ML was not identified in our cohort. In fact, 2 cases were coded as intrathoracic MLs at the beginning. However, one was proved to be a metastatic tumor, and another was revised as DDL (case 32) which was *MDM2*-amplified but *DDIT3*-nonrearranged. Although 64 primary intrathoracic MLs have been reported, only one tumor was *DDIT3*-rearranged (10, 26). Hence, primary intrathoracic ML does exist, but it may be quite rare.

The correct diagnosis and classification of intrathoracic liposarcoma subtypes is of considerable importance and may be challenging for difficult cases, particularly in small biopsy specimens. Moreover, intrathoracic liposarcomas should be differentiated from a variety of other types of neoplastic and nonneoplastic lesions, such as benign adipose tissue tumors, inflammatory lesions, and other spindle cell lesions. It should be emphasized that intrathoracic DDL especially in the pleuropulmonary area is extremely rare and can mimic other types of adipocytic and nonadipocytic tumors, such as IMT, solitary fibrous tumor (SFT), synovial sarcoma, malignant peripheral nerve sheath tumor (MPNST), smooth muscle tumor, pulmonary adenofibroma, intimal sarcoma, sarcomatoid carcinoma, and other types of liposarcoma.

In this study, one lipoma-like WDL (case 13) and one inflammatory WDL case (case 16) were diagnosed as lipoma and inflammatory pseudotumor, respectively, at a local hospital. Careful histological inspection can aid in identifying atypical adipocytes of varying sizes, especially bizarre, hyperchromatic stromal cells. More importantly, MDM2 and CDK4 nuclear positivity, especially *MDM2* gene amplification, can be invaluable in distinguishing WDL from lipoma and inflammatory lesions.

IMT is the more common tumor type in the pleuropulmonary area, outnumbering liposarcomas. This study cohort comprised 3 IMT-like DDL tumors and could be easily confused with IMT. However, extensive sampling identified typical areas of a WDL component, suggestive of the diagnosis of DDL. More importantly, IMT can be excluded because of the presence of high-level amplification of the *MDM2* locus and the absence of *ALK, ROS1*, *NTRK3, RET*, or *PDGFRB* gene rearrangement. It should be pointed out that the diagnosis of *MDM2*-amplified IMT should be extremely cautious, as *MDM2* amplification is the genetic hallmark of DDL, although a few IMT cases harboring *MDM2* amplification have been reported (57, 58).

SFT is one of the commonest pleuropulmonary soft tissue tumors and might share some morphologic features with DDL. SFT could be distinguished from DDL in the following aspects. First, SFT usually exhibits strong and diffuse nuclear positivity of STAT6 although a subset of DDL may also show moderate or weak STAT6 expression caused by the *STAT6* amplification (59). Most importantly, SFT can be excluded because of the presence of *MDM2* gene amplification and absence of *NAB2-STAT6* gene fusion (15, 60).

Primary pleuropulmonary synovial sarcoma has gradually been recognized as a clinicopathological entity. Sometimes the histologic features of DDL and synovial sarcoma can overlap significantly, especially in small biopsy samples. Careful morphologic inspection and ancillary immunohistochemical markers including EMA, TLE1, cytokeratins, and MDM2 are helpful in distinguishing between these lesions. Of note, ancillary molecular studies testing of t(X;18)(p11.2;q11.2) for synovial sarcoma and *MDM2* amplification can be invaluable in secure the diagnosis (61).

MPNST could resemble DDL and appears to be the most challenging tumor type in the differential diagnosis of DDL in any location. MPNST usually shows complete loss of staining for H3K27me3 but negativity for MDM2 expression. Notably, detection of *MDM2* amplification, combined with the absence of the genetic loss of *SUZ12* or *EED*, can help to confirm the diagnosis of DDL (62).

This cohort comprised one peculiar DDL with leiomyosarcomatous differentiation (case no. 33), posing

diagnostic challenges on morphologic grounds only. The distinction can be aided through extensive sampling of the lesion. For example, in the current case, 10 blocks were taken at the very beginning, and the tumor was almost entirely composed of smooth muscle tumor elements, mimicking smooth muscle tumor. Additionally, the tumor component within the lung parenchyma showed a leaf-like pattern and could be confused with pulmonary adenofibroma. However, typical areas of WDL were found both in the pleural areas and pulmonary areas of the mass after an extra 12 blocks were taken. Moreover, the identification of *MDM2* amplification in the tumor further helped us to make the diagnosis.

Four DDLs of our study were located within the lung parenchyma, which were extremely rare in this site. It should be pointed out that all the 4 DDLs were *MDM2*-amplified. Moreover, the imaging of the 4 patients did not found tumors elsewhere of the body. The WDL component was identified in 1 case and lipomatous components were found radiologically in 2 biopsy samples. While the WDL component was not observed in another surgical resected tumor (case 34). Such case might be confused with tumors carrying *MDM2* amplification, such as intimal sarcoma and a few pulmonary sarcomatoid carcinomas (PSC). Firstly, the diagnosis of intimal sarcoma was excluded as the different location of the two entities. Intimal sarcomas mainly arise from pulmonary arteries and major systemic arteries, while the DDLs were all located within the lung parenchyma (63). Secondly, all the four documented *MDM2*-amplified PSCs had adenocarcinoma components. In contrast, carcinomatous component was not detected in our DDL case (64, 65). In combination with the clinicopathologic, genetic and radiologic results, this case (case 34) was diagnosed as DDL.

In fact, both of the MPL cases in our series were diagnosed as PL in the local hospital. MPL is an exceptionally rare emerging entity of liposarcoma, and most general surgical pathologists are not familiar with this peculiar tumor. However, careful histological inspection revealed that both tumors exhibited conspicuous myxoid areas, showing mixed features of classic PL and ML. Additionally, these tumors were negative for *DDIT3* rearrangement and *MDM2* amplification. Finally, the diagnosis of MPL was established.

PL is extremely rare in the intrathoracic location and should be distinguished from other tumors especially DDL with homologous lipoblastic differentiation. It is noteworthy to point out that a minority of DDL cases can exhibit pleomorphic liposarcoma-like differentiation, making it indistinguishable from PL (66, 67). DDL usually comprises typical areas of WDL component within the tumor. Importantly, negativity for MDM2 overexpression, especially lack of amplification of *MDM2* gene can help distinguish PL from the above mentioned variant of DDL.

The results of this study showed that tumor subtype was an important prognostic factor for the OS of intrathoracic liposarcoma patients. In our cohort, only 3 of 19 (15.8%) WDL and 3 of 12 (25.0%) DDL cases, but both MPLs (2/2,100%), died of disease. In previously reported cases with follow-up information, disease-related death was found in 5 of 73 (6.8%) WDLs, 10 of 42 (23.8%) DDLs and 15 of 26 (57.7%) MPL cases. Similar to our study, the mortality was highest in MPL and lowest in WDL cases, suggesting that the intrathoracic tumor subtype was related to the overall survival of the cases. Our research also found that OS and DFS were related to marginal or complete resection of the tumor, as none of the 13 patients who received complete tumor resection died of disease, while 44.5% (8/18) patients who underwent marginal resection died of disease. Chen et al. found that surgical resection was associated with the OS of tumors, further indicating that the surgical procedure can influence the behavior and prognosis of the disease (11).

In conclusion, we present clinicopathological and molecular features of 43 primary intrathoracic liposarcomas. In our study, WDL/DDL is the overwhelming subtype, followed by MPL and PL. Notably, ML was not identified. MPL is extremely rare in liposarcoma, but it is not the rarest subtype in thorax. One *FRS2*+/*MDM2*-/*CDK4*- WDL was identified, indicating that analysis of the *FRS2*, in combination with *MDM2* and other genes located at 12q13-15, may more precisely characterize WDL/DDLs. Both MPLs exhibited somatic *TP53* mutations, showing overlapping features with conventional PL. MPL is the most fatal subtype of this site, suggesting that correct classification is of considerable significance.

Data availability statement

The data presented in the study are deposited in the NCBI database, accession number SAMD00514799 and SAMD00514800.

Author contributions

YX: data analysis, histopathological examinations and writing. WJ: histopathological examinations and writing. WZ: data analysis and histopathological examinations. RP: data analysis. MC: help molecular experiments. TL: data analysis. HP: help molecular experiments. XH: histopathological examinations. HC: histopathological examinations. ZZ: histopathological examinations. HZ: the corresponding author, study design, histopathological and molecular examinations, and the manuscript revision. All authors contributed to the article and approved the submitted version.

Funding

This work was supported by the National Natural Science Foundation of China (No. 81972520) and the 1·3·5 project for disciplines of excellence–Clinical Research Incubation Project, West China Hospital, Sichuan University (No. 2018HXFH011).

Conflict of interest

The authors declare that the research was conducted in the absence of any commercial or financial relationships that could be construed as a potential conflict of interest.

Publisher's note

Supplementary material

The Supplementary Material for this article can be found online at: https://www.frontiersin.org/articles/10.3389/fonc.2022.949962/full#supplementary-material

References

1. Sbaraglia M, Dei Tos AP, Pedeutour F. Atypical lipomatous tumour/well-differentiated liposarcoma. In: *WHO classification of tumours editorial board ed. world health organization classification of soft tissue and bone tumours, 5th ed.* Lyon: IARC Press (2020). p. 36–8.

2. Dei Tos AP, Marino-Enriquez A, Pedeutour F. Dedifferentiated liposarcoma. In: *WHO classification of tumours editorial board ed. world health organization classification of soft tissue and bone tumours, 5th ed.* Lyon: IARC Press (2020). p. 39–41.

3. Thway K, Nielsen TO. Myxoid liposarcoma. In: *WHO classification of tumours editorial board ed. world health organization classification of soft tissue and bone tumours, 5th ed.* Lyon: IARC Press (2020). p. 42–4.

4. Pedeutour F, Montgomerry EA. Pleomorphic liposarcoma. In: *WHO classification of tumours editorial board ed. world health organization classification of soft tissue and bone tumours, 5th ed.* Lyon: IARC Press (2020). p. 45–6.

5. Alaggio R, Creytens D. Myxoid pleomorphic liposarcoma. In: *WHO classification of tumours editorial board ed. world health organization classification of soft tissue and bone tumours, 5th ed.* Lyon: IARC Press (2020). p. 47–8.

6. Evans HL. Liposarcoma: a study of 55 cases with a reassessment of its classification. *Am J Surg Pathol* (1979) 3:507–23. doi: 10.1097/00000478-197912000-00004

7. Cicciarelli FE, Soule EH, McGoon DC. Lipoma and liposarcoma of the mediastinum: A report of 14 tumors including one lipoma of the thymus. *J Thorac Cardiovasc Surg* (1964) 47:411–29. doi: 10.1016/s0022-5223(19)33575-5

8. Klimstra DS, Moran CA, Perino G, Koss MN, Rosai J. Liposarcoma of the anterior mediastinum and thymus. A clinicopathologic study of 28 cases. *Am J Surg Pathol* (1995) 19:782–91. doi: 10.1097/00000478-199507000-00006

9. Hahn HP, Fletcher CD. Primary mediastinal liposarcoma: Clinicopathologic analysis of 24 cases. *Am J Surg Pathol* (2007) 31:1868–74. doi: 10.1097/PAS.0b013e318093f925

10. Boland JM, Colby TV, Folpe AL. Liposarcomas of the mediastinum and thorax: a clinicopathologic and molecular cytogenetic study of 24 cases, emphasizing unusual and diverse histologic features. *Am J Surg Pathol* (2012) 36:1395–403. doi: 10.1097/PAS.0b013e3182562bc1

11. Chen M, Yang J, Zhu L, Zhou C, Zhao H. Primary intrathoracic liposarcoma: A clinicopathologic study and prognostic analysis of 23 cases. *J Cardiothorac Surg* (2014) 9:119. doi: 10.1186/1749-8090-9-119

12. Ortega P, Suster D, Falconieri G, Zambrano E, Moran CA, Morrison C, et al. Liposarcomas of the posterior mediastinum: clinicopathologic study of 18 cases. *Mod Pathol* (2015) 28:721–31. doi: 10.1038/modpathol.2014.152

13. Fu Z, Yang K, Yang X, Chen S, Wang W, Chen D, et al. Primary intrathoracic liposarcoma: A clinical analysis of 31 cases. *Cancer Commun (Lond)* (2019) 39:15. doi: 10.1186/s40880-019-0358-8

14. Coindre JM. Grading of soft tissue sarcomas: Review and update. *Arch Pathol Lab Med* (2006) 130:1448–53. doi: 10.1043/1543-2165(2006)130[1448:gostsr]2.0.co;2

15. Peng R, Li N, Lan T, Chen H, Du T, He X, et al. Liposarcoma in children and young adults: A clinicopathologic and molecular study of 23 cases in one of the largest institutions of China. *Virchows Arch* (2021) 479:537–49. doi: 10.1007/s00428-021-03076-8

16. Zhang H, Erickson-Johnson M, Wang X, Oliveira JL, Nascimento AG, Sim FH, et al. Molecular testing for lipomatous tumors: Critical analysis and test recommendations based on the analysis of 405 extremity-based tumors. *Am J Surg Pathol* (2010) 34:1304–11. doi: 10.1097/PAS.0b013e3181e92d0b

17. He X, Pang Z, Zhang X, Lan T, Chen H, Chen M, et al. Consistent amplification of FRS2 and MDM2 in low-grade osteosarcoma: A genetic study of 22 cases with clinicopathologic analysis. *Am J Surg Pathol* (2018) 42:1143–55. doi: 10.1097/PAS.0000000000001125

18. Longano A, DuGuesclin A, Mitchell C. Primary dedifferentiated liposarcoma of the lung with rhabdomyoblastic and chrondroblastic differentiation. *Histopathology* (2015) 67:923–5. doi: 10.1111/his.12410

19. Achir A, Ouadnouni Y, Smahi M, Bouchikh M, Msougar Y, Benosman A. Primary pulmonary liposarcoma–a case report. *Thorac Cardiovasc Surg* (2009) 57:119–20. doi: 10.1055/s-2006-955885

20. Trahan S, Erickson-Johnson MR, Rodriguez F, Aubry MC, Cheville JC, Myers JL, et al. Formation of the 12q14-q15 amplicon precedes the development of a well-differentiated liposarcoma arising from a nonchondroid pulmonary hamartoma. *Am J Surg Pathol* (2006) 30:1326–9. doi: 10.1097/01.pas.0000213257.69478.2f

21. Loddenkemper C, Pérez-Canto A, Leschber G, Stein H. Primary dedifferentiated liposarcoma of the lung. *Histopathology* (2005) 46:710–2. doi: 10.1111/j.1365-2559.2005.02041.x

22. Said M, Migaw H, Hafsa C, Braham R, Golli M, Moussa A, et al. Imaging features of primary pulmonary liposarcoma. *Australas Radiol* (2003) 47:313–7. doi: 10.1046/j.1440-1673.2003.01198.x

23. Krygier G, Amado A, Salisbury S, Fernandez I, Maedo N, Vazquez T. Primary lung liposarcoma. *Lung Cancer* (1997) 17:271–5. doi: 10.1016/s0169-5002(97)00030-5

24. Sheppard MN. Primary liposarcoma of the lung in a young woman. *Thorax* (1990) 45:908. doi: 10.1136/thx.45.11.908

25. Rossi G, Cavazza A, Valli R, Torricelli P, Richeldi L, Rivasi F, et al. Atypical lipomatous tumour (lipoma-like well-differentiated liposarcoma) arising in a pulmonary hamartoma and clinically presenting with pneumothorax. *Lung Cancer* (2003) 39:103–6. doi: 10.1016/s0169-5002(02)00393-8

26. Son C, Choi PJ, Roh MS. Primary pulmonary myxoid liposarcoma with translocation t(12;16)(q13;p11) in a young female patient: A brief case report. *Korean J Pathol* (2012) 46:392–4. doi: 10.4132/KoreanJPathol.2012.46.4.392

27. Uchikov A, Poriazova E, Zaprianov Z, Markova D. Low-grade pulmonary myxoid liposarcoma. *Interact Cardiovasc Thorac Surg* (2005) 4:402–3. doi: 10.1510/icvts.2005.108332

28. Ibe T, Otani Y, Shimizu K, Nakano T, Sano T, Morishita Y. Pulmonary pleomorphic liposarcoma. *Jpn J Thorac Cardiovasc Surg* (2005) 53:443–7. doi: 10.1007/s11748-005-0082-y

29. Folpe AL, Weiss SW. Lipoleiomyosarcoma (well-differentiated liposarcoma with leiomyosarcomatous differentiation): A clinicopathologic study of nine cases including one with dedifferentiation. *Am J Surg Pathol* (2002) 26:742–9. doi: 10.1097/01.pas.0000016311.09846.57

30. Setsu N, Miyake M, Wakai S, Nakatani F, Kobayashi E, Chuman H, et al. Primary retroperitoneal myxoid liposarcomas. *Am J Surg Pathol* (2016) 40:1286–90. doi: 10.1097/PAS.0000000000000657

31. Furlan K, Miller I, Rohra P, Mir F, Ocampo Gonzalez FA, Gattuso P. Well-differentiated liposarcoma primary from thymic stroma: Case report and literature review. *Exp Mol Pathol* (2020) 116:104517. doi: 10.1016/j.yexmp.2020.104517

32. Iwamoto N, Matsuura Y, Ninomiya H, Ichinose J, Nakao M, Ishikawa Y, et al. An extremely rare case of rapidly growing mediastinal well-differentiated liposarcoma with a sclerosing variant: A case report. *Surg Case Rep* (2020) 6:158. doi: 10.1186/s40792-020-00928-4

33. Zhang M, Zhang S, Shi H, Li W, Wei Z. Resection of a huge mediastinal well-differentiated liposarcoma involving left thoracic cavity. *J Cardiothorac Surg* (2019) 14:148. doi: 10.1186/s13019-019-0965-0

34. Tong JJ, Li XJ, Li GX, Qian GQ. Lipoleiomyosarcoma of the posterior mediastinum. *QJM* (2018) 111:191–2. doi: 10.1093/qjmed/hcx256

35. Wang X, Asmann YW, Erickson-Johnson MR, Oliveira JL, Zhang H, Moura RD, et al. High-resolution genomic mapping reveals consistent amplification of the fibroblast growth factor receptor substrate 2 gene in well-differentiated and dedifferentiated liposarcoma. *Genes Chromosomes Cancer* (2011) 50:849–58. doi: 10.1002/gcc.20906

36. Jing W, Lan T, Chen H, Zhang Z, Chen M, Peng R, et al. Amplification of FRS2 in atypical lipomatous tumour/well-differentiated liposarcoma and de-differentiated liposarcoma: A clinicopathological and genetic study of 146 cases. *Histopathology.* (2018) 72:1145–55. doi: 10.1111/his.13473

37. Lucas DR, Shukla A, Thomas DG, Patel RM, Kubat AJ, McHugh JB. Dedifferentiated liposarcoma with inflammatory myofibroblastic tumor-like features. *Am J Surg Pathol* (2010) 34:844–51. doi: 10.1097/PAS.0b013e3181db34d8

38. Kai K, Udo K, Yamaguchi K, Tobu S, Noguchi M, Aishima S. A dedifferentiated liposarcoma with inflammatory myofibroblastic tumor-like features. *Pathol Int* (2018) 68:262–4. doi: 10.1111/pin.12645

39. Chen S, He S, Huang H, Li L, Wang W, Cui Z, et al. Unusual subcutaneous dedifferentiated liposarcoma exhibiting coexistence of meningothelial-like whorls and inflammatory myofibroblastic tumor-like structures. *J Cutan Pathol* (2020) 47:171–8. doi: 10.1111/cup.13621

40. Boatright C, Walker CM, Donald J, Cui W, Nagji AS. Incidental dedifferentiated mediastinal liposarcoma on f-18-fluciclovine PET/CT. *Clin Imaging* (2020) 59:21–4. doi: 10.1016/j.clinimag.2019.08.004

41. Fukai R, Fukumura Y, Suzuki K. A dedifferentiated liposarcoma of the anterior mediastinum. *Int J Clin Oncol* (2009) 14:174–7. doi: 10.1007/s10147-008-0819-6

42. Benchetritt M, Hofman V, Venissac N, Brennetot C, Italiano A, Aurias A, et al. Dedifferentiated liposarcoma of the pleura mimicking a malignant solitary fibrous tumor and associated with dedifferentiated liposarcoma of the mediastinum: Usefulness of cytogenetic and molecular genetic analyses. *Cancer Genet Cytogenet* (2007) 179:150–5. doi: 10.1016/j.cancergencyto.2007.09.006

43. Ye YW, Liao MY, Mou ZM, Shi XX, Xie YC. Thoracoscopic resection of a huge esophageal dedifferentiated liposarcoma: A case report. *World J Clin Cases.* (2020) 8:1698–704. doi: 10.12998/wjcc.v8.i9.1698

44. Kim SY, Froelich JJ, Dawson H, Peters AA, Tappero C, Heverhagen JT. Inflammatory calcified de-differentiated liposarcoma of the anterior mediastinum. *ANZ J Surg* (2019) 89:1326–7. doi: 10.1111/ans.14697

45. Harth S, Litzlbauer HD, Behrens CB, Roller FC, Gamerdinger U, Burchert D, et al. Dedifferentiated liposarcoma of the anterior mediastinum: A rare case. *Rofo.* (2016) 188:95–7. doi: 10.1055/s-0035-1553367

46. Asaka S, Yoshida K, Hashizume M, Ito K. A mediastinal liposarcoma resected using a double approach with a thoracoscope. *Thorac Cardiovasc Surg Rep* (2013) 2:46–9. doi: 10.1055/s-0033-1358605

47. Coulibaly B, Bouvier C, Payan MJ, Thomas P. Recurrent dedifferentiated liposarcoma of mediastinum involving lung and pleura. *Interact Cardiovasc Thorac Surg* (2009) 9:741–2. doi: 10.1510/icvts.2009.209494

48. Alaggio R, Coffin CM, Weiss SW, Bridge JA, Issakov J, Oliveira AM, et al. Liposarcomas in young patients a study of 82 cases occurring in patients younger than 22 years of age. *Am J Surg pathol* (2009) 33:645–58. doi: 10.1097/Pas.0b013e3181963c9c

49. Huh WW, Yuen C, Munsell M, Hayes-Jordan A, Lazar AJ, Patel S, et al. Liposarcoma in children and young adults: a multi-institutional experience. *Pediatr Blood Cancer* (2011) 57:1142–6. doi: 10.1002/pbc.23095

50. Creytens D, van Gorp J, Ferdinande L, Van Roy N, Libbrecht L. Array-based comparative genomic hybridization analysis of a pleomorphic myxoid liposarcoma. *J Clin Pathol* (2014) 67:834–5. doi: 10.1136/jclinpath-2014-202420

51. Hofvander J, Jo VY, Ghanei I, Gisselsson D, Martensson E, Mertens F. Comprehensive genetic analysis of a paediatric pleomorphic myxoid liposarcoma reveals near-haploidization and loss of the RB1 gene. *Histopathology.* (2016) 69:141–7. doi: 10.1111/his.12913

52. Sinclair TJ, Thorson CM, Alvarez E, Tan S, Spunt SL, Chao SD. Pleomorphic myxoid liposarcoma in an adolescent with Li-fraumeni syndrome. *Pediatr Surg Int* (2017) 33:631–5. doi: 10.1007/s00383-017-4063-x

53. Francom CR, Leoniak SM, Lovell MA, Herrmann BW. Head and neck pleomorphic myxoid liposarcoma in a child with Li-fraumeni syndrome. *Int J Pediatr Otorhinolaryngol* (2019) 123:191–4. doi: 10.1016/j.ijporl.2019.05.016

54. Zare SY, Leivo M, Fadare O. Recurrent pleomorphic myxoid liposarcoma in a patient with Li-fraumeni syndrome. *Int J Surg Pathol* (2020) 28:225–8. doi: 10.1177/1066896919878804

55. Creytens D, Folpe AL, Koelsche C, Mentzel T, Ferdinande L, van Gorp JM, et al. Myxoid pleomorphic liposarcoma–a clinicopathologic, immunohistochemical, molecular genetic and epigenetic study of 12 cases, suggesting a possible relationship with conventional pleomorphic liposarcoma. *Modern Pathol* (2021). 34:2043–9. doi: 10.1038/s41379-021-00862-2

56. Barretina J, Taylor BS, Banerji S, Ramos AH, Lagos-Quintana M, Decarolis PL, et al. Subtype-specific genomic alterations define new targets for soft-tissue sarcoma therapy. *Nat Genet* (2010) 42:715–21. doi: 10.1038/ng.619

57. Yamamoto H, Oda Y, Saito T, Sakamoto A, Miyajima K, Tamiya S, et al. p53 mutation and MDM2 amplification in inflammatory myofibroblastic tumors. *Histopathology.* (2003) 42:431–9. doi: 10.1046/j.1365-2559.2003.01611.x

58. Antonescu CR, Suurmeijer AJ, Zhang L, Sung YS, Jungbluth AA, Travis WD, et al. Molecular characterization of inflammatory myofibroblastic tumors with frequent ALK and ROS1 gene fusions and rare novel RET rearrangement. *Am J Surg Pathol* (2015) 39:957–67. doi: 10.1097/PAS.0000000000000404

59. Doyle LA, Tao D, Mariño-Enríquez A. STAT6 is amplified in a subset of dedifferentiated liposarcoma. *Modern Pathol* (2014) 27:1231–7. doi: 10.1038/modpathol.2013.247

60. Robinson DR, Wu YM, Kalyana-Sundaram S, Cao X, Lonigro RJ, Sung YS, et al. Identification of recurrent NAB2-STAT6 gene fusions in solitary fibrous tumor by integrative sequencing. *Nat Genet* (2013) 45:180–5. doi: 10.1038/ng.2509

61. Lan T, Chen H, Xiong B, Zhou T, Peng R, Chen M, et al. Primary pleuropulmonary and mediastinal synovial sarcoma: A clinicopathologic and molecular study of 26 genetically confirmed cases in the largest institution of southwest China. *Diagn Pathol* (2016) 11:62. doi: 10.1186/s13000-016-0513-3

62. Qiu Y, Jing W, Zhou Y, Chen H, Chen M, Zhang H. Unusual split green-orange signals in USP6 fluorescence *in situ* hybridization in a malignant peripheral nerve sheath tumor with a novel NF1-SCIMP fusion: a potential diagnostic pitfall. *Virchows Arch* (2022) 480:1255–60. doi: 10.1007/s00428-021-03179-2

63. Zhang H, Macdonald WD, Erickson-Johnson M, Wang X, Jenkins RB, Oliveira AM. Cytogenetic and molecular cytogenetic findings of intimal sarcoma. *Cancer Genet Cytogenet* (2007) 179:146–9. doi: 10.1016/j.cancergencyto.2007.08.013

64. Qin J, Chen B, Li C, Yan J, Lu H. Genetic heterogeneity and predictive biomarker for pulmonary sarcomatoid carcinomas. *Cancer Genet* (2021) 250-251:12–9. doi: 10.1016/j.cancergen.2020.11.004

65. Jimbo N, Komatsu M, Itoh T, Hirose T. MDM2 dual-color *in situ* hybridization (DISH) aids the diagnosis of intimal sarcomas. *Cardiovasc Pathol* (2019) 43:107142. doi: 10.1016/j.carpath.2019.07.001

66. Boland JM, Weiss SW, Oliveira AM, Erickson-Johnson ML, Folpe AL. Liposarcomas with mixed well-differentiated and pleomorphic features: A clinicopathologic study of 12 cases. *Am J Surg Pathol* (2010) 34:837–43. doi: 10.1097/PAS.0b013e3181dbf2f7

67. Marino-Enriquez A, Fletcher CDM, Dal Cin P, Hornick JL. Dedifferentiated liposarcoma with "Homologous" lipoblastic (Pleomorphic liposarcoma-like) differentiation: Clinicopathologic and molecular analysis of a series suggesting revised diagnostic criteria. *Am J Surg pathol* (2010) 34:1122–31. doi: 10.1097/PAS.0b013e3181e5dc49

frontiers | Frontiers in Oncology

TYPE Original Research
PUBLISHED 15 September 2022
DOI 10.3389/fonc.2022.950114

OPEN ACCESS

EDITED BY
Ming Zhao,
Zhejiang Provincial People's Hospital, China

REVIEWED BY
Alexandra Kovach,
Children's Hospital of Los Angeles, United States
Sam Sadigh,
Brigham and Women's Hospital and Harvard Medical School, United States

*CORRESPONDENCE
Xia Liu,
mdcg2014bl@163.com

†These authors have contributed equally to this work

SPECIALTY SECTION
This article was submitted to Surgical Oncology, a section of the journal Frontiers in Oncology

RECEIVED 22 May 2022
ACCEPTED 23 August 2022
PUBLISHED 15 September 2022

CITATION
Weng X, Yang YJ, Zhang M, Cai C, Sun YH, Wu XK, Zhang RR, Gui HH, Li W, Xu QZ and Liu X (2022) Primary intraosseous Rosai–Dorfman disease: An analysis of clinicopathologic characteristics, molecular genetics, and prognostic features. *Front. Oncol.* 12:950114. doi: 10.3389/fonc.2022.950114

Primary intraosseous Rosai–Dorfman disease: An analysis of clinicopathologic characteristics, molecular genetics, and prognostic features

Xin Weng[1†], Yajie Yang[1†], Meng Zhang[1], Chang Cai[1], Yanhua Sun[1], Xikang Wu[1], Rongrong Zhang[1], Huihui Gui[1], Wei Li[2], Qizhong Xu[3] and Xia Liu[1*]

[1]Department of Pathology, Shenzhen Second People's Hospital, Shenzhen University First Affiliated Hospital, Shenzhen, China, [2]Department of Joint and Musculoskeletal Tumor, Shenzhen Second People's Hospital, Shenzhen University First Affiliated Hospital, Shenzhen, China, [3]Department of Radiology, Shenzhen Second People's Hospital, Shenzhen University First Affiliated Hospital, Shenzhen, China

Background: Rosai–Dorfman disease (RDD) is a rare histiocytic proliferative disorder of uncertain pathogenesis. Most patients present with proliferation in the lymph nodes manifesting as adenopathy; however, RDD may primarily arise in a variety of extranodal sites, including the bone, which is a great challenge in the diagnosis. The clinicopathological characteristics and prognostic features of primary intraosseous RDD have not been well characterized.

Methods: We retrospectively analyzed the clinicopathologic and prognostic features of four cases of primary intraosseous RDD during the past 10 years in our hospital, with a review of an additional 62 cases with complete follow-up data from the literature.

Results: Primary intraosseous RDD was identified in 0.14% (4/2,800) of total bone biopsies performed at our institution over the study period. According to our retrospective analysis, a total of 18 cases of primary lymph node, skin, or other non-osseous site-based RDD were diagnosed in our hospital. The ages of the 66 total patients ranged from 1.5 to 76 years, with a median age of 25 years. There were 31 male and 35 female patients, with a male-to-female ratio of 0.89:1. Primary intraosseous RDD occurred most often in the bones of the extremities (60.6%, 40/66), with the proximal tibia being the most common location; 39.4% (26/66) of the cases arose in the axial skeleton, predominantly in the vertebra and craniofacial bones. Solitary masses and multiple tumors were present in 84.8% (56/66) and 15.2% (10/66) of the cases, respectively. Pain of the affected area was the most common presenting symptom. Radiographically, the lesions were lytic with well-defined and usually sclerotic margins. Immunohistochemistry showed that large histiocytes from

patients with RDD were positive for OCT2, in addition to S100 and CD68. Molecular tests were performed in seven reported cases and four of our cases. All the 11 cases were non-decalcified. PCR results showed that there were no *BRAF-V600E*, *KRAS*, or *NRAS* mutations in primary intraosseous RDD; only one case with both RDD and Langerhans cell histiocytosis showed *BRAF-V600E* mutation. The survival data showed that 22.7% (15/66) of the patients experienced recurrences or developed RDD at distant sites during the follow-up period (median follow-up, 13 months; range, 1–106 months). The 5-year progression-free survival (PFS) of the patients with primary intraosseous RDD was 57.5%. We found that there was a significant difference in PFS between female and male patients (p = 0.031). However, there was no statistically significant difference in PFS between patients with solitary masses and multiple tumors (p = 0.698). Similarly, no statistically significant differences in PFS were found between the different age groups (p = 0.908) or tumor locations (p = 0.728).

Conclusion: Primary intraosseous RDD is an extremely rare disease. The diagnosis of RDD may be quite challenging because of its non-specific clinical presentation and imaging. Immunohistochemistry showed that large histiocytes were positive for OCT2 in addition to S100 and CD68, which may be helpful for differential diagnosis. Molecular detection showed that RDD may be related to the MAPK pathway, though these results are also ultimately not specific. The pathogenesis of RDD is yet to be elucidated, but recent studies suggest possible clonality of hyperproliferative histiocytes.

KEYWORDS

primary, bone, Rosai–Dorfman disease, clinicopathologic features, OCT2, cyclin D1, progression-free survival (PFS), MAPK pathway

1 Introduction

Rosai–Dorfman disease (RDD), as a synonym for sinus histiocytosis with massive lymphadenopathy, was first described in 1965 (1), although it was not recognized as a distinct clinical entity until 1969 (2). RDD is a histiocytic proliferation disorder characterized by large S100-positive histiocytes exhibiting emperipolesis (3). RDD usually involves the lymph nodes, most frequently in the neck. As a result, patients typically present with painless bilateral cervical lymphadenopathy, in conjunction with fever, leukocytosis, and elevated erythrocyte sedimentation rate (4). Extranodal disease may occur as a primary process or in association with bone involvement.

Primary intraosseous RDD is an extremely rare disease. To date, only about 100 cases of intraosseous RDD have been reported, mainly as case reports rather than as study series. Because of its rarity, the clinicopathological characteristics and prognostic features of primary intraosseous RDD have not been well described. In an attempt to expand the known clinicopathologic and molecular genetic characteristics, as well as prognostic features, we retrospectively analyzed four cases of primary intraosseous RDD in our hospital with a review of an additional 62 cases with complete follow-up data from the literature.

Abbreviations: IRD, IgG4-related disease; LCH, Langerhans cell histiocytosis; PFS, progression-free survival; RDD, Rosai–Dorfman disease.

2 Materials and methods

2.1 Case selection

All cases of primary intraosseous RDD diagnosed from January 2012 to July 2022 in the Department of Pathology, Shenzhen Second People's Hospital, Shenzhen University First Affiliated Hospital, Shenzhen, Guangdong, China, were retrospectively analyzed. Primary intraosseous RDD cases were collected. The inclusion criteria of this retrospective

study were as follows: 1) imaging showed no cervical mass or systemic superficial lymph node enlargement and 2) intraosseous lesion as the initial presentation without extraskeletal or lymph node manifestations at presentation. Patients with RDD with evidence of systemic disease or associated lymphadenopathy were excluded. The clinical data collected for analysis included age, gender, location, clinical presentation, imaging, treatment regimens, and survival data. All patients provided written informed consent for the collection and publication of their medical information during their first visit to the hospital.

We also performed an extensive literature search for reported cases of primary intraosseous RDD in PubMed (www.ncbi.nlm.nih.gov/pubmed/) using different combinations of keywords in the title/abstract field, including "primary", "bone", "intraosseous", "sinus histiocytosis with massive lymphadenopathy", "RDD", and "Rosai–Dorfman". Cases in English-language literature were carefully reviewed to extract essential clinicopathologic and prognostic data and to combine the cases that were repeatedly studied in different papers. A total of 62 cases of primary intraosseous RDD were retrieved from the literature and included in our review.

2.2 Immunohistochemical staining and *in-situ* hybridization

The specimens of these four cases of primary intraosseous RDD cases were formalin-fixed and paraffin-embedded and then sectioned at 4.0 μm thickness. The sections were stained using hematoxylin and eosin staining or were used for immunohistochemical examination. The immunohistochemical stains were performed on a Leica BOND-III Fully Automated IHC & ISH Staining System (Leica Biosystems Newcastle Ltd., England) with Bond Polymer Refine Detection Kit (Leica Biosystems; Catalog no. DS9800). Appropriate negative and positive controls were performed with satisfactory staining. The pretreatment methods, primary antibodies, and their working dilutions are listed in Table S1.

The EBV Probe *In Situ* Hybridization Kit (Zhongshan Golden Bridge Biotechnology Co. Ltd., Beijing, China; Catalog no. ISH-7001) was used to detect Epstein–Barr virus-encoded small RNAs according to the manufacturer's protocol. The positive signals were a brownish-yellow color localized in the nuclei.

2.3 Molecular assays for gene mutations

BRAF-V600E, *KRAS*, and *NRAS* mutations were detected in the undecalcified and formalin-fixed paraffin-embedded samples using real-time PCR. Genomic DNA was extracted from tumor cell samples *via* the commercial AmoyDx® FFPE DNA Kit (Amoy Diagnostic Co. Ltd., Xiamen, China; Catalog no. 8.02.23501X036G) according to the kit's instructions. DNA (15 ng) was then examined for *BRAF-V600E*, *KRAS*, and *NRAS* mutations using commercial kits with a detection sensitivity of 1% mutation load (Human BRAF Gene V600E Mutation Fluorescence PCR Diagnostic Kit, Amoy, Catalog no. 8.0120301X024A; AmoyDx® KRAS/NRAS Mutations Detection Kit, Amoy, Catalog no. 8.01.25402W006A) in an ABI 7500 real-time PCR machine (Applied Biosystems, CA, USA). FAM signals from the mutation detection system indicated the mutation status of the sample.

2.4 Statistical analysis

Progression-free survival (PFS) was defined as the years from the first diagnosis of primary intraosseous RDD to local recurrence, secondary lesions in other locations, or last follow-up. Those without evidence of the disease at last follow-up were treated as censored. The Kaplan–Meier method was used to estimate overall distributions, and the log-rank test was used to compare survival distributions between patient groups. p-values <0.05 (two-sided) were considered to be statistically significant. The life table method was used to estimate overall distributions. SPSS software (version 26.0 for Mac; SPSS Statistics Inc., IL, USA) was used for the analysis.

3 Results

3.1 Patients' clinical characteristics

The major clinical features of the four cases of primary intraosseous RDD are summarized in Table 1. There were one female and three male patients, with ages ranging from 25 to 35 years. Primary intraosseous RDD was identified in 0.14% (4/2,800) of total bone biopsies performed at our institution over the study period. After retrospective analysis, a total of 18 cases of primary lymph node, skin, or other non-osseous site-based RDD in our hospital were diagnosed. All patients were Chinese without a history of RDD, and imaging showed no cervical mass or systemic superficial lymph node enlargement. The lesions arose in the humerus, skull, and vertebra, respectively. Clinically, patient #1 complained of pain in the left shoulder, with limited activity for more than 1 month. Patient #2 found a subcutaneous mass in his right forehead for 6 months. Patient #3 presented with limb numbness for 2 months when visiting the hospital. Patient #4 complained of left middle finger pain for 2 months.

After an extensive search of the English literature, we found 62 cases of primary intraosseous RDD with complete follow-up data (5–42). Some cases were included in two articles with different study purposes, and the data from these cases were carefully extracted and combined. The clinicopathologic features of these cases are summarized in Table S2. The brief

TABLE 1 Clinical features of the four cases of primary intraosseous RDD in our hospital.

Case	Age (years)	Gender	Location	Clinical presentation	Imaging	Lesion	Treatment	Outcome (mo)
#1	25	M	Left proximal humerus metaphysis, extended into the adjacent epiphysis	Left shoulder pain with limited activity for more than 1 month	Irregular cystic transparent area with focal sclerotic margins	S	Lesion curettage	NED, 12
#2	28	F	Right frontal bone	Subcutaneous mass of right forehead was found for 6 months	Bone defect area, soft tissue mass	S	Lesion excised	NED, 65
#3	32	M	Spinous process of C2–C5	Limbs with numbness for 2 months	MRI showed an enhancing intramedullary mass	S	Lesion excised	NED, 10
#4	35	M	Middle phalanx of the left middle finger	Left middle finger pain for 2 months	Irregular cystic transparent area with trabecular destruction and absorption	S	Lesion excised	NED, 2

F, female; M, male; mo, months; M, multiple; MRI, magnetic resonance imaging; NED, no evidence of disease; S, single.

clinicopathologic characteristics of the cases from the literature and our institution are summarized in Table 2.

The ages of the 66 total patients ranged from 1.5 to 76 years, with a median age of 25 years. There were 31 male and 35 female patients, with a male-to-female ratio of 0.89:1. Primary intraosseous RDD occurred most often in the bones of the extremities (60.6%, 40/66), with the proximal tibia being the most common location; 39.4% (26/66) of the cases arose in the axial skeleton, predominantly in the vertebra and craniofacial bones. A solitary mass and multiple tumors were present in 84.8% (56/66) and 15.2% (10/66) of the cases, respectively. Pain of the affected area was the most common presenting symptom.

3.2 Radiology findings

Imaging was available for the four patients. Patient #1 had an irregular cystic transparent area in the left proximal humerus metaphysis which extended into the adjacent epiphysis, with focal sclerotic margins (Figures 1A, B). The right frontal bone of patient #2 was damaged locally, with the inner and outer plates becoming thinner and extending into the soft tissue locally(Figures 1C). Patient #3 had an enhanced intramedullary mass in the spinous process of C2–C5, extending into the adjacent soft tissue and epidural space and causing compression of the spinal cord (Figures 1D). Patient #4 showed an irregular cystic transparent area with trabecular destruction and absorption (Figures 1E, F).

3.3 Pathology findings

3.3.1 Histology

The histomorphologic features of RDD in the bone and lymph nodes are not exactly the same. Classically, nodal RDD shows prominent sinusoidal involvement, but primary intraosseous RDD is poorly defined, replaces the marrow, infiltrates Haversian systems, and is associated with local bone resorption (Figure 2A). The mass is characterized by sheets and clusters of large histiocytes, with nuclei that range from round or oval to reniform, with fine or vesicular chromatin and prominent eosinophilic nucleoli (Figure 2B). The cytoplasm is abundant and pale eosinophilic, with conspicuous emperipolesis

TABLE 2 Summary of the brief clinicopathologic features of primary intraosseous RDD in the present study and the literature.

Characteristics	Present study	Literature	Total
Total cases	4	62	66
Male/female	3/1	28/34	31/35
Median age (range) (years)	/(25–35)	23 (1.5–76)	25 (1.5–76)
Location (extremital bone/axial skeleton)	2/2	38/24	40/26
Lesions (single/multiple)	4/0	52/10	56/10
BRAF-V600E mutation (positive/negative/unknown)	0/4/0	1/6/55	1/10/55
KRAS mutation (positive/negative/unknown)	0/4/0	0/7/55	0/11/55
NRAS mutation (positive/negative/unknown)	0/4/0	0/0/62	0/4/62
Median follow-up (mo)	/(n = 4)	14 (n = 62)	13 (n = 66)
5-year PFS	/	/	57.5%
Outcome (recurrence or progression/NED)	0/4	15/47	16/50

mo, months; NED, no evidence of disease; PFS, progression-free survival.

10.3389/fonc.2022.950114

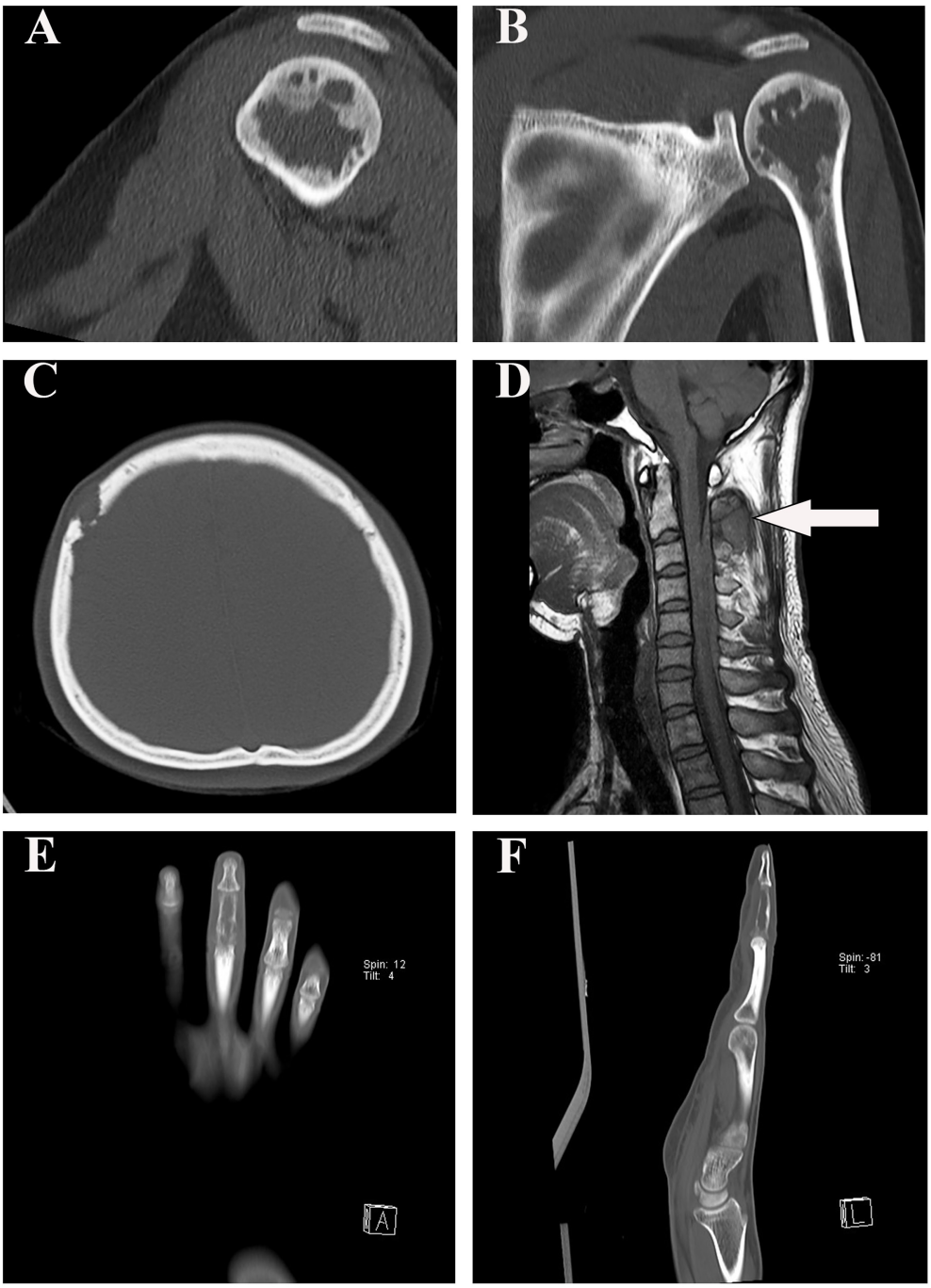

FIGURE 1
Radiographic findings in our four patients. **(A, B)** The sagittal and coronal computed tomography scan demonstrated that patient #1 had an irregular cystic transparent area in the left proximal humerus metaphysis, extended into the adjacent epiphysis. **(C)** Computed tomography image showed that the right frontal bone of patient #2 was damaged locally. **(D)** T1-weighted MRI showed that patient #3 had a hypointense epidural lesion in the spinous process of C2–C5 (arrow). **(E, F)** Patient #4 showed an irregular cystic transparent area with trabecular destruction and absorption in the coronal and sagittal computed tomography scan.

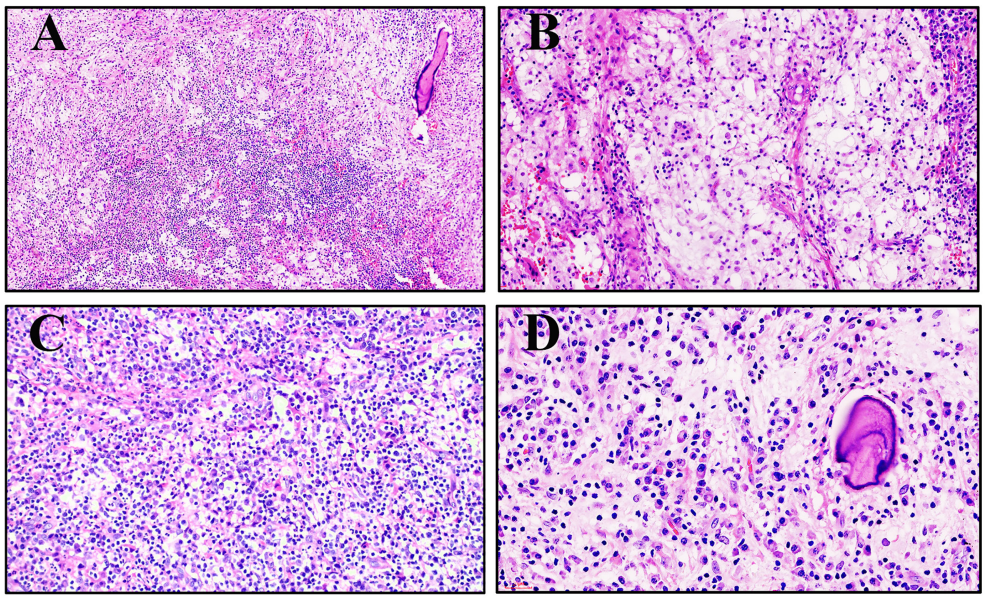

FIGURE 2
Morphology of primary intraosseous Rosai–Dorfman disease (RDD). **(A)** An infiltrative pattern of RDD in the medullary cavity (patient #3, hematoxylin and eosin ×100). **(B)** Large histiocytes with abundant clear to eosinophilic cytoplasm tended to form loose clusters surrounded by a mixed inflammatory infiltrate (patient #2, hematoxylin and eosin ×200). **(C)** Large histiocytes demonstrated emperipolesis of the neutrophils, lymphocytes, and plasma cells (patient #4, hematoxylin and eosin ×200). **(D)** The tumor cells are enmeshed in a fibrotic stroma that contains a great quantity of intermixed lymphocytes and plasma cells (patient #1, hematoxylin and eosin ×400).

of the lymphocytes (lymphocytophagocytosis), plasma cells, or neutrophils (Figure 2C). The tumor cells were enmeshed in a fibrotic stroma that contained a great quantity of intermixed lymphocytes and plasma cells in patient #1 (Figure 2D).

3.3.2 Immunophenotype

The results of immunohistochemistry are summarized in Table 3. All four cases had large histiocytes that were strongly positive for S100 and CD68 (Figures 3A, B). Nuclear immunoreactivity for cyclin D1 and OCT2 was observed in these cases (Figures 3C, D). Only one of the four cases showed CD163 positivity, and the other three were negative. All cases were negative for langerin (Figure 3G), CD1a, and EBER (Figure 3H). The biopsy specimens of patient #1 had more than 100 IgG4-positive plasma cells per high-power field and an IgG4/IgG ratio of more than 0.4:1 (Figures 3E, F). However, serum IgG4 (1.82 g/L, reference range: 0.03–2.01 g/L) and IgG (15.96 g/L, reference range: 7–16 g/L) levels were normal.

3.3.3 Molecular pathology

PCR assays for *BRAF-V600E*, *KRAS*, and *NRAS* gene mutations were performed on the four cases. All four cases showed no mutations in *BRAF-V600E*, *KRAS*, or *NRAS*. However, due to limited conditions in our department, a larger next-generation sequencing (NGS) panel was not performed on these four cases, to assess for the presence of mutations in other genes within the MAPK pathway.

3.3.4 Treatment and outcome

All four patients underwent surgical resections and did not accept further treatment. These four patients were followed up

TABLE 3 Immunophenotype and EBV infection status of four primary intraosseous RDD.

Case	S100	OCT2	Cyclin D1	CD68	CD163	Langerin	CD1a	IgG4/IgG	EBER
#1	+	+	+	+	–	–	–	>40%	–
#2	+	+	+	+	–	–	–	/	–
#3	+	+	+	+	–	–	–	<40%	–
#4	+	+	+	+	+	–	–	<40%	–

+, positive; –, negative.

10.3389/fonc.2022.950114

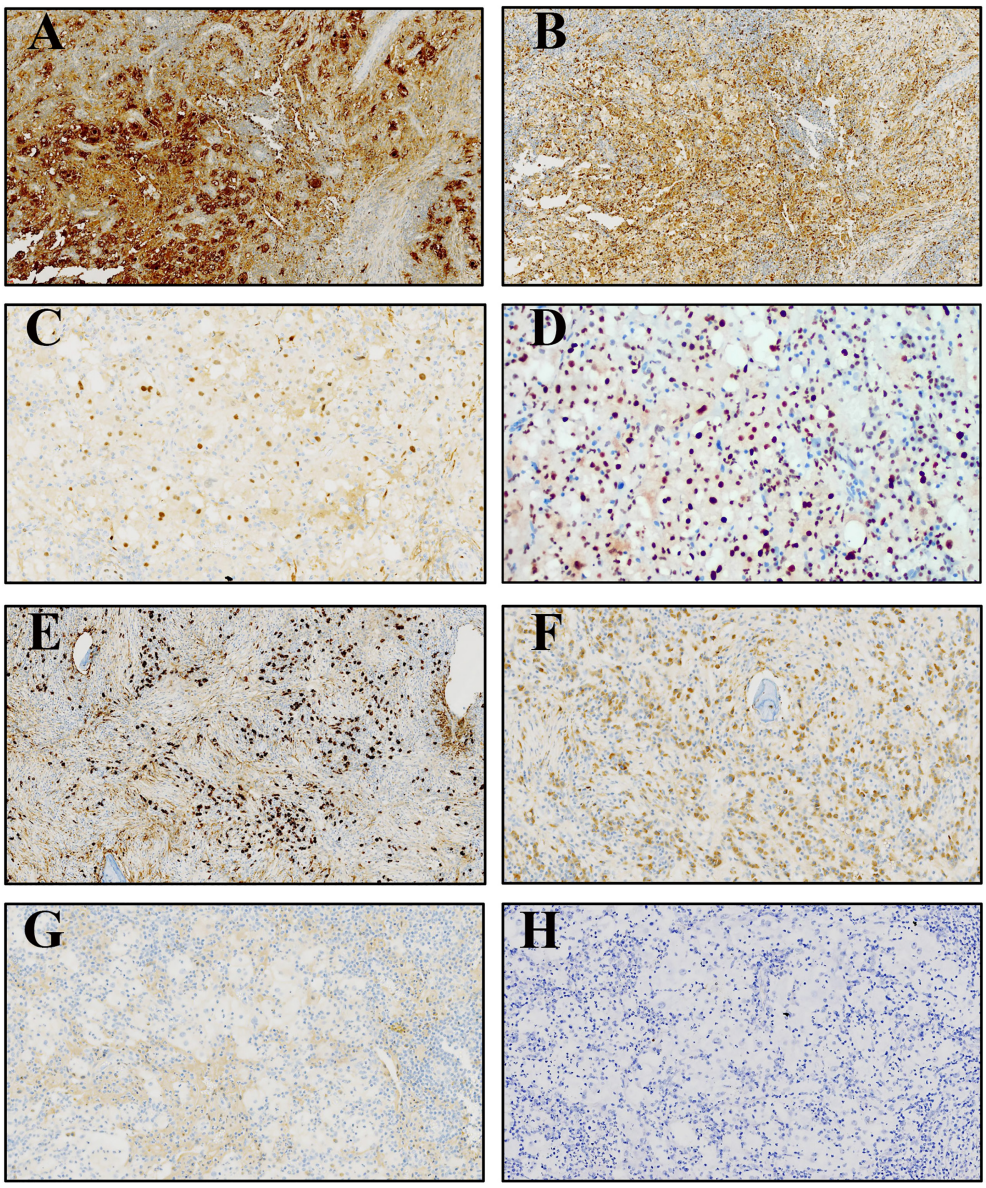

FIGURE 3
Immunophenotype of primary intraosseous RDD. **(A, B)** The large histiocytes were strongly positive for S100 and CD68, respectively. **(C)** The nuclear immunoreactivity for cyclin D1 was observed. **(D)** All cases were positive for OCT2. **(E, F)** The biopsy specimens of patient 1# had a large quantity of IgG4-positive and IgG-positive plasma cells. **(G, H)** Langerin and EBER were negative.

successfully until 18 April 2022. The follow-up interval ranged from 2 to 65 months. All patients survived without disease during the follow-up period.

Of the 66 patients with survival data from our present study and reported in the literature, local recurrence and secondary lesions in other locations occurred in 22.7% (15/66) of the patients during the follow-up period (median follow-up, 13 months; range, 1–106 months). The 5-year PFS of the patients with primary intraosseous RDD was 57.5% (Figure 4A). Of note, the male patients had significantly lower 5-year PFS (50.5%) than the female patients (66.0%; $p = 0.031$) (Figure 4B). However, there was no statistically significant difference in PFS between patients with solitary masses and multiple tumors ($p = 0.698$). Similarly, no statistically significant differences were found in PFS between age groups ($p = 0.908$) and different tumor locations ($p = 0.728$).

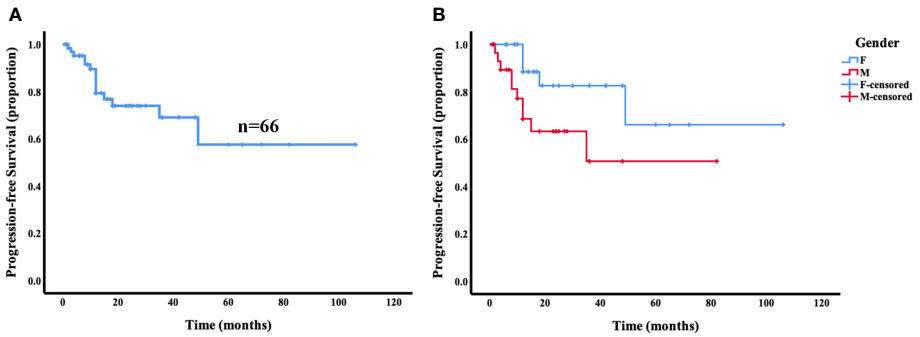

FIGURE 4
Progression-free survival (PFS) analysis for primary intraosseous RDD. The 5-year PFS of the patients with primary intraosseous RDD was 57.5% **(A)**. Female patients showed a trend toward superior progression-free survival compared with male patients (p = 0.031) **(B)**.

4 Discussion

RDD is a rare histiocytic proliferative disorder of uncertain pathogenesis, which was first described in 1965 (1) and recognized as a distinct clinical entity in 1969 by Rosai and Dorfman (2). In the fifth edition of the WHO classification of soft tissue and bone tumors, RDD was classified as a hematopoietic neoplasm of the bone (3). Most of the patients present with lymph node involvement manifesting as adenopathy. In the present retrospective study, a total of 18 cases of primary lymph node, skin, or other non-osseous site-based RDD were diagnosed in our hospital. Extranodal disease may occur as a primary process or in association with nodal involvement (5). However, primary RDD of the bone is extremely rare and the occurrence of this entity remains unknown. Primary intraosseous RDD was identified in 0.14% (4/2,800) of total bone biopsies at our institution over the study period.

Due to its rarity, the clinicopathologic features and prognosis of primary intraosseous RDD have not been well characterized. To date, no known risk factors have been identified. After an extensive search of the English literature, only 62 cases of primary intraosseous RDD with complete survival data were identified. The median age of the patients was 24 years old, and there was no significant difference in age between genders. Pain of the affected area was the most common presenting symptom. Interestingly, we found that primary intraosseous RDD most occurred in the bones of the extremities, with the proximal tibia being the most common location. In addition, most of the tumors were single osteolytic lesions.

The etiology of RDD remains uncertain. The proposed mechanisms include immune dysfunction and possible viral infection. A few studies have reported that RDD may be related to the Epstein–Barr virus, human herpesvirus infections, and so on (43, 44). However, no Epstein–Barr virus or human herpesvirus infections were observed in primary intraosseous RDD from our present study and those reported in the literature, so any potential correlation between viral infection and the pathogenesis of primary intraosseous RDD cannot be clarified.

RDD has always been considered as a disease of histiocytic polyclonal hyperplasia, but in recent years, molecular genetics suggests that it may have a potential monoclonal pathogenesis. Fatobene and Haroche reported one case of nodal RDD with confirmed *BRAF-V600E* mutation, representing a promising therapeutic target, especially for patients with refractory or extensive disease (45). In addition, mutually exclusive *KRAS* and *MAP2K1* mutations were described in one-third of the cases of RDD, suggesting that this subgroup is clonal and involves activation of the MAPK/ERK pathway (46). Wu et al. reported an *NRAS* mutation in cutaneous RDD (47), indicating that *NRAS* mutations in the MAPK/ERK pathway may be involved in the pathogenesis of cutaneous RDD. Nevertheless, there was only one report on the molecular genetics of primary intraosseous RDD. Dong et al. detected *BRAF-V600E* and *KRAS* mutations in seven undecalcified primary intraosseous RDD cases, which showed that only one case with the concurrence of RDD and Langerhans cell histiocytosis (LCH) had *BRAF-V600E* mutation, suggesting that the *BRAF-V600E* mutation may be caused by LCH lesions rather than RDD lesions. Similarly, no *BRAF-V600E*, *KRAS*, and *NRAS* mutations were detected in our cases and all samples were not decalcified. Unfortunately, a larger NGS panel was not performed on our cases and the reported cases to assess for the presence of mutations in other genes within the MAPK pathway. Like our results, some studies (25, 48) have demonstrated immunohistochemical cyclin D1 expression in RDD cases including bone lesions, reflecting constitutive MAPK pathway activation in the pathogenesis of RDD. However, since few studies have been reported and no larger NGS panel has

been performed, it is still unclear whether the primary intraosseous RDD is related to the activation of the MAPK pathway. Therefore, not only more cases but also more robust mutational analysis are needed to further confirm the findings.

Tracht et al. demonstrated a possible histologic overlap between RDD and the more common IgG4-related disease (IRD), which could cause problems in pathologic diagnosis (49). Another study demonstrated that RDD of the breast can show a significant increase in IgG4+ plasma cells as well as fibrosis, which may further complicate matters (50). In our present study, one case showed increased IgG4-positive plasma cells and IgG4/IgG ratio, but serum IgG4 and IgG levels were normal. Therefore, we speculate that RDD histomorphology may be associated with that of IRD, but a relationship between RDD and IRD has not been definitively established. A diagnosis of concurrence of RDD and IRD should integrate the pathological features, the number of IgG4-positive plasma cells, clinical manifestations, serological examinations. and so on.

The imaging characteristics of primary intraosseous RDD are not specific and often misleading. Radiographically, bone lesions are often misdiagnosed as osteomyelitis or LCH. Other entities in differential diagnosis include Erdheim–Chester disease, lymphoma, plasma cell myeloma, and metastatic disease (5). Osteomyelitis is a necrotizing and sclerosing bone disease dominated by inflammation, often including numerous neutrophils and with frequent periosteal reactive bone formation. Histologically, the mixed inflammatory infiltrate with focal neutrophilic micro-abscesses, occasional multinucleated giant cells, and granuloma-like histiocyte collections may suggest infection or granulomatous disease. However, the characteristic S100-positive histiocytes with emperipolesis are not seen in either condition. As the name suggests, LCH is dominated by the proliferation of Langerhans histiocytes. Langerhans histiocytes are usually found in granuloma-like clusters and have characteristic elongated, indented, grooved, or convoluted nuclei with inconspicuous nucleoli. In addition to the S100 protein, they are consistently positive for CD1a and langerin, which are not expressed by RDD histiocytes. Erdheim–Chester disease is a multisystemic proliferative histiocytic disorder, characterized by long bone involvement with bilateral and symmetrical sclerotic lesions. Frequently, there is extraskeletal involvement including the cardiovascular system, central nervous system, kidneys, and lungs. Histologically, there is a proliferation of foamy histiocytes within the marrow spaces with associated fibrosis and thickening of bone trabeculae. The proliferating histiocytes are positive for CD163 and CD68 and are usually negative for S100. They are also negative for CD1a and langerin. Emperipolesis is not seen in Erdheim–Chester disease. Metastatic carcinoma and melanoma can be ruled out by histomorphology and the lack of expression of epithelial and melanocytic markers.

Surgical resection or curettage is the most common treatment of primary intraosseous RDD. At present, there is great controversy about the relative benefits of postoperative adjuvant radiotherapy and steroids therapy (51). The prognosis is good, but local recurrences or secondary lesions in other locations may occur after surgery in some cases. Our analysis showed that the 5-year PFS of patients with primary intraosseous RDD was 57.5%. Interestingly, our analysis of all prior reported cases showed that female patients had a trend toward superior PFS compared with male patients. No statistically significant difference was found in PFS between patients with different age groups, tumor locations, or number of lesions.

4.1 Conclusions

Primary intraosseous RDD is an extremely rare disease. Diagnosis of the disease may be quite challenging because of its variable clinical manifestations, non-specific imaging findings, and background mixed with inflammatory infiltrate. Immunohistochemistry showed that large histiocytes from patients with RDD were positive for OCT2 in addition to S100 and CD68 and negative for CD163, which may be helpful for differential diagnosis. Molecular detection showed that RDD may be related to the MAPK pathway, though these findings are ultimately not specific. The pathogenesis of RDD is yet to be elucidated, but recent studies suggest possible clonality.

Data availability statement

The original contributions presented in the study are included in the article/Supplementary Material. Further inquiries can be directed to the corresponding author.

Ethics statement

All patients provided written informed consent for the collection and publication of their medical information during the first visit to the hospital.

Author contributions

XW designed the study and wrote the manuscript. YJY and MZ contributed to the clinical collection, as well as data analysis. CC and YHS provided the cases. XKW performed molecular detection. RRZ and HHG performed immunohistochemical staining and *in-situ* hybridization (ISH). WL collected the follow-up information. QZX offered imaging data. XL provided supervision, conceived the project, and provided leadership. All authors contributed to the article and approved the submitted version.

Conflict of interest

The authors declare that the research was conducted in the absence of any commercial or financial relationships that could be construed as a potential conflict of interest.

Publisher's note

All claims expressed in this article are solely those of the authors and do not necessarily represent those of their affiliated organizations, or those of the publisher, the editors and the reviewers. Any product that may be evaluated in this article, or claim that may be made by its manufacturer, is not guaranteed or endorsed by the publisher.

Supplementary material

The Supplementary Material for this article can be found online at: https://www.frontiersin.org/articles/10.3389/fonc.2022.950114/full#supplementary-material

References

1. Destombes P. [Adenitis with lipid excess, in children or young adults, seen in the antilles and in mali. (4 cases)]. *Bull Soc Pathol Exot Filiales* (1965) 58:1169–75.

2. Rosai J, Dorfman RF. Sinus histiocytosis with massive lymphadenopathy. A newly recognized benign clinicopathological entity. *Arch Pathol* (1969) 87:63–70.

3. WHO Classification of Tumours Editorial Board. *WHO classification of tumours. Soft tissue and bone tumours [M].5th* ed. Lyon: IARC Press, 2020: 498–9.

4. Foucar E, Rosai J, Dorfman RF. Sinus histiocytosis with massive lymphadenopathy. an analysis of 14 deaths occurring in a patient registry. *Cancer.* (1984) 54:1834–40. doi: 10.1002/1097-0142(19841101)54:9<1834::AID-CNCR2820540911>3.0.CO;2-F

5. Demicco EG, Rosenberg AE, Björnsson J, Rybak LD, Unni KK, Nielsen GP. Primary rosai-dorfman disease of bone: A clinicopathologic study of 15 cases. *Am J Surg Pathol* (2010) 34:1324–33. doi: 10.1097/PAS.0b013e3181ea50b2

6. Xu J, Liu CH, Wang YS, Chen CX. Extranodal rosai-dorfman disease as isolated lesion of the tibia diagnosed by fine-needle aspiration cytology: A case report. *Med (Baltimore)* (2015) 94:e2038. doi: 10.1097/MD.0000000000002038

7. Vithran DTA, Wang JZ, Xiang F, Wen J, Xiao S, Tang WZ, et al. Osseous rosai-dorfman disease of tibia in children: A case report. *World J Clin Cases* (2021) 9:1416–23. doi: 10.12998/wjcc.v9.i6.1416

8. Tripathy K, Misra A, Sahu AK, Patnaik K. Extranodal rosai-dorfman disease in a carpal bone. *Indian J Orthop* (2012) 46:487–9. doi: 10.4103/0019-5413.98836

9. Tekin U, Tuz HH, Gunhan O. Reconstruction of a patient with rosai-dorfman disease using ramus graft and osseointegrated implants: A case report. *J Oral Implantol* (2012) 38:79–83. doi: 10.1563/AAID-JOI-D-10-00056.1

10. Sundaram C, Uppin Shantveer G, Chandrashekar P, Prasad VB, Umadevi M. Multifocal osseous involvement as the sole manifestation of rosai-dorfman disease. *Skeletal Radiol* (2005) 34:658–64. doi: 10.1007/s00256-005-0951-6

11. Shulman S, Katzenstein H, Abramowsky C, Broecker J, Wulkan M, Shehata B. Unusual presentation of rosai-dorfman disease (RDD) in the bone in adolescents. *Fetal Pediatr Pathol* (2011) 30:442–7. doi: 10.3109/15513815.2011.618873

12. Ross AB, Davis KW, Buehler D, Chan BY. Primary rosai-dorfman disease of bone: A report of two cases. *Case Rep Radiol* (2019) 2019:1720131. doi: 10.1155/2019/1720131

13. Robert EG, Fallon KB, Tender GC. Isolated rosai-dorfman disease of the sacrum. *Case Illustration J Neurosurg Spine* (2006) 4:425. doi: 10.3171/spi.2006.4.5.425

14. Paryani NN, Daugherty LC, O'Connor MI, Jiang L. Extranodal rosai-dorfman disease of the bone treated with surgery and radiotherapy. *Rare Tumors* (2014) 6:5531. doi: 10.4081/rt.2014.5531

15. Paryani NN, Daugherty LC, O'Connor MI, Jiang L. Osseous rosai-dorfman disease presenting as a solitary lesion of the distal radius. *J Handb Surg Am* (2019) 44:70 e71–5. doi: 10.1016/j.jhsa.2018.03.019

16. Miniello TG, Araujo JP, Sugaya NN, Elias FM, de Almeida OP, Alves FA. Rosai-dorfman disease affecting the maxilla. *Autops Case Rep* (2016) 6:49–55. doi: 10.4322/acr.2016.057

17. Mansoori J, Fisher O, Akinyeye IO, Sobolevsky MA, Quinn RH. Primary rosai-dorfman disease in 39-Year-Old woman with osseous tibial lesion manifestion: A case report and literature review. *Foot Ankle Orthop* (2021) 6:24730114211060058. doi: 10.1177/24730114211060058

18. Izubuchi Y, Suzuki K, Imamura Y, Katayama H, Ohshima Y, Matsumine A. Primary rosai-dorfman disease of bone arising in the infantile ilium: A case report. *Exp Ther Med* (2020) 19:2983–8. doi: 10.3892/etm.2020.8568

19. Hsu AR, Bhatia S, Kang RW, Arvanitis L, Nicholson GP, Virkus WW. Extranodal rosai-dorfman disease presenting as an isolated glenoid lesion in a high school athlete. *J Shoulder Elbow Surg* (2012) 21:e6–11. doi: 10.1016/j.jse.2011.05.017

20. Goel MM, Agarwal PK, Agarwal S. Primary rosai-dorfman disease of bone without lymphadenopathy diagnosed by fine needle aspiration cytology. *A Case Rep Acta Cytol* (2003) 47:1119–22. doi: 10.1159/000326661

21. George J, Stacy G, Peabody T, Montag A. Rosai-dorfman disease manifesting as a solitary lesion of the radius in a 41-year-old woman. *Skeletal Radiol* (2003) 32:236–9. doi: 10.1007/s00256-002-0613-x

22. Baker JC, Kyriakos M, McDonald DJ, Rubin DA. Primary rosai-dorfman disease of the femur. *Skeletal Radiol* (2017) 46:129–35. doi: 10.1007/s00256-016-2515-3

23. Rittner RE, Baumann U, Laenger F, Hartung D, Rosenthal H, Hueper K. Whole-body diffusion-weighted MRI in a case of rosai-dorfman disease with exclusive multifocal skeletal involvement. *Skeletal Radiol* (2012) 41:709–13. doi: 10.1007/s00256-011-1328-7

24. Okay E, Yıldız Y, Sarı T, Yildirim ANT, Ozkan K. Rosai-dorfman disease of the talus in a child: A case report. *J Am Podiatr Med Assoc* (2021) 1:111. doi: 10.7547/20-050

25. Dong RF, Gong LH, Zhang W, Li L, Sun XQ, Zhang M. Primary intraosseous rosai-dorfman disease: A clinicopathological analysis of fourteen cases. *Zhonghua Bing Li Xue Za Zhi* (2020) 49:904–9. doi: 10.3760/cma.j.cn112151-20191202-00772

26. Kumar A, Thirugnanam B, Kareem SA, Ajay Kumar SP, Vidyadhara S. Report of isolated epidural extra-nodal rosai-dorfman disease of cervicothoracic spine. *Spinal Cord Ser Cases* (2020) 6:82. doi: 10.1038/s41394-020-00332-y

27. El Molla M, Mahasneh T, Holmes SE, Al-Khawaja D. Rare presentation of rosai-dorfman disease mimicking a cervical intramedullary spinal cord tumor. *World Neurosurg* (2014) 81:442 e447–449. doi: 10.1016/j.wneu.2013.01.002

28. Nguyen PX, Nguyen NV, Le TD. Spinal extranodal rosai-dorfman disease: A case report and literature review. *Int J Surg Case Rep* (2021) 88:106491. doi: 10.1016/j.ijscr.2021.106491

29. Hamels J, Fiasse L, Thiery J. Atypical lymphohistiocytic bone tumour (osseous variant of rosai-dorfman disease?). *Virchows Arch A Pathol Anat Histopathol* (1985) 408:183–9. doi: 10.1007/BF00707981

30. Lewin JR, Das SK, Blumenthal BI, D'Cruz C, Patel RB, Howell GE, et al. Osseous pseudotumor. the sole manifestation of sinus histiocytosis with massive lymphadenopathy. *Am J Clin Pathol* (1985) 84:547–50. doi: 10.1093/ajcp/84.4.547

31. Nawroz IM, Wilson-Storey D. Sinus histiocytosis with massive lymphadenopathy (Rosai-dorfman disease). *Histopathology* (1989) 14:91–9. doi: 10.1111/j.1365-2559.1989.tb02118.x

32. Allegranza A, Barbareschi M, Solero CL, Fornari M, Lasio G. Primary lymphohistiocytic tumour of bone: A primary osseous localization of rosai-

dorfman disease. *Histopathology* (1991) 18:83–6. doi: 10.1111/j.1365-2559.1991.tb00820.x

33. Kademani D, Patel SG, Prasad ML, Huvos AG, Shah JP. Intraoral presentation of rosai-dorfman disease: A case report and review of the literature. *Oral Surg Oral Med Oral Pathol Oral Radiol Endod* (2002) 93:699–704. doi: 10.1067/moe.2002.123495

34. Loh SY, Tan KB, Wong YS, Lee YS. Rosai-dorfman disease of the triquetrum without lymphadenopathy. *A Case Rep J Bone Joint Surg Am* (2004) 86:595–8. doi: 10.2106/00004623-200403000-00021

35. Mota Gamboa JD, Caleiras E, Rosas-Uribe A. Extranodal rosai-dorfman disease. clinical and pathological characteristics in a patient with a pseudotumor of bone. *Pathol Res Pract* (2004) 200:423–6. discussion 427-428. doi: 10.1016/j.prp.2004.01.005

36. Rodriguez-Galindo C, Helton KJ, Sánchez ND, Rieman M, Jeng M, Wang W. Extranodal rosai-dorfman disease in children. *J Pediatr Hematol Oncol* (2004) 26:19–24. doi: 10.1097/00043426-200401000-00007

37. Al-Saad K, Thorner P, Ngan BY, Gerstle JT, Kulkarni AV, Babyn P. Extranodal rosai-dorfman disease with multifocal bone and epidural involvement causing recurrent spinal cord compression. *Pediatr Dev Pathol* (2005) 8:593–8. doi: 10.1007/s10024-005-8102-6

38. Miyake M, Tateishi U, Maeda T, Arai Y, Sugimura K, Hasegawa T. Extranodal rosai-dorfman disease: A solitary lesion with soft tissue reaction. *Radiat Med* (2005) 23:439–42.

39. Tubbs RS, Kelly DR, Mroczek-Musulman EC, Hammers YA, Berkow RL, Oakes WJ, et al. Spinal cord compression as a result of rosai-dorfman disease of the upper cervical spine in a child. *Childs Nerv Syst* (2005) 21:951–4. doi: 10.1007/s00381-004-1121-1

40. Yoon AJ, Parisien M, Feldman F, Young-In Lee F. Extranodal rosai-dorfman disease of bone, subcutaneous tissue and paranasal sinus mucosa with a review of its pathogenesis. *Skeletal Radiol* (2005) 34:653–7. doi: 10.1007/s00256-005-0953-4

41. Keskin A, Genç F, Günhan O. Rosai-dorfman disease involving maxilla: A case report. *J Oral Maxillofac Surg* (2007) 65:2563–8. doi: 10.1016/j.joms.2006.10.003

42. DeFelice DS, Srinivas ML, Wobker SE, Parr JB. Going bone deep: Osseous rosai-dorfman disease in an adult with recurrent, culture-negative osteomyelitis. *Case Rep Infect Dis* (2018) 2018:6151738. doi: 10.1155/2018/6151738

43. Foucar E, Rosai J, Dorfman RF, Eyman JM. Immunologic abnormalities and their significance in sinus histiocytosis with massive lymphadenopathy. *Am J Clin Pathol* (1984) 82:515–25. doi: 10.1093/ajcp/82.5.515

44. Levine PH, Jahan N, Murari P, Manak M, Jaffe ES. Detection of human herpesvirus 6 in tissues involved by sinus histiocytosis with massive lymphadenopathy (Rosai-dorfman disease). *J Infect Dis* (1992) 166:291–5. doi: 10.1093/infdis/166.2.291

45. Fatobene G, Haroche J, Hélias-Rodzwicz Z, Charlotte F, Taly V, Ferreira AM. BRAF V600E mutation detected in a case of rosai-dorfman disease. *Haematologica* (2018) 103:e377–9. doi: 10.3324/haematol.2018.190934

46. Garces S, Medeiros LJ, Patel KP, Li S, Pina-Oviedo S, Li J. Mutually exclusive recurrent KRAS and MAP2K1 mutations in rosai-dorfman disease. *Mod Pathol* (2017) 30:1367–77. doi: 10.1038/modpathol.2017.55

47. Wu KJ, Li SH, Liao JB, Chiou CC, Wu CS, Chen CC. NRAS mutations may be involved in the pathogenesis of cutaneous rosai dorfman disease: A pilot study. *Biol (Basel)* (2021) 10:396. doi: 10.3390/biology10050396

48. Baraban E, Sadigh S, Rosenbaum J, Van Arnam J, Bogusz AM, Mehr C, et al. Cyclin D1 expression and novel mutational findings in rosai-dorfman disease. *Br J Haematol* (2019) 186:837–44. doi: 10.1111/bjh.16006

49. Tracht J, Reid MD, Xue Y, Madrigal E, Sarmiento JM, Kooby D, et al. Rosai-dorfman disease of the pancreas shows significant histologic overlap with IgG4-related disease. *Am J Surg Pathol* (2019) 43:1536–46. doi: 10.1097/PAS.0000000000001334

50. Hoffmann JC, Lin CY, Bhattacharyya S, Weinberg OK, Chisholm KM, Bayerl M, et al. Rosai-Dorfman Disease of the Breast With Variable IgG4+ Plasma Cells: A Diagnostic Mimicker of Other Malignant and Reactive Entities. *Am J Surg Pathol* (2019) 43:1653–60. doi: 10.1097/PAS.0000000000001347

51. Dalia S, Sagatys E, Sokol L, Kubal T. Rosai-dorfman disease: Tumor biology, clinical features, pathology, and treatment. *Cancer Control* (2014) 21:322–7. doi: 10.1177/107327481402100408

frontiers | Frontiers in Oncology

TYPE Case Report
PUBLISHED 05 October 2022
DOI 10.3389/fonc.2022.993414

OPEN ACCESS

EDITED BY
Nicoleta Arva,
Northwestern University, United States

REVIEWED BY
Bonnie Choy,
Northwestern Medicine, United States
Bogdan Isaila,
Northwestern Medicine, United States

*CORRESPONDENCE
Ming Zhao
zhaomingpathol@163.com

†These authors have contributed equally to this work

SPECIALTY SECTION
This article was submitted to Surgical Oncology, a section of the journal Frontiers in Oncology

RECEIVED 13 July 2022
ACCEPTED 21 September 2022
PUBLISHED 05 October 2022

CITATION
Fan Y, Yu J and Zhao M (2022) Metanephric stromal tumor with *BRAF* V600E mutation in an adult patient: Case report and literature review. *Front. Oncol.* 12:993414. doi: 10.3389/fonc.2022.993414

Metanephric stromal tumor with *BRAF* V600E mutation in an adult patient: Case report and literature review

Yuqian Fan[1,2†], Jingjing Yu[3†] and Ming Zhao[1*]

[1]Cancer Center, Department of Pathology, Zhejiang Provincial People's Hospital, Affiliated People's Hospital of Hangzhou Medical College, Hangzhou, China, [2]Department of Pathology, Tangshan Gongren Hospital, Tangshan, China, [3]Department of Pathology, Ningbo Yinzhou Second Hospital, Ningbo, China

Metanephric stromal tumor (MST) is a rare, benign pediatric renal neoplasm of uncertain histogenesis that belongs to the metanephric family of tumors. MST involving adult patients is very uncommon, which could cause significant diagnostic confusions. Recent molecular studies have revealed recurrent *BRAF* mutations in MST in pediatric patients which may serve as powerful diagnostic tools for distinguishing MST from other renal stromal tumors. We present a *BRAF*-mutated MST in an adult patient with a brief review of the pertinent literature. To our knowledge, our case represents to date the sixth report of adult MST and the first adult MST proven to harbor *BRAF* mutation. This is a 41-year-old man who was incidentally identified to have a left renal mass by ultrasonography. He had a 5-year history of hypertension which could be controlled with oral antihypertensive drug. Partial nephrectomy was performed which demonstrated a 2.6-cm, oval, circumscribed mass with a fibrotic and firm texture. Microscopic examination showed a hypocellular, spindle cell neoplasm with entrapped nephrons, within a predominantly fibrous and focally myxoid stroma. Foci of hyalinized stroma surrounding entrapped native renal tubules or blood vessels to form concentric collarettes-like structures, and small-sized arterioles showing angiodysplasia, were observed. Immunostains showed the tumor cells to be diffusely positive for CD34. Fluorescence *in-situ* hybridization analysis was negative for rearrangements involving both the *EWSR1* and *FUS* loci. Targeted next-generation sequencing disclosed a pathogenic mutation of *BRAF* exon15: c.1799T>A (p.V600E). The patient's hypertension normalized without oral antihypertensive drugs 2 months postoperatively and he was in good status 12 months after the surgery. Our case highlights the diagnostic dilemma of MST occurring in adults and points to the usefulness of molecular detection of *BRAF* mutation for arriving at accurate diagnosis.

KEYWORDS

NGS: next-generation sequencing, FISH: fluorescence in-situ hybridization, BRAF V600E mutation, metanephric stromal tumor, metanephric tumors, mesenchymal tumor

Introduction

Metanephric stromal tumor (MST) is a rare, benign stromal neoplasm unique to the kidney that is thought to be part of a spectrum of metanephric family of tumors which also includes the epithelial lesion metanephric adenoma (MA) and the mixed stromal-epithelial lesion metanephric adenofibroma (MAF) (1). The vast majority of MSTs occur in children in their first three years (2), with only few cases involving adults have been documented (3–6). Recently, several molecular studies have revealed that most pediatric MSTs have a *BRAF* V600E mutation (7, 8). Because of its rarity, the preoperative diagnosis of adult MST is often difficult, and the etiology and clinical biology are largely undetermined. We herein present a MST in a 41-year-old man mimicking a low-grade fibroblastic tumor of the kidney and harboring a *BRAF* V600E mutation by targeted next-generation sequencing. To our knowledge, our case represents to date the sixth report of adult MST and the first adult MST proven to harbor *BRAF* mutation in the literature.

Case presentation

A 41-year-old man was incidentally identified to have a left renal mass by ultrasonography for physical examination. His medical history was unremarkable except for a 5-year history of hypertension, which could be controlled with the oral antihypertensive drug hydrochlorothiazide. Workup for 24-hour urine metanephrines and norepinephrine was negative. Computed tomography scan showed a focally low-enhancing, circumscribed, oval mass in the upper pole of the left kidney (Figure 1A). A subsequent magnetic resonance imaging revealed that the mass had iso-signal intensity on T1-weighted and low-signal intensity on T2-wighted with enhancement after contrast injection (Figure 1B). Neither local invasion nor lymphadenopathy was identified. A benign or low-grade mesenchymal tumor was suspected, and the patient underwent left laparoscopic partial nephrectomy.

Grossly, the resection specimen showed a well-circumscribed, nodular mass measuring 2.6×2.0×1.0 cm, centered on the renal cortex of the kidney. On sectioning, the mass was non-encapsulated, firm and fibrotic in consistency and whitish in color. Histologically, the tumor had overall expansile but focally infiltrative, scalloped margins, and numerous entrapped native renal tubules were noted throughout the tumor (Figures 2A–C). The tumor was composed of hypocellular, bland-appearing, ovoid- to spindle- or stellate-shaped cells, set in a predominantly collagenous and focally myxoid stroma (Figures 2D–F). Frequently, the highly hyalinized stroma surrounded entrapped native renal tubules or blood vessels forming concentric collarettes-like structures (Figure 2E). Occasionally, small-sized arterioles showing angiodysplasia were observed (Figure 2F). Mitotic figure was absent. By immunohistochemistry, the neoplastic cells were diffusely positive for CD34 (Figure 3), and focally positive for estrogen and progesterone receptors; they were negative for PAX8, S100 protein, STAT6, MUC4, cytokeratin, WT1, and actin. The Ki67 proliferation index was less than 1%. Fluorescence *in-situ* hybridization analysis revealed negative for rearrangements involving both the *EWSR1* and *FUS* loci (Figures 4A, B). Genetic testing using targeted next-generation sequencing for 425 cancer-relevant genes (GENESEEQ PRIME) disclosed the pathogenic mutation of *BRAF* exon15: c.1799T>A (p.V600E) in the tumor (Figure 4C). On the basis of the pathological and molecular genetic features, a diagnosis of adult MST was rendered.

The tumor was completely removed with negative resection margins. The operation was uneventful, and the patient was

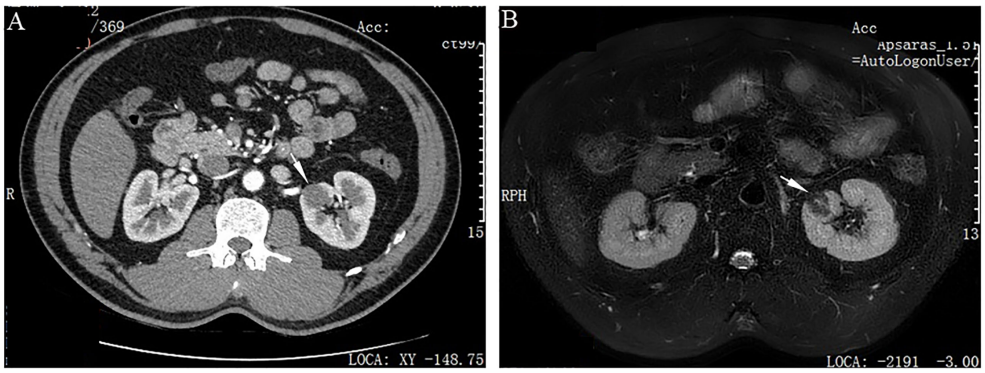

FIGURE 1
Imaging features of adult metanephric stromal tumor with *BRAF* V600E mutation. **(A)** Computed tomography scan shows a slightly enhanced, well-defined, oval mass (white arrow), in the upper pole of the left kidney. **(B)** Magnetic resonance imaging demonstrates that the mass has low-signal intensity on T2-wighted imaging (white arrow).

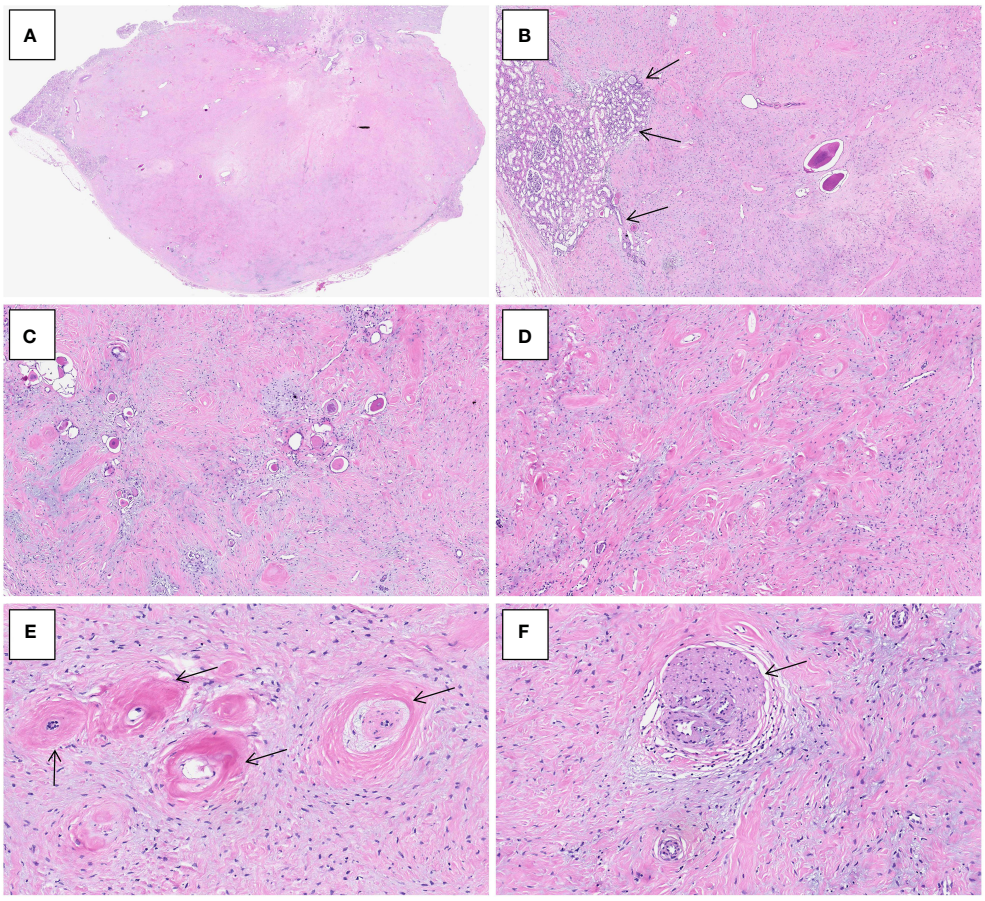

FIGURE 2
Histological characteristics of adult metanephric stromal tumor with *BRAF* V600E mutation. **(A)** At low power, the tumor is non-encapsulated and has an overall expansile contour. H&E×15. **(B)** Subtly infiltrative border of the tumor with adjacent normal renal parenchyma (arrows). H&E×40. **(C)** Numerous entrapped native renal tubules are noted. H&E×100. **(D)** The tumor is composed of bland, spindle- or stellate-shaped cells, set in a predominantly collagenous and focally myxoid stroma. H&E×100. **(E)** The highly hyalinized stroma encircles and entraps native renal tubules (arrows). H&E×300. **(F)** The tumor induces angiodysplasia within entrapped blood vessels (arrow). H&E×300.

discharged home on postoperative day 5. As of 2 months postnephrectomy, the patient's hypertension has normalized without oral antihypertensive drugs and he was in good status 12-month after the surgery.

Discussion

MST typically occurs in the first years of life (mean: 2 years) with only a few cases documented after 3 years (2). MST affecting adult patients is even rarer with only 6 cases (including the current one) have been described to date (Table 1) (3–6). There is no sex predilection with age ranging from 43 to 77 years (mean: 54 years). The clinical presentations are similar to those in pediatric patients, including abdominal pain or mass in 3 cases, hematuria in 1, and hypertension in 2 (3–6). Hypertension as a symptom is uncommonly seen in MST, presenting in less than 10% of pediatric cases (2). The previously reported adult MST with hypertension by McDonald et al. (5) in 2011 was a 55-year-old woman who had a 30-year history of neurofibromatosis type I and new-onset of refractory hypertension. As with our case, the patient's hypertension normalized in a short period after resection of the tumor. It is believed that the symptom of hypertension may be associated with the tumor's ability to entrap cortical glomeruli and induce juxtaglomerular cell hyperplasia and subsequent renin secretion (2, 5).

Adult MSTs exhibited identical histological features to those in pediatric patients. The tumors could be solid or mixed solid and cystic with size ranging from 2.5 to 21 cm (mean: 7.3cm) (3–6). Morphologically, MST is typically a subtly infiltrative tumor composed of variably cellular, bland-looking, spindle cells embedded in a diffusely fibrous to focally myxoid stroma. It characteristically encircles entrapped native renal tubules in a

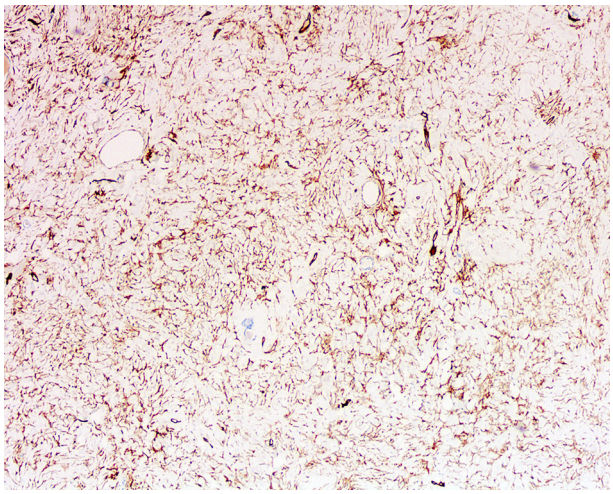

FIGURE 3
Immunohistochemistry of adult metanephric stromal tumor with *BRAF* V600E mutation. The tumor cells are diffusely and strongly positive for CD34. ×100.

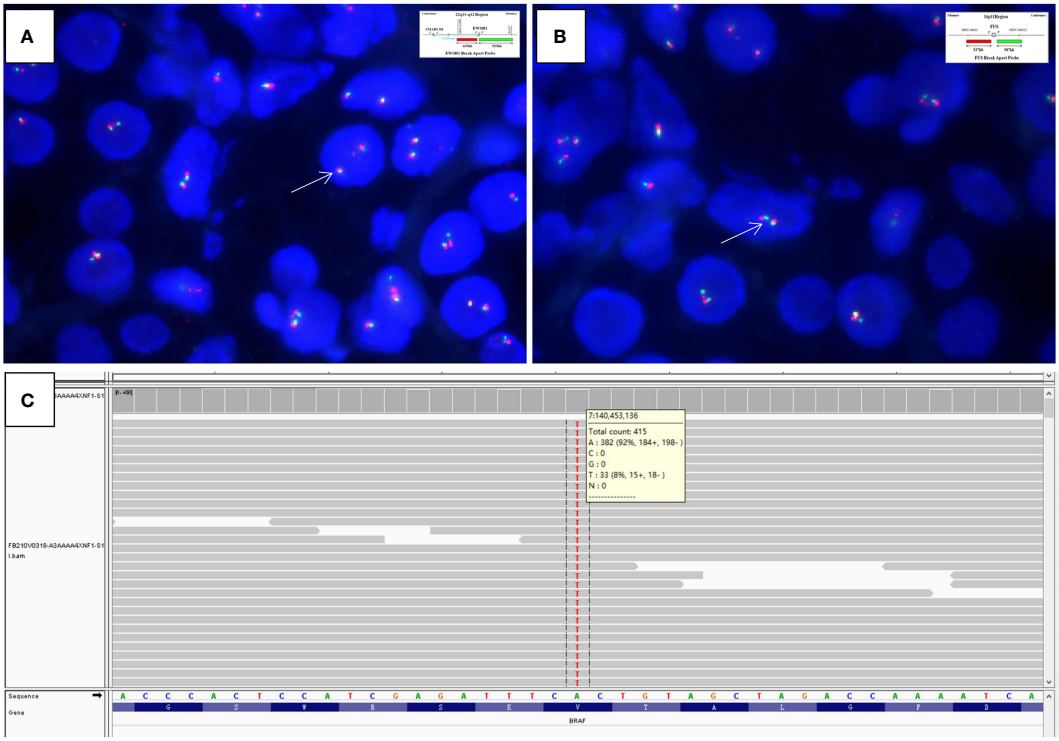

FIGURE 4
Fluorescence *in-situ* hybridization analysis is negative for rearrangements of both the **(A)** *EWSR1* (×1500, arrows indicate fused green and orange signals) and **(B)** *FUS* (×2000, arrows indicate fused green and orange signals) loci (Insets in A and B indicate schematic diagram of break-apart probes flanking *EWSR1* and *FUS*, respectively). **(C)** Targeted next-generation sequencing discloses the pathogenic mutation of *BRAF* exon15: c.1799T>A (p.V600E) in the tumor, as illustrated by the Integrative Genomics Viewer screenshot.

TABLE 1 Summary of adult metanephric stromal tumor reported in the literature.

Case (reference)	Age (years)/ Sex	Clinical presentations	Imaging features	Size	Molecular analysis	Follow-up (months)
1 (3)	53/ Female	Incidentally identified on workup for other diseases	CT: enhancing mixed solid cystic mass with mural calcifications in the right kidney	5.5-cm	NA	NA
2 (4)	72/Male	Abdominal mass with pain	NA	21-cm	NA	NED (120)
3 (4)	77/Male	Abdominal mass with pain	NA	18-cm	NA	NED (48)
4 (5, 7)*	55/ Female	30-year history of neurofibromatosis type I and new-onset of refractory hypertension	CT: complex cystic mass abutting the renal pelvis in the lower pole of the left kidney	2.5-cm	Negative for *BRAF* mutation by RT-PCR	Blood pressure returned to normal status 3-month postnephrectomy
5 (6)	56/ Female	Left lower abdominal pain; hematuria	CT: focally low-enhancing, sharply circumscribed, central mass in the upper pole of the right kidney	9-cm	NA	NA
6 Current case	41/Male	Incidentally identified by ultrasonography for physical examination; 5-year history of hypertension	CT: focally low-enhancing, circumscribed, oval mass in the upper pole of the left kidney. MRI: iso-signal intensity on T1-weighted and low-signal intensity on T2-wighted with enhancement after contrast injection	2.6-cm	Positive for mutation of *BRAF* exon15: c.1799T>A (p.V600E) by targeted NGS; negative for rearrangements involving both the *EWSR1* and *FUS* loci by FISH analysis.	Blood pressure returned to normal status 2-month postnephrectomy. NED (8)

*The case in reference 5 was the same to the 7th case in reference 7.
CT, computed tomography; MRI, magnetic resonance imaging; NA, not available; NED, no evidence of disease; NGS, next-generation sequencing; FISH, fluorescence in-situ hybridization.

concentric, onion skin pattern and frequently induces angiodysplasia in adjacent blood vessels and/or juxtaglomerular cell hyperplasia in entrapped glomeruli (1, 2). It often shows strong immunoreactivity to antibodies against CD34 and vimentin (2). The molecular basis of MST remains largely unknown until most recently when two separate groups identified mutations in *BRAF* gene (specifically V600E) in 6/7 (86%) and 11/17 (65%) of cases of MST, respectively (7, 8). These findings provide a common consistent genetic alteration that unifies all 3 members of the proposed metanephric neoplasia family, MST, MAF, and MA, given the fact that the latter two entities also frequently harbor *BRAF* V600E mutations (9, 10). For the previously reported cases of adult MST, only 1 had been tested for *BRAF* mutation and was negative (7). To our knowledge, the current case represents to date the first report of adult MST which has been proven to harbor *BRAF* mutation. However, further studies with more cases will be necessary to fully characterize the genetic underpinnings of this rare entity.

Although being rare, it remains a formal possibility that MST may be under-recognized in adults, with some cases have been diagnosed as other adult renal neoplasms that can closely resemble MST with entrapped nephrons. The most useful morphological clues for diagnosing MST include onion-skinning, concentric pattern of tumor cells surrounding entrapped renal tubules, and associated angiodysplasia and juxtaglomerular cell hyperplasia; however, these features maybe only subtle and not well-developed in a subset of cases. The differential diagnostic considerations for MST in adults are quite different from those in pediatric patients because of different clinical settings. For pediatric MST, the most important differential diagnosis is cellular congenital mesoblastic nephroma (CCMN) and clear cell sarcoma of the kidney (CCSK) (2). Both entities typically affect children in less than 3 years and vary rarely occur in adults. However, CCMN usually has a pushing border and is composed of sheets of mitotically-active spindle cells identical to infantile fibrosarcoma. Unlike MST, CCMN lacks expression of CD34 while harbors the characteristic gene fusion involving *ETV6-NTRK3* (11). CCSK is histologically characterized by regular branching capillary vasculature, cords cells with open chromatin, and multiple variants pattern. CCSK shows positivity to BCOR and cyclinD1 but negativity to CD34 by immunohistochemistry (12). Molecularly, most CCSKs have a *BCOR* internal tandem duplication, and small subset have gene fusions involving *YWHAE-NUTM2B* or *BCOR-CCNB3* (13, 14). The main differential diagnosis for adult MST includes sclerosing epithelioid fibrosarcoma (SEF) and solitary fibrous tumor (SFT). Both tumors can rarely occur primarily within the kidney and show bland, spindle to epithelioid cells infiltrating or entrapping native tubules with extensive sclerosis, and positivity for CD34 by immunostain (15, 16). SEF usually shows immunoreactivity for MUC4 and harbors the characteristic

gene rearrangements involving *EWSR1*, or less commonly *FUS* (15), which are absent in MST. SFT commonly has prominent HPC-like vessels and demonstrates the characteristic gene fusion of *NAB2-STAT6*, leading to the extensive expression of STAT6 (16); these features are unexpected in MST. Lastly, mixed epithelial and stromal tumor (MEST) of the kidney, which is characterized by biphasic epithelial and stromal components with spindle stroma, glands, and cysts, may also enter into the differential diagnosis of MST. However, MEST mostly occurs in perimenopausal women; the epithelial structures in MEST are more complex and are often lined by hobnail cells, and the stromal cells usually show smooth muscle and mullerian differentiation, which are typically positive for actin, desmin, CD10, and estrogen and progesterone receptors (17). Importantly, as *BRAF* V600E mutation has not been identified in other renal stromal tumors, the presence of this mutation may support the diagnosis of MST in difficult cases (8), just as our case has illustrated.

Adult MST is very rare and accurate diagnosis has important clinical significance. All the reported adult MSTs have had a benign course without recurrence or metastasis (3–6). Excision of the tumor is adequate therapy. The extra-renal angiodysplasia symptom induced by MST, such as hypertension, can relieve after resection of the tumor. Our case highlights the diagnostic dilemma of MST occurring in adults and points to the usefulness of molecular detection of *BRAF* mutation for arriving at accurate diagnosis.

Data availability statement

The raw data supporting the conclusions of this article will be made available by the authors, without undue reservation.

Ethics statement

The studies involving human participants were reviewed and approved by the Institutional Review Board Committee of Zhejiang Provincial People's Hospital, Affiliated People's Hospital, Hangzhou Medical College. Written informed consent for participation was not required for this study in accordance with the institutional requirements.

Author contributions

YF, JY, and MZ were involved in conception and design of the work, acquisition, analysis and interpretation of data, drafting the manuscript and revising it critically for important intellectual content and scientific integrity. All authors have read and approved the final manuscript.

Funding

This work was supported by Zhejiang Provincial Natural Science Foundation (LY21H160052) and Zhejiang Provincial Medicine and Health Research Foundation (2023KY040). The funder did not have any role in the design and conduct of the study, the analysis and interpretation of the data, and preparation of the manuscript.

Acknowledgments

The authors are grateful to Anbiping Laboratory, Guangzhou, China, for FISH analysis.

Conflict of interest

The authors declare that the research was conducted in the absence of any commercial or financial relationships that could be construed as a potential conflict of interest.

Publisher's note

References

1. WHO Classification of Tumours Editorial Board. *WHO Classification of Tumours. Urinary and Male Genital Tumours. 5th ed.* Lyon: International Agency for Research on Cancer (2022) p. 87–93.

2. Argani P, Beckwith JB. Metanephric stromal tumor: report of 31 cases of a distinctive pediatric renal neoplasm. *Am J Surg Pathol* (2000) 24(7):917–26. doi: 10.1097/00000478-200007000-00003

3. Bluebond-Langner R, Pinto PA, Argani P, Chan TY, Halushka M, Jarrett TW. Adult presentation of metanephric stromal tumor. *J Urol* (2002) 168(4 Pt 1):1482–3. doi: 10.1097/01.ju.0000030152.14265.e9

4. Amat Villegas I, Gómez Dorronsoro ML, López Caballero MC, del Llano Varela P, Pascual Piérola JI, Begoña Larrinaga M. Tumor del estroma metanéfrico: presentación de dos casos en adultos y revisión de la literatura [Metanephric stromal tumor: report of two cases and bibliographic review]. *Arch Esp Urol* (2006) 59(1):88–90. doi: 10.4321/s0004-06142006000100015

5. McDonald OG, Rodriguez R, Bergner A, Argani P. Metanephric stromal tumor arising in a patient with neurofibromatosis type 1 syndrome. *Int J Surg Pathol* (2011) 19(5):667–71. doi: 10.1177/1066896909344850

6. Chaudhri AA, Lee L, Das K. Cellular metanephric stromal tumor in a postmenopausal woman: a case report with review of the literature. *Int J Surg Pathol* (2013) 21(2):153–60. doi: 10.1177/1066896912453851

7. Argani P, Lee J, Netto GJ, Zheng G, Tseh-Lin M, Park BH. Frequent BRAF V600E mutations in metanephric stromal tumor. *Am J Surg Pathol* (2016) 40 (5):719–22. doi: 10.1097/PAS.0000000000000603

8. Marsden L, Jennings LJ, Gadd S, Yu M, Perlman EJ, Cajaiba MM. BRAF exon 15 mutations in pediatric renal stromal tumors: prevalence in metanephric stromal tumors. *Hum Pathol* (2017) 60:32–6. doi: 10.1016/j.humpath.2016.09.025

9. Choueiri TK, Cheville J, Palescandolo E, Fay AP, Kantoff PW, Atkins MB, et al. BRAF mutations in metanephric adenoma of the kidney. *Eur Urol* (2012) 62 (5):917–22. doi: 10.1016/j.eururo.2012.05.051

10. Mangray S, Breese V, Jackson CL, Lombardo K, Taliano R, Resnick M, et al. Application of BRAF V600E mutation analysis for the diagnosis of metanephric adenofibroma. *Am J Surg Pathol* (2015) 39(9):1301–4. doi: 10.1097/PAS.0000000000000501

11. El Demellawy D, Cundiff CA, Nasr A, Ozolek JA, Elawabdeh N, Caltharp SA, et al. Congenital mesoblastic nephroma: a study of 19 cases using immunohistochemistry and ETV6-NTRK3 fusion gene rearrangement. *Pathology* (2016) 48(1):47–50. doi: 10.1016/j.pathol.2015.11.007

12. Singh V, Gupta K, Saraswati A, Peters NJ, Trehan A. Role of cyclin D1 and BCOR immunohistochemistry in differentiating clear cell sarcoma of kidney from its mimics. *J Pediatr Hematol Oncol* (2021) 43(8):294–300. doi: 10.1097/MPH.0000000000002262

13. Roy A, Kumar V, Zorman B, Fang E, Haines KM, Doddapaneni H, et al. Recurrent internal tandem duplications of BCOR in clear cell sarcoma of the kidney. *Nat Commun* (2015) 6:8891. doi: 10.1038/ncomms9891

14. O'Meara E, Stack D, Lee CH, Garvin AJ, Morris T, Argani P, et al. Characterization of the chromosomal translocation t(10;17)(q22;p13) in clear cell sarcoma of kidney. *J Pathol* (2012) 227(1):72–80. doi: 10.1002/path.3985

15. Argani P, Lewin JR, Edmonds P, Netto GJ, Prieto-Granada C, Zhang L, et al. Primary renal sclerosing epithelioid fibrosarcoma: report of 2 cases with EWSR1-CREB3L1 gene fusion. *Am J Surg Pathol* (2015) 39(3):365–73. doi: 10.1097/PAS.0000000000000338

16. Zhao M, He H, Cao D, Fan D, Xu M, Zhang X, et al. Solitary fibrous tumor with extensive epithelial inclusions. *Am J Clin Pathol* (2022) 158(1):35–46. doi: 10.1093/ajcp/aqab211.

17. WHO Classification of Tumours Editorial Board. *WHO Classification of Tumours. Urinary and Male Genital Tumours. 5th ed.* Lyon: International Agency for Research on Cancer (2022) p. 94–5.

frontiers | Frontiers in Oncology

TYPE Original Research
PUBLISHED 14 October 2022
DOI 10.3389/fonc.2022.1020456

OPEN ACCESS

EDITED BY
Jinping Lai,
Kaiser Permanente Sacramento Medical Center, United States

REVIEWED BY
Kenneth Chang,
KK Women's and Children's Hospital, Singapore
José Manuel Lopes,
University of Porto, Portugal

*CORRESPONDENCE
Ni Chen
chenni1@163.com

SPECIALTY SECTION
This article was submitted to Surgical Oncology, a section of the journal Frontiers in Oncology

RECEIVED 16 August 2022
ACCEPTED 30 September 2022
PUBLISHED 14 October 2022

CITATION
Yin X, Zhang X, Pan X, Tan J, Zheng L, Zhou Q and Chen N (2022) Atypical metanephric adenoma: Shares similar histopathological features and molecular changes of metanephric adenoma and epithelial-predominant Wilms' tumor.
Front. Oncol. 12:1020456.
doi: 10.3389/fonc.2022.1020456

Atypical metanephric adenoma: Shares similar histopathological features and molecular changes of metanephric adenoma and epithelial-predominant Wilms' tumor

Xiaoxue Yin[1], Xingming Zhang[2], Xiuyi Pan[1], Junya Tan[1], Linmao Zheng[1], Qiao Zhou[1] and Ni Chen[1]*

[1]Department of Pathology, Laboratory of Pathology, West China Hospital, West China Medical School, Sichuan University, Chengdu, China, [2]Department of Urology, West China Hospital, West China Medical School, Sichuan University, Chengdu, China

Background: Metanephric adenomas (MAs) are rare, benign renal tumors. Wilms' tumors (WTs) are malignant embryonic tumors that originated from nephrogenic blastemal cells. However, some tumors have similar morphology to both MA and epithelial-predominant WT, which makes differential diagnosis difficult. We aimed to analyze the morphological, immunophenotypic and molecular changes in overlapping cases to explore their attribution.

Methods and results: Twenty MAs, ten WTs, and nine cases with MA/WT overlapping histological features were studied. Twenty tumors demonstrated the typical morphological spectrum of MA with high cellularity and were composed of tightly packed small, uniform, round acini with a lower Ki67 index. Almost all MAs (94.7%, 18/19) were detected with *BRAF* V600E mutation. The ten WTs were epithelial-predominant WTs with glands, rosettes and glomerular structures, which also showed a higher Ki-67 index (up to 60%), invasive growth patterns, and a lack of *BRAF* mutation. However, the other nine overlapping cases showed two components: typical MA-like areas and epithelial WT-like areas. The cells of the WT-like areas were tubular, columnar and showed marked cytological atypia, with a Ki-67 proliferative index of up to 30%. The immunophenotype of these overlapping lesions was not significantly different from that of typical MA and they positively expressed WT1 and CD57. The *BRAF* V600E mutation was detected in both WT-like and MA-like areas in nine overlapping tumors. The follow-up data of 31 patients were analyzed, with a median follow-up time of 66 months (range, 8-45 months). Even though most patients with WT underwent radiotherapy or chemotherapy after surgery, two died, and one had liver metastasis. No MA or overlapping cases showed any evidence of recurrence or metastasis after surgery.

Conclusions: The molecular changes in tumors with overlapping morphological features were the same as those of typical MA; thus, we think that these tumors should be classified as MA and further called atypical MA. It is important to note that atypical MA is not a neglected subtype of MA. It possesses different histological morphology and a higher Ki-67 index but has the common imaging characteristics, immunophenotype and gene expression as typical MA, and patients usually have a good prognosis.

KEYWORDS

metanephric adenoma, atypical metanephric adenoma, Wilms' tumor, clinicopathological features, *BRAF* V600 mutation

Introduction

Metanephric adenoma (MA) is an uncommon kidney neoplasm that accounts for 0.2-0.7% of primary renal epithelial tumors (1). It is often asymptomatic, generally occurs in adults and has a significant predominance in females (2, 3). Most MAs feature a small solid, well-circumscribed, unilateral renal mass composed of primitive metanephric tubular cells and can be diagnosed by routine hematoxylin and eosin staining. Nevertheless, some MAs may also exhibit atypical morphology or overlap with other tumors. MA should be differentially diagnosed as the solid variant of papillary renal cell carcinoma (PRCC), epithelial-predominant Wilms' tumor (WT), and mucinous tubular and spindle cell carcinoma (4, 5). MA can also be challenging to diagnose due to its confusing histopathological morphology.

WT, also known as nephroblastoma, is another tumor that can form primitive renal tubules. In contrast to MA, WT has a younger onset age and is the most common embryonal tumor in children (6). Tumors generally mimic the cell types observed during normal nephrogenesis, with the classical triphasic WT comprising undifferentiated blastemal cells with differentiation toward both stromal and epithelial elements (7). Epithelial-predominant WT is a rare subtype of WT, that belongs to intermediate-risk tumors, and more than 67% of the tumor cells are epithelial structures (8). The epithelial components of tumors are usually rosette-like but may also be tubular or papillary, with or without heterologous epithelial differentiation. Degeneration, liquefaction, necrosis, hemorrhage, and metastasis are common in embryonal tumors.

It is worth noting that some renal tumors have overlapping morphologic features of epithelial-predominant WT and MA. Overlapping lesions were first reported in 1995, and the author occasionally found some epithelial renal tumors with features of epithelial WT, however, the cells had a bland and adenomatous appearance with focal areas similar to MA (9). Subsequently, more cases with overlapping features have been reported, which were described as either typical MA with active mitotic activity or MA with a morphology similar to epithelial WT (5, 10). However, in addition to morphological descriptions, the diagnosis and attribution of these cases remain unclear.

In this study, we summarized a series of MA/WT overlapping tumors and compared their morphology, Ki-67 index, *BRAF* mutation status, and prognosis with typical MA and epithelial WT, with the aim of highlighting and further clarifying the attribution of these tumors.

Materials and methods

Patients and samples

We reviewed MAs and epithelial-predominant WTs diagnosed at the West China Hospital of Sichuan University from 2008 to 2021. Formalin-fixed paraffin-embedded (FFPE) blocks were retrieved, and the corresponding slides from all cases were re-reviewed independently by two genitourinary pathologists (YXX, CN). Finally, 39 tumors were studied: 20 typical MAs, 9 renal tumors with overlapping morphological features of epithelial-predominant WT and MA, and 10 other cases of epithelial-predominant WT were selected as controls.

Immunohistochemistry (IHC)

IHC staining was performed on 4-μm-thick formalin-fixed paraffin embedded tissue sections by using the following antibodies: WT1 (6F-H2, DAKO, 1:100), CD57 (NK-1, Zhongshan Golden Bridge, 1:100), CD56 (123C3, Zhongshan Golden Bridge, 1:100), EMA (M0613, DAKO, 1:100), CK7 (OV-TL12/30, Zhongshan Golden Bridge, 1:100), and Ki-67 (MIB-1, Maixin, 1:100). All immunohistochemical staining was

performed using the Roche BenchMark ULTRA automated staining system (Roche, Basel, Switzerland) according to the manufacturer's protocols. Ki-67 was assessed as follows: five random fields of tumor sections were randomly selected to calculate the average proportion of positive cells under a magnification of ×400, and the Ki-67 index was presented as a percentage.

Detection of *BRAF* V600 mutation by polymerase chain reaction (PCR)

An FFPE DNA Kit (Qiagen, Hilden, Germany) was used to extract DNA from FFPE tissue samples from the tumor according to the manufacturer's protocol. Polymerase chain reaction (PCR) experiments were carried out with Taq HS (TaKaRa, Shiga, Japan), forward primer (5'-TCATAATGCTTGCTCTGATAGGA-3') and reverse primer (5'- GCCAAAAATTTAATCAGTGG A-3') primers. The PCR conditions were as follows: 94°C for 3 minutes (min); 35 cycles of denaturation at 94°C for 1 min, annealing at 60°C for 50 seconds (s), and extension at 72°C for 90 s; and a final extension at 72°C for 10 min. The amplified fragments were resolved by agarose gel electrophoresis, recovered by gel extraction (Qiagen, Hilden, Germany), and sequenced. For cases with overlapping morphology of WT and MA, manual microdissection was performed to distinguish WT-like and MA-like areas, DNA was then extracted from different areas for further PCR and sequencing.

Results

Typical MA (N = 20)

Twenty cases of typical MA (case 1-20) are listed in Table 1, involving 14 females and 6 males, and the age at diagnosis ranged from 3 to 70 years (median = 39 years). Most MA patients had no symptoms and were usually discovered by physical examination, while some patients had gross hematuria, bellyache, and abdominal mass as their primary clinical features. All patients had unilateral renal masses, and MA appeared to be more in the right kidney (left: right = 7: 13). Computer tomography scan showed a renal round exophytic soft tissue dense mass with a clear boundary, with or without a capsule. The mass density on the unenhanced scan was equal to or slightly higher than that on the kidney, which has uniform density. On enhanced scan, the mass density changed gradually mild to moderately uneven.

Macroscopically, most tumors were nodular, including one solid-cystic tumor and two tumors with macroscopic necrosis. The maximum tumor diameter ranged from 1.5 to 18.0 cm (median, 4.5 cm). Histologically, these tumors were well defined and usually abutted directly against normal renal tissue without a pseudocapsule. All 20 cases were highly cellular and composed of crowded small, round acini, tubular, glandular, antler tubular, papillary, and solid patterns, along with glomeruloid bodies. Tumor cells were bland, uniform, round, or oval with scant cytoplasm, monomorphic nuclei, fine chromatin, and small and inconspicuous nucleoli. The stroma ranged from inconspicuous to loose and edematous. Hyaline degeneration and psammoma bodies were common and might be numerous. Mitotic figures were rare or absent. In addition, all 19 cases were tested positive for WT1 and CD57 expression by IHC, and the Ki-67 index ranged from 1% to 15%. Sanger sequencing showed that 18 of these 19 (94.7%) cases had the *BRAF* V600E mutation. The 1799 base in exon 15 of the *BRAF* gene was changed from T to A, leading to the related valine being replaced by glutamic acid (Figure 1).

All patients received nephron-sparing surgery or radical nephrectomy without postoperative adjuvant therapy, including targeted therapy, chemotherapy or radiotherapy after surgery. The follow-up lasted anywhere from 12 to 143 months (mean = 74.5 months, median = 67.5 months), and no patients showed signs of a recurrence or metastasis.

WT (N = 10)

Ten epithelial-predominant WTs (case 21-30), with more than 67% of the tumor cells being epithelial structures, were enrolled as the control group. The patients included 5 males and 5 females with ages ranging from 1 to 38 years (median = 5 years). An abdominal mass was the most common symptom in patients, and computer tomography scan revealed a large lesion in the kidney. In contrast to the crescent-like enhancement of the residual renal parenchyma, the tumors were heterogeneous in density with mild to moderate uneven enhancement. Some tumors demonstrated pushy growth and infiltrated the peripheral blood vessels and nerve tissue.

All patients underwent radical nephrectomy, and half of them were treated with vincristine-based therapy or radiotherapy after surgery. Most lesions were accompanied by hemorrhage, necrosis, calcification, or cystic degeneration due to excessive growth. These tumors showed epithelial differentiation and were composed of tubules, rosettes, and primitive glomeruli. The tumor cells were more heteromorphic, with active mitosis and more pathological mitosis. The Ki-67 index was usually ≥ 30%, and WT1 was positively expressed in 60% (6/10) of tumors. *BRAF* mutations were performed, but none of these lesions were detected with the V600 mutation (Figure 2). By the end of follow-up, nine patients were contacted, and the follow-up lasted anywhere from 8 to 81 months (mean = 56.3 months, median = 70 months). Unfortunately, two patients died, and one patient developed liver metastases two years after the surgery.

TABLE 1 Cases in this study.

Case	Age (Y) \Sex	Tumor Size (cm)	Tumor Morphology (%)	Treatment	Ki-67 (%)	WT 1	CD 57	CD 56	EMA	CK 7	*BRAF* Status	Follow up (mo)	Status
1	26/F	4.0	MA	NA	2	+	+	NA	–	–	V600E	NA	NA
2	28/F	7.5	MA	NSS	5	+	+	NA	–	–	V600E	143	NED
3	49/F	3.0	MA	NSS	NA	+	+	–	–	–	NA	126	NED
4	59/M	7.0	MA	RN	1	+	+	–	–	–	V600E	105	NED
5	14/M	18.0	MA	RN	5	+	+	–	–	–	V600E	103	NED
6	27/F	5.5	MA	RN	5	+	+	+	–	–	V600E	111	NED
7	50/F	4.5	MA	RN	1	+	+	+	NA	–	V600E	96	NED
8	52/M	15.0	MA	RN	3	NA	NA	NA	NA	NA	V600E	74	NED
9	60/F	2.5	MA	NSS	3	+	+	NA	–	–	V600E	69	NED
10	30/F	9.0	MA	NA	NA	+	+	+	–	–	V600E	66	NED
11	20/F	NA	MA	NA	5	+	+	+	–	NA	V600E	NA	NA
12	28/F	3.5	MA	NSS	15	+	+	+	NA	–	V600E	60	NED
13	58/M	3.5	MA	RN	5	+	+	+	–	–	V600E	59	NED
14	3/M	5.5	MA	RN	2	+	+	+	NA	–	V600E	56	NED
15	48/F	4.7	MA	NSS	2	+	+	–	–	–	V600E	53	NED
16	70/M	4.0	MA	NSS	3	+	+	+	NA	–	V600E	NA	NA
17	36/F	4.5	MA	RN	15	+	+	–	–	–	–	35	NED
18	33/F	1.5	MA	NSS	5	+	+	NA	NA	–	V600E	24	NED
19	42/F	2.5	MA	NSS	10	+	+	NA	–	–	V600E	12	NED
20	65/F	4.0	MA	NSS	5	+	+	–	–	–	V600E	NA	NA
21	17/M	3.0	WT	NSS	25	–	–	NA	–	–	–	8	**Dead**
22	13/M	2.5	WT	RN + chemotherapy +radiotherapy	30	–	–	+	–	–	–	53	**NED, liver metastasis occurred 2 years after surgery**
23	38/F	4.5	WT	RN + chemotherapy + radiotherapy	40	+	NA	+	+	–	–	41	NED
24	3/M	10.0	WT	RN	60	–	NA	NA	–	+	–	NA	NA
25	5/F	12.0	WT	RN	40	+	NA	NA	NA	NA	–	76	NED
26	3/F	14.0	WT	RN + radiotherapy	25	+	NA	+	–	NA	–	17	**Dead**
27	5/M	10.0	WT	RN + chemotherapy	NA	+	NA	+	NA	NA	–	70	NED
28	1/F	8.0	WT	RN	30	+	NA	NA	+	+	–	81	NED
29	5/F	5.0	WT	RN	40	–	–	+	–	NA	–	81	NED
30	1/M	4.5	WT	RN + chemotherapy	30	+	+	+	+	NA	–	80	NED
31	21/M	6.0	MA-like(95) + WT-like(5)	RN	MA-like(2) + WT-like (5)	+	NA	NA	NA	NA	MA-like: V600E, WT-like: V600E	145	NED
32	20/F	NA	MA-like(60) +WT-like(40)	NA	MA-like(1) + WT-like (10)	+	NA	NA	–	–	MA-like: V600E, WT-like: V600E	NA	NA

(Continued)

TABLE 1 Continued

Case	Age (Y) \Sex	Tumor Size (cm)	Tumor Morphology (%)	Treatment	Ki-67 (%)	WT 1	CD 57	CD 56	EMA	CK 7	*BRAF* Status	Follow up (mo)	Status
33	20/F	4.5	MA-like(60) +WT-like(40)	NSS	MA-like(2) + WT-like (10)	+	+	+	–	NA	MA-like: V600E, WT-like: V600E	66	NED
34	14/F	3.7	MA-like(40) +WT-like(60)	NSS	NA	+	+	NA	–	NA	MA-like: V600E, WT-like: V600E	NA	NA
35	31/F	5.0	MA-like(30) +WT-like(70)	RN	MA-like(1) + WT-like (15)	+	+	+	–	–	MA-like: V600E, WT-like: V600E	130	NED
36	31/M	4.8	MA-like(20) +WT-like(80)	RN	MA-like(2) + WT-like (10)	+	+	+	–	–	MA-like: V600E, WT-like: V600E	NA	NA
37	37/F	2.0	MA-like(20) +WT-like(80)	RN	MA-like(2) + WT-like (30)	+	NA	NA	–	NA	MA-like: V600E, WT-like: V600E	20	NED
38	38/F	6.1	MA-like(10) +WT-like(90)	NSS	MA-like(5) + WT-like (20)	+	+	NA	–	–	MA-like: V600E, WT-like: V600E	46	NED
39	51/M	3.0	MA-like(5) +WT-like(95)	RN	MA-like(5) + WT-like (30)	+	+	NA	–	NA	MA-like: V600E, WT-like: V600E	35	NED

Y, year; F, female; M, male; MA, metanephric adenoma; WT, Wilms' tumor, NSS, nephron-sparing surgery; RN, radical nephrectomy, mo, month; NA, not available; NED, no evidence of disease.

Renal tumors with overlapping morphological features of MA and epithelial-predominant WT (N = 9)

Nine tumors (case 31-39) shared the overlapping morphological features of epithelial-predominant WT and MA. The patients included 6 females and 3 males, with a median age of 31 years (range, 14-51 years). Most tumors showed heterogeneous-enhancement on computer tomography scans, and the imaging features were similar to those of typical MA. The tumors were nodular or multinodular, well-circumscribed, and expanded in size.

Both typical MA-like areas and primitive epithelial components (WT-like areas) were observed in these lesions, and epithelial WT-like areas accounted for 5-95% of the neoplasms in different cases. The tumor cells demonstrated marked cytological atypia; some of them were oval or polygonal and tightly packed into the solid and nested structures, while others were cubic or highly columnar and showed different epithelial differentiation into tubules (with

10.3389/fonc.2022.1020456

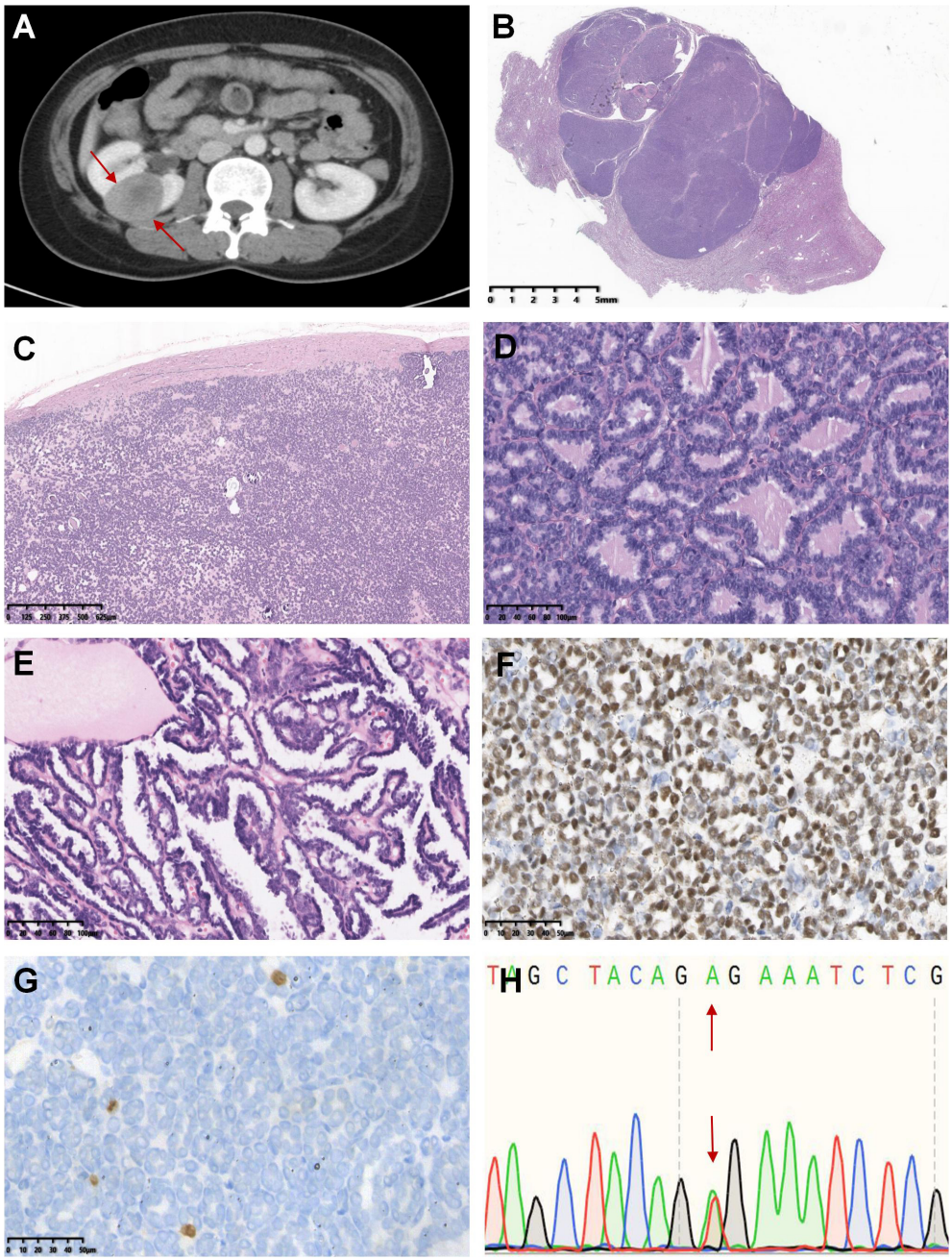

FIGURE 1
Case 1-20 demonstrated the typical histomorphological spectrum of MA. The representative morphological images were shown below: Axial computer tomography scan displayed a soft tissue mass of 3.1 cm × 3.7 cm in the upper pole of the right kidney, with a clear boundary and obvious enhancement (case 2, **A**). The tumor was multinodular, well-defined and usually abutted directly against the normal renal tissue without a pseudocapsule (case 18, **B**). Psammoma bodies were common and may be numerous, and the stroma ranged from inconspicuous to loose and edematous (case 16, **C**). Tumors were highly cellular and composed of crowded small, round acini, papillae or antler tubular structures, and mitotic figures were rare or absent (case 19 and 7, **D, E**). Tumor cells showed diffusely positive staining for WT1 (case 7, **F**) but negative expression or only a few cells expressed Ki-67 (case 7, **G**). Sanger sequencing revealed that the tumor harbored the T1799A mutation in exon 15 of the *BRAF* gene (V600E mutation) (case 7, **H**).

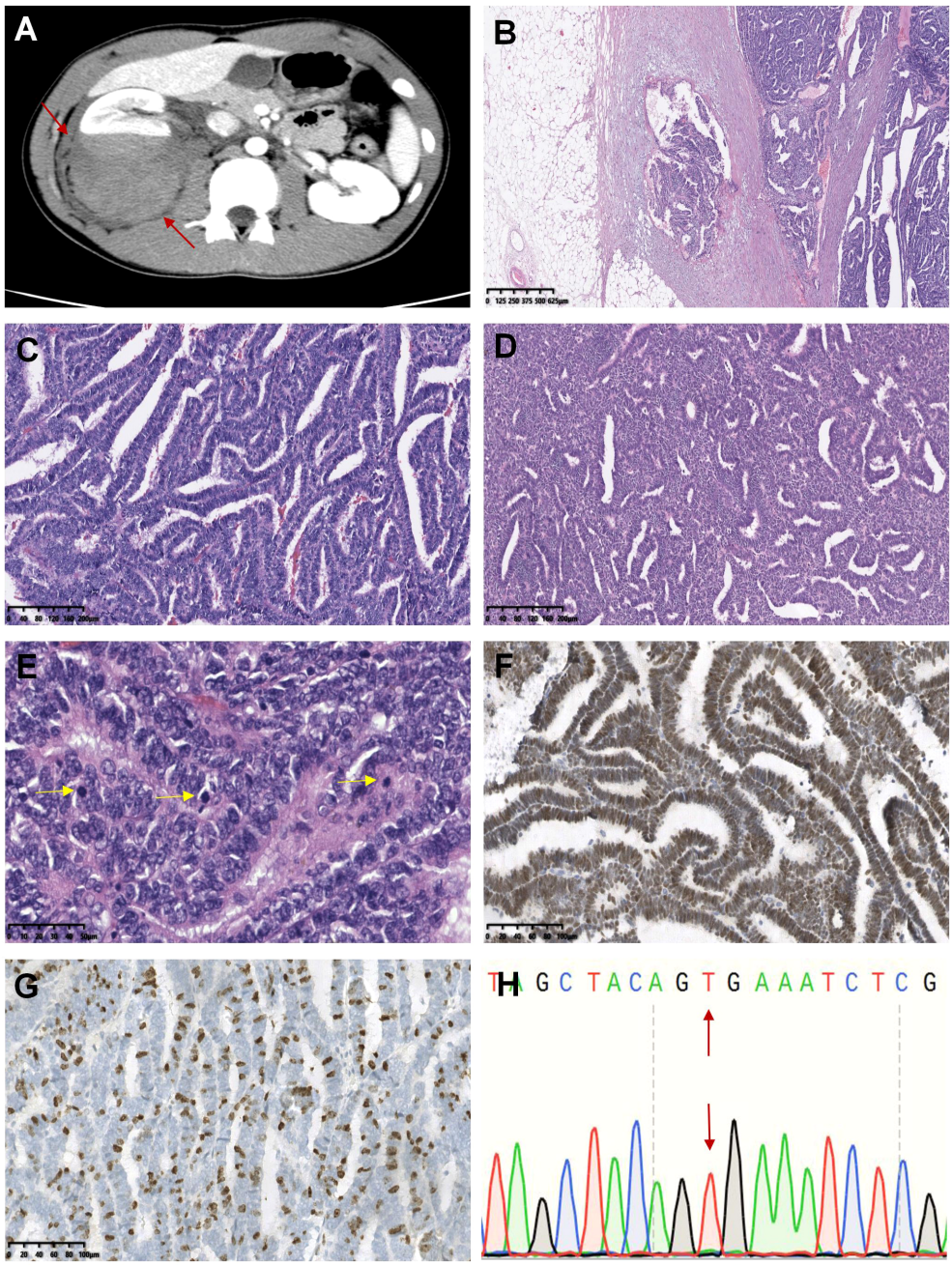

FIGURE 2
Case 21-30 were epithelial-predominant WT. The representative histomorphological images were as follows: In the axial computer tomography scan, the patient's right kidney was characterized by a large swollen mass with uneven density and a clear boundary with the surrounding renal parenchyma, which appeared to invade the perirenal tissue (case 22, **A**). Microscopically, the tumor invaded the renal capsule, and carcinoma was observed in the renal fibrous membrane (case 22, **B**). Tumor cells were arranged in obvious papillary, acinar or duct structures (case 22 and 23, **C, D**). Pathological mitotic figures were easily seen and were indicated by the yellow arrows (case 22, **E**). WT1 (case 22, **F**) and Ki-67 (case 22, **G**) were highly expressed in tumors. No *BRAF* V600E mutation was observed (case 22, **H**).

earlier forms resembling rosettes), papillae, glands, cystic degeneration with fine chromatin, high nucleocytoplasmic ratio, scant and pale or light pink cytoplasm, and obvious mitotic activity. Calcification and psammoma bodies were easily observed. Notably, we observed significant hyaline degeneration and calcification in the tumor stroma, forming a thick pseudocapsule (case 36). The immunohistochemistry staining results are listed in Table 1. All tumors expressed

WT1 (9/9) and CD57 (6/6). The Ki-67 index was significantly higher in the epithelial WT-like area (5-30%) than in the MA-like area (1-5%) for the nine tumors. *BRAF* mutation analysis was performed separately on tissues from both MA-like and WT-like areas and yielded identical V600E mutation (Figure 3).

Among them, two cases were almost completely composed of papillotubular architecture in the primitive epithelial components, and the WT-like areas accounted for more than 90% of the tumor. The first case (case 38) was a 31-year-old woman who presented with a 5.0 cm renal mass that was partially covered by a membrane on the surface. Necrosis, hemorrhage, and hyalinized stroma were observed in the lesion. The tumor demonstrated discrete areas that were predominantly composed of epithelial WT and had a narrow strip area associated with cuboidal mitotically inactive epithelium consistent with MA. Tumor cells in the WT-like area were highly-columnar, with crowded high-columnar nuclei and active mitotic features. The second case (case 39) was a 51-year-old man with a 3.0 cm renal neoplasm. The tumor was multinodular and invaded the perirenal fat of the kidney, which was morphologically consistent with epithelial WT in most areas, and MA-like epithelium in a few areas. The tumor was well demarcated from the surrounding renal tissue, but the demarcation between the WT-like and MA-like areas was unclear.

In summary, these overlapping lesions in the 9 cases showed different proportions of MA-like and WT-like areas, with positive expression of WT1 in both areas. The Ki-67 index was lower in the MA-like area and higher in the epithelial-predominant WT-like area, reflecting the different mitotic activities within the lesions. However, *BRAF* V600E mutations coexisted in both morphological areas of the tumor (Figure 4). At the end of follow-up, no recurrence or metastasis was observed in the 6 patients with follow-up data (ranging from 20-145 months, mean = 73.6 months, median = 56 months). Therefore, based on morphological features, immunomarkers, molecular changes, and prognosis, we believe that these 9 overlapping lesions were more similar to MA and could be called atypical MA.

Discussion

MA is a rare renal tumor characterized by the proliferation of small epithelial cells and is classified as a benign renal epithelial tumor. WT is a malignant embryonic tumor derived from renal blastemal cells. However, in cases with overlapping morphological features of WT and MA, it is difficult to diagnose (4). In this study, we summarized and analyzed a group of cases, including typical MAs, epithelial-predominant WTs and renal tumors with overlapping morphological features of MA and WT (Table 2). Based on the comparison of their clinicopathological features and molecular changes, we found that cases with WT/MA overlapping features were closer to MA due to the same immunophenotype, molecular changes, and clinical outcomes, while these cases had different morphologies and a higher Ki-67 index. Therefore, we classified these overlapping cases as MA and named them atypical MA.

To date, more than 300 cases of MA have been reported (1–3, 10–13). The patients ranged from children to elderly individuals, with a median age of approximately 50 years, with an obvious female preponderance (female/male = 1/2-1/3) (10, 11, 14). The most common symptoms are pyrexia, hematuria, lumbar pain and an abdominal mass; however, most patients have no symptoms and are found incidentally (3). In our study, the ages of 20 patients with typical MA were younger than those of most previously reported cases, ranging from 3 to 70 years (median = 39 years), with a significant female tendency (male-to-female ratio, 6:14). However, the median age of 9 atypical MAs was 31 years, with no significant difference from the typical MAs, but much older than the epithelial-predominant WT (median = 5 years). Overall, atypical MA is more similar to typical MA in terms of age at onset.

Macroscopically, MA is usually a nodular mass of various sizes, but multifocality and cystic degeneration are rare (15–18). In the present study, 9/29 tumors showed multifocality, and 3 tumors showed cystic degeneration. Histologically, all 9 atypical MAs were composed of different proportions of MA-like and WT-like structures. Epithelial WT-like areas accounted for 5%-95% of the tumors. Among them, two tumors were composed of papillotubular architecture (more than 90% of the tumor area) with a high nucleocytoplasmic ratio, active mitotic features, and significant necrosis. These 9 cases showed different levels of tumor cytological atypia, and it was difficult to differentiate them from WT based on cellular morphological features. In fact, many tumors with similar morphology of epithelial components that need to be distinguished from MA, especially the solid variant of PRCC and epithelial-predominant WT (17).

Some uncommon histological morphologies of MA still exist. The first case of MA with an atypical morphology was reported in 1995 (19). In 2007, Jain *et al.* proposed the concept of atypical MA. A case of MA with atypical histological features characterized by various-sized nuclei, hyperchromasia, prominent nucleoli, and approximately 2/10 high-power fields of mitotic activity was observed in the cellular areas (20). Subsequently, “malignant MA” was proposed, which was considered to comprise hypercellular uniform cells in a solid-acini pattern, and the cells varied in size with small uniform nuclei, prominent nucleoli and with or without increased numbers of mitoses (12). Wobker *et al.* reported a group of cases that morphologically overlapped MA and WT, which were divided into typical MAs with unusually prominent mitotic activity, and epithelial WTs with areas resembling MA (4). In addition to WT, composite tumors of MA with other malignant components have also been reported (12, 21–26). However, no consensus has been established on the attribution and

10.3389/fonc.2022.1020456

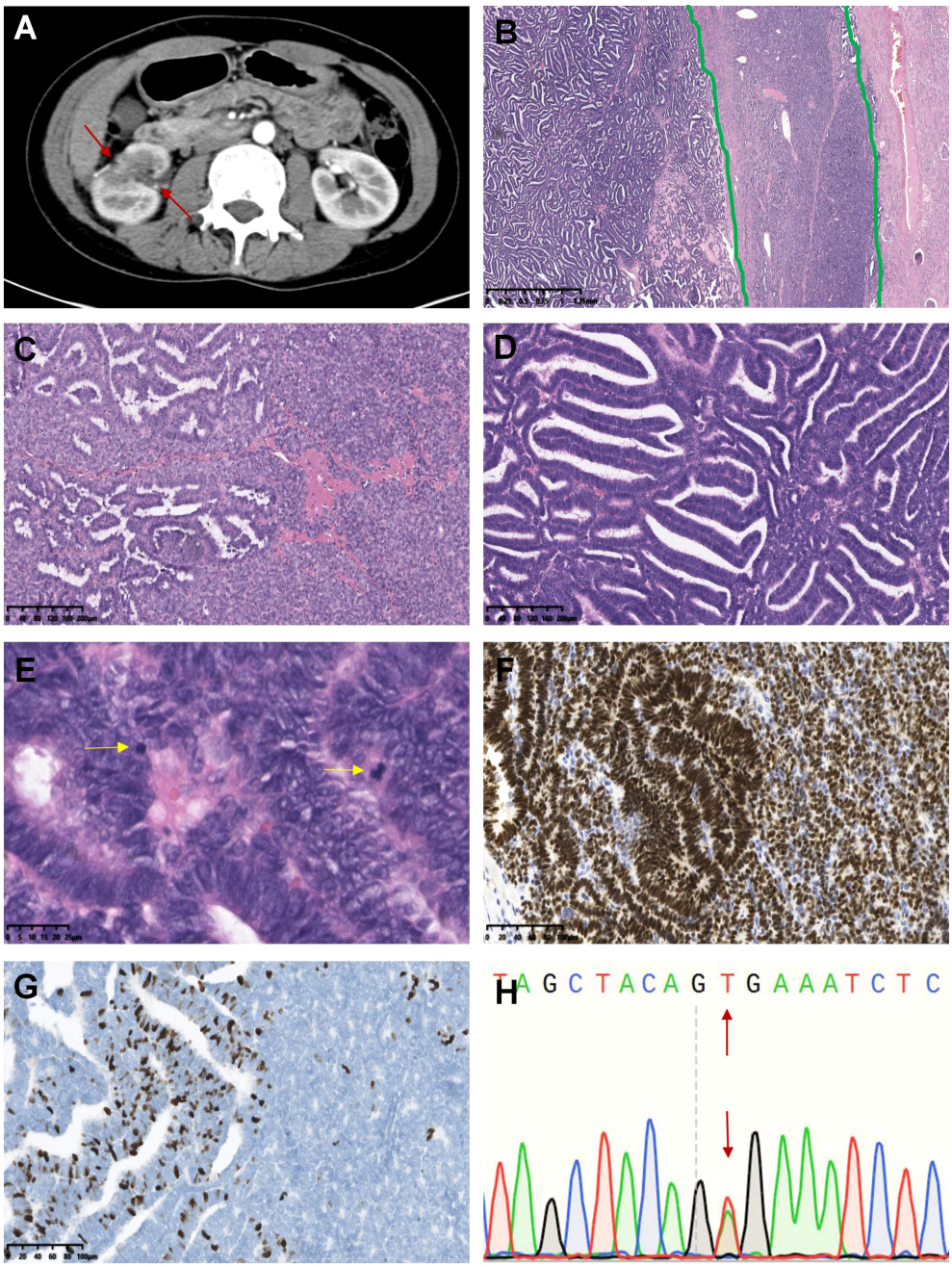

FIGURE 3
Tumors with overlapping morphologic features of MA and epithelial-predominant WT (case 31-39). The representative morphological images were displayed as follows: A large mass was observed in the middle and upper parts of the right kidney in computer tomography scan (axial, case 38). The mass was irregularly bound, compressing the surrounding renal tissue, and the tumor parenchyma was markedly heterogeneously enhanced **(A)**. The green lines divided the tissue into three areas: the tumor demonstrated discrete areas that were predominantly composed of epithelial WT (left) but had a narrow strip area (middle) associated with cuboidal mitotically inactive epithelium consistent with MA **(B)**. Excessive abruptness and unclear boundaries between the two structures of the tumor **(C)**. The majority of tumors demonstrated primitive columnar-shaped neoplastic cells with papillotubular or rosette-like architectures, typical of epithelial-predominant WT **(D)**. The yellow arrow indicates pathological mitotic figures **(E)**. WT1 was positively expressed in the tumor **(F)**, and Ki-67 expression in the WT-like area was significantly higher than that in the MA-like area **(G)**. The tumor showed the *BRAF* V600E mutation **(H)**.

10.3389/fonc.2022.1020456

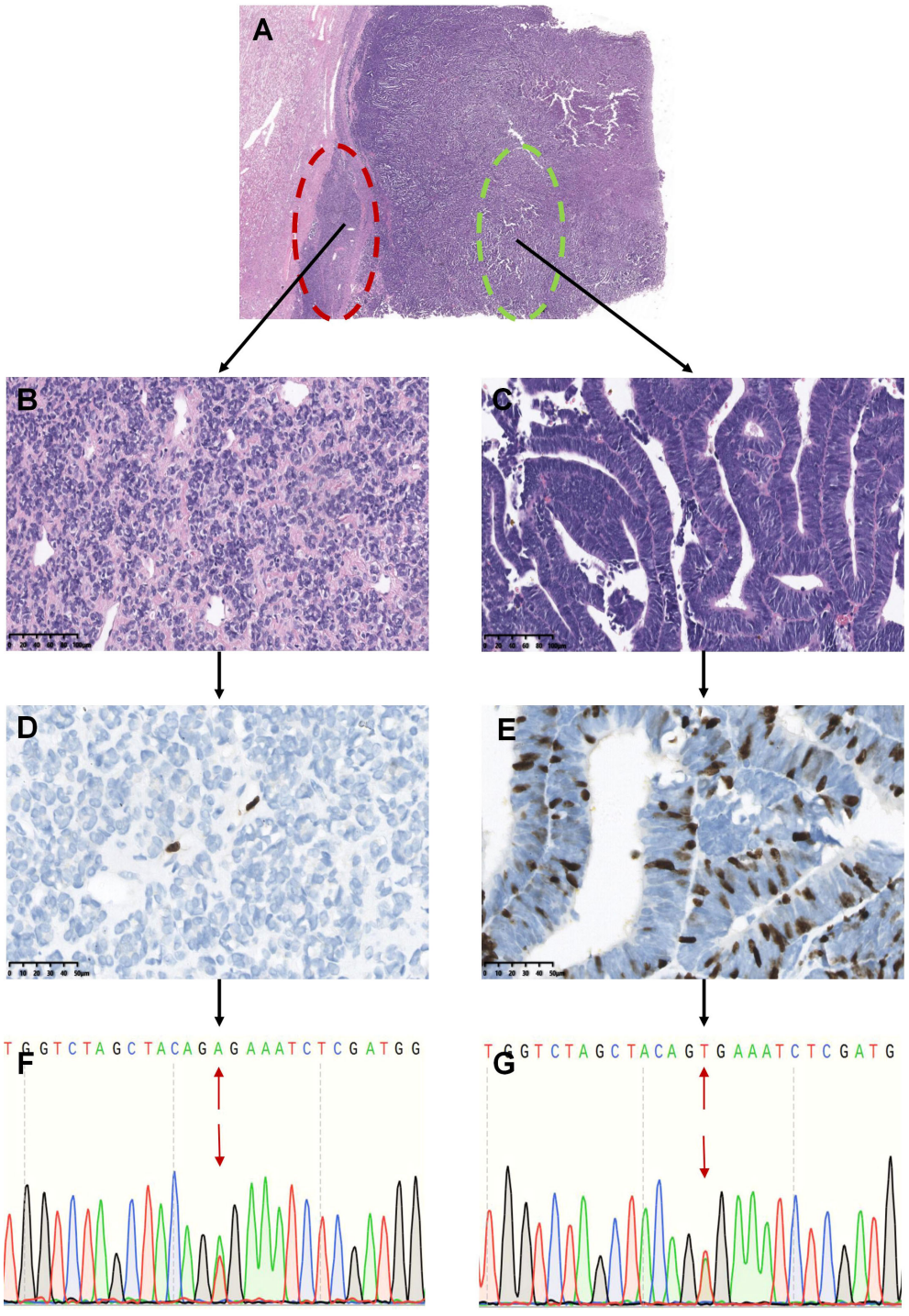

FIGURE 4
Analysis of *BRAF* mutations in different areas of renal tumors with overlapping morphology (Represented by case 37). The tumors showed overlapping morphological features of epithelial-predominant WT and MA **(A)**. The red circle indicates typical MA-like features with mild cells and hyalinized stroma, and the tumor cells were oval or polygonal and tightly packed in the solid and nested areas **(B)**. The green circle shows that the tumor consisted of primitive epithelial components with a papillotubular architecture, similar to epithelial WT. The tumor cells were tall columnar, with fine chromatin, a high nucleocytoplasmic ratio, crowded high columnar nuclei, and minimal mitotic activity **(C)**. Only a few cells expressed Ki-67 in the typical MA-like areas **(D)**, whereas more Ki-67 was expressed in the epithelial WT-like areas **(E)**. Tumor cells from both areas showed the *BRAF* V600E mutation **(F, G)**.

TABLE 2 The histological criteria used to classify tumors into three groups.

	Border	Tumor parenchymal cells	Tumor stromal cells	Secondary changes
MA	The junction with the kidney is usually abrupt and without a pseudocapsule.	The tumor is typically highly cellular and consist of densely arranged small, uniform vesicles or tubules. The tubules can show branching and intraluminal tufts, producing glomeruloid structures with small cuboidal cells of uniform size, scanty cytoplasm, round or ovoid nuclei, fine nuclear chromatin, inconspicuous nucleoli, and rare or absent mitotic figures.	The stroma ranges from inconspicuous to loose and oedematous, with no obvious vascular structure.	Hyaline degeneration, calcifications and psammoma bodies are common, with hemorrhages and cystic changes visible.
Epithelial-predominant WT	Typical circumscribed, encapsulated, pushing border.	The viable tumor consists of at least 66% of epithelial structures. The tumor cells are arranged in tubular, vesicular or papillary structures with short or high columnar nuclei perpendicular to the basement membrane, marked nuclear atypia, coarse nuclear chromatin and more mitotic figures.	The mesenchymal component is diverse and differentiation of smooth muscle, striated muscle, fibroblasts, adipose tissue, cartilage and bone can be seen.	Tumors are often associated with hemorrhage, necrosis, calcification, etc.
Atypical MA	With or without a pseudocapsule.	Tumors share the overlapping morphologic features of epithelial-predominant WT and MA, both typical MA-like and WT-like areas were observed in these lesions.		

MA, metanephric adenoma; WT, Wilms' tumor.

nomenclature of these tumors, and the term "malignant MA" remains controversial.

Due to the overexpression of WT1 and CD57 in both MA and WT, IHC is less useful for differential diagnosis. In the present study, WT1 and CD57 were positively expressed in 19 typical MAs, whereas 6/10 and 1/3 of the epithelial-predominant WTs expressed WT1 and CD57, respectively. In addition, Ki-67 indices ranged from 1% to 15% in typical MAs and 25% to 60% in WTs, with significant differences between the two tumors. For the 9 renal tumors with overlapping morphologic features of MA and WT, WT1 and CD57 were positively expressed in both MA-like areas and epithelial WT-like areas, and Ki-67 indices of MA-like areas were 1-5%, less than that in epithelial WT-like areas (5-30%). These results suggest that the cell proliferative activity and immunophenotype of tumors with overlapping morphology were between those of typical MA and WT, and that they were closer to MA.

Molecular analyses play an important role in the differential diagnosis of renal epithelial neoplasms. The *BRAF* V600E mutation has been found in 66.7% to 100% of MA tumors, and the V600D missense mutation, V600K mutation, and compound V600D and K601L missense mutations have recently been reported (2, 11, 27–30). However, only two molecular studies have reported on tumors with overlapping WT/MA morphological features, especially *BRAF* mutations. One article reported 9 overlapping cases, 4 of which showed a *BRAF* V600E mutation in both epithelial WT-like and MA-like areas (4). Another study found that *BRAF* mutations were of diagnostic interest in overlapping lesions because *BRAF* mutations were detected only in typical MA and overlapping cases, but did not exist in epithelial WT (31).

In the present study, we performed manual microdissection of the tissue to distinguish WT-like areas and MA-like areas for overlapping lesions and further separately detected the *BRAF* mutation status. Finally, both WT-like areas and MA-like areas showed that the 1799 base in exon 15 of the *BRAF* gene changed from T to A, and only the *BRAF* V600E mutation was detected in our cases. In total, 94.8% (18/19) of the typical MAs and 100% (9/9) of the atypical MAs showed this genetic change. The absence of other *BRAF* mutations in our cases may be due to ethnic differences in the Chinese population. Moreover, *BRAF* V600E mutations in common non-MA renal tumors were either extremely infrequent (less than 1%) or absent. *BRAF* mutations were not found in our WT cases. To date, only a few epithelial WTs have been found to harbor this mutation (4, 11, 28, 31, 32). Therefore, *BRAF* mutation detection is helpful in differentiating MA from epithelial-predominant WT cases.

Currently, most MAs have a good prognosis. However, the ability of MA to become malignant has also been reported. Some studies have found that a small subset of these tumors have atypical histological characteristics, an exponential growth pattern (12) or even coexist with other malignant tumors (21, 24, 33). The duration of follow-up for our cases (including typical and atypical MA) ranged from 12 to 145 months, and none of them showed any evidence of recurrence or metastasis. Therefore, we tend to consider MA to be an indolent tumor, and cases 31-39 in our study are more suitable to temporarily named atypical MA rather than malignant MA or epithelial-predominant WT resembling MA with the *BRAF* V600E mutation.

Conclusion

In this study, we reported 9 atypical MAs that were younger than most reported patients, and all cases harbored the *BRAF* V600E mutation in both MA-like and epithelial-predominant WT-like areas. Atypical MA is not a neglected subtype of MA,

possessing an uncommon histological morphology and a higher Ki-67 index, but shares common features of imaging, immunophenotype and gene expression with typical MA, and patients usually have a good clinical outcome. Differentiating atypical MA from other renal tumors with epithelial components is important because of their totally different prognoses. Thus, since *BRAF* V600E gene is extremely infrequent or absent in non-MA renal tumors, its high mutation rate led to its application as a specific marker for MA.

Data availability statement

The original contributions presented in the study are included in the article/supplementary material. Further inquiries can be directed to the corresponding author.

Ethics statement

The studies involving human participants were reviewed and approved by the ethics committee of the West China Hospital of Sichuan University. Written informed consent to participate in this study was provided by the participants' legal guardian/next of kin. Written informed consent was obtained from the individual(s), and minor(s)' legal guardian/next of kin, for the publication of any potentially identifiable images or data included in this article.

Author contributions

NC, conceptualization, methodology, and manuscript revision. XY, conceptualization, validation and writing of the original draft. XP, JT, and LZ, data curation and visualization. XZ, formal analysis. QZ, supervision. All authors listed have made substantial, direct, and intellectual contributions to the work.

Funding

This study was supported by grants from the National Natural Science Foundation of China (NSFC 81872107, 81872108), Sichuan Province Science and Technology Support Program (2021YFS0114), and Fundamental Research Funds for the Central Universities (2022SCU12042).

Acknowledgments

We thank the patients and their families for their support and understanding of this study and the pathologists and urologists of West China Hospital for providing the clinicopathological data of the patients.

Conflict of interest

The authors declare that the research was conducted in the absence of any commercial or financial relationships that could be construed as a potential conflict of interest.

Publisher's note

All claims expressed in this article are solely those of the authors and do not necessarily represent those of their affiliated organizations, or those of the publisher, the editors and the reviewers. Any product that may be evaluated in this article, or claim that may be made by its manufacturer, is not guaranteed or endorsed by the publisher.

References

1. Rodriguez-Zarco E, Machuca-Aguado J, Macias-Garcia L, Vallejo-Benitez A, Rios-Martin JJ. Metanephric adenoma: Molecular study and review of the literature. *Oncotarget* (2022) 13:387–92. doi: 10.18632/oncotarget.28192

2. Ding Y, Wang C, Li X, Jiang Y, Mei P, Huang W, et al. Novel clinicopathological and molecular characterization of metanephric adenoma: A study of 28 cases. *Diagn Pathol* (2018) 13(1):54. doi: 10.1186/s13000-018-0732-x

3. Nie DX, Xie BS, Zhang TX, Shi JX, Xu XT, Zhang CW, et al. Clinical diagnosis and treatment of 27 cases of metanephric adenoma. *Zhonghua Yi Xue Za Zhi* (2021) 101(19):1433–5. doi: 10.3760/cma.j.cn112137-20200830-02496

4. Wobker SE, Matoso A, Pratilas CA, Mangray S, Zheng G, Lin MT, et al. Metanephric adenoma-epithelial wilms tumor overlap lesions: An analysis of braf status. *Am J Surg Pathol* (2019) 43(9):1157–69. doi: 10.1097/PAS.0000000000001240

5. Sarlos DP, Banyai D, Peterfi L, Szanto A, Kovacs G. Embryonal origin of metanephric adenoma and its differential diagnosis. *Anticancer Res* (2018) 38 (12):6663–7. doi: 10.21873/anticanres.13033

6. Al-Hadidi A, Rinehardt HN, Sutthatarn P, Talbot LJ, Murphy AJ, Whitlock R, et al. Incidence and management of pleural effusions in patients with wilms tumor: A pediatric surgical oncology research collaborative study. *Int J Cancer* (2022) 151(10):1696–702. doi: 10.1002/ijc.34188

7. Maschietto M, Trape AP, Piccoli FS, Ricca TI, Dias AA, Coudry RA, et al. Temporal blastemal cell gene expression analysis in the kidney reveals new wnt and related signaling pathway genes to be essential for wilms' tumor onset. *Cell Death Dis* (2011) 2:e224. doi: 10.1038/cddis.2011.105

8. Vujanic GM, Sandstedt B. The pathology of wilms' tumour (Nephroblastoma): The international society of paediatric oncology approach. *J Clin Pathol* (2010) 63(2):102–9. doi: 10.1136/jcp.2009.064600

9. Davis CJJr., Barton JH, Sesterhenn IA, Mostofi FK. Metanephric adenoma. clinicopathological study of fifty patients. *Am J Surg Pathol* (1995) 19(10):1101–14. doi: 10.1097/00000478-199510000-00001

10. Jia Z, Zhang CJ, Xi CG, Gong YQ, Yang KW, Peng D, et al. Clinical features analysis of metanephric adenoma: A series of 16 cases. *Zhonghua Wai Ke Za Zhi* (2018) 56(3):227–30. doi: 10.3760/cma.j.issn.0529-5815.2018.03.012

11. Calio A, Eble JN, Hes O, Martignoni G, Harari SE, Williamson SR, et al. Distinct clinicopathological features in metanephric adenoma harboring braf mutation. *Oncotarget* (2017) 8(33):54096–105. doi: 10.18632/oncotarget.11117

12. Li G, Tang Y, Zhang R, Song H, Zhang S, Niu Y. Adult metanephric adenoma presumed to be all benign? a clinical perspective. *BMC Cancer* (2015) 15:310. doi: 10.1186/s12885-015-1211-3

13. Jiang T, Li W, Lin D, Wang J, Liu F, Ding Z. Imaging features of metanephric adenoma and their pathological correlation. *Clin Radiol* (2019) 74 (5):408 e9– e17. doi: 10.1016/j.crad.2019.01.013

14. Fan H, Shao QQ, Li HZ, Xiao Y, Zhang YS. The clinical characteristics of metanephric adenoma: A case report and literature review. *Medicine* (2016) 95(21): e3486. doi: 10.1097/MD.0000000000003486

15. Muir TE, Cheville JC, Lager DJ. Metanephric adenoma, nephrogenic rests, and wilms' tumor: A histologic and immunophenotypic comparison. *Am J Surg Pathol* (2001) 25(10):1290–6. doi: 10.1097/00000478-200110000-00010

16. Kohashi K, Oda Y, Nakamori M, Yamamoto H, Tamiya S, Toubo T, et al. Multifocal metanephric adenoma in childhood. *Pathol Int* (2009) 59(1):49–52. doi: 10.1111/j.1440-1827.2008.02324.x

17. Kinney SN, Eble JN, Hes O, Williamson SR, Grignon DJ, Wang M, et al. Metanephric adenoma: The utility of immunohistochemical and cytogenetic analyses in differential diagnosis, including solid variant papillary renal cell carcinoma and epithelial-predominant nephroblastoma. *Mod Pathol* (2015) 28 (9):1236–48. doi: 10.1038/modpathol.2015.81

18. Saltzman AF, Carrasco AJr., Maccini MA, Caldwell BT, Treece AL, Cost NG. Large Cystic metanephric adenoma in a 15-Year-Old girl. *Urology* (2017) 101:147–50. doi: 10.1016/j.urology.2016.12.019

19. Pins MR, Jones EC, Martul EV, Kamat BR, Umlas J, Renshaw AA. Metanephric adenoma-like tumors of the kidney: Report of 3 malignancies with emphasis on discriminating features. *Arch Pathol Lab Med* (1999) 123(5):415–20. doi: 10.5858/1999-123-0415-MALTOT

20. Jain M, Rastogi A, Gupta RK. Atypical metanephric adenoma - a case report and review of literature. *Int Urol Nephrol* (2007) 39(1):123–7. doi: 10.1007/s11255-005-4970-y

21. Zhu P, Yan F, Yang Z, Meng L, Ao Q. Composite tumor of metanephric adenoma and wilms' tumor of the kidney: A case report and review of the literature. *Oncol Lett* (2013) 5(4):1311–4. doi: 10.3892/ol.2013.1148

22. Drut R, Drut RM, Ortolani C. Metastatic metanephric adenoma with foci of papillary carcinoma in a child: A combined histologic, immunohistochemical, and fish study. *Int J Surg Pathol* (2001) 9(3):241–7. doi: 10.1177/106689690100900313

23. Argani P. Metanephric neoplasms: The hyperdifferentiated, benign end of the wilms tumor spectrum? *Clinics Lab Med* (2005) 25(2):379–92. doi: 10.1016/j.cll.2005.01.002

24. Pasricha S, Gandhi JS, Gupta G, Mehta A, Beg S. Bilateral, multicenteric metanephric adenoma associated with wilms' tumor in a child: A rare presentation with important diagnostic and therapeutic implications. *Int J Urol* (2012) 19 (12):1114–7. doi: 10.1111/j.1442-2042.2012.03134.x

25. Kastan R, Zizlavska M. Metanephric adenoma. A case report and literature review. *Cesk Patol* (2019) 55(3):165–9.

26. Zhang Z, Chen J, Zhou J, Liu Y, Feng Z, Tang L, et al. Clinicopathological study and diagnosis of rhabdoid tumor of kidney combined with metanephric adenoma. *Chin Med J* (2014) 127(24):4290–1. doi: 10.3760/cma.j.issn.0366-6999.20141121

27. Udager AM, Pan J, Magers MJ, Palapattu GS, Morgan TM, Montgomery JS, et al. Molecular and immunohistochemical characterization reveals novel braf mutations in metanephric adenoma. *Am J Surg Pathol* (2015) 39(4):549–57. doi: 10.1097/PAS.0000000000000377

28. Choueiri TK, Cheville J, Palescandolo E, Fay AP, Kantoff PW, Atkins MB, et al. Braf mutations in metanephric adenoma of the kidney. *Eur Urol* (2012) 62 (5):917–22. doi: 10.1016/j.eururo.2012.05.051

29. Lenci N, Francesco P, Scarciglia E, Fiorentino V, Schino M, Palermo G, et al. Metanephric adenoma with braf V600k mutation and a doubtful radiological imaging: Pitfalls in the diagnostic process. *Med Mol Morphol* (2021) 54(2):187–91. doi: 10.1007/s00795-020-00269-z

30. Wang X, Shi SS, Yang WR, Ye SB, Li R, Ma HH, et al. Molecular features of metanephric adenoma and their values in differential diagnosis. *Zhonghua bing li xue za zhi* (2017) 46(1):38–42. doi: 10.3760/cma.j.issn.0529-5807.2017.01.009

31. Pan CC, Tseng CE, Kuroda N, Yano M, Yasuda M, Nagashima Y, et al. Molecular characterization of metanephric adenoma, epithelial wilms tumor, and overlap lesions: An integrated whole-exome and transcriptome sequencing analysis. *Appl Immunohistochem Mol Morphol* (2022) 30(4):257–63. doi: 10.1097/PAI.0000000000000996

32. Argani P, Tickoo SK, Matoso A, Pratilas CA, Mehra R, Tretiakova M, et al. Adult wilms tumor: Genetic evidence of origin of a subset of cases from metanephric adenoma. *Am J Surg Pathol* (2022) 46(7):988–99. doi: 10.1097/PAS.0000000000001864

33. Mohammad H, Madsen K, Graumann O, Loya AC, Jensen NV, Dahlrot RH. Metastatic atypical renal tumour with metanephric characteristics treated with sunitinib. *Urol Case Rep* (2022) 40:101880. doi: 10.1016/j.eucr.2021.101880

frontiers | Frontiers in Oncology

TYPE Case Report
PUBLISHED 26 October 2022
DOI 10.3389/fonc.2022.1007296

OPEN ACCESS

EDITED BY
Jen-Chieh Lee,
National Taiwan University Hospital, Taiwan

REVIEWED BY
Husan-Ying Huang,
Kaohsiung Chang Gung Memorial Hospital, Taiwan
Ashley M. Holder,
University of Alabama at Birmingham, United States

*CORRESPONDENCE
Qi-Xing Gong
gongqixing@hotmail.com
Ming Zhao
zhaomingpathol@163.com

†These authors have contributed equally to this work

SPECIALTY SECTION
This article was submitted to Surgical Oncology, a section of the journal Frontiers in Oncology

RECEIVED 30 July 2022
ACCEPTED 10 October 2022
PUBLISHED 26 October 2022

CITATION
Sheng S-J, Li J-M, Fan Q-H, Liu Y, Chen S-Y, Zhao M and Gong Q-X (2022) Case report: *ALK*-rearranged spindle and epithelioid cell neoplasms with S100 and CD34 co-expression: additional evidence of kinase fusion–positive soft tissue tumors. *Front. Oncol.* 12:1007296. doi: 10.3389/fonc.2022.1007296

Case report: *ALK*-rearranged spindle and epithelioid cell neoplasms with S100 and CD34 co-expression: Additional evidence of kinase fusion–positive soft tissue tumors

Shao-Jie Sheng[1,2†], Ju-Ming Li[3†], Qin-He Fan[1], Yang Liu[1], Shao-Yu Chen[4], Ming Zhao[5*] and Qi-Xing Gong[1*]

[1]Department of Pathology, The First Affiliated Hospital of Nanjing Medical University, Nanjing, China, [2]Department of Pathology, The First People's Hospital of Changzhou, Changzhou, China, [3]Department of Orthopedics, The First Affiliated Hospital of Nanjing Medical University, Nanjing, China, [4]R & D department, Guangzhou LBP Medicine Science & Technology Co., Ltd, Guangzhou, China, [5]Cancer Center, Department of Pathology, Zhejiang Province People's Hospital, People's Hospital of Hangzhou Medical College, Hangzhou, China

ALK rearrangements have rarely been reported in S100- and CD34-co-expressing soft tissue neoplasms with lipofibromatosis-like neural tumor (LPFNT) pattern or stromal and perivascular hyalinization, mimicking *NTRK*-rearranged spindle cell tumors. Here, we reported *ALK* fusions involving related partner genes in two adult soft tissue tumors with S100 and CD34 co-expression, and conducted a literature review of mesenchymal tumors harboring *ALK* or other kinase fusions. Case 1 was a 25-year-old female who underwent excision of a soft tissue mass in the anterior thigh region. Morphologically, the tumor was composed of spindle cells adjacent to epithelioid cells embedded in myxedematous and hyalinized stroma, with infiltrative boundary. Spindle cells mixed with inflammatory infiltration resembling inflammatory myofibroblastic tumor (IMT) were seen sporadically. However, brisk mitosis and focal necrosis was also observed, indicating an intermediate-grade sarcoma. In case 2, the left side of the neck of a 34-year-old man was affected. The tumor was composed of monomorphic spindle cells arranged in fascicular growth or patternless pattern, with stromal and perivascular hyalinization. Sparse inflammatory cell infiltration was also observed. Both tumors showed CD34, S100, and ALK-D5F3 immunoreactivity. Next generation sequencing (NGS) test identified a *PLEKHH2::ALK* fusion in case 1, which was confirmed by RT-PCR and Sanger sequencing, whereas the RT-PCR (ARMS method) test detected an *EML4::ALK* fusion in case 2. In conclusion, this study

expands the morphological and genetic landscape of tumors with S100 and CD34 co-expression harboring kinase fusions, and suggests that kinase fusion–positive mesenchymal neoplasms are becoming an enlarging entity with a variety of morphological patterns.

KEYWORDS

ALK, *PLEKHH2*, *EML4*, S100 and CD34 co-expression, soft tissue tumor

Introduction

According to the 2020 WHO classification of soft tissue tumors (STTs), *NTRK*-rearranged spindle cell tumors are an emerging entity, which spans a wide spectrum of morphologies and histologic grades, with frequent immunohistochemical co-expression of S100 and CD34. Notably, the family of this entity is expanding, as tumors with similar clinicopathological features and morphology but alternative kinase genes fusions are constantly identified; among them, STTs with *ALK* gene rearrangement have emerged as a recent hot spot (1–20).

The *ALK* gene (2p23) encodes a cell membrane receptor tyrosine kinase (RTK), which plays an important role in brain development and specific neurons in the nervous system. Oncogenic activation of ALK kinase following *ALK* rearrangement has been reported in a variety of tumors, including non-small cell lung cancer (NSCLC), anaplastic large cell lymphoma (ALCL), IMT, epithelioid fibrous histiocytoma (EFH) (21), *ALK*-positive histiocytosis (22), renal cell carcinoma (23), thyroid cancer (24), secretory carcinomas (25), and gastrointestinal stromal tumor (GIST) (26). Recently, *ALK* rearrangements have been reported in S100- and CD34-co-expressing soft tissue tumors (5–14). A provisionally termed entity, superficial *ALK*-rearranged myxoid spindle cell neoplasm, has been coined to emphasize the characteristic swirling pattern of spindle cells arranged in myxoid or myohyaline stroma (6). Later, Kao YC et al. reported an additional case of superficial *ALK*-rearranged spindle cell neoplasm, which showed ovoid tumor cells predominantly arranged in reticular and cord-like patterns in a hyalinized stroma, with only focal presence of whorl-like pattern (7). However, the emerging tumor was also characterized by frequent S100 protein and CD34 co-expression, perivascular hyalinization, and collagenous stroma, and it partly showed LPFNT pattern, which could not sufficiently distinguish it from other *ALK*-rearranged tumors with S100 and CD34 co-expression. Furthermore, infantile fibrosarcoma (IFS)-like pattern, which is normally reported in the wide morphological spectrum of *NTRK*-rearranged STTs, including infantile fibrosarcoma and *NTRK*-rearranged spindle cell tumors, has also been documented with *ALK* rearrangements (8, 27).

Therefore, more cases are needed to recognize the innate character of such soft tissue tumors with *ALK* rearrangements and improve their classification and nomenclature. In this study, we identified two S100- and CD34-co-expressing STTs with *ALK* rearrangement and summarized the clinicopathological characteristics of the reported kinase fusion–positive mesenchymal neoplasms, hoping to enlighten new ideas.

Case presentation

Clinicopathological findings

Case 1 was a 25-year-old woman with an egg-sized, movable, painless mass in the left anterior thigh region for more than 1 year, with a gradual increase in size associated with pain for 2 months. Magnetic resonance imaging (MRI) suggested an intramuscular mass between the anterior rectus and vastus lateralis muscles in the left thigh (Supplementary Figure 1). The patient underwent resection of the mass. Macroscopically, the resected specimen comprised a soft solid tumor mass measuring 6.5 × 3.5 × 2.8 cm with a gray-white, fleshy, or myxoid cut surface. Microscopically, the tumor was composed of spindle cells juxtaposed with epithelioid cells embedded in myxedematous and hyalinized stroma (Figure 1A), partially infiltrating surrounding striated muscles and adipose tissue. The spindle cells were arranged in sheet-like, intersecting fascicles, or in patternless patterns, showing indistinct cytoplasmic borders and moderate nuclear pleomorphism (Figure 1B). The epithelioid cells were arranged in a nest- or cord-like pattern in a myohyaline background with ample eosinophilic cytoplasm and round to ovoid nuclei (Figure 1C). The mitotic figures (MFs) were plentiful, especially in the cellular area (about 8 MFs/10 high-power fields (HPFs)) (Figure 1D). Focal hemorrhage and necrosis were also observed in the spindle cell area (Figure 1E). Prominent branching of thin-walled blood vessels of different sizes was also found (Figure 1F). At the periphery, some spindle tumor cells admixed with infiltrating inflammatory cells, closely resembling IMT (Figure 1G). According to the French

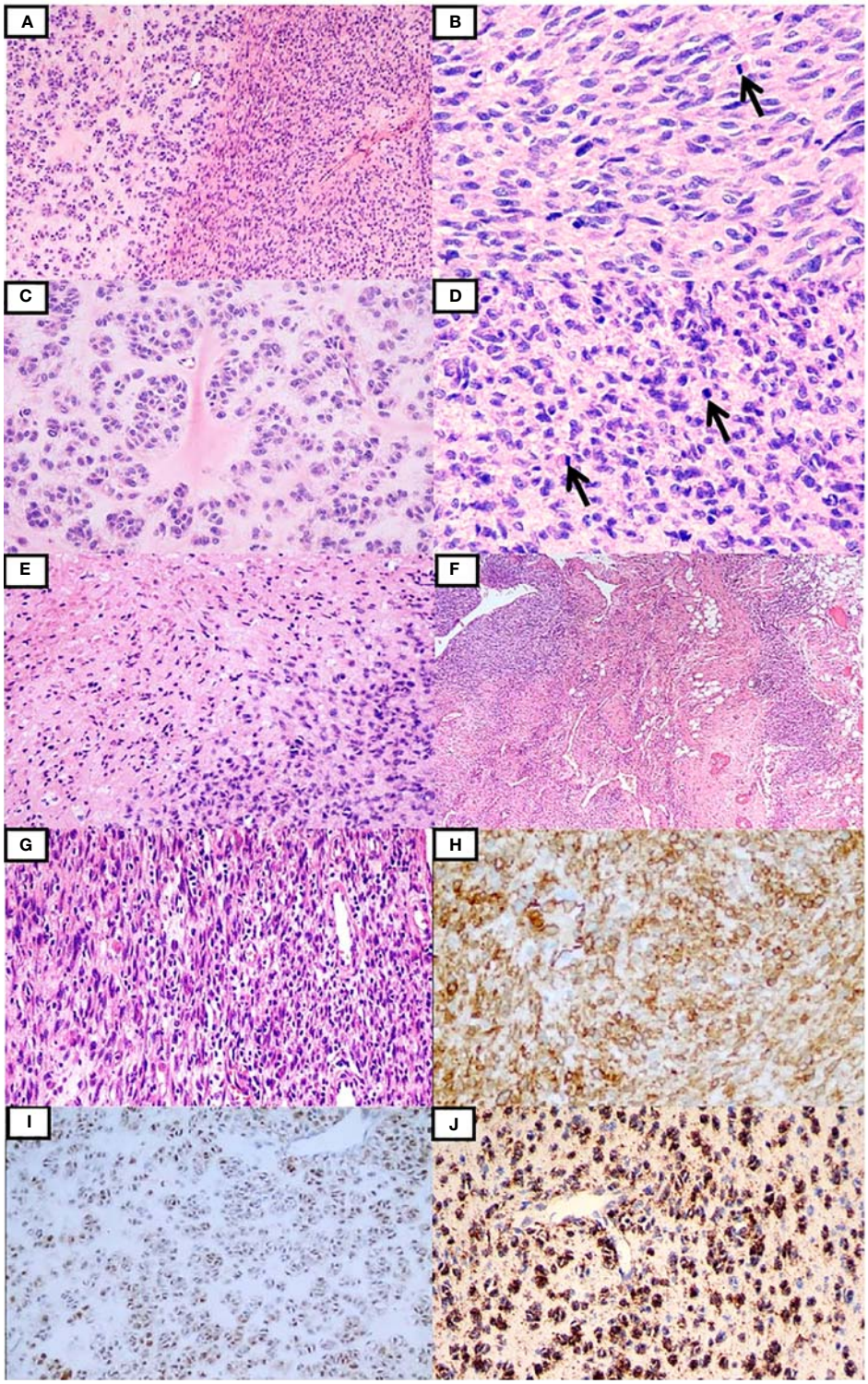

FIGURE 1
Clinicopathological findings of the tumor in case 1. The tumor was composed of the spindle and epithelioid cells embedded in myxedematous and hyalinized stroma **(A)**. The spindle cells were focally arranged in the intersecting fascicles with frequently observed mitotic figures **(B)**, while the epithelioid cells were arranged in the nest- or cord-like pattern in the myohyaline background **(C)**. In some areas, the tumor cells were more cellular with relatively brisk mitoses **(D)**. Focal necrosis was recognized **(E)**. Tumor cells infiltrating the surrounding adipose tissues and thin-walled branching vessels were seen **(F)**. Inflammatory cell infiltration was observed locally **(G)**. Tumor cells were positive for CD34 **(H)**, S100 **(I)**, and ALK-D5F3 **(J)**.

Federation of Cancer Centers Sarcoma Group (FNCLCC) grading, the morphology of the neoplasm was intermediate grade. The tumor cells were immunohistochemically positive for CD34 (Figure 1H), S100 (Figure 1I), ALK-D5F3 (Figure 1J), H3K27me3, vimentin, and CD99 (paranuclear dot-like staining), and they were negative for STAT6, CK-pan, EMA, desmin, SMA, CD31, WT-1, and pan-TRK. The average Ki-67 index was 35%. The patient underwent postoperative radiotherapy(70Gy/35F), and there were no signs of recurrence or metastasis 48 months after surgery.

Case 2 was a 34-year-old man with a mass on the left side of his neck. The tumor was marginally removed without further treatment. Grossly, the mass was partially encapsulated measuring 8 × 5 × 4 cm in size. The texture was soft, and the

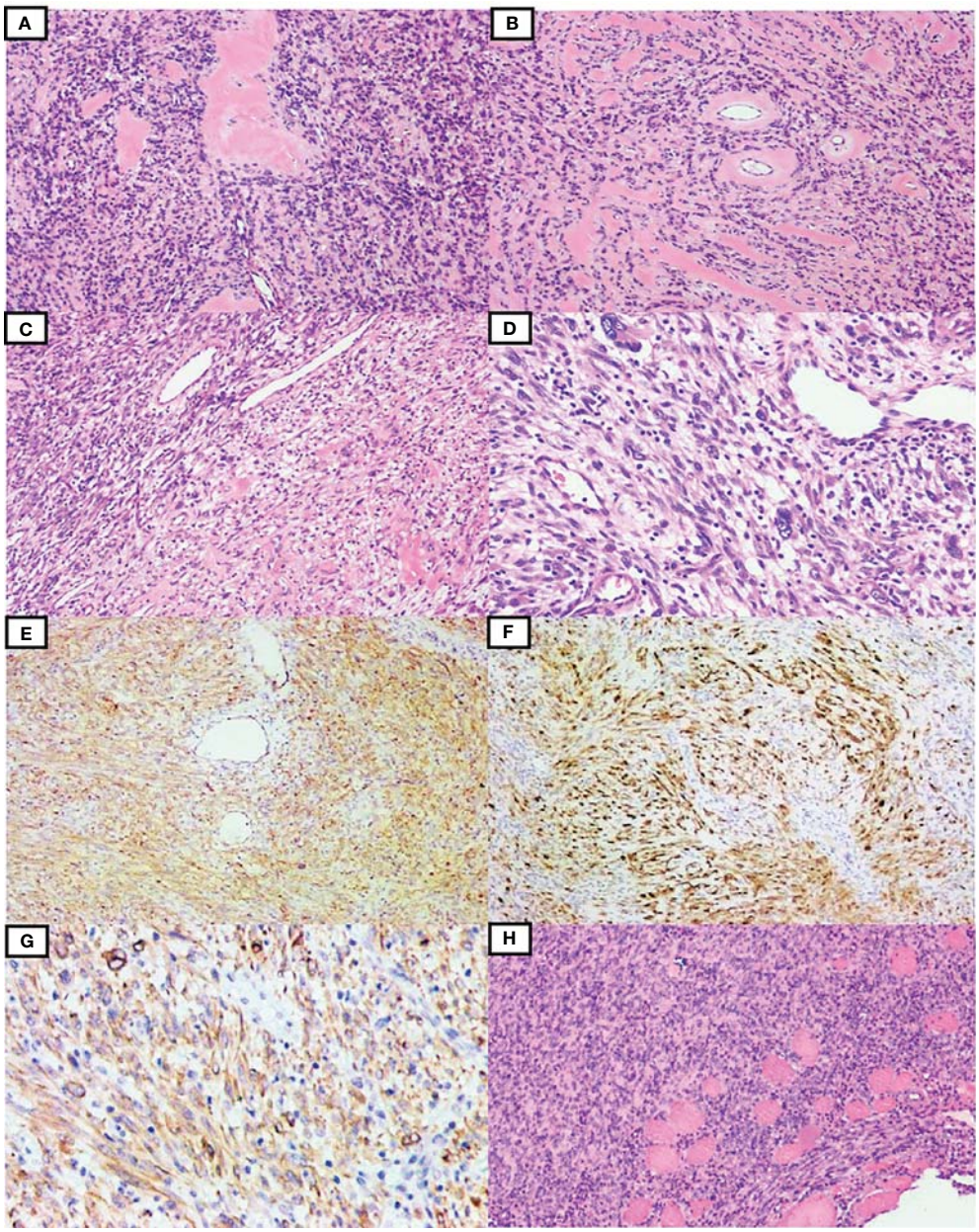

FIGURE 2
Clinicopathological findings of the tumor in case 2. The tumor consisted of spindle-shaped mesenchymal cells with stromal and perivascular hyalinization **(A, B)**. Focal staghorn vessels and clusters of clear cytoplasmic cells were observed **(C)**. Giant multinucleated tumor cells and inflammatory infiltration were also seen **(D)**. The tumor cells were diffusely positive for CD34 **(E)**, S100 **(F)**, and ALK-D5F3 **(G)**. The relapsed tumor showed diffuse proliferation of compact spindle cells, also infiltrating striated muscles **(H)**.

cut surface was gray-white to gray-yellow. Microscopically, the lesion was composed of spindle-shaped mesenchymal cells infiltrating the fat tissue and striated muscle, with stromal and perivascular hyalinization (Figures 2A, B). A higher-power view showed bland spindle cells arranged in a patternless pattern with fusiform nuclei and fine chromatin. Focal clusters of cells showed clear cytoplasm (Figure 2C). Pleomorphic and multinucleate cells were occasionally seen. Sparse inflammatory cell infiltration was also observed (Figure 2D). The mitotic count was 1 MF/10 HPFs. Necrosis was not found. According to FNCLCC grading, the morphology of the neoplasm was low grade. The tumor cells were immunohistochemically positive for CD34 (Figure 2E), S100 (Figure 2F), and ALK-D5F3 (Figure 2G), and negative for AE1/3, SMA, desmin, STAT6, and SOX10. H3K27me3 staining was retained. The available clinical follow-up information of the patient revealed that the tumor recurred at the original site 27 months after surgery. Pathologically, the relapsed tumor showed similar morphology and immunophenotype to the original tumor, with more compact tumor cells (Figure 2H).

Molecular findings

Genomic DNA was extracted from formaldehyde-fixed paraffin-embedded (FFPE) tumor tissues using the QIAamp DNA mini kit (Qiagen, Hilden, Germany). Targeted deep sequencing of mutational hot spots was conducted using a capture-based targeted sequencing panel (Burning Rock Biotech, Guangzhou, China), including a panel of 520 genes to detect genomic alterations including single base substitution, short and long insertions/deletions, copy number variations, gene fusions, and rearrangement. NGS test identified a transcript comprising intron 6 of *PLEKHH2* and intron 20 of *ALK* in case 1, which was validated by RT-PCR and Sanger sequencing (Figure 3A).

Genomic RNA was extracted from tumor FFPE tissues using RNeasy FFPE (Qiagen, Hilden, Germany) and reverse transcribed using SuperScript IV First-Strand Synthesis System (Invitrogen, Carlsbad, CA, USA). The mutation of *EML4::ALK* was detected according to the ARMS methods using a human multigene mutation detection kit (PCR fluorescence probe method) (Amoy Diagnostics Co. Ltd., Xiamen, China). The PCR product was analyzed by Sanger sequencing using Big Dye Terminator Sequencing kit (Applied Biosystems, Foster City, CA, USA). ARMS test detected a transcript comprising exon 6 of *EML4* and exon 20 of *ALK* in case 2 (Figure 3B).

The predicted chimeric proteins consisted of an N-terminal part with the coiled-coil domains of *PLEKHH2* or *EML4* and a C-terminal part with the complete kinase domain of *ALK* (Figures 3C, D).

Fluorescence *in situ* hybridization (FISH) analysis was performed on 3-μm-thick FFPE tumor sections using the dual-color break-apart probe of *ALK* (Abbot Molecular, Abbott Park, IL, USA). A hundred nonoverlapping cells were scored, and more than 20% of tumor cells with abnormal signals were considered positive for gene rearrangement. FISH results confirm *ALK* rearrangements in both cases (Figures 3E, F).

Discussion

In this study, we reported two cases of STTs with S100 and CD34 co-expression harboring ALK gene rearrangements with some distinct features. Morphologically, case 1 was intermediate-grade sarcoma composed of uniform spindle cells and epithelioid cells arranged in myxedematous and hyalinized stroma, with brisk mitosis, focal necrosis, and inflammatory cell infiltration. Although most of the kinase fusion–positive STTs were defined as spindle cell tumors, epithelioid cells have been observed in some areas of S100- and CD34-co-expressing tumors harboring *RAF1*, *BRAF*, and *ALK* gene rearrangements (3, 9, 19). Myxedematous stroma has been found in some cases of *ALK*-rearranged STTs with S100 and CD34 co-expression (6–11). However, tumor cells with brisk mitosis and focal necrosis, which were the features of intermediate- to high-grade sarcoma, have rarely been reported in *ALK*-rearranged STTs. The tumor in case 2 showed moderate to high cellular proliferation and stromal and perivascular hyalinization, which are consistent with morphological features reported by Suurmeijer et al. (15). Similar to other reported S100- and CD34-co-expressing mesenchymal tumors harboring *ALK* rearrangement (6, 8, 9, 12, 13), inflammatory infiltration was found in both our cases. However, case 1 even showed IMT-like morphology, suggesting IMT in the differential diagnosis, but then we discarded the hypothesis due to the absence of myogenic expression and S100 and CD34 co-expression. To the best of our knowledge, IMT-like morphology has not been revealed in S100- and CD34-co-expressing mesenchymal tumors harboring *ALK* rearrangement. Nevertheless, it has been reported in *NTRK*-rearranged spindle cell tumors, presented primarily (28) or as a morphological transformation after chemotherapy (29). Based on the case reported here and the literature reviewed in the Introduction section, we speculate that similar to *NTRK*-rearranged spindle cell tumors, *ALK*-rearranged soft tissue tumors also span a wide spectrum of morphologies and histologic grades. Furthermore, the IMT-like pattern, analogous to the LPFNT pattern, might overlap with other patterns in the wide spectrum of kinase fusion–positive mesenchymal neoplasms.

Genetically, the tumor in case 1 was identified to harbor *PLEKHH2::ALK* fusion gene, whereas the tumor in case 2 showed *EML4::ALK* gene fusion. The *PLEKHH2* gene (2p21) encodes an intracellular protein highly enriched in renal glomerular podocytes, which plays a structural and functional role in the podocyte foot processes. The presence of a putative a-helical coiled-coil domain was observed in the N-terminus of

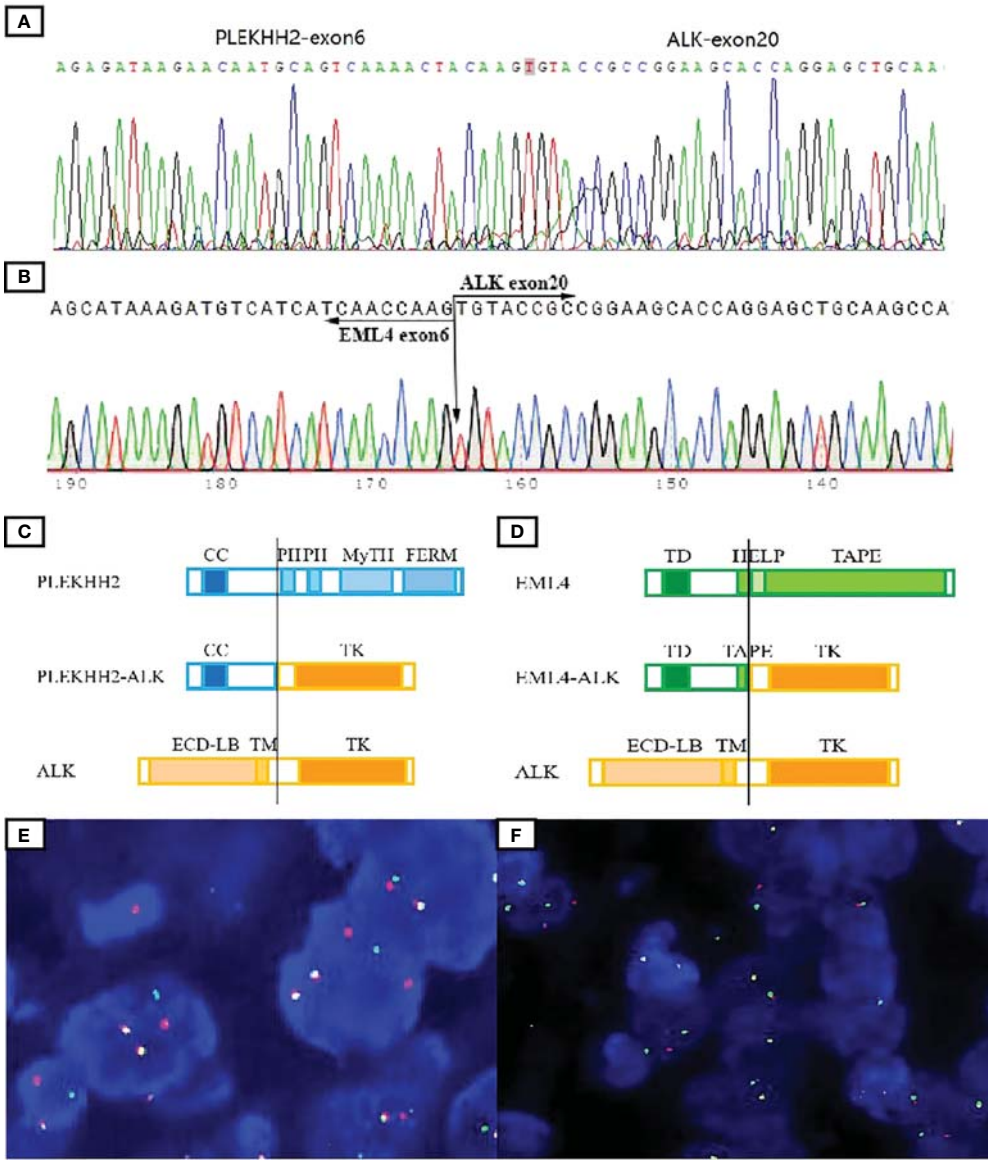

FIGURE 3
Molecular tests to validate ALK fusions. The presence of the *PLEKHH2::ALK* fusion transcript was validated by Sanger sequencing **(A)**. Direct sequencing of the purified RT-PCR products revealed the chimeric transcripts between exon 6 of *EML4* and exon 20 of *ALK* **(B)**. Schematic representation of the predicted chimeric proteins **(C, D)**. By ALK break-apart FISH test, most tumor cells in both cases demonstrated a signal pattern consisting of isolated 5′ (green) and isolated 3′ (orange), along with fused 3′/5′ signals **(E, F)**. TD, trimerization domain; HELP, hydrophobic motif in EML proteins; TAPE, tandem atypical propeller domain; ECD-LB, extracellular ligand-binding domain; TM, transmembrane domain; TK, tyrosine kinase domain; CC, a-helical coiled-coil domain; PH, Pleckstrin homology domain; MyTH, MyTH4 domain; FERM, four-point-one ezrin radxin mesoin family.

PLEKHH2 (30). The *EML4* gene (2p21) encodes a microtubule-associated protein with a coiled-coil domain and may generate abnormal fusion with *ALK*, which has been identified in lung adenocarcinoma, breast cancer, colorectal cancer, IMT, and S100- and CD34-co-expressing neoplasms. Commonly, *ALK* fusions could activate the ALK kinase domain without a ligand through autophosphorylation due to dimerization. Both of the fusion genes in our study contained the entire intracellular kinase domain of *ALK* and the coiled-coil domain of the fusion partner genes, which mediated dimerization and activation of the ALK kinase domain. Therefore, the fusion proteins were presumed to have an oncogenic function.

Recently, an emerging class of spindle cell tumors characterized by frequent S100 protein and/or CD34 co-

expression and recurrent tyrosine kinase fusions, including *BRAF*, *RAF1*, *RET*, *MET*, *ROS1*, and *ALK*, has been documented, although it is unclear whether these tumors should be classified into one category (31). We tried to summarize their features and find some commonalities listed hereafter. First, the related kinase fusion genes are predominantly tyrosine kinase genes, which regulate downstream signaling pathways, including the MAPK/ERK, PI3K/AKT, and JAK3-STAT3. *BRAF* and *RAF1* even constitute the MAPK pathway components. Second, most of the oncogenic activation of kinase genes is through rearrangement. The kinase domain is reserved, and the partner gene is responsible for dimerization or other ways to mediate the activation of the kinase domain. Third, kinase fusion–positive neoplasms have been proven to be effective for targeted therapy (13, 27), not only in mesenchymal tumors but also in various epithelial neoplasms. Finally, these kinase fusion–positive mesenchymal neoplasms share similar clinicopathological features with *NTRK*-rearranged spindle cell tumors.

We have generalized the features of 47 mesenchymal neoplasms with oncogenic kinase alterations akin to *NTRK*-rearranged mesenchymal neoplasms searched in the available published literature, including 10 cases positive for RAF1, eight for RET, four for BRAF, 21 for *ALK*, one for *MET*, one for *ROS1*, and two for *ABL1* gene rearrangements (1–20). Among them, 15 were found in children (<10 years), seven were found in adolescents (age range of 10–20 years), and 25 were found in adult patients (>20 years old). Both sexes were affected (27 females and 20 males). The tumors were most commonly located in soft tissues of the trunk and extremities, while a few occurred in the head and neck region, viscera, and even skeleton. Tumor size ranged from 0.5 cm to 14 cm in 29 tumors with available data. The 47 tumors spanned a wide spectrum of morphologies and histologic grades, showing monomorphic spindle cell proliferation in a haphazard arrangement with occasional components of epithelioid or pleomorphic cells. In addition to the unified features mentioned above, some cases seem to show overlapped characteristics. Myxoid stroma was observed in some cases (14/47) and seemed to be more frequently present in *ALK*-rearranged tumors (6–11, 16). Some *ALK*-, *RAF1*-, or *RET*-rearranged tumors were characterized by the presence of tumor cells arranged in concentric whorls, which was also observed in *NTRK*-rearranged tumors (6, 7, 17, 18, 32). Staghorn or hemangiopericytoma-like vessels were also observed in some *ALK*-, *RET*-, *RAF1*-, or *BRAF*-rearranged tumors (8/47), which has also been recognized as one of the characteristics of *NTRK*-rearranged STTs (6, 14, 16, 18, 19). Inflammatory infiltration was readily witnessed in nearly one-third of cases, closely correlating with LPFNT morphology (20). Tumors with low-grade morphological features were common (32/47, 68.1%), while intermediate- to advanced-grade tumors were relatively rare. Certainly, with the deepening understanding of these tumors, some less common features will be reported and summarized, even under the name of other provisionally termed entities. The prognosis of the tumors appears to be related to histologic grade. Low-grade tumors with positive margins showed a propensity for local recurrence, whereas high-grade tumors showed aggressive clinical behavior and metastasized to lungs or other organs. Thus, in view of increasing cases of kinase fusion–positive mesenchymal neoplasms, we believe that the emerging entity of mesenchymal neoplasms with oncogenic kinase alterations akin to NTRK-rearranged spindle cell tumors could develop into a constantly expanding family of kinase fusion–positive soft tissue tumors.

Conclusions

Herein, we reported two spindle and epithelioid cell neoplasms with S100 and CD34 co-expression showing recurrent *ALK* rearrangements. Our report adds to the morphological and genetic spectrum of the novel, recently described entity with S100 and CD34 co-expression harboring kinase fusions. We believe that more reported cases will unveil the panoramic view of the clinicopathological features of kinase fusion–positive STTs and improve patient treatment strategies and prognosis *via* targeted therapies.

Data availability statement

The original contributions presented in the study are included in the article/Supplementary Material. Further inquiries can be directed to the corresponding authors.

Ethics statement

The studies involving human participants were reviewed and approved by the Ethics Committee of the First Affiliated Hospital of Nanjing Medical University. The patients/participants provided their written informed consent to participate in this study.

Author contributions

S-JS, J-ML, Q-HF, MZ, and Q-XG designed the study. S-JS, J-ML and YL participated in patient treatment and analyzed clinical data. S-YC performed molecular testing and analyzed the data. S-JS and J-ML drafted the manuscript. Q-XG and MZ supervised the work and revised the manuscript. Q-HF helped revised the manuscript. All authors contributed to the article and approved the submitted version.

Funding

This work was supported by Technology Support Programs of Suqian city (S201519), Natural Science Foundation of Zhejiang Province (LY21H160052), and Zhejiang Provincial Medicine and Health Research Foundation (2023KY040). The funders did not have any role in the design and conduct of the study, the analysis and interpretation of the data, and preparation of the manuscript.

Conflict of interest

Author S-YC was employed by Guangzhou LBP Medicine Science & Technology Co., Ltd.

The remaining authors declare that the research was conducted in the absence of any commercial or financial relationships that could be construed as a potential conflict of interest.

Publisher's note

Supplementary material

The Supplementary Material for this article can be found online at: https://www.frontiersin.org/articles/10.3389/fonc.2022.1007296/full#supplementary-material

SUPPLEMENTARY FIGURE 1
Imaging studies of the left thigh in case 1. The lesion situated between the anterior rectus and vastus lateralis muscles **(A)** and was slightly hypointense in T1 weighted imaging **(B)** and significant hyperintense in T2 weighted imaging **(C)**.

References

1. Subbiah V, Westin SN, Wang K, Araujo D, Wang WL, Miller VA, et al. Targeted therapy by combined inhibition of the RAF and mTOR kinases in malignant spindle cell neoplasm harboring the KIAA1549-BRAF fusion protein. *J Hematol Oncol* (2014) 7:8. doi: 10.1186/1756-8722-7-8

2. Flucke U, van Noesel MM, Wijnen M, Zhang L, Chen CL, Sung YS, et al. TFG-MET fusion in an infantile spindle cell sarcoma with neural features. *Genes Chromosomes Cancer* (2017) 56(9):663–7. doi: 10.1002/gcc.22470

3. Hicks JK, Henderson-Jackson E, Duggan J, Joyce DM, Brohl AS. Identification of a novel MTAP-RAF1 fusion in a soft tissue sarcoma. *Diagn Pathol* (2018) 13(1):77. doi: 10.1186/s13000-018-0759-z

4. Antonescu CR, Dickson BC, Swanson D, Zhang L, Sung YS, Kao YC, et al. Spindle cell tumors with RET gene fusions exhibit a morphologic spectrum akin to tumors with NTRK gene fusions. *Am J Surg Pathol* (2019) 43(10):1384–91. doi: 10.1097/PAS.0000000000001297

5. Abs D, Landman S, Osio A, Lepesant P, Schneider P, Obadia D, et al. Spindle cell tumor with CD34 and S100 co-expression and distinctive stromal and perivascular hyalinization showing EML4-ALK fusion. *J Cutan Pathol* (2021) 48 (7):896–901. doi: 10.1111/cup.13926

6. Dermawan JK, Azzato EM, Goldblum JR, Rubin BP, Billings SD, Ko JS, et al. Superficial ALK-rearranged myxoid spindle cell neoplasm: a cutaneous soft tissue tumor with distinctive morphology and immunophenotypic profile. *Mod Pathol* (2021) 34(9):1710–8. doi: 10.1038/s41379-021-00830-w

7. Kao YC, Lee PH, Wu CL, Yu SC, Huang HY. Superficial ALK-rearranged myxoid spindle cell neoplasm with a novel FMR1-ALK fusion gene. *Mod Pathol* (2022) 35(3):438–41. doi: 10.1038/s41379-021-00952-1

8. Tan SY, Al-Ibraheemi A, Ahrens WA, Oesterheld JE, Fanburg-Smith JC, Liu YJ, et al. ALK rearrangements in infantile fibrosarcoma-like spindle cell tumours of soft tissue and kidney. *Histopathology* (2022) 80(4):698–707. doi: 10.1111/his.14603

9. Coppock JD, Schneider MA, Surrey LF, Karakousis GC, Maki RG, Cooper K, et al. S100 and CD34 expressing mesenchymal neoplasm with rare PLEKHH2:: ALK fusion and response to ALK inhibition. *Am J Surg Pathol* (2022) 46(9):1309–13. doi: 10.1097/PAS.0000000000001887

10. Lopez-Nunez O, Surrey LF, Alaggio R, Fritchie KJ, John I. Novel PPP1CB-ALK fusion in spindle cell tumor defined by S100 and CD34 coexpression and distinctive stromal and perivascular hyalinization. *Genes Chromosomes Cancer* (2020) 59(8):495–9. doi: 10.1002/gcc.22844

11. Mantilla JG, Cheung H, Ha AS, Hoch BL, Liu YJ, Ricciotti RW, et al. Spindle cell neoplasm with EML4-ALK gene fusion presenting as an intraosseous vertebral mass. *Genes Chromosomes Cancer* (2021) 60(4):282–6. doi: 10.1002/gcc.22917

12. Kao YC, Suurmeijer AJH, Argani P, Ickson BC, Zhang L, Sung YS, et al. Soft tissue tumors characterized by a wide spectrum of kinase fusions share a lipofibromatosis-like neural tumor pattern. *Genes Chromosomes Cancer* (2020) 59(10):575–83. doi: 10.1002/gcc.22877

13. Rakheja D, Park JY, Fernandes NJ, Watt TC, Laetsch TW, Collins RRJ, et al. Pediatric non-myofibroblastic primitive spindle cell tumors with ALK gene rearrangements and response to crizotinib. *Int J Surg Pathol* (2022) 30(6):706–15. doi: 10.1177/10668969221080072

14. Agaram NP, Zhang L, Sung YS, Chen CL, Chung CT, Antonescu CRc, et al. Recurrent NTRK1 gene fusions define a novel subset of locally aggressive lipofibromatosis-like neural tumors. *Am J Surg Pathol* (2016) 40:1407–16. doi: 10.1097/PAS.0000000000000675

15. Suurmeijer AJH, Dickson BC, Swanson D, Zhang L, Sung YS, Cotzia P, et al. A novel group of spindle cell tumors defined by S100 and CD34 co-expression shows recurrent fusions involving RAF1, BRAF, and NTRK1/2 genes. *Genes Chromosomes Cancer* (2018) 57(12):611–21. doi: 10.1002/gcc.22671

16. Loong S, Lian DWQ, Kuick CH, Lim TH, Nah SA, Wong KPL, et al. Novel TFG-RET fusion in a spindle cell tumour with S100 and CD34 coexpresssion. *Histopathology* (2020) 76(2):333–6. doi: 10.1111/his.13971

17. Michal M, Ptáková N, Martínek P, Gatalica Z, Kazakov DV, Michalová K, et al. S100 and CD34 positive spindle cell tumor with prominent perivascular hyalinization and a novel NCOA4-RET fusion. *Genes Chromosomes Cancer* (2019) 58(9):680–5. doi: 10.1002/gcc.22758

18. Mok Y, Kimpo MS, Chen H, Kuick CH, Chang KT, Lee VKM, et al. Spindle cell tumour with S100 and CD34 co-expression showing PDZRN3-RAF1 rearrangement–a recently described entity. *Histopathology* (2019) 74(7):1109–11. doi: 10.1111/his.13841

19. Sheng SJ, Li JM, Zou YF, Peng XJ, Wang QY, Fang HS, et al. A low-grade malignant soft tissue tumor with S100 and CD34 co-expression showing novel CDC42SE2-BRAF fusion with distinct features. *Genes Chromosomes Cancer* (2020) 59(10):595–600. doi: 10.1002/gcc.22875

20. Choo F, Rakheja D, Davis LE, Davare M, Park JY, Timmons CF, et al. GAB1-ABL1 fusions in tumors that have histologic overlap with NTRK-rearranged spindle cell tumors. *Genes Chromosomes Cancer* (2021) 60(9):623–30. doi: 10.1002/gcc.22972

21. Dickson BC, Swanson D, Charames GS, Fletcher CD, Hornick JL. Epithelioid fibrous histiocytoma: molecular characterization of ALK fusion partners in 23 cases. *Mod Pathol* (2018) 31(5):753–62. doi: 10.1038/modpathol.2017.191

22. Kemps PG, Picarsic J, Durham BH, Hélias-Rodzewicz Z, Hiemcke- Jiwa L, van den Bos C, et al. ALK-positive histiocytosis: a new clinicopathologic spectrum highlighting neurologic involvement and responses to ALK inhibition. *Blood* (2022) 139(2):256–80. doi: 10.1182/blood.2021013338

23. Kuroda N, Trpkov K, Gao Y, Tretiakova M, Liu YJ, Ulamec M, et al. ALK rearranged renal cell carcinoma (ALK-RCC): a multi-institutional study of twelve cases with identification of novel partner genes CLIP1, KIF5B and KIAA1217. *Mod Pathol* (2020) 33(12):2564–79. doi: 10.1038/s41379-020-0578-0

24. Panebianco F, Nikitski AV, Nikiforova MN, Kaya C, Yip L, Condello V, et al. Characterization of thyroid cancer driven by known and novel ALK fusions. *Endocr Relat Cancer* (2019) 26(11):803–14. doi: 10.1530/ERC-19-0325

25. Sasaki E, Masago K, Fujita S, Suzuki H, Hanai N, Hosoda W. Salivary secretory carcinoma harboring a novel ALK fusion: Expanding the molecular characterization of carcinomas beyond the ETV6 gene. *Am J Surg Pathol* (2020) 44 (7):962–9. doi: 10.1097/PAS.0000000000001471

26. Zhao L, Nathenson MJ, Nowak JA, Fairweather M, Hornick JL. ALK rearrangement in a gastrointestinal stromal tumour of the small bowel. *Histopathology* (2020) 77(3):513–5. doi: 10.1111/his.14133

27. Chen T, Wang Y, Goetz L, Corey Z, Dougher MC, Smith JD, et al. Novel fusion sarcomas including targetable NTRK and ALK. *Ann Diagn Pathol* (2021) 54:151800. doi: 10.1016/j.anndiagpath.2021.151800

28. Wong DD, Vargas AC, Bonar F, Maclean F, Kattampallil J, Stewart C, et al. NTRK-rearranged mesenchymal tumours: diagnostic challenges, morphological patterns and proposed testing algorithm. *Pathology* (2020) 52(4):401–9. doi: 10.1016/j.pathol.2020.02.004

29. Pavlick D, Schrock AB, Malicki D, Stephens PJ, Kuo DJ, Ahn H, et al. Identification of NTRK fusions in pediatric mesenchymal tumors. *Pediatr Blood Cancer* (2017) 64(8):e26433. doi: 10.1002/pbc.26433

30. Perisic L, Lal M, Hulkko J, Hultenby K, Önfelt B, Sun Y, et al. Plekhh2, a novel podocyte protein downregulated in human focal segmental glomerulosclerosis, is involved in matrix adhesion and actin dynamics. *Kidney Int* (2012) 82(10):1071–83. doi: 10.1038/ki.2012.252

31. Antonescu CR. Emerging soft tissue tumors with kinase fusions: An overview of the recent literature with an emphasis on diagnostic criteria. *Genes Chromosomes Cancer* (2020) 59(8):437–44. doi: 10.1002/gcc.22846

32. Suurmeijer AJ, Dickson BC, Swanson D, Zhang L, Sung YS, Huang HY, et al. The histologic spectrum of soft tissue spindle cell tumors with NTRK3 gene rearrangements. *Genes Chromosomes Cancer* (2019) 58(11):739–46. doi: 10.1002/gcc.22767

frontiers | Frontiers in Oncology

TYPE Case Report
PUBLISHED 10 November 2022
DOI 10.3389/fonc.2022.1033114

OPEN ACCESS

EDITED BY
Ming Zhao,
Zhejiang Provincial People's Hospital, China

REVIEWED BY
Steven Christopher Smith,
Virginia Commonwealth University Health System, United States
Deepika Mishra,
All India Institute of Medical Sciences, India

*CORRESPONDENCE
Jiro Ichikawa
jichi@sb4.so-net.ne.jp

SPECIALTY SECTION
This article was submitted to Surgical Oncology, a section of the journal Frontiers in Oncology

RECEIVED 31 August 2022
ACCEPTED 17 October 2022
PUBLISHED 10 November 2022

CITATION
Ichikawa J, Kawasaki T, Imada H, Kanno S, Taniguchi N, Ashizawa T and Haro H (2022) Case report: Atypical spindle cell/pleomorphic lipomatous tumor masquerading as a myxoid liposarcoma or intramuscular myxoma. *Front. Oncol.* 12:1033114. doi: 10.3389/fonc.2022.1033114

Case report: Atypical spindle cell/pleomorphic lipomatous tumor masquerading as a myxoid liposarcoma or intramuscular myxoma

Jiro Ichikawa[1]*, Tomonori Kawasaki[2], Hiroki Imada[3], Satoshi Kanno[2], Naofumi Taniguchi[1], Tomoyuki Ashizawa[1] and Hirotaka Haro[1]

[1]Department of Orthopaedic Surgery, Interdisciplinary Graduate School of Medicine, University of Yamanashi, Chuo, Yamanashi, Japan, [2]Department of Pathology, Saitama Medical University International Medical Center, Hidaka, Saitama, Japan, [3]Department of Pathology, Saitama Medical Center, Saitama Medical University, Kawagoe, Saitama, Japan

Atypical spindle cell/pleomorphic lipomatous tumors (ASPLTs) were recently categorized as benign lipomatous tumors. However, accurate and complete preoperative diagnosis of ASPLTs may be difficult. Furthermore, diagnosis based on magnetic resonance imaging (MRI) findings is uncertain because of the varying ratios of the fat component within the tumor. Here, we report a case of ASPLT masquerading as a myxoid tumor. Although MRI findings were consistent with a myxoid liposarcoma, needle biopsy findings suggested a myxoma, and we performed marginal resection. Histopathological findings revealed infiltrating spindle cells with atypia. In addition, immunohistochemistry (IHC) showed positive staining for CD34 and heterogeneous retinoblastoma deficiency, and fluorescence *in situ* hybridization (FISH) showed no amplification of mouse double minute 2 homolog and no rearrangement of *FUS* or *EWSR1*. When MRI and histopathological findings suggest a myxoid tumor, IHC and FISH should be considered and performed for a precise and accurate diagnosis.

KEYWORDS

atypical spindle cell/pleomorphic lipomatous tumor, differential diagnosis, magnetic resonance imaging, histopathology, immunohistochemistry, fluorescence *in situ* hybridization

Abbreviations: ASPLT, atypical spindle cell/pleomorphic lipomatous tumor; MRI, magnetic resonance imaging; IHC, immunohistochemistry; FISH, fluorescence *in situ* hybridization; MLS, myxoid liposarcoma; RB1, retinoblastoma; MDM2, mouse double minute 2 homolog; ALT/WDL, atypical lipomatous tumor/well-differentiated liposarcoma; SCL, spindle cell lipoma; DDLS, dedifferentiated liposarcoma; PLS, pleomorphic liposarcoma; PET-CT, Positron emission tomography-computed tomography; CDK4, cyclin-dependent kinase.

Introduction

Dei Tos et al. were the first to describe atypical spindle cell/pleomorphic lipomatous tumors (ASPLTs), which are similar to spindle cell liposarcomas, well-differentiated liposarcomas, and atypical spindle cell lipomas (1). Further molecular analysis showed that ASPLTs could be further subclassified as atypical spindle cell lipomatous tumors and atypical pleomorphic lipomatous tumors, which are benign lipomatous tumors (2). Although histopathological findings are essential for diagnosing ASPLT, diagnosis is complex because of the presence of varying proportions of atypical spindle cells, adipocytes, lipoblasts, and multinucleated cells and an extracellular matrix that consists of varying proportions of myxoid and collagenous components (3). Therefore, the differential diagnosis of ASPLT may encompass a broad range of conditions, from fatty tumors to fibrous tumors. Accordingly, histopathology, immunohistochemistry (IHC), and fluorescence *in situ* hybridization (FISH) are indispensable for an accurate diagnosis (4, 5). Although there have been few reports on the magnetic resonance imaging (MRI) findings of ASPLT, ASPLTs have varying T1 intensities, which may reflect their pathological diversity (6–8). Herein, we report a case of ASPLT masquerading as a myxoid tumor and review the pathological and MRI findings of ASPLT.

Case description

A 64-year-old man presented with a mass on his right buttock. The mass had been apparent for 1 year and was painless and gradually increased in size. Physical examination revealed no pain, swelling, or numbness. Moreover, the Tinel sign was negative, and the hip range of motion was normal. Furthermore, there was no gait disturbance. MRI revealed a low-intensity signal on T1-weighted images with a few high-intensity signals that suggested the presence of intratumoral fat (Figure 1A). High signal intensity on T2-weighted images (Figure 1B) and T2 short tau inversion recovery images (Figure 1C) suggested the presence of myxoid components. Heterogeneous enhancement was noted on gadolinium-enhanced T1-weighted images (Figures 1D, E). Positron emission tomography-computed tomography (PET-CT) showed slight ^{18}F-fluorodeoxyglucose uptake in the right buttock mass, with an SUVmax of 2.8 (Figure 1F). The imaging findings suggested myxoid liposarcoma (MLS). However, needle biopsy findings suggested myxoma, because there were few atypical spindle cells (Figures 2A, B). Collectively, the preoperative findings indicated intramuscular myxoma; therefore, marginal resection was performed. The tumor was located within the gluteus maximus (Figure 3A). Macroscopically, the tumor measured 16 × 15 × 12 cm in size and consisted of mainly myxoid components with little fat

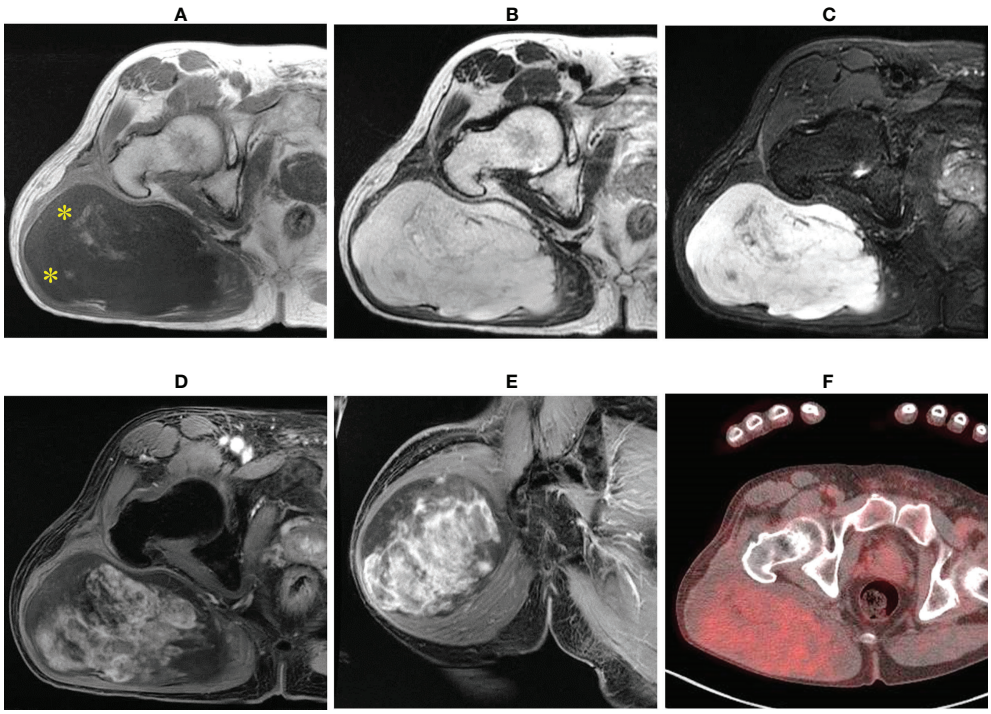

FIGURE 1
Imaging findings. T1-weighted axial images showing low and slightly high signals (yellow asterisk) **(A)**; almost homogeneous high signal on T2-weighted images **(B)** and short tau inversion recovery images **(C)**; and axial and central enhancement on a gadolinium-enhanced T1-weighted axial image **(D, E)**. Axial fluorodeoxyglucose (FDG) positron emission tomography-computed tomography (PET-CT) showing a hypometabolic tumor **(F)**.

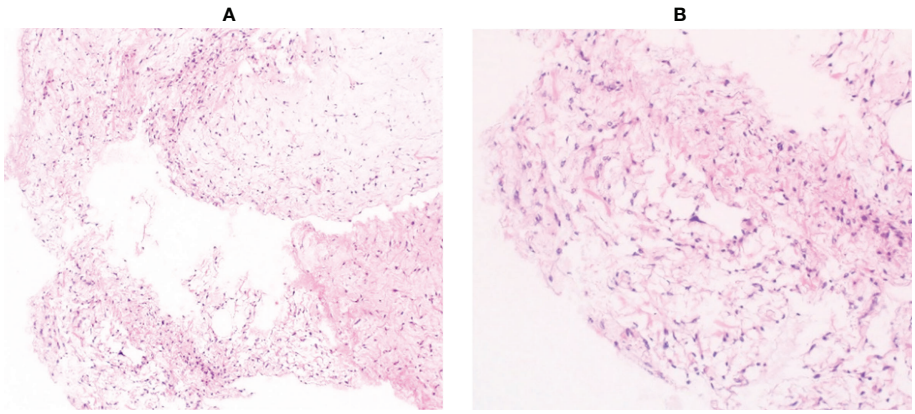

FIGURE 2
Histological findings of the needle biopsy specimen. Pathological examination showed mild proliferation of spindle cells with few atypical cells in a myxoid background (**A**, ×100 **B**, ×200).

tissue (Figures 3B, C). Histopathologically, the tumor infiltrated the muscle and had an ill-defined border (Figure 4A). While most of the tumor cells were bland and short-spindled with a myxoid matrix, some of the cells showed cytological atypia and pleomorphism. Mitosis was rare. In addition, there were areas with fatty lipid and lipoblast components (Figures 4B, C). IHC indicated that the tumor was positive for CD34 (Figure 4D) and S100 (Figure 4E), negative for retinoblastoma (RB1) (Figure 4F), and negative for desmin, estrogen receptor, Muc4, and BCL2 (data not shown). FISH showed no amplification of mouse double minute 2 homolog (*MDM2*) (Figure 4G) and no rearrangement of *FUS* (Figure 4H) or *EWSR1* (Figure 4I). A final diagnosis of ASPLT was made based on of the IHC and FISH results and the imaging and pathological findings.

Considering the clinical features of the tumor, we decided to conduct follow-up using imaging studies. The patient was free of recurrence 1 year after surgery.

Discussion

ASPLT was originally reported as a spindle cell liposarcoma, a well-differentiated liposarcoma, and an atypical spindle cell lipoma (1). Although ASPLT was initially considered a subtype of atypical lipomatous tumor/well-differentiated liposarcoma (ALT/WDL), further analysis of clinicopathologic characterizations led to separate categorizations (9). Marino-Enriquez et al. suggested that ASPLTs were atypical spindle cell lipomatous tumors (4). However, analysis of the genetic and pathological features of atypical pleomorphic lipomatous tumors (10) led to classifying both atypical pleomorphic lipomatous tumors and atypical spindle cell lipomatous tumors as ASPLTs, which are categorized as benign lipomatous tumors (2). Although the exact mechanism of ASPLT tumorigenesis has not been elucidated, a subset of cases showed a loss of *RB1*, which comprises the 13q/RB1 family of tumors (2, 11).

The differential diagnosis of ASPLT based on histopathology is broad, ranging from benign to malignant lipomatous tumors as summarized in Table 1 (3). The characteristics of both ASPLT and other tumors highly overlap, implying that differential diagnosis is very complex. Thus, IHC and FISH, in addition to histological examination, are essential for the correct diagnosis of ASPLT.

The distinctive differences in clinical features between ASPLT and spindle cell lipoma (SCL) are sex and anatomic location (4, 12). Approximately 60% of patients with ASPLT are men, and most are in their 50s. With regard to tumor location, 60% of tumors occur in the limbs and limb girdles and approximately 60% occur in subcutaneous tissues. The average tumor size is approximately 5 cm (4). However, the size, depth, and anatomical location of the tumor in our case were different from those of typical ASPLT cases. There are several histological differences between SCL and ASPLT, including the presence of atypical spindle cells, atypical multivacuolated lipoblasts, bizarre pleomorphic cells, and mitotic activity. Floret-like multinucleated cells and ropey collagen are typical of SCL. These findings are uncommon in ASPLT, but they have been observed previously (3, 11). SCL and ASPLT share similar immunohistochemical features, such as CD34 positivity and the loss of RB1 (11). Although these features are observed in almost all SCL cases, ASPLT has about 50–70% positive expression of CD34 and about 60–70% RB1 loss (4, 13). In addition, although 40% of ASPLT cases are positive for S100, 90% of SCL cases have no S100 expression (4, 14). Nonetheless, ASPLT and SCL have many overlapping histological and IHC findings. Therefore, extreme caution is required during diagnosis.

Differentiating ALT/WDL, dedifferentiated liposarcoma (DDLS), and ASPLT is clinically important. The expression of

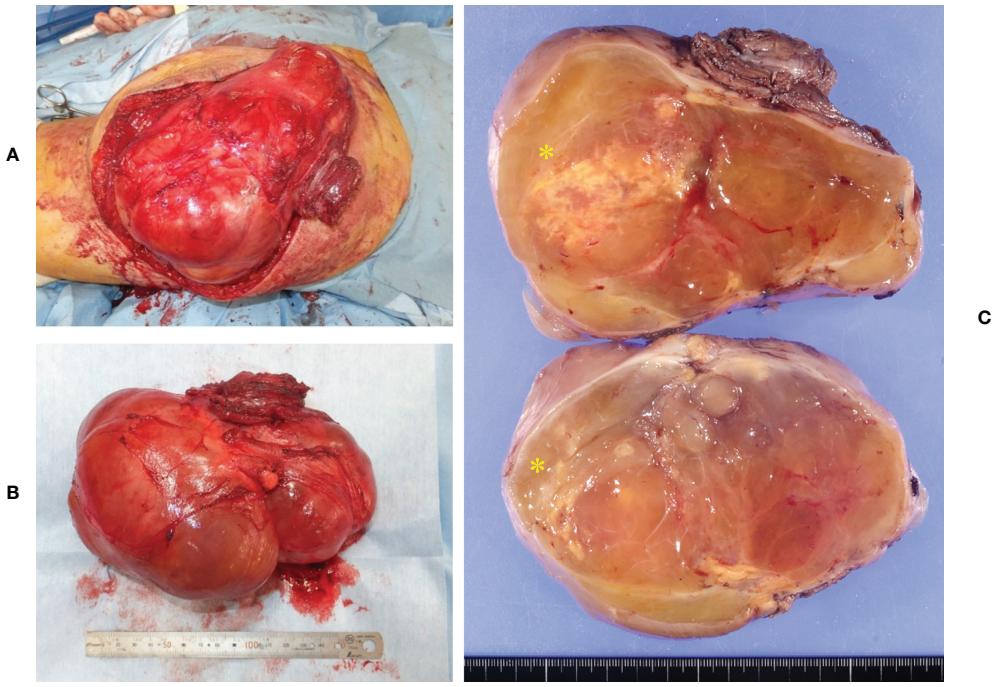

FIGURE 3
Intraoperative and pathological findings of the resection specimen. The tumor was located inside the gluteus maximus **(A)**. Macroscopically, the tumor measured 16 × 15 × 12 cm in size **(B)**. The tumor consisted of large myxoid components and small fatty components (yellow asterisk) **(C)**.

MDM2 and CDK4 in IHC are key findings (3). ALT/WDL and DDLS have both MDM2 and CDK4 expression, whereas ASPLT is usually negative for both markers (3). However, care should be taken because some cases of ASPLT have shown CDK4 or MDM2 positivity (13). In these cases, no positivity may be observed in both MDM2 and CDK4, and no amplification of *MDM2* is observed using FISH (4, 13).

The presence of pleomorphism, high mitotic activity, and tumor necrosis and the lack of floret-like multinucleated cells are important for differentiating pleomorphic liposarcoma (PLS) from ASPLT (10). PLS has no characteristic IHC or FISH findings. Various MRI findings of PLS have been observed because of necrosis and intratumoral bleeding, making diagnosis based on MRI difficult (15, 16). In our case, myxoid liposarcoma (MLS) and myxoma were strongly suspected based on MRI findings. To differentiate ASPLT from MLS, confirmation of *FUS* and *EWSR1* rearrangements using FISH is required (17). Additionally, histological and morphological findings may be useful for differentiating these tumor types, as myxoma is positive for CD34 and negative for S100 and desmin (18). Therefore, complete pathological assessment, IHC, and FISH should be performed to obtain a correct diagnosis.

Previous reports of ASPLT have mainly analyzed pathological findings with no analyses of imaging findings, especially those of MRI (4, 5, 10, 11, 13). In general, the T1 intensity on MRI is important for differentiating lipomatous tumors (16); therefore, we focused on the intensity of T1-weighted images (only CT was available in one case). Based on the results of three previous cases, the T1 intensity of ASPLT can be divided into three groups: (i) high (7), (ii) high and low (6), and (iii) low (8). ASPLT and SCL tend to have similar enhancement patterns on T1-weighted images, which reflect their similar pathological findings (19). In our case, MRI showed a low intensity on T1-weighted images (pattern iii) and a high intensity on STIR images, which is caused by fat tissue within the muscle. These imaging findings suggested MLS and intramuscular myxoma rather than ASPLT. The MRI findings of myxoma and MLS include hazy, nodular internal enhancement, the presence of fat, and the tumor size (20). Based on these features, the MRI findings in our case were consistent with MLS. For tumors with high T1 intensity, ALT/WDL should be considered, and for tumors with high and low T1 intensity, DDLS should be considered. When differentiating ASPLT from ALT/WDL and DDLS, diagnosis using only MRI is nearly impossible; therefore, histology, IHC, and FISH are required for a definite diagnosis.

This is the first case of ASPLT for which positron emission tomography-computed tomography was reported. However, we did

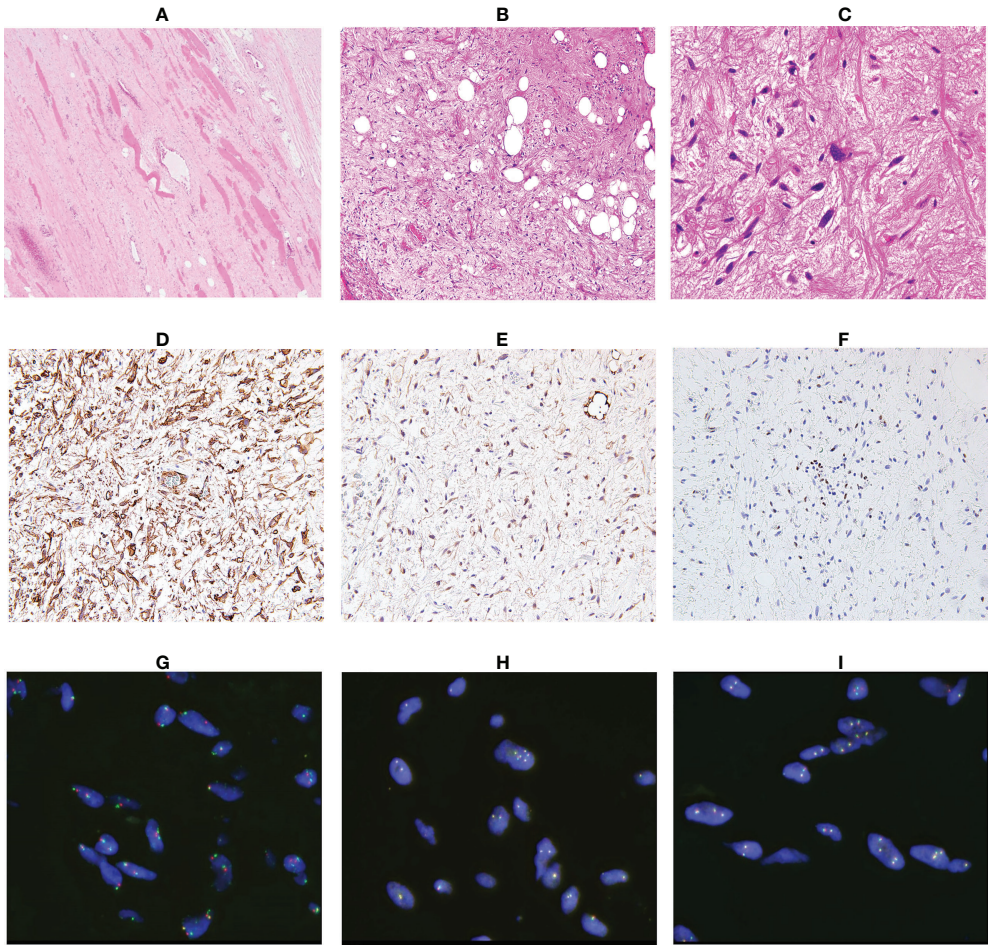

FIGURE 4
Analysis of the resected specimen. The resected specimen showed an ill-defined border (**A**, ×100) and a myxoid and fibrous lesion with spindle cells; some spindle cells had cytological atypia (**B**, ×100 **C**, ×200). Immunohistochemical results for CD34 **(D)**, S100 **(E)** and RB1 **(F)** (×200). Fluorescence *in situ* hybridization indicated no amplification of MDM2 **(G)** and no rearrangement of FUS **(H)** or EWSR1 **(I)**.

TABLE 1 Differential diagnosis of atypical spindle cell/pleomorphic lipomatous tumor.

	ASPLT	SCL	ALT/WDL	DDLS	PLS	MLS	Myxoma
Clinical							
Age (decade)	6th	5th to 6th	4th to 6th	5th to 6th	7th	4th to 5th	4th to 7th
Location	Superficial > deep	Superficial	deep	deep	deep	deep	deep
Size (mean or median)	5cm	<5cm	> 10cm	>10cm	8-10cm	8- 12cm	< 10 cm
Histology							
Atypical spindle cells	yes	no	possible	possible	possible	no	no
lipoblasts	common	rare	possible	possible	yes	rare	no
Immunohisto-Chemistry	Rb loss (50-70%)CD34 (60-70%)	Rb loss CD34	MDM2/CDK4	MDM2/CDK4	NA	NA	CD34S100(-)
Molecular features	*Rbl* deletion	*Rbl* deletion	*MDM2* amplification	*MDM2* amplification	NA	*FUS/EWSR1::DDIT3*	*GNAS* mutation

ASPLT, atypical spindle cell/pleomorphic lipomatous tumor; SCL, spindle cell lipoma; ALT/WDL, atypical lipomatous tumor/well differentiated liposarcoma; DDLS, dedifferentiated liposarcoma; PLS, pleomorphic liposarcoma; MLS, myxoid liposarcoma; RB, retinoblastoma; MDM2, mouse double minute 2 homolog; CDK4, cyclin dependent kinase 4. NA; not applicable.

not find PET-CT useful in differential diagnosis because the SUVmax and SUC were similar to those of myxoma and MLS (20).

Generally, precise preoperative diagnosis as either benign or malignant soft tissue tumor is important because wide resection is essential for malignant soft tissue tumors and, in addition, radiotherapy and chemotherapy are needed for some histological types. These are the reasons why we should differentiate MLS from myxoma and ASPLT. In our case, preoperative imaging findings suggested MLS rather than myxoma. Notably, wide resection is needed for MLS and ASPLT, while marginal resection is sufficient for myxoma. In addition, MLS has radiosensitivity, suggesting that preoperative radiotherapy for MLS is advantageous in reducing both tumor size and local recurrence. The preoperative diagnosis using needle biopsy was intramuscular myxoma; however, the presence of spindle cells with atypia could not be confirmed. We should consider ASPLT when myxoid tumors, including myxoid liposarcoma and myxoma, are suspected based on imaging findings and needle biopsy. Although the recurrence rate is 10–15% in ASPLT cases with incomplete resection, no cases of metastasis or dedifferentiation have been reported (2, 4). In contrast, MLS has a high recurrence rate of 60% with marginal resection and metastasis rate of 30–60% (17, 21). Considering the differences in clinical features between ASPLT and MLS and although additional surgery or radiotherapy was performed in case of MLS, we decided to conduct a follow-up of our ASPLT case using imaging studies. Follow-up is essential in cases like ours, and long-term follow-up is preferable because the interval of recurrence has been reported to be 6 months to 17 years (4).

Conclusion

Here, we present an atypical case of ASPLT and the difficulties in its differential diagnosis. Although the combination of imaging and pathological findings is essential for the precise diagnosis of soft tissue tumors, pathological findings are more advantageous than imaging findings for ASPLT because MRI findings are heterogeneous. If benign or malignant lipomatous tumors cannot be accurately diagnosed by histology, IHC and FISH should be performed. A wide resection is recommended; however, there will be some cases, such as our case, where preoperative diagnosis is inconclusive. Because ASPLT is a benign tumor that does not metastasize, careful, long-term follow-up may be more beneficial than additional surgery.

Data availability statement

The datasets presented in this study can be found in online repositories. The names of the repository/repositories and accession number(s) can be found in the article/supplementary material.

Ethics statement

Written informed consent was obtained from the individual(s) for the publication of any potentially identifiable images or data included in this article.

Author contributions

Conception/design: JI, TK, and HI. Provision of study material or patients: JI, NT, TA, and HH. Data collection and analysis: JI, TK, HI, and SK. Manuscript writing: JI, TK, and HI. All authors contributed to the article and approved the submitted version.

Acknowledgments

The authors thank Ms. Kahori Sano and Azusa Sakamoto for secretarial assistance.

Conflict of interest

The authors declare that the research was conducted in the absence of any commercial or financial relationships that could be construed as a potential conflict of interest.

Publisher's note

References

1. Dei Tos AP, Mentzel T, Newman PL, Fletcher CD. Spindle cell liposarcoma, a hitherto unrecognized variant of liposarcoma. Analysis of six cases. *Am J Surg Pathol* (1994) 18:913–21. doi: 10.1097/00000478-199409000-00006

2. Creytens D, Mariño-Enriquez AWHO Classification of Tumours Editorial Board. Atypical spindle cell/pleomorphic lipomatous tumor. In: *WHO classification of tumours*, *5th ed*. Lyon: IARC Press (2020). p. 334–5.

3. Lecoutere E, Creytens D. Atypical spindle cell/pleomorphic lipomatous tumor. *Histol Histopathol* (2020) 35:769–78. doi: 10.14670/HH-18-210

4. Mariño-Enriquez A, Nascimento AF, Ligon AH, Liang C, Fletcher CD. Atypical spindle cell lipomatous tumor: Clinicopathologic characterization of 232 cases demonstrating a morphologic spectrum. *Am J Surg Pathol* (2017) 41:234–44. doi: 10.1097/pas.0000000000000770

5. Bahadır B, Behzatoğlu K, Hacıhasanoğlu E, Koca SB, Sığırcı BB, Tokat F. Atypical spindle cell/pleomorphic lipomatous tumor: Clinicopathologic, immunohistochemical, and molecular study of 20 cases. *Pathol Int* (2018) 68:550–6. doi: 10.1111/pin.12719

6. Sugita S, Sugawara T, Emori M, Aoyama T, Hosaka M, Segawa K, et al. Atypical spindle cell/pleomorphic lipomatous tumor with a sarcomatous component showing high mitotic activity and ki-67 labeling index: Report of a unique case mimicking dedifferentiated liposarcoma. *Med Mol Morphol* (2022). doi: 10.1007/s00795-022-00327-8

7. Bae JM, Jung CY, Yun WS, Choi JH. Large Retroperitoneal atypical spindle cell lipomatous tumor, an extremely rare neoplasm: A case report. *World J Clin cases* (2022) 10:2584–90. doi: 10.12998/wjcc.v10.i8.2584

8. Wehrle CJ, Daigle JW, Ullah A, Sharma S, Ritter EF, Kruse EJ. Atypical spindle cell lipomatous lesion resected from patient with history of CLL. *Am Surg* (2020) 86:1208–11. doi: 10.1177/0003134820933601

9. Mentzel T, Palmedo G, Kuhnen C. Well-differentiated spindle cell liposarcoma (A'typical spindle cell lipomatous tumor') does not belong to the spectrum of atypical lipomatous tumor but has a close relationship to spindle cell lipoma: clinicopathologic, immunohistochemical, and molecular analysis of six cases. *Mod Pathol* (2010) 23:729–36. doi: 10.1038/modpathol.2010.66

10. Creytens D, Mentzel T, Ferdinande L, Lecoutere E, van Gorp J, Atanesyan L, et al. "Atypical" pleomorphic lipomatous tumor: A clinicopathologic, immunohistochemical and molecular study of 21 cases, emphasizing its relationship to atypical spindle cell lipomatous tumor and suggesting a morphologic spectrum (atypical spindle cell/pleomorphic lipomatous tumor). *Am J Surg Pathol* (2017) 41:1443–55. doi: 10.1097/PAS.0000000000000936

11. Creytens D, van Gorp J, Savola S, Ferdinande L, Mentzel T, Libbrecht L. Atypical spindle cell lipoma: A clinicopathologic, immunohistochemical, and molecular study emphasizing its relationship to classical spindle cell lipoma. *Virchows Arch* (2014) 465:97–108. doi: 10.1007/s00428-014-1568-8

12. Ichikawa J, Kawasaki T, Imada H, Enomoto A, Taniguchi N, Tatsuno R, et al. Spindle cell lipoma with ossification mimicking atypical lipomatous tumor/well-differentiated liposarcoma: a case report. *Int J Surg Pathol* (2022) 30:413–8. doi: 10.1177/10668969211055798

13. Anderson WJ, Fletcher CDM, Jo VY. Atypical pleomorphic lipomatous tumor: expanding our current understanding in a clinicopathologic analysis of 64 cases. *Am J Surg Pathol* (2021) 45:1282–92. doi: 10.1097/PAS.0000000000001706

14. Chen S, Huang H, He S, Wang W, Zhao R, Li L, et al. Spindle cell lipoma: clinicopathologic characterization of 40 cases. *Int J Clin Exp Pathol* (2019) 12:2613–21.

15. Anderson WJ, Jo VY. Pleomorphic liposarcoma: updates and current differential diagnosis. *Semin Diagn Pathol* (2019) 36:122–8. doi: 10.1053/j.semdp.2019.02.007

16. Teniola O, Wang KY, Wang WL, Tseng WW, Amini B. Imaging of liposarcomas for clinicians: characteristic features and differential considerations. *J Surg Oncol* (2018) 117:1195–203. doi: 10.1002/jso.24949

17. Thway KWHO Classification of Tumours Editorial Board. Myxoid liposarcoma. In: *WHO classification of tumours*, *5th ed*. Lyon: IARC Press (2020). p. 42–4.

18. Liegl-Atzwanger BHP, Nielsen GPWHO Classification of Tumours Editorial Board. Intramuscular myxoma. In: *WHO classification of tumours*, *5th ed*. Lyon: IARC Press (2020). p. 261–3.

19. Jelinek JS, Wu A, Wallace M, Kumar D, Henshaw RM, Murphey MJ, et al. Imaging of spindle cell lipoma. *Clin Radiol* (2020) 75:396.e15–e21. doi: 10.1016/j.crad.2019.11.020

20. Lunn BW, Littrell LA, Wenger DE, Broski SM. 18F-FDG PET/CT and MRI features of myxoid liposarcomas and intramuscular myxomas. *Skeletal Radiol* (2018) 47:1641–50. doi: 10.1007/s00256-018-3000-y

21. Tfayli Y, Baydoun A, Naja AS, Saghieh S. Management of myxoid liposarcoma of the extremity. *Rev Oncol Lett* (2021) 22:596. doi: 10.3892/ol.2021.12857

frontiers | Frontiers in Oncology

TYPE Original Research
PUBLISHED 24 November 2022
DOI 10.3389/fonc.2022.980059

OPEN ACCESS

EDITED BY
Dengfeng Cao,
Washington University in St. Louis,
United States

REVIEWED BY
Fuyou Guo,
First Affiliated Hospital of Zhengzhou University, China
Renu Madan,
Post Graduate Institute of Medical Education and Research (PGIMER), India

*CORRESPONDENCE
Qiu Rao
raoqiu1103@126.com
Nan Wu
55152572@163.com

SPECIALTY SECTION
This article was submitted to Surgical Oncology, a section of the journal Frontiers in Oncology

RECEIVED 28 June 2022
ACCEPTED 04 November 2022
PUBLISHED 24 November 2022

CITATION
Pan R, Wang X, Fang R, Xia Q, Wu N and Rao Q (2022) Epithelioid glioblastoma exhibits a heterogeneous molecular feature: A targeted next-generation sequencing study. *Front. Oncol.* 12:980059. doi: 10.3389/fonc.2022.980059

Epithelioid glioblastoma exhibits a heterogeneous molecular feature: A targeted next-generation sequencing study

Rui Pan, Xiaotong Wang, Ru Fang, Qiuyuan Xia, Nan Wu* and Qiu Rao*

Department of Pathology, Affiliated Jinling Hospital, Medical School of Nanjing University, Nanjing, China

Introduction: Epithelioid glioblastoma (eGBM) is one of the rare glioblastoma (GBM) variants in the current World Health Organization (WHO) categorization of central nervous system (CNS) tumours. However, the diagnostic basis and molecular features of eGBM have not been clearly defined to date. In this study, we aimed to molecularly characterize these tumours.

Methods: The clinicopathological, molecular, and immunohistochemical characteristics of 12 cases of eGBM were investigated.

Results: The tumours were found to be made up of epithelioid and rhabdoid cells when examined under a microscope. Six cases (50%) harboured the BRAF V600E mutation, and NF1 mutation was detected in 2 eGBM cases (16.7%). CDKN2A/B homozygous deletion was seen in 5 cases (41.7%). TP53 mutation was recognized in 2 instances (16.7%), and TERT promoter mutation was recognized in 5 cases (41.7%).

Discussion: eGBM is characterized by high molecular heterogeneity and has molecular overlaps between low-grade gliomas. Moreover, rather than being a variant or entity, the biological significance of the "epithelioid" appearance may be reduced to a simply morphological pattern. In order to target the proper treatment to suitable patients, molecular stratification via genome-wide molecular profiling will be crucial.

KEYWORDS

glioblastoma, epithelioid glioblastoma, BRAF V600E, molecular genetics, central nervous system tumour

Introduction

GBM is the extremely frequent and aggressive tumour of the human brain. Epithelioid glioblastoma (eGBM) is the rare type of GBM variables in the 2021 WHO CNS tumours classification. This entity is mostly made up of epithelioid cells with abundant cytoplasm, eccentrically placed nuclei, and prominent nucleoli (1). Due to the

lack of particular immunohistochemical or molecular markers for eGBM, diagnosis can be difficult. The *BRAF V600E* mutation has been identified in eGBMs at a relatively great frequency, despite being rare in conventional GBM (54%) (2–5). Moreover, low-grade glioma components in eGBM were reported in recent studies, and a few eGBM patients were previously diagnosed with pleomorphic xanthoastrocytoma (PXA) (6–9). Therefore, several studies have suggested that eGBM and PXA may be either the same entity or closely related (6, 10–13).

eGBM is commonly considered more devastating than classical GBM and has a higher molecular heterogeneity (12, 14). Nevertheless, the clinical features, pathological results and molecular characteristics of eGBM are still poorly understood. Moreover, the diagnostic basis and molecular features of eGBM have not been clearly defined to date. Wide panels of molecular and immunohistochemical markers are required to achieve the correct diagnosis. We described the clinicopathological and molecular characteristics of 12 eGBMs and discussed their molecular genetic features.

Methods

Data collection

The Institute Research Ethics Committee of Jinling Hospital approved this study. Slides from glioblastomas were retrieved from 2014 to 2022 surgical pathology files of the authors' institution (Affiliated Jinling Hospital, Medical School of Nanjing University) and were involved in the study if they were diagnosed as eGBM on the basis of characteristic morphological and molecular features. Two pathologists performed a blinded review of the pathological materials according to the pathological and molecular definition of eGBM in the 2021 WHO categorization of CNS tumours. Thirteen GBM cases were consistent with epithelioid morphology. Case 13 was eliminated from the series because of the involvement of an *IDH1* mutation. In total, 12 eGBMs were gathered in this study. The clinical, radiological and pathological data were obtained from the Department of Pathology, Affiliated Jingling Hospital, Medical School of Nanjing University. Reviewing electronic health records and attempting to contact referring pathologists and clinicians yielded clinical and demographic follow-up information.

Immunohistochemistry

Tumour tissues were embedded in paraffin after being fixed in 10% formalin. Sections were cut out at 3 µm thickness and immunohistochemically stained with conventional antibodies as well as several available commercially antibodies against gene expression targets identified throughout the gene expression analysis. The following proteins were chosen as targets: GFAP (MAB-0764, 1:150, Maixin Bio (MXB)), INI1 (ZA-0696, ready-to-use, Zhongshan (ZSGB)), IDH1 (ZM-0447, ready-to-use, ZSGB), BRAF V600E (790-5095, ready-to-use, Roche), CKpan (kit-0004, 1:200, MXB), ATRX (MAB-0855, ready-to-use, MXB), EMA(ZM-0095, ready-to-use, ZSGB) and TP53 (ZM-0408, 1:200, ZSGB).

TP53 immunostaining was identified as a missense mutation when higher than 10% nuclear positivity was exist (15). Immunostaining was defined as a frameshift when tumour cells demonstrated a full absence of nuclear staining, and intrinsic control cells showed focal nuclear staining (16, 17). Both missense and frameshift mutations were considered TP53 mutants (15, 16). Internal negative or positive controls, including endothelial cells and/or trapped cortical neurons, were identified in all immunostainings.

Targeted next-generation sequencing

Sequencing of a 425-gene panel was performed on the cases (Supplementary Table S1). Nucleic acid isolation for NGS was performed on formalin-fixed paraffin-embedded (FFPE) tumour tissue from a microdissected representative block. Following the generator's instructions, five 10 µm tumour slices were utilized for DNA extraction utilizing the QIAamp DNA FFPE Kit (QIAGEN, Valencia, CA, USA). The quality of the DNA was determined using spectrophotometry with absorbance at 230, 260, and 280 nm, and the DNA was measured using Qubit 2.0. Sequencing libraries were created utilizing the KAPA Hyper Prep Kit (KAPA Biosystems) based on the manufacturer's recommendations for various specimen types.

In summary, end repair, A-tailing, and ligation with indexed adapters were applied to 1 g of fragmented genomic DNA prior to size selection with Agencourt AMPure XP beads (Beckman Coulter). For hybridization-based target enrichment, the GeneseeqOneTM pan cancer gene panel (425 cancer-relevant genes, Geneseeq Technology Inc.) and the xGen Lockdown Hybridization and Wash Reagents Kit were utilized (Integrated DNA Technologies). Libraries captured by Dynabeads M-270 (Life Technologies) were amplified in KAPA HiFi HotStart ReadyMix (KAPA Biosystems), and their quantities were assessed by qPCR through KAPA Library Quantification Kit (KAPA Biosystems). On the Illumina HiSeq4000 platform, target-enriched libraries were sequenced with 2×150 bp paired-end reads. The Burrows-Wheeler Aligner was applied to match the sequencing dataset to the reference hg19 genome (Human Genome version 19). Sequencing data collected were demultiplexed by bcl2fastq (v2.19), analysed by Trimmomatic (18) to eliminate low-quality (quality <15) or N bases, and afterwards aligned to the reference hg19 genome (19). By using Picard (found at https://broadinstitute.github.io/picard/), PCR duplicates were eliminated. For base quality assurance and local realignments around indels, the Genome

Analysis Toolkit (GATK) was used (20).SNPs and indels were identified by VarScan2 (21) and Haplotype Caller/Unified Genotyper in GATK, with a mutant allele frequency (MAF) cut-off of 0.5% for tissue cases and a least of three optimal mutant reads. Frequent variants were eliminated utilizing dbSNP and the 1000 Genome Project. An internal list of repeated sequencing errors generated from more than 10000 normal control cases sequenced on the same platform was used to further filter the resulting somatic variants. FACTERA identified gene fusions (22), and copy number variations (CNVs) were measured with ADTEx (23). For tissue samples, the log2 ratio cut-off for copy number gain was given as 2.0. All specimen types were used to detect copy number loss using a log2 ratio cut-off of 0.67. The thresholds were established from the absolute CNVs found by droplet digital PCR, which was used for earlier assay validation (ddPCR). FACETS (24) was used to estimate allele-specific CNVs with a 0.2 drift cut-off for unstable joint segments. By splitting the size of drifted segments by the overall segment size, the chromosomal instability's percentage (CIN) was recorded.

Results

Clinical data

The clinical and histopathological data of eGBMs were tabulated and are presented in Table 1. There were 9 female and 3 male cases with ages varying from 28 to 70 years. The frontal lobe involving was 3, the temporal lobe involving was 5, the parietal lobe involving was 2, and the basal ganglia was 2. The most common symptoms were headaches and seizures. Radiological examination demonstrated gadolinium-enhancing, comparatively circumscribed lesions with significant perilesional oedema and central necrosis in all cases (Figure 1). In 1 case, there was a midline shift (8.33%). All patients had gross total resection. After surgery, 7 patients (58.3%) received radiation or chemotherapy. One patient received targeted therapy (case 12), and have not demonstrated tumour recurrence or metastatic disease to date. The follow-up period varied from 1 to 30 months. One patient was lost to followed-up. At the time of data cut-off, 4 cases developed local recurrences, and succumbed to complications (case 4, case 5, case 6 and case 7). One case developed a pulmonary metastasis (case 2). No radiological or histological evidence of cerebrospinal fluid dissemination was found.

Histopathological findings

The histological results are presented in Table 1 and Figure 2. The main notable features of most eGBMs were abundant epithelioid cells and extensive necrosis (Figure 2). In all 12 cases analyzed, microscopy revealed eGBM histopathological types (or melanoma or epithelioid-like cells' sheets with abundant cytoplasm, eccentric nuclei, and loose cohesion). All tumours showed signs of microvascular proliferation, brisk mitotic activity, and necrosis. However, 4 cases had focal areas that resembled PXA (WHO grade 2) appearance (the set of spindled cells forming fascicles, single large bizarre cells, and vacuolated tumour cells with perivascular lymphocytic cuffing).

Immunohistochemistry

The immunohistochemistry outcomes are presented in Table 2 and Figure 3. eGBM showed diffuse and strong staining with vimentin. GFAP (glial fibrillary acidic protein) immunoreactivity was diffusely observed in epithelioid cells and lower-grade glioma cells. eGBMs did not show cytokeratin (CK) or epithelial membrane antigen (EMA) staining. The SMARCB1 (INI1) staining was universally intact. Mutant TP53 was observed in 2 cases, and both cases were frameshift mutations. The ATRX loss expression was not observed in any case. IDH1 expression was also not observed in any case. BRAF V600E expression occurred in 50% (6/12) of cases.

Genetic analysis

The findings of genetic analysis are outlined in Figure 4 and Supplementary Table S2. Six cases (50%) harboured the *BRAF V600E* mutation, and *CDKN2A/B* homozygous deletion was seen in 5 cases (41.7%). *TP53* mutation was detected in 2 cases (16.7%), and *TERT* promoter mutation was detected in 5 cases (41.7%). *PTEN* deletion was detected in 2 cases (16.7%). Two of 6 cases without *BRAF V600E* mutation showed *NF1* mutation. *IDH* and *H3 K27M* mutations were not found in any cases. In conclusion, eGBMs are complex and heterogeneous tumours, exhibiting multiple genetic mutations.

Discussion

Epithelioid glioblastoma is a rare and extremely aggressive variant of GBM. Kepes et al. first characterized it in 1982, and it was suggested as a histological subtype in the WHO classification of CNS tumours in 2021 (25, 26). However, the radiological, histological and molecular signature of eGBM have not been clearly defined (10, 27). In this study, we applied combined NGS, histology, radiology and immunohistochemistry to describe the clinicopathological and molecular characterization of eGBM.

TABLE 1 Summary of the clinical parameters of 12 eGBM patients.

Case	1	2	3	4	5	6	7	8	9	10	11	12
Age/Sex	F*/58	F/59	F/51	M*/53	F/61	F/69	M/30	F/42	M/55	F/62	F/70	M/28
Location	Right Parietal lobe	Right Temporal lobe	Left Frontal lobe	Left Frontal lobe	Right Temporal lobe	Left Frontal lobe	Left Temporal lobe	Right Temporoparietal	Bilateral Frontal lobe	Right Basal ganglia	Left Basal ganglia	Right Parietal lobe
Symptoms	Myodynamia weakness	Headache	Headache	Slurred speech	Headache	Headache, slurred speech	Headache, seizures	Seizures	Headache, memory loss	Limited limb mobility	Headache, slurred speech	Headache, seizures
Follow up in months	24 (Alive)	30 (Alive)	(Lost to follow-up)	12 (Dead)	15 (Dead)	10 (Dead)	1 (Dead)	8 (Alive)	16 (Alive)	12 (Alive)	18 (Alive)	28 (Alive)
Resection type	GTR*	GTR	GTR	GTR	GTR	GTR	GTR	GTR	GTR	GTR	GTR	GTR
Chemotherapy/ radiation therapy	Radiation therapy	Radiation therapy	(Lost to follow-up)	Radiation therapy	Radiation therapy	None	None	None	Chemotherapy	None	Chemotherapy	Radiation therapy, Chemotherapy
Microvascular proliferation	Present	Present	Present	Present	Present	Present	Present	Present	Present	Present	Present	Present
Epithelioid cells	≥30%	≥30%	≥30%	≥30%	≥30%	≥30%	≥30%	≥20%	≥20%	≥20%	≥20%	≥30%
Necrosis	Confluent	Confluent	Confluent	Confluent	Confluent	Confluent	Confluent	Confluent	Confluent	Confluent	Confluent	Confluent
Recurrence	None	None	None	Recurrence	Recurrence	Recurrence	Recurrence	None	None	None	None	None
Metastasis	None	Pulmonary	None	None	None	None	None	None	None	None	None	None
Cerebrospinal fluid dissemination	None	None	None	None	None	None	None	None	None	None	None	None

*GTR, gross total resection; F, female; M, male.

10.3389/fonc.2022.980059

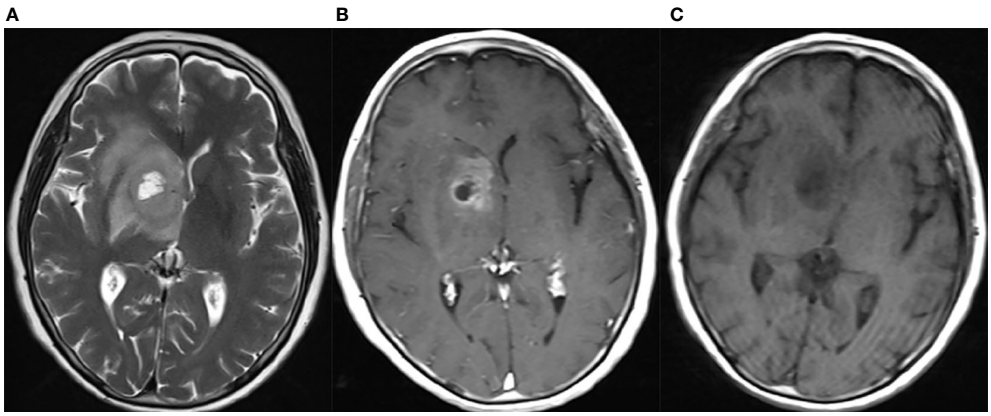

FIGURE 1
Neuroradiological findings for eGBM case 11. Neuroradiological results for eGBM case 11. **(A)** A heterogeneous lesion with necrosis and perilesional oedema on T1 in the right basal ganglia with significant midline shift, 23 mm × 28 mm × 17 mm in size. **(B)** A heterogeneous lesion with perilesional oedema (T2). **(C)** A rim-enhancing mass with perilesional oedema (T1-weighted enhanced).

Histologically, eGBMs are dominated by a population of epithelioid cells with focal discohension, eosinophilic cytoplasm, a differentiated cell membrane, and a nucleus placed laterally. The tumour is richly vascularized, involving thick- and thin-walled vessels with microvascular proliferation and hyaline degeneration, and also glomerulus-like vasculature. Extensive palisading necrosis has also been observed in eGBM. Although the exact aetiology and origin of epithelioid cells are unidentified, there have been numerous studies of eGBMs occurring concurrently with PXA, particularly tumours with anaplastic transformation and epithelioid characteristics, or occurring years after initial tumour resection (5, 10). Four eGBM cases in our series also presented PXA-like (WHO grade 2) morphological characteristics focally. PXA-like components (WHO grade 2) coexisting with eGBM demonstrated a spindle-shaped cells with some mono- or multinucleated pleomorphic cells (Figure 2). Intercellular reticlin meshwork and perivascular lymphocytic cuffing were noticed. Although eGBM is commonly considered to be a primary/*de novo* lesion, numerous cases of eGBM with a pre- or coexisting lower-grade component have been noted (2, 4, 6, 9, 13, 28). The majority of the lower-grade lesions identified thus far were PXA (WHO grade 2), and a few were low-grade diffuse glioma-like lesions (6–9). We speculate that these unique pathological features may be associated with the molecular heterogeneity.

Consistent with those reported in the literature, half of the eGBMs (50%) in our series were involved in the *BRAF V600E* mutation. *NF1* mutation was detected in 2 eGBM cases (16.7%). The *NF1* mutation was mutually exclusive to the *BRAF V600E* mutation. The codon 600 mutation (V600E) is the main mutation site for the *BRAF* gene, which is located on chromosome 7q34. *BRAF* is the gene that encodes cytoplasmic serine-threonine kinase. Subsequent activation of the mitogen-activated protein kinase (MAPK) signaling pathway occurs through the mutated BRAF protein, which in turn promotes tumourigenesis, cellular proliferation, as well as resistance to apoptosis (3, 14). The *NF1* gene is located on 17q11.2 and encodes a tumour suppressor that works as a GTPase-activating protein to deactivate the RAS/MAPK signalling pathway, finally causing the occurrence of tumours (29, 30). Hence, both *NF1* mutations and *BRAF V600E* mutations contribute to the constitutive stimulation of downstream RAS/MAPK signalling pathways (31–33), which may be associated with unique pathological features similar to eGBM and PXA (30, 34). Several studies have reported that part of *wt-IDH* glioblastomas with *NF1* mutation also presented a xanthomatous histological appearance (34, 35). Consequently, in addition to *BRAF V600E*, *NF1* mutation may be another meaningful biomarker for the diagnosis of eGBMs. However, the proportion of *NF1* mutation in *BRAF V600E* negative eGBMs demands further investigation.

The work of Korshunov et al. has also illustrated the molecular heterogeneity of eGBM (11) (Table 3). They identified three distinct, previously described subtypes of tumours by combining data from methylation types, copy number alterations, as well as mutations analysis with outcomes from clinical trials. According to the authors, histopathologically defined eGBM is divided into at least 3 molecularly and biologically distinguishable classifications. Consequently, the outcome that eGBM molecularly shares overlaps with other subtypes of glioblastoma may reduce their epithelioid appearance to a morphological pattern, and decrease the biological significance of it.

Molecularly, in this series, *TERT* promoter mutation was detected in 41.7% (5/12) of cases. *CDKN2A/B* homozygous

10.3389/fonc.2022.980059

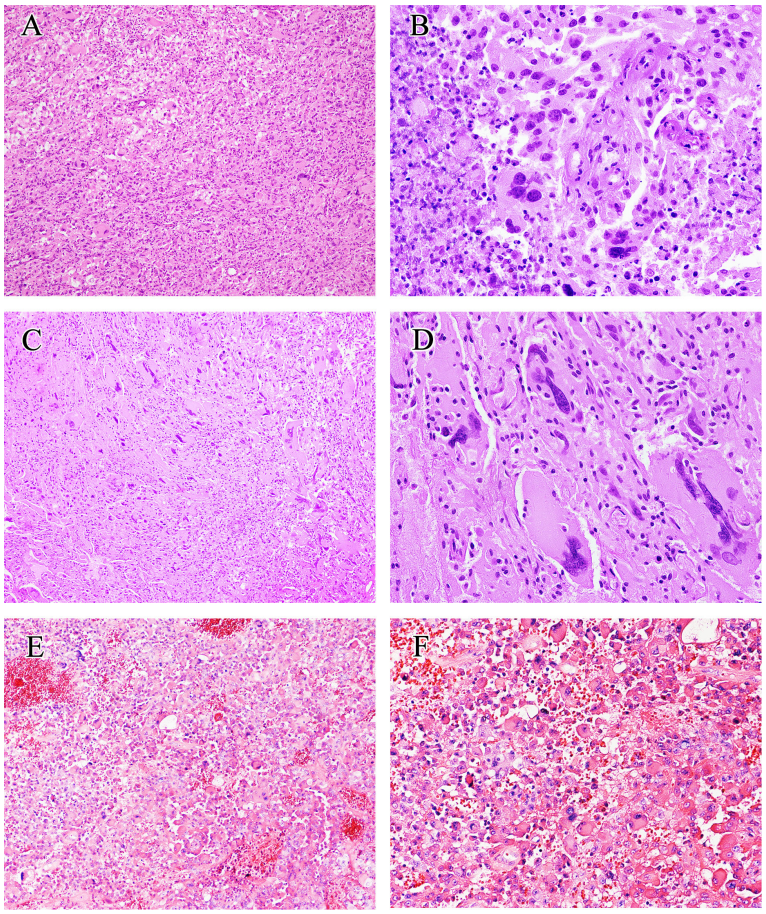

FIGURE 2
Histological findings of eGBM. **(A)** Patches of epithelioid and rhabdoid cells were presented (×200). **(B)** The tumour showed microvascular proliferation and zonal necrosis, and epithelioid and rhabdoid cells constituted abundant and uniformly eosinophilic cytoplasm and laterally located oval to pleomorphically shaped nuclei. Mitoses could easily be seen (×400). (**C, D**) PXA-like components in eGBM cases showed multinucleated pleomorphic cells, a fascicular arrangement of spindle-shaped cells and single large bizarre cells (×200 and ×400). **(E, F)** Histopathological findings of case 13 (*IDH*-mutant astrocytoma). The tumour presented epithelioid morphology (×200 and ×400).

TABLE 2 Immunohistochemistry of 12 eGBM cases.

	1	2	3	4	5	6	7	9	10	11	12	13
GFAP*	3+	2+	2+	3+	3+	3+	3+	1+	3+	2+	3+	3+
S-100	3+	3+	–	1+	3+	2+	3+	3+	3+	2+	2+	2+
ATRX	3+	3+	3+	3+	3+	3+	3+	3+	3+	3+	3+	3+
BRAF V600E	–	–	–	–	3+	–	2+	1+	–	–	3+	3+
INI-1*	Intact	Intact	Intact	Intact	Intact	Intact	Intact	Intact	Intact	Intact	Intact	Intact
IDH1	–	–	–	–	–	–	–	–	–	–	–	–
TP53	–	–	Mutated	–	–	–	–	–	–	–	Mutated	–
CK*	–	–	–	–	–	–	–	–	–	–	–	–

*GFAP, glial fibrillary acidic protein; CK, cytokeratini; EMA, epithelial membrane antigen; INI1, SMARCB1.

deletion was seen in 41.7% of cases and *TP53* mutation was detected in 16.7% of cases. A total of 16.7% of cases were confirmed to have *PTEN* deletion (Figure 4). Some reports documented the *TERT* promoter mutation in GBMs, suggesting its role in the aggressive clinical course (4, 36). *TERT* promoter mutation is a poor prognostic indicator in *wt-IDH* gliomas. Moreover, the exitance of *pTERT* mutation partially clarifies the aggressive nature of GBMs, and its

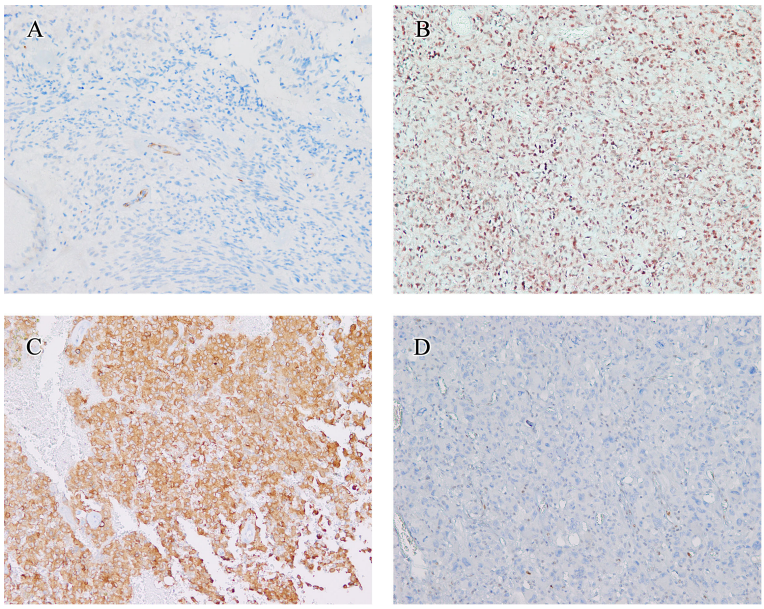

FIGURE 3
Immunohistochemical findings. The immunohistochemical findings of eGBMs. **(A)** Immunohistochemical studies showed negtive PTEN expression in 2 cases. Vascular endothelial cells provided an internal positive control (×200). **(B)** INI1 staining was universally intact (×200). **(C)** Positive expression of BRAF V600E in eGBM (×200). **(D)** The tumour cells demonstrated a complete absence of TP53 staining and lymphocytes showed TP53 nuclear staining focally (×200).

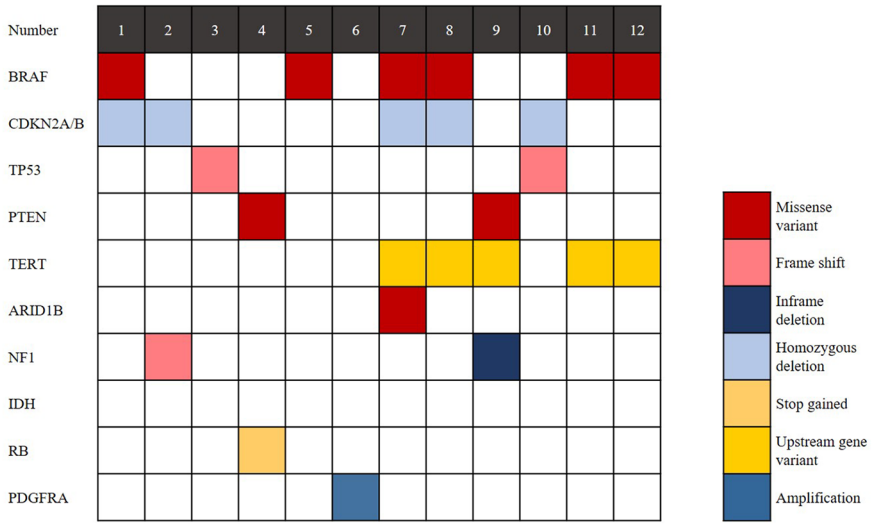

FIGURE 4
Genomic landscape of eGBM. Clinical and genomic features of 12 eGBM cases. In addition to *BRAF V600E* mutation, eGBM also showed *TP53* mutation, *CDKN2A/B* homozygous deletions and *NF1* mutation.

correlation with the tumour's ability to overcome escape apoptosis and replicative senescence (the fundamental steps in tumourigenesis). *CDKN2A* is a tumour suppressor gene located on chromosome 9p21. It encodes the p16 protein, a negative regulator of cell cycle progression. The *CDKN2B* gene is located next to *CDKN2A*. The mutation to either *CDKN2A* or *CDKN2B* will lead to cellular proliferation and the disruption of proapoptotic pathways (37). In *IDH*-mutated gliomas,

TABLE 3 Review of previous studies including mutational analysis.

Author/ year	No. of cases	Age/ Sex	Necrosis (% of cases)	Follow up in months	MVP* (% of cases)	IDH1	CDKN2A/ B	PTEN	Braf V600E	TP53	TERT	NF
Kahanna et al., 2018	7	13~50/ M-3 F-4	100%	3~6	28%	None	Not Done	None	28%	Not Done	40%	Not Done
Kleinschmidt et al., 2013	13	10~69/ M-9 F-4	92%	5~82	7%	9%	Not Done	Deletion (33%) Monosomy (33%) Negative (33%)	54%	33%	Not Done	Not Done
Alexandrescu et al., 2015	11	2~79/M-9 F-2	93%	2~38	87%	None	Not Done	Deletion (12%) Monosomy (12%)	53%	36% (IHC)	Not Done	36% (IHC)
Korshunov et al., 2020	64	3~67/M-45 F-19	100%	5~72	Not Applicable	None	55%	Not Done	56%	Not Done	38%	Not Done
Ying et al., 2020	15	18~77/ M-12 F-3	100%	One week~32	Not Applicable	None	Not Done	Not Done	47%	47% (IHC)	Not Done	Not Done
Debajyoti et al., 2020		3~54/M-12 F-12	96%	5~38	100%	None (IHC)	Not Done	Not Done	52% (IHC)	Not Done	Not Done	Not Done
Our Present study	12	28~70/ M-4 F-8	100%	1~30	100%	None	42%	Deletion (17%)	50%	17%	42%	17%

*MVP, microvascular proliferation.

CDKN2A homozygous deletion is a strong adverse prognostic factor (38). *PTEN* is located on 10q23.3 and consists of 9 exons. *PTEN* deletion has been proven to correlate with poor survival in glioblastoma, suggesting that *PTEN* plays a role in patient outcomes (39). In this study, most cases (83.3%, 10/12) showed at least 1 mutation mentioned above, which has been detected frequently in gliomas and associated with poor prognosis. Even though, the prognosis of patients are quite different (Table 1), which further illustrates the clinical heterogeneity of eGBM.

Interestingly, case 13 in our study, which exhibited an epithelioid morphology (Figure 2), had both the *BRAF V600E* mutation and an *IDH1* mutation. Consistent with the reports of *IDH*-mutated glioblastomas, this patient had a relatively long overall survival of up to 30 months. In consequence, this case should be diagnosed as *IDH*-mutant astrocytoma (WHO grade 4). Accordingly, when high-grade gliomas present epithelioid morphology, the diagnosis of eGBM may not be necessary. Another study also reported that *K3 K27M*-altered gliomas exhibited an epithelioid appearance (10).

In summary, we studied 12 eGBM cases and further described the clinicopathological and molecular features of the tumours. Our study indicates clinical and molecular heterogeneity among eGBMs. We propose that in addition to *BRAF V600E*, *NF1* mutation may be another meaningful biomarker for the diagnosis of eGBMs. Instead of being a variant or entity, the "epithelioid" GBM phenotype might be a histologic subtype. In order to target the proper treatment to suitable patients, molecular stratification *via* genome-wide molecular profiling will be crucial in the upcoming years.

Data availability statement

The datasets presented in this study can be found in online repositories. The names of the repository/repositories and accession number(s) can be found below: Dryad, doi: 10.5061/dryad.2280gb5w0.

Ethics statement

Approval for this study was granted by the Institute Research Ethics Committee of Jinling Hospital.

Author contributions

RP: Methodology, Formal analysis, Data curation, Writing-Original draft preparation. XW: Conceptualization, Formal analysis. RF: Data curation, Visualization. QX: Conceptualization. NW: Conceptualization, Project administration. QR: Conceptualization, Methodology, Project administration. All authors contributed to the article and approved the submitted version.

Funding

This work was supported by grants from the National Natural Science Foundation of China (81802557 to QX and 81872095 to QR).

Conflict of interest

The authors declare that the research was conducted in the absence of any commercial or financial relationships that could be construed as a potential conflict of interest.

Publisher's note

All claims expressed in this article are solely those of the authors and do not necessarily represent those of their affiliated organizations, or those of the publisher, the editors and the reviewers. Any product that may be evaluated in this article, or claim that may be made by its manufacturer, is not guaranteed or endorsed by the publisher.

Supplementary material

The Supplementary Material for this article can be found online at: https://www.frontiersin.org/articles/10.3389/fonc.2022.980059/full#supplementary-material

References

1. Louis DN, Ohgaki H, Wiestler DO, Cavenee WK. *WHO classification of tumours of the central nervous system. 4th ed*. Revised Lyon: International Agency for Research on Cancer (2016) 33(6):710–1. doi: 10.1111/j.1365-2990.2007.00905.x

2. Kleinschmidt-Demasters BK, Aisner DL, Birks DK, Foreman NK. Epithelioid GBMs show a high percentage of BRAF V600E mutation. *Am J Surg Pathol* (2013) 37:685–98. doi: 10.1097/PAS.0b013e31827f9c5e

3. Kleinschmidt-DeMasters BK, Aisner DL, Foreman NK. BRAF VE1 immunoreactivity patterns in epithelioid glioblastomas positive for BRAF V600E mutation. *Am J Surg Pathol* (2015) 39:528–40. doi: 10.1097/PAS.0000000000000363

4. Matsumura N, Nakajima N, Yamazaki T, Nagano T, Kagoshima K, Nobusawa S, et al. Concurrent TERT promoter and BRAF V600E mutation in epithelioid glioblastoma and concomitant low-grade astrocytoma. *Neuropathology* (2017) 37:58–63. doi: 10.1111/neup.12318

5. Tanaka S, Nakada M, Nobusawa S, Suzuki SO, Sabit H, Miyashita K, et al. Epithelioid glioblastoma arising from pleomorphic xanthoastrocytoma with the BRAF V600E mutation. *Brain Tumour Pathol* (2014) 31:172–6. doi: 10.1007/s10014-014-0192-2

6. Kuroda J, Nobusawa S, Nakamura H, Yokoo H, Ueda R, Makino K, et al. A case of an epithelioid glioblastoma with the BRAF V600E mutation colocalized with BRAF intact low-grade diffuse astrocytoma. *Neuropathology* (2016) 36:181–6. doi: 10.1111/neup.12258

7. Wang J, Liu Z, Cui Y, Liu Y, Fang J, Xu L, et al. Evaluation of EZH2 expression, BRAF V600E mutation, and CDKN2A/B deletions in epithelioid glioblastoma and anaplastic pleomorphic xanthoastrocytoma. *J Neurooncol* (2019) 144:137–46. doi: 10.1007/s11060-019-03212-0

8. Vaubel R, Zschernack V, Tran QT, Jenkins S, Caron A, Milosevic D, et al. Biology and grading of pleomorphic xanthoastrocytoma-what have we learned about it? *Brain Pathol* (2021) 31:20–32. doi: 10.1111/bpa.12874

9. Funata N, Nobusawa S, Yamada R, Shinoura N. A case of osteoclast-like giant cell-rich epithelioid glioblastoma with BRAF V600E mutation. *Brain Tumour Pathol* (2016) 33:57–62. doi: 10.1007/s10014-015-0239-z

10. Alexandrescu S, Korshunov A, Lai SH, Dabiri S, Patil S, Li R, et al. Epithelioid glioblastomas and anaplastic epithelioid pleomorphic xanthoastrocytomas–same entity or first cousins? *Brain Pathol* (2016) 26:215–23. doi: 10.1111/bpa.12295

11. Korshunov A, Chavez L, Sharma T, Ryzhova M, Schrimpf D, Stichel D, et al. Epithelioid glioblastomas stratify into established diagnostic subsets upon integrated molecular analysis. *Brain Pathol* (2017) 28(5):656–62. doi: 10.1111/bpa.12566

12. Nobusawa S, Hirato J, Kurihara H, Ogawa A, Okura N, Nagaishi M, et al. Intratumoural heterogeneity of genomic imbalance in a case of epithelioid glioblastoma with BRAF V600E mutation. *Brain Pathol* (2014) 24:239–46. doi: 10.1111/bpa.12114

13. Vaubel RA, Caron AA, Yamada S, Decker PA, Eckel Passow JE, Rodriguez FJ, et al. Recurrent copy number alterations in low-grade and anaplastic pleomorphic xanthoastrocytoma with and without BRAF V600E mutation. *Brain Pathol* (2018) 28:172–82. doi: 10.1111/bpa.12495

14. Nakajima N, Nobusawa S, Nakata S, Nakada M, Yamazaki T, Matsumura N, et al. BRAF V600E, TERT promoter mutations and CDKN2A/B homozygous deletions are frequent in epithelioid glioblastomas: a histological and molecular analysis focusing on intratumoural heterogeneity. *Brain Pathol* (2018) 28:663–73. doi: 10.1111/bpa.12572

15. Takami H, Yoshida A, Fukushima S, Arita H, Matsushita Y, Nakamura T, et al. Revisiting TP53 mutations and immunohistochemistry–a comparative study in 157 diffuse gliomas. *Brain Pathol* (2015) 25:256–65. doi: 10.1111/bpa.12173

16. Köbel M, Piskorz AM, Lee S, Lui S, LePage C, Marass F, et al. Optimized p53 immunohistochemistry is an accurate predictor of mutation in ovarian carcinoma. *J Pathol Clin Res* (2016) 2:247–58. doi: 10.1002/cjp2.53

17. Köbel M, Ronnett BM, Singh N, Soslow RA, Gilks CB, McCluggage WG. Interpretation of P53 immunohistochemistry in endometrial carcinomas: Toward increased reproducibility. *Int J Gynecol Pathol* (2019) 38 Suppl 1:S123–31. doi: 10.1097/PGP.0000000000000488

18. Bolger AM, Lohse M, Usadel B. Trimmomatic: A flexible trimmer for illumina sequence data. *Bioinformatics* (2014) 30:2114–20. doi: 10.1093/bioinformatics/btu170

19. Li H, Durbin R. Fast and accurate short read alignment with burrows-wheeler transform. *Bioinformatics* (2009) 25:1754–60. doi: 10.1093/bioinformatics/btp324

20. DePristo MA, Banks E, Poplin R, Garimella KV, Maguire JR, Hartl C, et al. A framework for variation discovery and genotyping using next-generation DNA sequencing data. *Nat Genet* (2011) 43:491–8. doi: 10.1038/ng.806

21. Koboldt DC, Zhang Q, Larson DE, Shen D, McLellan MD, Lin L, et al. VarScan 2: Somatic mutation and copy number alteration discovery in cancer by exome sequencing. *Genome Res* (2012) 22:568–76. doi: 10.1101/gr.129684.111

22. Newman AM, Bratman SV, Stehr H, Lee LJ, Liu CL, Diehn M, et al. FACTERA: A practical method for the discovery of genomic rearrangements at breakpoint resolution. *Bioinformatics* (2014) 30:3390–3. doi: 10.1093/bioinformatics/btu549

23. Amarasinghe KC, Li J, Halgamuge SK. CoNVEX: copy number variation estimation in exome sequencing data using HMM. *BMC Bioinformatics*. (2013) 14 (Suppl 2):S2. doi: 10.1186/1471-2105-14-S2-S2

24. Shen R, Seshan VE. FACETS: allele-specific copy number and clonal heterogeneity analysis tool for high-throughput DNA sequencing. *Nucleic Acids Res* (2016) 44:e131–1. doi: 10.1093/nar/gkw520

25. Kepes JJ, Fulling KH, Garcia JH. The clinical significance of "adenoid" formations of neoplastic astrocytes, imitating metastatic carcinoma, in gliosarcomas. *A Rev Five Cases Clin Neuropathol* (1982) 1:139–50.

26. Louis DN, Perry A, Wesseling P, Brat DJ, Cree IA, Figarella-Branger D, et al. The 2021 WHO classification of tumours of the central nervous system: A summary. *Neuro Oncol* (2021) 23:1231–51. doi: 10.1093/neuonc/noab106

27. Broniscer A, Tatevossian RG, Sabin ND, Klimo P Jr, Dalton J, Lee R, et al. Clinical, radiological, histological and molecular characteristics of paediatric epithelioid glioblastoma. *Neuropathol Appl Neurobiol* (2014) 40:327–36. doi: 10.1111/nan.12093

28. Miyahara M, Nobusawa S, Inoue M, Okamoto K, Mochizuki M, Hara T. Glioblastoma with rhabdoid features: Report of two young adult cases and review of the literature. *World Neurosurg* (2016) 86:515.e511–519. doi: 10.1016/j.wneu.2015.10.065

29. Jett K, Friedman JM. Clinical and genetic aspects of neurofibromatosis 1. *Genet Med* (2010) 12:1–11. doi: 10.1097/GIM.0b013e3181bf15e3

30. Bettegowda C, Agrawal N, Jiao Y, Wang Y, Wood LD, Rodriguez FJ, et al. Exomic sequencing of four rare central nervous system tumour types. *Oncotarget* (2013) 4:572–83. doi: 10.18632/oncotarget.964

31. Hsiao SJ, Karajannis MA, Diolaiti D, Mansukhani MM, Bender JG, Kung AL, et al. A novel, potentially targetable TMEM106B-BRAF fusion in pleomorphic xanthoastrocytoma. *Cold Spring Harb Mol Case Stud* (2017) 3:a001396. doi: 10.1101/mcs.a001396

32. Phillips JJ, Gong H, Chen K, Joseph NM, van Ziffle J, Jin LW, et al. Activating NRF1-BRAF and ATG7-RAF1 fusions in anaplastic pleomorphic xanthoastrocytoma without BRAF p.V600E mutation. *Acta Neuropathol* (2016) 132:757–60. doi: 10.1007/s00401-016-1616-3

33. Pratt D, Camelo-Piragua S, McFadden K, Leung D, Mody R, Chinnaiyan A, et al. BRAF activating mutations involving the beta3-alphaC loop in V600E-negative anaplastic pleomorphic xanthoastrocytoma. *Acta Neuropathol Commun* (2018) 6:24. doi: 10.1186/s40478-018-0525-1

34. Shibahara I, Sonoda Y, Suzuki H, Mayama A, Kanamori M, Saito R, et al. Glioblastoma in neurofibromatosis 1 patients without IDH1, BRAF V600E, and TERT promoter mutations. *Brain Tumour Pathol* (2018) 35:10–8. doi: 10.1007/s10014-017-0302-z

35. Verhaak RG, Hoadley KA, Purdom E, Wang V, Qi Y, Wilkerson MD, et al. Integrated genomic analysis identifies clinically relevant subtypes of glioblastoma characterized by abnormalities in PDGFRA, IDH1, EGFR, and NF1. *Cancer Cell* (2010) 17:98–110. doi: 10.1016/j.ccr.2009.12.020

36. Khanna G, Pathak P, Suri V, Sharma MC, Chaturvedi S, Ahuja A, et al. Immunohistochemical and molecular genetic study on epithelioid glioblastoma: Series of seven cases with review of literature. *Pathol Res Pract* (2018) 214:679–85. doi: 10.1016/j.prp.2018.03.019

37. Purkait S, Sharma V, Jha P, Sharma MC, Suri V, Suri A, et al. EZH2 expression in gliomas: Correlation with CDKN2A gene deletion/ p16 loss and MIB-1 proliferation index. *Neuropathology* (2015) 35:421–31. doi: 10.1111/neup.12201

38. Appay R, Dehais C, Maurage CA, Alentorn A, Carpentier C, Colin C, et al. CDKN2A homozygous deletion is a strong adverse prognosis factor in diffuse malignant IDH-mutant gliomas. *Neuro Oncol* (2019) 21:1519–28. doi: 10.1093/neuonc/noz126.000

39. Koul D. PTEN signaling pathways in glioblastoma. *Cancer Biol Ther* (2008) 7:1321–5. doi: 10.4161/cbt.7.9.6954

frontiers | Frontiers in Oncology

TYPE Original Research
PUBLISHED 16 January 2023
DOI 10.3389/fonc.2022.1065071

OPEN ACCESS

EDITED BY
Ming Zhao,
Zhejiang Provincial People's Hospital, China

REVIEWED BY
Sean R. Williamson,
Cleveland Clinic, United States
Isidro Machado,
Instituto Valenciano de Oncologia, Spain

*CORRESPONDENCE
Hongying Zhang
hy_zhang@scu.edu.cn

†These authors have contributed equally to this work

SPECIALTY SECTION
This article was submitted to Surgical Oncology, a section of the journal Frontiers in Oncology

RECEIVED 09 October 2022
ACCEPTED 30 December 2022
PUBLISHED 16 January 2023

CITATION
Zhang Y, Qiu Y, Zhang X, He X, Chen C, Chen M and Zhang H (2023) *USP6*-associated soft tissue tumors with bone metaplasia: Clinicopathologic and genetic analysis and the identification of novel *USP6* fusion partners.
Front. Oncol. 12:1065071.
doi: 10.3389/fonc.2022.1065071

USP6-associated soft tissue tumors with bone metaplasia: Clinicopathologic and genetic analysis and the identification of novel *USP6* fusion partners

Yahan Zhang†, Yan Qiu†, Xianliang Zhang, Xin He, Chen Chen, Min Chen and Hongying Zhang*

Department of Pathology, West China Hospital, Sichuan University, Chengdu, China

Introduction: Among those tumors with consistent USP6 rearrangement, some arise from soft tissue and show bone metaplasia, including myositis ossificans (MO), fibro-osseous pseudotumor of digits (FOPD), soft tissue aneurysmal bone cyst (ST-ABC) and fasciitis ossificans (FO). These lesions are easily confused with malignancies because they show a rapid growth rate and brisk mitoses. Here, we aim to clarify the clinicopathologic and genetic characteristics of this entity and analyze the correlations among the different subtypes in one of the largest cohorts.

Materials and Methods: The clinicopathologic features of 73 cases of MO, FOPD, ST-ABC and FO diagnosed at West China Hospital, Sichuan University from January 2010 to December 2021 were retrospectively analyzed. Forty-three undecalcified samples were analyzed by systematic genetic studies, including fluorescence in situ hybridization (FISH), reverse transcription polymerase chain reaction (RT-PCR), Sanger sequencing and next-generation-based sequencing were performed.

Results: This series included 40 males and 33 females aged 2 to 80 years old (median: 31 years). FOPD occurred in extremal soft tissue, while lower extremities (38/58, 65.5%) were the most commonly involved lesions in the other three subgroups. Histologically, proliferative myofibroblasts/fibroblasts with varying degrees of osteoid tissue were present. Fluorescence in situ hybridization (FISH) results indicated that 22 cases (22/27, 81.5%) were positive for USP6 rearrangement, and 5 cases were negative. Among those cases with positive FISH results, 18 underwent reverse transcription-polymerase chain reaction (RT-PCR) detection that successfully detected common USP6 fusion types. Thirteen cases showed COL1A1::USP6 fusion, one showed MYH9::USP6 fusion, and 4 were negative for common fusion types. Next-generation-based sequencing technology was performed on two lesions with negative RT–PCR results and novel fusion partners SNHG3 and UBE2G1 were discovered.

Conclusions: Our findings revealed that COL1A1 is the most common fusion partner in this entity, unlike primary aneurysmal bone cysts and nodular fasciitis. Notably, we believed that FO may demonstrate more similar clinicopathologic and genetic manifestations with MO/FOPD and ST-ABC instead of nodular fasciitis for involving lower limbs most frequently and showing recurrent COL1A1::USP6 fusion. Additionally, this study also found two novel USP6 fusion partners, which further expanded our knowledge of this neoplastic spectrum.

KEYWORDS

USP6 rearrangement, myositis ossificans, fibro-osseous pseudotumor of digits, soft tissue aneurysmal bone cyst, fasciitis ossificans, differential diagnosis, *USP6*-associated neoplasms

Introduction

The ubiquitin-specific protease 6 gene (*USP6*), also known as Tre-2, encodes chromosome 17p13.2 (1). In 2004, Oliveira and colleagues found recurrent *USP6* rearrangement in primary aneurysmal bone cysts (ABCs) (63%) (2). Subsequent studies confirmed that *CDH11* was the most common fusion partner for *USP6* in primary ABC (2, 3). In 2011, Erickson-Johnson et al. recognized recurrent *USP6* rearrangement and the most common fusion partner *MYH9* in nodular fasciitis (NF) (4). Thereafter, these two entities were included as *USP6*-associated neoplasms (1). In recent years, a growing number of molecular genetic studies (including research from our group) have expanded the families of *USP6*-associated neoplasms. The family also includes (1) variants of NF: cranial fasciitis (CF), intravascular fasciitis (IVF) and fasciitis ossificans (FO); and (2) other spindle cell neoplastic lesions: fibroma of tendon sheath (FTS), benign infiltrative myofibroblastic neoplasms, myositis ossificans (MO), fibro-osseous pseudotumor of digits (FOPD) and soft tissue aneurysmal bone cyst (ST-ABC) (5–14).

Notably, *USP6*-associated neoplasms are characterized by proliferative myofibroblasts/fibroblasts with or without metaplasia of osteoid components. In this family, many tumors are classic pseudosarcomatoid lesions, which are easily confused with malignancies in the diagnostic process, especially for those with bone metaplasia. Our group has previously conducted some related studies on NF and its variants (some results have been published) (11, 15). This study will focus on *USP6*-associated soft tissue tumors with bone metaplasia.

USP6-associated soft tissue tumors with bone metaplasia predominantly consist of MO, FOPD, ST-ABC and FO. MO and FOPD have been previously recognized as tumors belonging to the same spectrum from the perspective of morphology, and recent studies have further confirmed the conclusion from the perspective of genetics for identifying consistent *USP6* rearrangements in both MO and FOPDs (8, 9). Recent research has revealed that the most common fusion partner in MO and FOPD is *COL1A1* (10), which is different from the primary ABC and NF. Recently, clinicopathological features and genetic changes similar to MO/FOPD have been identified in ST-ABC, while the 2020 WHO classification of soft tissue and bone tumors and some recent researchers have suggested that rare ST-ABC, MO and FOPD should be classified into the same subclass of *USP6*-associated tumors (5, 16). Notably, FO also showed ossifying components in morphology, but there are only a few studies with a small sample size on these tumors, Further studies are needed to determine whether there is a closer affinity between FO and MO, FOPD, and ST-ABC.

Based on the aforementioned background, this study will include one of the largest cohorts of MO, FOPD, ST-ABC, and FO cases to further clarify the clinicopathologic and genetic characteristics of this entity and analyze the correlations and differences among different subtypes.

Materials and methods

Case selection

This study was approved by the Ethics Committee on Biomedical Research, West China Hospital of Sichuan University (No. 793, 2021). A SNOMED search of the hospital surgical pathology files from January 2010 to December 2021 identified 73 *USP6*-associated soft tissue tumors with bone metaplasia, which included 44 MO cases, 15 FOPD cases, 12 FO cases and 2 ST-ABC cases. Clinical, pathological, and follow-up information was collected from clinical records and pathology reports. Follow-up information was collected by telephone interviews. The follow-up duration was calculated from the date of the first surgery to the date of recurrence, death, or last follow-up.

Histologic review

Hematoxylin and eosin-stained and immunohistochemically stained slides were obtained from the surgical and pathological bank of the hospital, and all cases were reviewed independently by 2 experienced pathologists (Hongying Zhang and Xianliang Zhang) with expertise in soft tissue and bone tumor pathology and 1 general surgical pathologist (Yahan Zhang).

Fluorescence *in situ* hybridization

Fluorescence in situ hybridization (FISH) was conducted on formalin-fixed, paraffin-embedded (FFPE) tissue sections using a *USP6* break-apart probe (Lbp Medicine Science & Technology, Guangzhou, China) following the manufacturer-provided instructions for 43 cases (including 24 MOs, 6 FOPDs, 11 FOs and 2 ST-ABCs) with available undecalcified tissues. Thirty decalcified cases did not perform FISH because the strong acid decalcification method routinely used would damage the sample DNA. Tumor samples were evaluated by two pathologists in 100 neoplastic cells in a blind fashion using an Olympus BX53 fluorescence microscope (Japan). A red-green split signal pattern was considered positive for *USP6* gene rearrangement if the distance between the green and red signals was greater than the diameter of any two signals. A case was considered positive for *USP6* rearrangement when 10% or more counted cells showed red-green split signals.

Reverse transcription-polymerase chain reaction and Sanger sequencing

Total RNA was extracted using the miRNeasy FFPE Kit (Qiagen, Hilden, Germany), and the concentration and quality of RNA were measured using NanoDrop Microvolume Spectrophotometers (Thermo Fisher Scientific, Massachusetts, USA). cDNA was synthesized using the PrimeScript RT reagent kit (Takara, Tokyo, Japan). All polymerase chain reactions (PCRs) were performed for 40 cycles using a TB Green™ Premix Ex Taq™ II kit (Takara, Tokyo, Japan) with the following cycle conditions: denaturation at 94°C for 40 s, annealing at 50~60°C for 30 s, and extension at 72°C for 30 s using primers for commonly reported *USP6* fusion genes, including *MYH9::USP6, CDH11::USP6, COL1A1::USP6, SEC31A::USP6, RUNX2::USP6, PAFAH1B1::USP6, PPP6R3::USP6* and *COL1A2::USP6* (Supplemental Table 1). Ten microliters of each amplified product were subjected to 2% agarose gel electrophoresis and photographed by a Bio-Rad imager for visualization. Sanger sequencing was performed to verify the positive reverse transcription-polymerase chain reaction (RT-PCR) products.

Next-generation-based technology

The FFPE tissue was sent to the sequencing core (242 gene DNA panels, Yousu™, OrigiMed, Shanghai, China). DNA was extracted from FFPE tissues using the QIAamp DNA FFPE Tissue Kit according to the manufacturer's protocol (Qiagen, Hilden, Germany). A total of 0.5 μg of DNA per sample was applied as input for the DNA library preparations. Assays were performed using an Illumina MiSeq Platform (Illumina, San Diego, CA, USA) following the manufacturer's recommendations.

Results

Clinical findings

This subgroup included 40 males and 33 females with diagnosed ages ranging from 2 to 80 years old (median: 31 years). Most cases manifested as a painful mass or swelling lesion, and the duration of these symptoms was 0.2 to 96 months (median: 1 month) in 66 patients with available data. Injury information was available for 48 patients, among which 14 (29.2%) had a history of trauma at the lesion site. Except for FOPD occurring in the soft tissues of the extremities (12 fingers and 3 toes), the lower limbs (38/58, 65.5%) were the most commonly involved sites, followed by the upper limbs (9/58, 15.5%), trunk (9/58, 15.5%), and head and neck (2/58, 3.5%) in MO, ST-ABC and FO. The range of maximum tumor diameter in 59 cases with available information was 0.5 cm to 20 cm (median: 5.0 cm).

Imaging data were available for 38 cases. MO was often in the deep muscle, FOPD was predominantly located in the subcutaneous soft tissue of the fingers and toes, ST-ABC was located in the deep soft tissue, and FO was essentially confined to the subcutaneous fat layer. Tumor boundary information was obtained in 30 cases, and most of them (21/30, 70.0%) were well circumscribed on imaging. MRI is mainly manifested as a mass with an abnormal signal in the intramuscular or subcutaneous tissues. CT and/or X-ray usually showed a slightly low-density mass in the soft tissue, with mostly high-density calcification in or around the mass (15/25, 60.0%) (Figures 1A–D).

Pathological findings

Histologically, the basic lesions of this entity are myofibroblast/fibroblast proliferation with varying degrees of osteoid components. The myofibroblasts/fibroblasts may show mild atypia. Osteoblasts were often found around the mature and braided bone, and multinucleated giant cells were shown in some areas. Some (29/71, 40.1%) lesions were accompanied by cartilage metaplasia. Varying numbers of mitoses with no atypia can be observed (0~20/10 HPFs). In those MO lesions, most cases demonstrated an ill-defined intramuscular mass. Microscopically, a zonation pattern, noted as transitions from the central immature osteoid component gradually to the peripheral mature trabecular bone, can be observed in most cases (Figure 2A). Part of MO cases (34.1%, 15/44) showed NF-like morphology in some foci, among which myofibroblasts/fibroblasts arranged as cell culture pattern, varying degree of myxoid change, extravasated erythrocytes, infiltrating inflammatory cells (Figure 2B). Extremely rare cases displayed extensive and prominent NF-like morphology (Figure 2C) and focal osteoid components with zonation patterns (Figure 2D). In terms of FOPD, the morphology was similar to MO; however, osteoid components in most FOPD cases showed a haphazard pattern instead of an obvious zonation pattern (Figures 2E, F). Most FO had classical NF-like morphology (10/12, 83.8%), and osteoid tissue of different maturation degrees were distributed haphazardly in tumors (Figure 3A). Extremely rare FO cases showed local infiltration and reverse zonal distribution that is similar to osteosarcoma (Figure 3B). The hyperplastic myofibroblasts/fibroblasts cells showed mild atypia, and immature osteoid tissue was scattered among them (Figure 3C). Besides, brisk mitosis with no atypia could be observed (Figure 3D). ST-ABC featured blood-filled cyst formation (Figure 3E), and MO-like morphology with a zonation structure was also found in some regions of one ST-ABC in this group (Figure 3F).

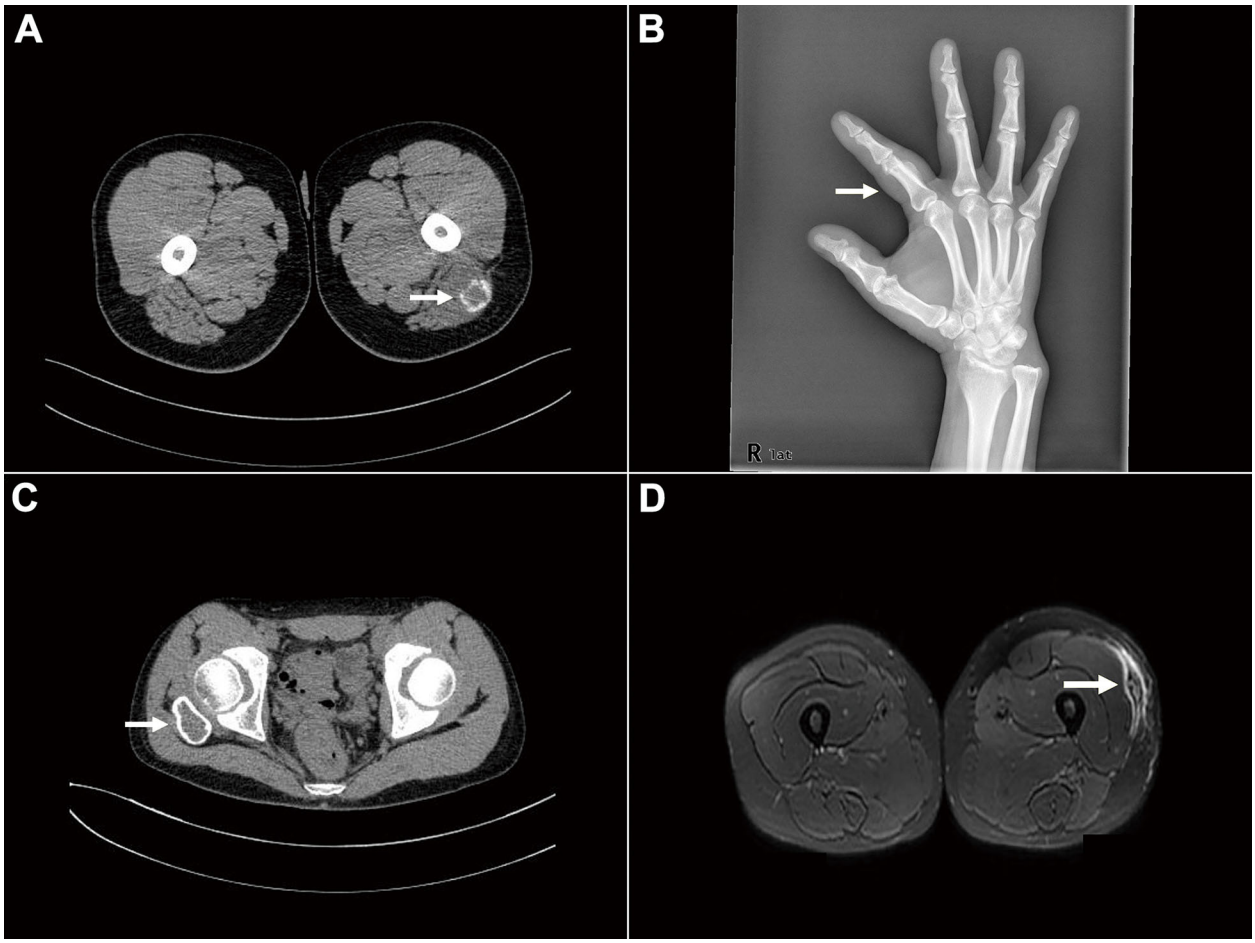

FIGURE 1
Imaging findings of *USP6*-associated soft tissue tumors with osteoid tissue. **(A)** CT showed a soft tissue density mass in the muscle, with well-defined boundaries and circumferentially circular density (arrow) (Case 33). **(B)** X-rays demonstrated a soft tissue mass in the right finger with calcification (arrow) (Case 54). **(C)** CT showed mixed-density shadows with clear boundaries around the right hip (arrow) (Case 60). **(D)** MRI showed mixed signals in the subcutaneous fat layer of the left thigh, with clear boundaries (arrow) (Case 63).

Pertinent immunohistochemical markers were performed for diagnosis in some cases. Smooth muscle actin (SMA) showed diffuse expression in all detected cases (21/21, 100%), six cases exhibited MSA expression (6/8, 75.0%), and expression of SATB2 was present in the bone metaplasia area (8/8, 100%). Lacked expression of desmin in 19 cases (19/20, 95.0%). S-100 protein (16/16, 100%), β-catenin (8/8, 100%) and MDM2 (8/8,100%) expression were consistently absent. The MIB-I positive index ranged from 1 to 30%.

Genetic findings

In current studies, FISH has been performed on tissues in 43 cases with available undecalcified tissues; 27 cases, including 17 MOs, 2 FOPDs, 2 ST-ABCs, and 6 FOs, were successfully detected, and 16 of them failed due to poor DNA quality or tissue falling. Among these cases with interpretable results, FISH showed rearrangements of *USP6* in 20%~60% of neoplastic cells in 22 cases (81.5%) (Figures 4A–D), and 5 cases were negative for *USP6* rearrangements (Table 1). The positive rates for *USP6* rearrangement among cases of MO, FOPD, ST-ABC and FO were 70.6% (12/17), 100.0% (2/2), 100% (2/2) and 100.0% (6/6), respectively.

Among those 22 patients with positive *USP6* rearrangements, RT–PCR was successfully performed in 18 cases (3 MOs and 1 FOPD with poor RNA quality failed testing); 13 cases (72.2%), including 5 MOs, 1 FOPD, 2 ST-ABCs and 5 FOs, were positive for *COL1A1::USP6* fusion, and one case with MO was positive for *MYH9::USP6* fusion. For *COL1A1::USP6* fusion types (Figure 4E), 1 MO, 1 FOPD and 3 FO cases were found with fusion transcript type 1 (nucleotide 103, NM_000088 exon 1; nucleotide 1330, NM_0004505 exon 2) (Figure 4F), 3 MO, 1 ST-ABC and 1 FO cases were found with fusion type II (nucleotide 219, NM_000088 exon 1; nucleotide 1338, NM_0004505 exon 2) (Figure 4G), and 1 MO and 1 ST-ABC demonstrated fusion transcript type III (nucleotide 130 exon 1, NM_000088; nucleotide 1231, NM_0004505 exon 1) (Figure 4H). One FO case was found with a special transcript type with *COL1A1* (nucleotide 222, NM_000088 exon 1) and *USP6* (nucleotide 1355, NM_0004505 exon 3) fusion (Figure 4I). Additionally, one MO case showed fusion of exon 1 (nucleotide 49, NM_000088) of *USP6* and exon 2 (nucleotide 1330, NM_0004505) of *MYH9* instead of any transcript type of *COL1A1::USP6* fusion (Figure 4J).

10.3389/fonc.2022.1065071

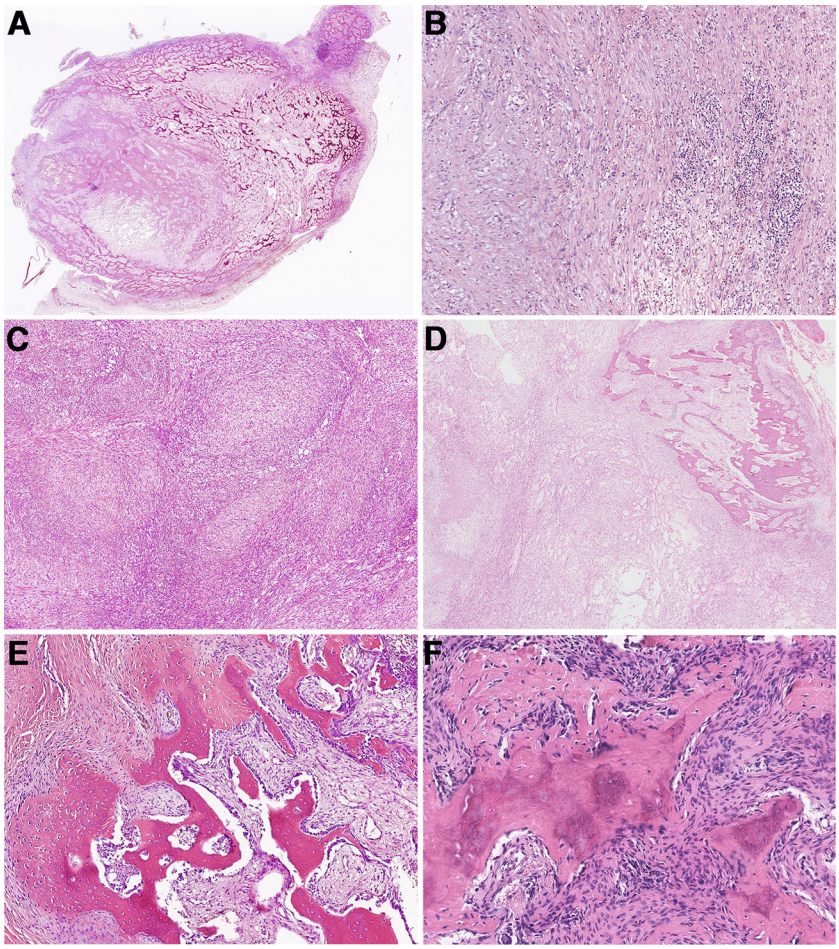

FIGURE 2
Histopathologic characteristics of myositis ossificans and fibro-osseous pseudotumors of digits. **(A)** Most myositis ossificans cases were well circumscribed with a typical zonation pattern (Case 33). **(B)** Myofibroblasts/fibroblasts were arranged in bundles in the myxoid stroma, accompanied by extravasated red blood cells and chronic inflammatory cells, showing NF-like morphology (Case 33). **(C)** Extensive NF-like morphology was observed in one myositis ossificans case (Case 42). **(D)** The tumor formed obvious zonal distribution focally (Case 42). **(E)** Osteoid components were mature and disorderly in fibro-osseous pseudotumors of digits (Case 46). **(F)** Immature osteoid components were observed scattered among the proliferative myofibroblast/fibroblast (Case 57).

Four *USP6*-rearranged lesions were negative for *COL1A1::USP6*, and only two of them (1 MO and 1 FO) underwent next-generation-based sequencing technology, while the tissues of the other two cases were not sufficient to perform a further study. A novel fusion of *UBE2G1* (exon 1, NM_003342) and *USP6* (exon 8-38, NM_001304284) was identified in one MO case (Case 39) (Figure 5A), while a novel fusion of *SNHG3* (exon 1, NR_002909) and *USP6* (exon 8-38, NM_001304284) was demonstrated in one FO case (Case 66) (Figure 5B). The presence of the fusion at the DNA level was further validated by RT–PCR and Sanger sequencing using corresponding primers (*UBE2G1-F*: 5'-AGGCTGGTCTTGAA CTCCTGA-3'and *USP6-R*: 5'-CGTGTGTGTTGCTTCTCTGGC-3'; *SNHG3-F*: 5'-TCTTAGTGGAGACGGGGTTTC-3' and *USP6-R*: 5'-AGCTAGAGGATCATGTGCGGA-3'). The process and results of genetic testing are summarized in Figure 6.

Treatment and follow-up

Treatment information was obtained in 63 cases. Sixteen patients underwent biopsy, 41 patients underwent local complete resection, 3 patients underwent wide resection, 2 patients underwent partial mass resection, and 1 patient underwent curettage. Follow-up information was obtained for 36 patients (4 patients underwent biopsy, and 32 patients underwent resection), and the follow-up times ranged from 1 to 127 months (median, 26 months). Four patients survived with tumors after the biopsy without tumor progression. Twenty-nine cases showed no tumor progression after biopsy or surgery, and 5 cases (5/34, 14.7%) experienced postoperative recurrence, including 1 MO with curettage, 2 FOPDs with partial mass resection, 1 MO and 1 FO with complete resection (Table 2).

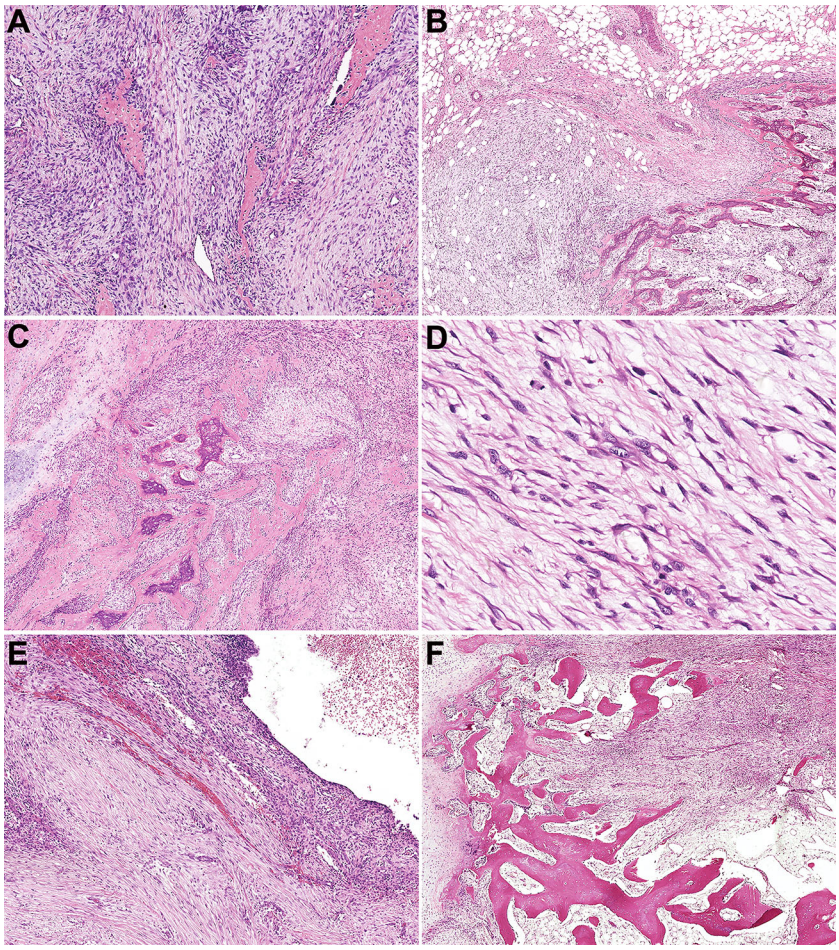

FIGURE 3
Histopathologic characteristics of fasciitis ossificans and soft tissue aneurysmal bone cyst. **(A)** Osteoid tissues were distributed disorderly in an NF-like background in fasciitis ossificans (Case 66). **(B)** In one fasciitis ossificans case, the tumor was locally invasive with a reverse zonation structure. (Case 63). **(C)** Myofibroblasts/fibroblasts cells were hyperplasia with mild atypia, and immature osteoid tissue was scattered among them. (Case 63). **(D)** Mitotic figures with no atypia were presented in myofibroblasts/fibroblasts (Case 63). **(E)** Soft tissue aneurysmal bone cyst showed a cystic cavity with hyperplastic myofibroblasts/fibroblasts and focal osteoid tissue in the cystic septum (Case 60). **(F)** In one soft tissue aneurysmal bone case, MO-like zone structure was observed and bone shell was formed around the tumor (Case 60).

Details of the clinicopathological and genetic characteristics of different subtypes of *USP6*-associated soft tissue tumors with bone metaplasia are shown in Supplemental Table 2.

Discussion

USP6-associated soft tissue tumors with bone metaplasia are a subgroup of myofibroblasts/fibroblastic proliferative lesions with metaplastic osteoid components, mainly including MO, FOPD, ST-ABC and FO. This group of neoplasms is not clinically common, but its histology shows pseudosarcomatous changes with the formation of an osteoid component, making it susceptible to misdiagnosis as a malignancy.

In our cohort, there were 73 cases of *USP6*-associated soft tissue tumors with bone metaplasia, including 44 MOs, 15 FOPDs, 2 ST-ABCs and 12 FOs. As we know, this is one of the largest groups for exploring the clinicopathologic and molecular characteristics of this entity. The diagnosis age in this group was wide, ranging from 2 to 80 years old (median: 31 years). Consistent with previous reports, these tumors can occur in all age groups, but they are more common in young adults between 20~40 years old (5, 16, 17). Fourteen patients (14/48, 29.2%) had a clear history of trauma, but the history of repeated minor trauma might be neglected. In this group, except for FOPD, the lesion sites of the other subtypes were mainly in the lower limbs. The predisposing site of our group was different from that of traditional NF, which more often involves the upper limbs and trunk (18). Notably, FO is currently classified as a special subtype of NF. However, according to the results of our study, we found that the most common site of FO was the lower limbs (9/12, 75%) instead of the upper limbs and trunk. Three FOs were also reported in the latest study, of which 2 cases were identified in the lower extremities, which was consistent with our findings (5). As for imaging examinations in our study, the results were consistent with those reported in previous literature (5, 9, 10, 16, 19).

Histologically, this group showed hyperplastic myofibroblasts/fibroblasts and osteoid tissues with different degrees of maturity. The histological morphology of MO/FOPD and ST-ABC in the present study were essentially consistent with the description in the literature (16, 17, 20). There have been few case reports of FO, and the

10.3389/fonc.2022.1065071

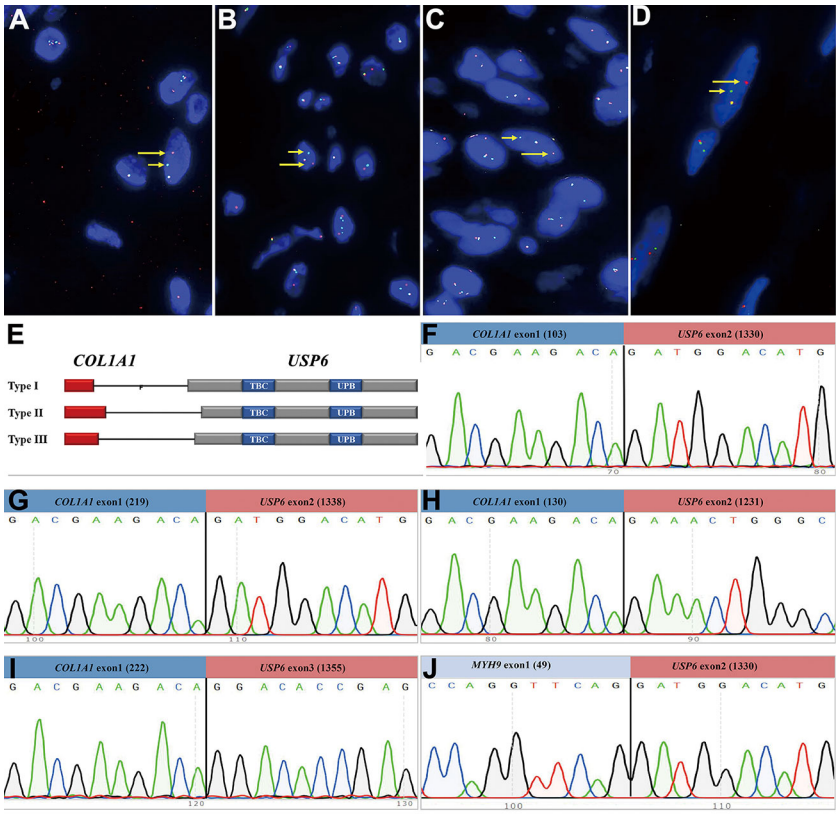

FIGURE 4
Findings of break-apart *USP6* fluorescence *in situ* hybridization and reverse transcription polymerase chain reaction for identifying common *USP6* fusion partners. **(A)** Break-apart *USP6* FISH showed split red (long arrow) and green (short arrow) signals in myositis ossificans (Case 42). **(B)** *USP6* FISH showed split red (long arrow) and green (short arrow) signals in fibro-osseous pseudotumor of digits (Case 49). **(C)** *USP6* FISH showed split red (long arrow) and green (short arrow) signals in soft tissue aneurysmal bone cyst (No. 60). **(D)** *USP6* FISH showed split red (long arrow) and green (short arrow) signals in fasciitis ossificans (No. 63). **(E)** Diagram showing the overall structure of *COL1A1::USP6* fusion genes. **(F)** One myositis ossificans (Case 22) showed the nucleotide (103, NM_000088) of *COL1A1* exon 1 fused with a nucleotide (1330, NM_0004505) of *USP6* exon 2 (type I). **(G)** One fasciitis ossificans (Case 71) showed the last nucleotide (219, NM_000088) of *COL1A1* exon 1 fused with a nucleotide (1338, NM_0004505) of *USP6* exon 2 (type II). **(H)** One myositis ossificans (Case 32) showed the last nucleotide (130, NM_000088) of *COL1A1* exon 1 fused with a nucleotide (1231, NM_0004505) of *USP6* exon 1 (type III). **(I)** One fasciitis ossificans (Case 63) showed a nucleotide (222, NM_000088) of *COL1A1* exon 1 fused with a nucleotide (1355, NM_0004505) of *USP6* exon 3. **(J)** One myositis ossificans (Case 42) showed the last nucleotide (49, NM_000088) of *MYH9* exon 1 fused with a nucleotide (1330, NM_0004505) of *USP6* exon 2.

deposition pattern of osteoid tissues is mainly described as having a haphazard distribution similar to that of FOPD. However, MO-like zonal deposition pattern was observed in 50% of FO cases in our group, which indicated that there was evident histological overlap between FO and the other three subtypes of *USP6*-associated soft tissue tumors with bone metaplasia.

At present, soft tissue tumors in osteoid tissues have been successively confirmed to be *USP6*-associated tumors. Studies have suggested that the positive rate of *USP6* rearrangement/fusion in MO/FOPD, ST-ABC and FO ranges from 16.7% to 100% (5, 8–10, 17, 19, 21). However, it should be emphasized that the overall sample size of existing studies is relatively small, with only 4 studies with more than 10 cases (11 cases (8), 12 cases (10), 12 cases (21), 14 cases (5)). Our study had the largest number of cases in a single center, and the positive rate of *USP6* rearrangement detected by FISH in this group of cases was 81.5% (22/27). In recent years, an increasing number of studies have focused on the fusion partners of these tumors and the relationship between them. Our study suggested that *COL1A1* (13/18, 72.2%) was the most frequent fusion partner in MO/FOPD, ST-ABC and FO, which was consistent with previous studies (67.7%~100%) and differed from classical primary ABC and NF (5, 10). Notably, despite the presence of significant ossification, FO is currently classified as a variant of NF. Although it has also been reported that *COL1A1* was found to be the fusion partner in a few NFs (22), *COL1A1* was the unique *USP6* fusion partner of FO in this study, which was consistent with the findings of Wang and colleagues (5). Meanwhile, we found that the most common site of FO was the lower limbs instead of the upper limbs of NF, suggesting that FO seemed to be more closely related to MO/FOPD and ST-ABC. Notably, in *USP6*-associated neoplasms, although an increasing number of partner genes have been identified, there is a preference for these partner genes in different tumor subtypes (5–7, 10, 14, 15, 17, 19, 23–35) (Figure 7A). Intriguingly, according to our study and previous literature, almost all of the *USP6*-associated neoplasms with bone metaplasia adopt *COL1A1* as the fusion partner, including MO, FOPD, ST-ABC and FO (5, 10, 17, 19, 25). As reported, *COL1A1* encodes the pro-alpha1 chain of type I collagen, which is associated with osteogenesis imperfecta and osteoporosis (36). It should be noted that the fusion of *COL1A1* and *USP6* still retained the whole *USP6* coding sequence of the open reading frame, namely, the fusion of the partner gene exon1 and the *USP6* gene exon1 or/and exon2. Although this fusion is expected to lead to the high

10.3389/fonc.2022.1065071

TABLE 1 Genetic findings of *USP6*-associated soft tissue tumors with bone metaplasia.

Case No.	Diagnosis	Location	Sex	Age	Trauma History	Size (cm)	*USP6* FISH	RT-PCR and Sanger sequencing/ Next-generation-based sequencing
4	MO	Elbow	M	49	NA	2.0	+	*COL1A1 exon1::USP6 exon2*
7	MO	Hip	F	14	No	4.1	+	*COL1A1 exon1::USP6 exon2*
10	MO	Back	M	14	No	3.5	+	–
14	MO	Arm	F	62	NA	6.0	–	ND
18	MO	Hip	M	46	No	5.3	+	*COL1A1 exon1::USP6 exon2*
19	MO	Thigh	F	60	No	3.0	–	ND
20	MO	inguinal region	M	21	Yes	NA	–	ND
22	MO	Neck	M	5	No	6.0	+	*COL1A1 exon1::USP6 exon2*
30	MO	Hip	M	12	No	NA	+	–
32	MO	Thigh	M	22	NA	10.0	+	*COL1A1 exon1::USP6 exon1*
33	MO	Thigh	M	36	No	7.0	+	ND (poor RNA quality)
37	MO	Thigh	M	36	NA	3.7	–	ND
39	MO	Hip	M	7	No	3.0	+	*UBE2G1 exon1::USP6 exon 8-38*
41	MO	Thigh	F	54	No	3.5	–	ND
42	MO	Hip	M	15	No	5.0	+	*MYH9 exon1::USP6 exon2*
43	MO	Crus	M	14	No	4.0	+	ND (poor RNA quality)
44	MO	Thigh	F	15	No	4.0	+	ND (poor RNA quality)
49	FOPD	Finger	M	64	NA	0.8	+	ND (poor RNA quality)
58	FOPD	Finger	M	20	Yes	NA	+	*COL1A1 exon1::USP6 exon2*
60	ST-ABC	Hip	M	14	Yes	5.0	+	*COL1A1 exon1::USP6 exon1*
61	ST-ABC	Lumbar vertebral side	M	15	No	4.0	+	*COL1A1 exon1::USP6 exon2*
63	FO	Thigh	F	44	No	12.0	+	*COL1A1 exon1::USP6 exon3*
64	FO	Infraclavicularis	M	28	No	4.0	+	*COL1A1 exon1::USP6 exon2*
65	FO	Knee	M	10	No	5.0	+	*COL1A1 exon1::USP6 exon2*
66	FO	Arm	M	32	No	2.0	+	*SNHG3 exon1::USP6 exon 8-38*
71	FO	Knee	M	18	No	5.0	+	*COL1A1 exon1::USP6 exon2*
72	FO	Thigh	F	36	No	5.0	+	*COL1A1 exon1::USP6 exon2*

MO, myositis ossificans; FOPD, fibro-osseous pseudotumor of digits; ST-ABC, soft tissue aneurysmal bone cyst; FO, fasciitis ossificans; F, female; M, male; NA, not available; ND, not done; FISH, Fluorescence in situ hybridization; RT-PCR, Reverse Transcription-Polymerase Chain Reaction. +, positive; -, negative.

expression of *USP6* or be the main mechanism of *USP6* gene-mediated tumor pathogenesis, the high percentage of *COL1A1* as a fusion partner in these tumor subtypes still likely has a potential association with the osteoid formation on the histology, but further research is needed. In addition, individual *USP6* fusion partners that overlap between these tumor subtypes have been identified (3, 7, 11, 15, 22, 35–39) (Figure 7B). Although such cases are limited, the possibility of some crossover or even transition between *USP6*-associated neoplasms cannot be ruled out.

Notably, although *COL1A1* was the most frequent fusion partner in this entity, we still identified *MYH9::USP6* fusion in one case of MO (Case 42). At present, after thoroughly reviewing the English literature, *MHY9* has not been reported as a *USP6* fusion partner in MO/FOPD, ST-ABC and FO. As reported, *MYH9::USP6* fusion is the most frequent fusion type in NF (including variants of NF) and FTS in *USP6*-associated tumors (4, 5, 40). After carefully reviewing the slides of this lesion, we found that it was an intramuscular mass and demonstrated a prominent zonation pattern in focal areas (Figure 2D) and obvious NF-like morphology in some foci (Figure 2C), which indicated there are some overlapping histological features as well as molecular findings among different subtypes of *USP6*-associated neoplasms, for example, as the major fusion type in the primary ABC, *CDH11::USP6* also can be detected in the NF, but how they work in building the bridge between them are still not clear and needs to be further studied in a larger cohort.

In this study, we also identified a novel ubiquitin-conjugating enzyme E2 G1 *(UBE2G1)::USP6* gene fusion in one case of MO (Case

10.3389/fonc.2022.1065071

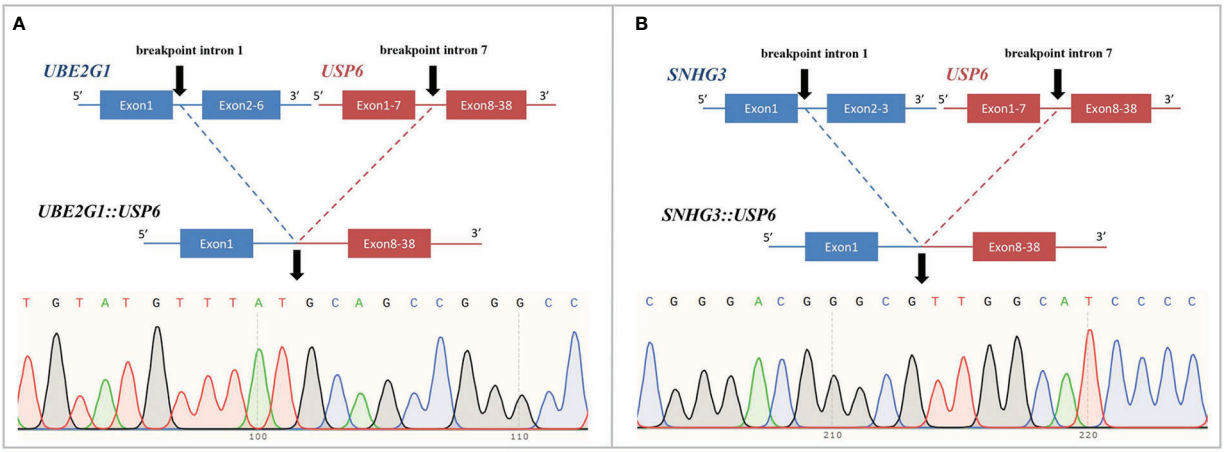

FIGURE 5
Novel fusion partners identified in *USP6*-associated soft tissue tumors with bone metaplasia. **(A)** NGS-based technology showing detection of *UBE2G1* (exon1):: *USP6* (exon8-38) fusion and breakpoint information between the two genes. Sanger sequencing analysis confirmed the presence of *UBE2G1*:: *USP6* fusion. **(B)** NGS-based technology showing detection of *SNHG3* (exon1)::*USP6* (exon8-38) fusion and breakpoint information between the two genes. Sanger sequencing analysis confirmed the presence of *SNHG3*::*USP6* fusion.

39) and a novel small nuclear protein RNA host gene 3 (*SNHG3*):: *USP6* fusion in one case of FO (Case 66). To our knowledge, fusions of these two genes with *USP6* have not been previously reported. *UBE2G1* is located on chromosome 17p13.2; it encodes a member of the E2 ubiquitin-conjugating enzyme family and catalyzes the covalent attachment of ubiquitin to other proteins (41). *SNHG3* is located on chromosome 1p35.3, which belongs to a group of long noncoding RNAs associated with multiple cancers and is dysregulated in multiple cancers (42). Recent studies have shown that *SNHG3* expression is higher in many tumors, such as osteosarcoma, breast cancer and hepatocellular carcinoma (42). Similar to previous findings (4, 43), the entire coding region of *USP6* was preserved in these two rearrangements, which likely leads to activat*ing USP6* *t*ranscription and subsequent neoplastic processes.

Notably, except for *MYH9*, *UBE2G1* and *SNHG3*, which were discovered in our study, the unusual *USP6* partner *ANGPTL2* has also been identified in one MO-like ST-ABC (17). However, despite the presence of uncommon fusion types, no peculiar clinicopathologic findings were identified in these 4 cases. Whether the novel fusions may be related to the clinicopathological features of these tumors remains to be further investigated. Additionally, according to many reported studies, in most cases of *USP6*-associated tumors, the fusion site of *USP6* was exon 1 or/and exon 2 (4, 5, 10). In the current study, we found rare fusion sites of the *USP6* gene, which were exon 3 and

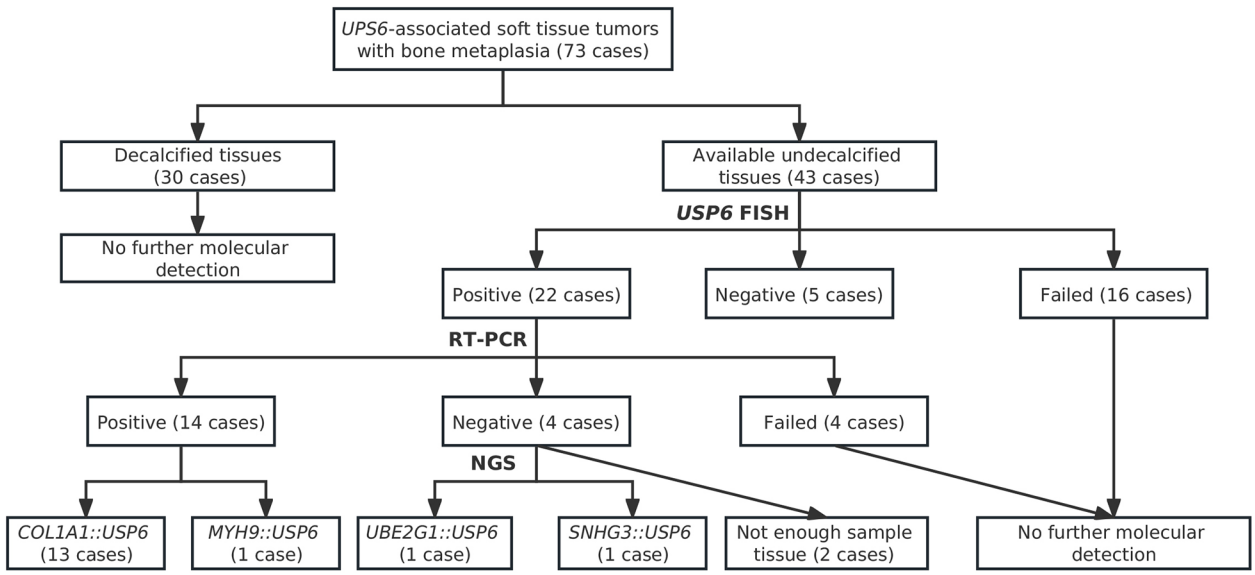

FIGURE 6
Summary of process and results for genetic testing of *USP6*-associated tumors.

10.3389/fonc.2022.1065071

TABLE 2 Clinicopathologic and genetic results of 5 recurrent cases.

Case No.	Final Diagnosis	Sex	Age	Truma History	Duration time (mo)	Location	Size (cm)	Depth	Histological morphology	mitosis	Case source	Referal diagnosis	Genetic findings	Treatment	Recurrence (mo)
3	MO	M	17	Yes	12	Elbow	6.0	Intramuscular	zonal	4/10HPF	Consultation cases/In-house case	Callus?	ND (decalcification)	Curettage	11
34	MO	F	13	No	8	Thigh	10.0	Intramuscular	zonal	6/10HPF	In-house case	MO?	ND (decalcification)	Local complete resection	24
55	FOPD	F	12	No	12	Toe	3.0	Subcutaneous	No zonal	0/10HPF	In-house case	osteochondroma?	ND (decalcification)	Partial resection	NA
59	FOPD	M	16	No	6	Finger	3.0	Subcutaneous	No zonal	0/10HPF	In-house case	FOPD	ND (decalcification)	Partial resection	6
63	FO	F	44	No	2	Thigh	12.0	Subcutaneous	Zonal, NF-like morphology	8/10HPF	Consultation cases/In-house case	FO? Osteosarcoma?	*COL1A1exon1::USP6 exon3*	Local complete resection	2

MO, myositis ossificans; FOPD, fibro-osseous pseudotumor of digits; FO, fasciitis ossificans; F, female; M, male; NF, nodular fasciitis; ND, not done; NA, not available.

exon 8 of *USP6* (NM_001304284). In addition, a previous study by our team also reported an equally rare case of atypical NF in children at the fusion site of exon 9 of *USP6* (NM_001304284) (15). However, whether these rare fusion sites are related to clinicopathologic characteristics still needs further study.

For differential diagnosis, *USP6*-associated soft tissue tumors with bone metaplasia are extremely easily confounded with extraskeletal osteosarcoma, especially in MO cases. Ten of 33 consultation cases were initially considered extraskeletal osteosarcoma in the local hospital. Clinically, extraskeletal osteosarcoma more commonly occurs in middle-aged and elderly populations and often lacks an injury history. Histologically, osteoid components of extraskeletal osteosarcoma are often arranged in a reverse zonation pattern. Obvious cell atypia with pathologic mitosis can be present among neoplastic cells (44). In addition, *USP6*-associated soft tissue tumors with bone metaplasia need to be differentiated from other osteogenic sarcomas, such as malignant peripheral nerve sheath tumors with heterogeneous bone differentiation and dedifferentiated liposarcomas with heterogeneous bone differentiation. Malignant peripheral nerve sheath tumors is usually a rare, high-grade sarcoma with high morphological heterogeneity. The tumor cells are long and fusiform with wavy, curved, comma-shaped or asymmetrically ovoid nuclei, the chromatin is usually uniform or dense, and pathological mitosis is easy to observe. Complete loss of H3K27me3 along with *SUZ12* and *EED* gene deletions are frequently seen in this entity (45), which are invaluable in the diagnosis of challenging cases. For dedifferentiated liposarcomas with heterogeneous bone differentiation, except for dedifferentiated bone elements, well-differentiated liposarcomatous components are characteristically present. More importantly, consistent *MDM2* and/or *CDK4* amplification is present in dedifferentiated liposarcomas (46), which is absent in *USP6*-associated soft tissue tumors with bone metaplasia. In addition to those malignant tumors, *USP6*-associated soft tissue tumors with bone metaplasia should also be differentiated from some benign lesions, including proliferative fasciitis/proliferative myositis, bizarre parosteal ostochondromatous proliferation (Nora's lesion) and subungual exostosis. Proliferative fasciitis/proliferative myositis is a type of myofibroblast/fibroblast proliferative disease that occurs in the subcutaneous fascia and muscle. It is characterized by a scattered distribution of ganglion-like cells, interstitial mucinous degeneration and collagenization in the background (47). In addition, no *USP6* rearrangement was identified in proliferative fasciitis/proliferative myositis, indicating that proliferative fasciitis/proliferative myositis is a real reparative lesion instead of a neoplastic change. Nora's lesion often presents bizarre, enlarged nuclei and stroma with a characteristically basophilic tinctorial quality. Additionally, genetic changes with t(1;17) (q32; q21) and inv (7) and inv (6) were recurrently identified in Nora's lesion and were not commonly seen in FOPD, MO and FO (48). FOPD should also be distinguished from subungual exostosis, as it is more prone to involve digits. Unlike FOPD, subungual exostosis commonly presents as a lesion with an irregular bone-cartilage interface with enlarged, atypical and binucleated chondrocytes histologically and harbors a t(X;6) (q24-q26; q15-q25) change genetically (49). In clinical practice, molecular testing is usually unnecessary for clinically and histologically typical cases. However, in challenging cases, *USP6* FISH, RT-PCR and/or NGS may be used to confirm the diagnosis. We recommend the

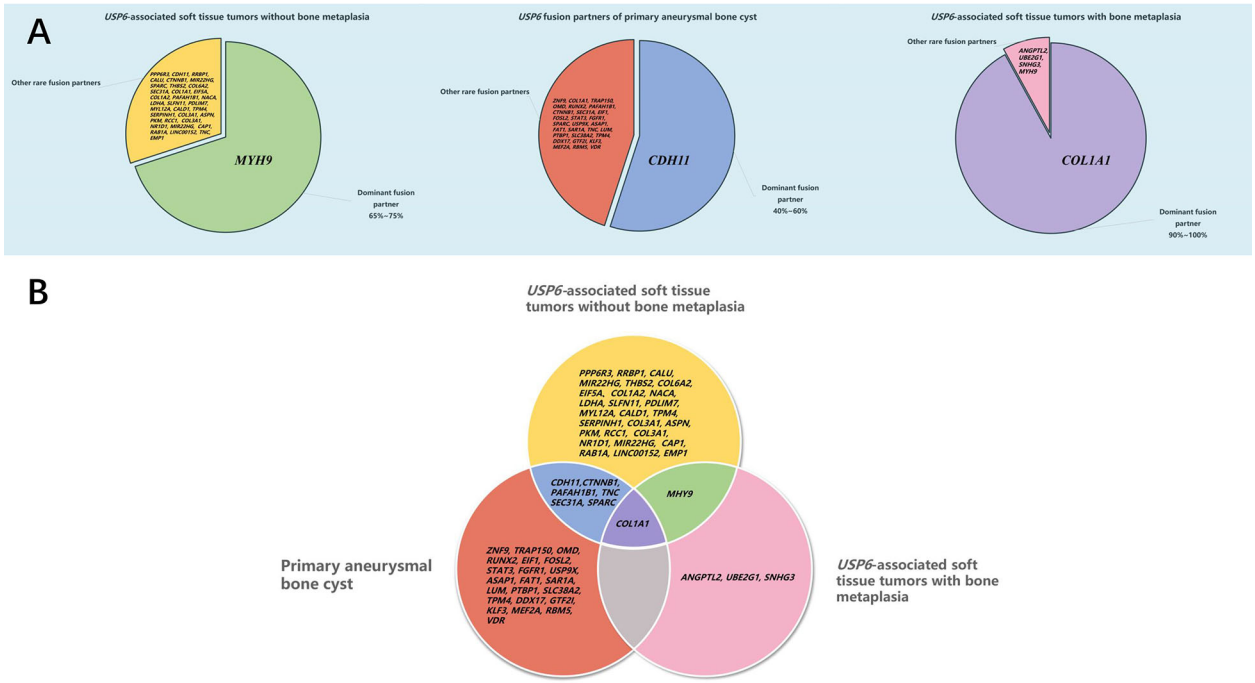

FIGURE 7
Distribution of *USP6* fusion partners in *USP6*-associated tumors. **(A)** Distribution of the *USP6* fusion gene in different *USP6*-associated tumors. **(B)** Overlap of the *USP6* fusion gene in different *USP6*-associated tumors.

diagnostic algorithm shown in the figure to reduce misdiagnosis as much as possible (Figure 8).

USP6-associated soft tissue tumors with bone metaplasia are benign lesions. Currently, local resection is the most commonly used and most effective treatment. Postoperative recurrence is rare (16). Patients with incomplete resection are likely to experience recurrence. In our study, among the patients with follow-up information, 4 patients who received biopsy only survived with tumors without tumor progression; most of the patients showed no evidence for recurrence, while 5 patients (5/32, 15.6%), including 2 MOs, 2 FOPDs and 1 FO, showed recurrence after surgery. Those two FOPD patients underwent partial resection with positive margins to retain the normal function of the finger or toe, and one MO was not completely curetted, which may lead to relapses of these tumors. Another MO and FO with recurrence underwent complete local

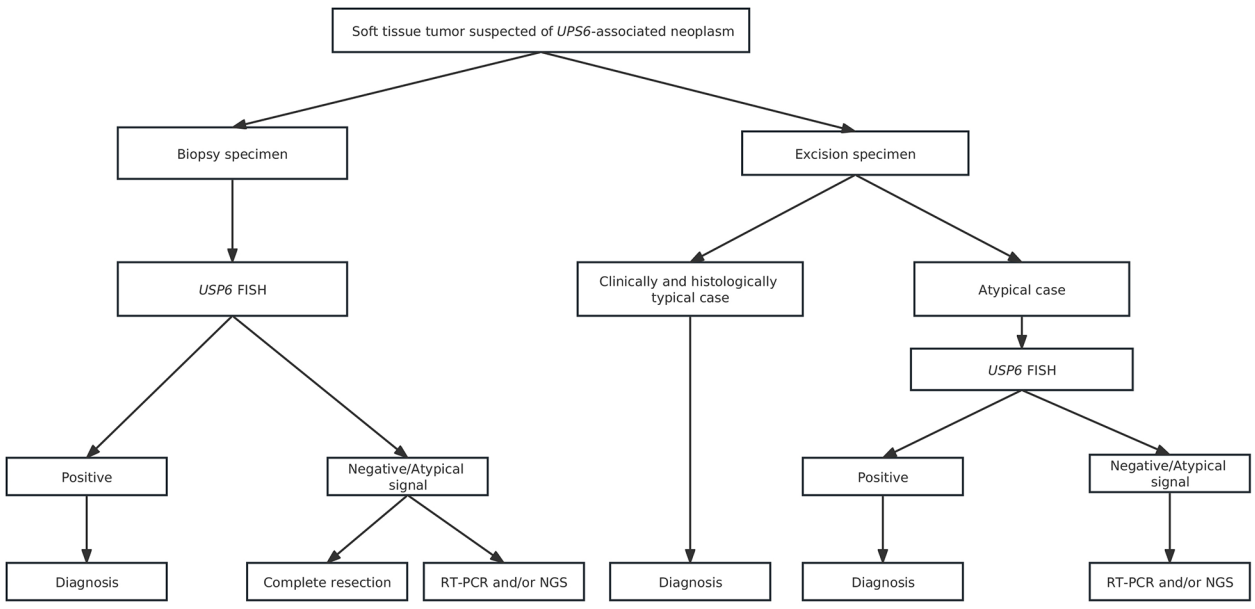

FIGURE 8
Diagnostic algorithm for soft tissue tumors suspected of *UPS6*-associated neoplasms.

resection and showed a large tumor size of over 10.0 cm (10.0 cm and 12.0 cm). In this study, the tumor volumes of 2 cases with recurrence after complete resection were large (over 10.0 cm), among which one case also harbored a rare fusion site (Case 63) (the other case did not undergo genetic testing due to sample decalcification). Notably, the FO recurrent case (Case 63) had special histological morphology. Some areas of the tumor showed invasive growth, with the active proliferation of myofibroblasts/fibroblasts, messy distribution of osteoid tissue, and reverse distribution of focal areas similar to osteosarcoma (Figures 3B–D). Due to the large size of the tumor, osteosarcoma could not be excluded from the original diagnosis after the lesion recurrence, and the diagnosis of FO was finally confirmed by *USP6* FISH test. However, whether these were related to clinical conditions (especially biological behavior) still needs to be further studied by increasing the number of cases. Given the nature of this group of tumors, if the lesion can be diagnosed in the biopsy, it may provide more treatment options for patients. However, due to the small size of biopsies, it is difficult to diagnose these tumors only by histology and immunohistochemistry. FISH detection of *USP6* rearrangement will be valuable for clarifying the diagnosis, and the method of surgery can be determined according to the tumor size, location, and follow-up.

Conclusions

In summary, *USP6*-associated soft tissue tumors with bone metaplasia include MO, FOPD, ST-ABC and FO. Here, we explored the peculiar clinicopathologic and molecular features of this entity in one of the largest cohorts. Tumors can occur in all age groups but most often affect young adults. Different subtypes of this entity not only share overlapping clinicopathological features but also exhibit similar genetic changes, namely, consistent *USP6* rearrangement and frequent *COL1A1*::*USP6* fusion. Notably, for FO, the lower limbs are commonly involved sites, and *COL1A1* is the most frequent fusion partner, suggesting that FO may be closer to MO/FOPD and ST-ABC than conventional NF. Another point we should address is that *MYH9*::*USP6* was first identified in MO, and the novel *USP6* fusion partners *UBE2G1* and *SNHG3* were uncovered in one case with MO and one case with FO, respectively, expanding our knowledge of *USP6*-associated soft tissue tumors with bone metaplasia. The prognosis of this entity is good, and local complete resection is the most effective treatment. Recurrence may be associated with incomplete resection and/or large tumor size (over 10.0 cm), and whether rare fusion sites or novel/uncommon fusion partners are correlated with clinical parameters still needs to be further studied in larger cohorts.

Data availability statement

The raw data supporting the conclusions of this article will be made available by the authors, without undue reservation.

Ethics statement

This study was approved by the Ethics Committee on Biomedical Research, West China Hospital of Sichuan University (No. 793, 2021). Approval for waiver of informed consent was obtained for this study.

Author contributions

YZ: collected the clinicopathological data, performed the histopathological examinations, and molecular detection, and prepared the manuscript. YQ: analyzed the molecular data and prepared the manuscript. XZ: performed the histopathological examinations. XH and CC: helped with data review. MC: helped with molecular experiments. HZ: the corresponding author, was responsible for study design, histopathological and molecular examinations, and manuscript revision. All authors contributed to the article and approved the submitted version.

Funding

This work was supported by the National Natural Science Foundation of China (No. 81972520) and the 1·3·5 project for disciplines of excellence–Clinical Research Incubation Project, West China Hospital, Sichuan University (No. 2018HXFH011).

Conflict of interest

The authors declare that the research was conducted in the absence of any commercial or financial relationships that could be construed as a potential conflict of interest.

Publisher's note

Supplementary material

The Supplementary Material for this article can be found online at: https://www.frontiersin.org/articles/10.3389/fonc.2022.1065071/full#supplementary-material

References

1. Oliveira AM, Chou MM. USP6-induced neoplasms: the biologic spectrum of aneurysmal bone cyst and nodular fasciitis. *Hum Pathol* (2014) 45(1):1–11. doi: 10.1016/j.humpath.2013.03.005

2. Oliveira AM, Perez-Atayde AR, Inwards CY, Medeiros F, Derr V, Hsi BL, et al. USP6 and CDH11 oncogenes identify the neoplastic cell in primary aneurysmal bone cysts and are absent in so-called secondary aneurysmal bone cysts. *Am J Pathol* (2004) 165 (5):1773–80. doi: 10.1016/s0002-9440(10)63432-3

3. Guseva NV, Jaber O, Tanas MR, Stence AA, Sompallae R, Schade J, et al. Anchored multiplex PCR for targeted next-generation sequencing reveals recurrent and novel USP6 fusions and upregulation of USP6 expression in aneurysmal bone cyst. *Genes Chromosomes Cancer* (2017) 56(4):266–77. doi: 10.1002/gcc.22432

4. Erickson-Johnson MR, Chou MM, Evers BR, Roth CW, Seys AR, Jin L, et al. Nodular fasciitis: a novel model of transient neoplasia induced by MYH9-USP6 gene fusion. *Lab Invest* (2011) 91(10):1427–33. doi: 10.1038/labinvest.2011.118

5. Wang JC, Li WS, Kao YC, Lee JC, Lee PH, Huang SC, et al. Clinicopathological and molecular characterisation of USP6-rearranged soft tissue neoplasms: the evidence of genetic relatedness indicates an expanding family with variable bone-forming capacity. *Histopathology* (2021) 78(5):676–89. doi: 10.1111/his.14268

6. Jacquot C, Szymanska J, Nemana LJ, Steinbach LS, Horvai AE. Soft-tissue aneurysmal bone cyst with translocation t(17;17)(p13;q21) corresponding to COL1A1 and USP6 loci. *Skeletal Radiol* (2015) 44(11):1695–9. doi: 10.1007/s00256-015-2205-6

7. Carter JM, Wang X, Dong J, Westendorf J, Chou MM, Oliveira AM. USP6 genetic rearrangements in cellular fibroma of tendon sheath. *Mod Pathol* (2016) 29(8):865–9. doi: 10.1038/modpathol.2016.83

8. Bekers EM, Eijkelenboom A, Grünberg K, Roverts RC, de Rooy JWJ, van der Geest ICM, et al. Myositis ossificans - another condition with USP6 rearrangement, providing evidence of a relationship with nodular fasciitis and aneurysmal bone cyst. *Ann Diagn Pathol* (2018) 34:56–9. doi: 10.1016/j.anndiagpath.2018.01.006

9. Flucke U, Shepard SJ, Bekers EM, Tirabosco R, van Diest PJ, Creytens D, et al. Fibro-osseous pseudotumor of digits - expanding the spectrum of clonal transient neoplasms harboring USP6 rearrangement. *Ann Diagn Pathol* (2018) 35:53–5. doi: 10.1016/j.anndiagpath.2018.05.003

10. Švajdler M, Michal M, Martínek P, Ptáková N, Kinkor Z, Szépe P, et al. Fibro-osseous pseudotumor of digits and myositis ossificans show consistent COL1A1-USP6 rearrangement: a clinicopathological and genetic study of 27 cases. *Hum Pathol* (2019) 88:39–47. doi: 10.1016/j.humpath.2019.02.009

11. Lu Y, He X, Qiu Y, Chen H, Zhuang H, Yao J, et al. Novel CTNNB1-USP6 fusion in intravascular fasciitis of the large vein identified by next-generation sequencing. *Virchows Arch* (2020) 477(3):455–59. doi: 10.1007/s00428-020-02792-x

12. Salib C, Edelman M, Lilly J, Fantasia JE, Yancoskie AE. USP6 gene rearrangement by FISH analysis in cranial fasciitis: A report of three cases. *Head Neck Pathol* (2020) 14 (1):257–61. doi: 10.1007/s12105-019-01018-0

13. Malik F, Wang L, Yu Z, Edelman MC, Miles L, Clay MR, et al. Benign infiltrative myofibroblastic neoplasms of childhood with USP6 gene rearrangement. *Histopathology* (2020) 77(5):760–68. doi: 10.1111/his.14182

14. Pižem J, Matjašič A, Zupan A, Luzar B, Šekoranja D, Dimnik K. Fibroma of tendon sheath is defined by a USP6 gene fusion-morphologic and molecular reappraisal of the entity. *Mod Pathol* (2021) 34(10):1876–88. doi: 10.1038/s41379-021-00836-4

15. Qiu Y, Peng R, Chen H, Zhuang H, He X, Zhang H. Atypical nodular fasciitis with a novel PAFAH1B1-USP6 fusion in a 22-month-old boy. *Virchows Arch* (2021) 479 (3):623–29. doi: 10.1007/s00428-020-02961-y

16. Oliveira AM, Rosenberg AE. Myositis ossificans and fibro-osseous pseudotumour of digits. In: *World health organization classification of tumors: soft tissue and bone tumours, 5th ed*. France: Lyon (2020). p. 53–4.

17. Zhang L, Hwang S, Benayed R, Zhu GG, Mullaney KA, Rios KM, et al. Myositis ossificans-like soft tissue aneurysmal bone cyst: a clinical, radiological, and pathological study of seven cases with COL1A1-USP6 fusion and a novel ANGPTL2-USP6 fusion. *Mod Pathol* (2020) 33(8):1492–504. doi: 10.1038/s41379-020-0513-4

18. Oliveira AM, Wang J, Wang WL. Nodular fasciitis. In: *World health organization classification of tumors: soft tissue and bone tumours, 5th ed*. Lyon: IARC press (2020). p. 49–50.

19. Song W, Suurmeijer AJH, Bollen SM, Cleton-Jansen AM, Bovée J, Kroon HM. Soft tissue aneurysmal bone cyst: six new cases with imaging details, molecular pathology, and review of the literature. *Skeletal Radiol* (2019) 48(7):1059–67. doi: 10.1007/s00256-018-3135-x

20. Nielsen GP, Fletcher CD, Smith MA, Rybak L, Rosenberg AE. Soft tissue aneurysmal bone cyst: a clinicopathologic study of five cases. *Am J Surg Pathol* (2002) 26(1):64–9. doi: 10.1097/00000478-200201000-00007

21. Sukov WR, Franco MF, Erickson-Johnson M, Chou MM, Unni KK, Wenger DE, et al. Frequency of USP6 rearrangements in myositis ossificans, brown tumor, and cherubism: molecular cytogenetic evidence that a subset of "myositis ossificans-like lesions" are the early phases in the formation of soft-tissue aneurysmal bone cyst. *Skeletal Radiol* (2008) 37(4):321–7. doi: 10.1007/s00256-007-0442-z

22. Stražar K, Šekoranja D, Matjašič A, Zupan A, Snoj Ž, Martinčič D, et al. Intraarticular nodular fasciitis-detection of USP6 gene fusions in three cases by targeted RNA sequencing. *Virchows Arch* (2021) 478(6):1117–24. doi: 10.1007/s00428-020-02991-6

23. Dermawan JK, Cheng YW, Tu ZJ, Meyer A, Habeeb O, Zou Y, et al. Diagnostic utility of a custom 34-gene anchored multiplex PCR-based next-generation sequencing fusion panel for the diagnosis of bone and soft tissue neoplasms with identification of novel USP6 fusion partners in aneurysmal bone cysts. *Arch Pathol Lab Med* (2021) 145 (7):851–63. doi: 10.5858/arpa.2020-0336-OA

24. Eisenberg JM, Buckwalter VJ, Snow AN, Davick J. Cellular fibroma of tendon sheath with novel TNC-USP6 gene fusion clinically mimicking arthritis in a 7-Year-Old boy. *Pediatr Dev Pathol* (2022) 25(2):192–96. doi: 10.1177/10935266211043869

25. Hiemcke-Jiwa LS, van Gorp JM, Fisher C, Creytens D, van Diest PJ, Flucke U. USP6-associated neoplasms: A rapidly expanding family of lesions. *Int J Surg Pathol* (2020) 28(8):816–25. doi: 10.1177/1066896920938878

26. Legrand M, Jourdan ML, Tallet A, Collin C, Audard V, Larousserie F, et al. Novel partners of USP6 gene in a spectrum of bone and soft tissue lesions. *Virchows Arch* (2021) 479(1):147–56. doi: 10.1007/s00428-021-03047-z

27. Lenz J, Michal M, Svajdler M, Ptakova N, Lenz D, Konecna P, et al. Novel EIF5A-USP6 gene fusion in nodular fasciitis associated with unusual pathologic features: A report of a case and review of the literature. *Am J Dermatopathol* (2020) 42(7):539–43. doi: 10.1097/dad.0000000000001602

28. Mantilla JG, Gross JM, Liu YJ, Hoch BL, Ricciotti RW. Characterization of novel USP6 gene rearrangements in a subset of so-called cellular fibroma of tendon sheath. *Mod Pathol* (2021) 34(1):13–9. doi: 10.1038/s41379-020-0621-1

29. Panagopoulos I, Gorunova L, Andersen K, Lobmaier I, Lund-Iversen M, Micci F, et al. Fusion of the lumican (LUM) gene with the ubiquitin specific peptidase 6 (USP6) gene in an aneurysmal bone cyst carrying a t(12;17)(q21;p13) chromosome translocation. *Cancer Genomics Proteomics* (2020) 17(5):555–61. doi: 10.21873/cgp.20211

30. Papke DJJr., Bredella MA, Lozano-Calderon S, Oliveira AM, Lennerz J, Nielsen GP. Aneurysmal bone cyst with an unusual clinical presentation and a novel VDR-USP6 fusion. *Genes Chromosomes Cancer* (2021) 60(12):833–36. doi: 10.1002/gcc.22989

31. Papke DJJr., Oliveira AM, Chou MM, Fletcher CDM. Morphologically malignant nodular fasciitis with CALD1-USP6 fusion. *Virchows Arch* (2021) 479(5):1007–12. doi: 10.1007/s00428-021-03149-8

32. Rodriguez Pena MDC, Morlote D, Prieto Granada CN. Cutaneous nodular fasciitis with rare TPM4-USP6 fusion. *J Cutan Pathol* (2022) 49(2):196–99. doi: 10.1111/cup.14151

33. Teramura Y, Yamazaki Y, Tanaka M, Sugiura Y, Takazawa Y, Takeuchi K, et al. Case of mesenchymal tumor with the PPP6R3-USP6 fusion, possible nodular fasciitis with malignant transformation. *Pathol Int* (2019) 69(12):706–09. doi: 10.1111/pin.12851

34. Tomassen T, van de Ven C, Anninga J, Koelsche C, Hiemcke-Jiwa LS, Ter Horst S, et al. Nodular fasciitis with malignant morphology and a COL6A2-USP6 fusion: A case report (of a 10-year-old boy). *Int J Surg Pathol* (2021) 29(6):642–47. doi: 10.1177/1066896921996045

35. Warren M, Xu D, Li X. Gene fusions PAFAH1B1-USP6 and RUNX2-USP6 in aneurysmal bone cysts identified by next generation sequencing. *Cancer Genet* (2017) 212-213:13–8. doi: 10.1016/j.cancergen.2017.03.007

36. Oliveira AM, Perez-Atayde AR, Dal Cin P, Gebhardt MC, Chen CJ, Neff JR, et al. Aneurysmal bone cyst variant translocations upregulate USP6 transcription by promoter swapping with the ZNF9, COL1A1, TRAP150, and OMD genes. *Oncogene* (2005) 24 (21):3419–26. doi: 10.1038/sj.onc.1208506

37. Lam SW, Cleton-Jansen AM, Cleven AHG, Ruano D, van Wezel T, Szuhai K, et al. Molecular analysis of gene fusions in bone and soft tissue tumors by anchored multiplex PCR-based targeted next-generation sequencing. *J Mol Diagn* (2018) 20(5):653–63. doi: 10.1016/j.jmoldx.2018.05.007

38. Parkinson B, Patton A, Rogers A, Farhadi HF, Oghumu S, Iwenofu OH. Intraneural nodular fasciitis of the femoral nerve with a unique CTNNB1::USP6 gene fusion: Apropos of a case and review of literature. *Int J Surg Pathol* (2022) 30(6):673–81. doi: 10.1177/10668969221080064

39. Cloutier JM, Kunder CA, Charville GW, Hosfield EM, García JJ, Brown RA, et al. Nodular fasciitis of the breast: clinicopathologic and molecular characterization with identification of novel USP6 fusion partners. *Mod Pathol* (2021) 34(10):1865–75. doi: 10.1038/s41379-021-00844-4

40. Patel NR, Chrisinger JSA, Demicco EG, Sarabia SF, Reuther J, Kumar E, et al. USP6 activation in nodular fasciitis by promoter-swapping gene fusions. *Mod Pathol* (2017) 30 (11):1577–88. doi: 10.1038/modpathol.2017.78

41. Chen G, Liu T, Yu B, Wang B, Peng Q. CircRNA-UBE2G1 regulates LPS-induced osteoarthritis through miR-373/HIF-1a axis. *Cell Cycle* (2020) 19(13):1696–705. doi: 10.1080/15384101.2020.1772545

42. Xu B, Mei J, Ji W, Bian Z, Jiao J, Sun J, et al. LncRNA SNHG3, a potential oncogene in human cancers. *Cancer Cell Int* (2020) 20(1):536. doi: 10.1186/s12935-020-01608-x

43. Paulson VA, Stojanov IA, Wasman JK, Restrepo T, Cano S, Plunkitt J, et al. Recurrent and novel USP6 fusions in cranial fasciitis identified by targeted RNA sequencing. *Mod Pathol* (2020) 33(5):775–80. doi: 10.1038/s41379-019-0422-6

44. Yamashita K, Hameed M. Extraskeletal osteosarcoma. In: *WHO classification of tumours of soft tissue and bone, 5th ed*. Lyon: IARC Press (2020). p. 224–25.

45. Lee W, Teckie S, Wiesner T, Ran L, Prieto Granada CN, Lin M, et al. PRC2 is recurrently inactivated through EED or SUZ12 loss in malignant peripheral nerve sheath tumors. *Nat Genet* (2014) 46(11):1227–32. doi: 10.1038/ng.3095

46. Dei Tos AP, Marino-Enriquez A, Pedeutour F. Dedifferentiated liposarcoma. In: *WHO classification of tumours of soft tissue and bone*, *5th ed*. Lyon: IARC Press (2020). p. 39–41.

47. Wang WL, Lazar AJ. Proliferative fasciitis/Proliferative myositis. In: *WHO classification of tumours of soft tissue and bone*, *5th ed*. Lyon: IARC Press (2020). p. 51–2.

48. Nilsson M, Domanski HA, Mertens F, Mandahl N. Molecular cytogenetic characterization of recurrent translocation breakpoints in bizarre parosteal osteochondromatous proliferation (Nora's lesion). *Hum Pathol* (2004) 35(9):1063–9. doi: 10.1016/j.humpath.2004.02.008

49. Storlazzi CT, Wozniak A, Panagopoulos I, Sciot R, Mandahl N, Mertens F, et al. Rearrangement of the COL12A1 and COL4A5 genes in subungual exostosis: molecular cytogenetic delineation of the tumor-specific translocation t(X;6)(q13-14;q22). *Int J Cancer* (2006) 118(8):1972–6. doi: 10.1002/ijc.21586

frontiers | Frontiers in Oncology

TYPE Original Research
PUBLISHED 27 January 2023
DOI 10.3389/fonc.2023.1017154

OPEN ACCESS

EDITED BY
Ming Zhao,
Zhejiang Provincial People's Hospital, China

REVIEWED BY
Thomas G. Salopek,
University of Alberta, Canada
Joon Hyuk Choi,
Yeungnam University, Republic of Korea

*CORRESPONDENCE
Hongying Zhang
hy_zhang@scu.edu.cn
hy_zh@263.net

†These authors have contributed equally to this work

SPECIALTY SECTION
This article was submitted to Surgical Oncology, a section of the journal Frontiers in Oncology

RECEIVED 11 August 2022
ACCEPTED 02 January 2023
PUBLISHED 27 January 2023

CITATION
Zhang Z, Lu Y, Shi C, Chen M, He X and Zhang H (2023) Pediatric dermatofibrosarcoma protuberans: A clinicopathologic and genetic analysis of 66 cases in the largest institution in Southwest China.
Front. Oncol. 13:1017154.
doi: 10.3389/fonc.2023.1017154

Pediatric dermatofibrosarcoma protuberans: A clinicopathologic and genetic analysis of 66 cases in the largest institution in Southwest China

Zhang Zhang†, Yang Lu†, Changle Shi, Min Chen, Xin He and Hongying Zhang*

Department of Pathology, West China Hospital, Sichuan University, Chengdu, China

Background: Dermatofibrosarcoma protuberans (DFSP) is an uncommon cutaneous tumor in children. Most published articles are sporadic or small series and lack systematically molecular analyses. The aim of our study is to better understand the clinicopathologic and genetic features of these rare lesions.

Methods: All patients diagnosed with DFSP aged ≤ 18 years were retrospectively reviewed from January 2006 to May 2022.

Results: A total of 66 cases (32 male and 34 female patients) were identified, with ages ranging from 0.3 to 18 years (median, 13 years). Tumor locations predominantly occurred on the trunk (38/66, 57.6%), followed by the extremities (20/66, 30.3%) and head/neck (8/66, 12.1%). Histological findings revealed classic (41/66, 62.1%), myxoid (4/66, 6.1%), pigmented (6/66, 9.1%), plaque-like (3/66, 4.5%), giant cell fibroblastoma (GCF; 6/66, 9.1%), and fibrosarcomatous (6/66, 9.1%) variants of DFSP. Immunochemistry revealed minority tumors (9/66, 13.6%) showing patchy or negative staining for CD34. Fluorescence *in situ* hybridization (FISH) indicated that 49 of 53 tested cases including all detected biopsy specimens (11/11) contained *COL1A1-PDGFB* fusion, in which the average copy number gain of *COL1A1-PDGFB* was 0.68. There were four cases negative for *COL1A1-PDGFB* rearrangement, one of which was found to harbor a novel *COL3A1-PDGFB* fusion by next-generation sequencing (NGS). Treatment for 63 patients comprised 40 marginal excisions and 23 wide local excisions (WLEs), including 1 with imatinib therapy. Follow-up information was available on 49 patients with a duration of 12–161 months (median, 60 months). Fourteen patients developed tumor recurrence, all with initial marginal excisions. The others survived with no evidence of disease.

Conclusions: This study of pediatric DFSP indicates certain discrepancies in clinicopathologic characteristics between children and adults. The majority of pediatric DFSPs contain *COL1A1-PDGFB* fusion, the same as their adult counterparts. The *COL3A1-PDGFB* chimerism might be associated with the special morphology of GCF, which needs further investigation. FISH is valuable in biopsy tissues and cases with atypical CD34 immunostaining, while

supplementary NGS could be helpful to identify the cytogenetically cryptic DFSP. Overall, an urgent accurate diagnosis is needed to formulate an optimal therapeutic strategy in the pediatric population.

KEYWORDS

dermatofibrosarcoma protuberans, giant cell fibroblastoma, pediatric sarcoma, COL1A1-PDGFB fusion, COL3A1-PDGFB fusion, fluorescence *in situ* hybridization, next generation sequencing

Introduction

Dermatofibrosarcoma protuberans (DFSP), one of the most common dermal sarcomas, is a locally infiltrative dermal and subcutaneous fibroblastic tumor of intermediate malignancy (1). According to the 2020 World Health Organization (WHO) classification of soft tissue and bone tumors, the lesion divides into several histologic subtypes, including classic DFSP, pigmented DFSP, myxoid DFSP, DFSP with myoid differentiation, plaque-like DFSP, giant cell fibroblastoma (GCF), and fibrosarcomatous DFSP (FS-DFSP) (1). DFSP can locally recur with a rate of 20%–50%, of which FS-DFSP is the only subtype associated with more aggressive behavior. Approximately 10%–16% of FS-DFSP may develop distant metastases, resulting in a worse prognosis (1–4).

Cytogenetically, more than 90% of DFSP cases are characterized with the collagen type I alpha 1 and platelet-derived growth factor B (*COL1A1-PDGFB*) fusion deriving from supernumerary ring r (17;22) or translocation t (17;22) (q22; q13) (5). The chimeric formation could result in upregulating the PDGFB expression, associated with tumorigenesis and accordingly designed to be the target by tyrosine kinase inhibitors like imatinib mesylate (6). In clinical routine practice, the critical molecular abnormality is exploited to be detected by fluorescence *in situ* hybridization (FISH), aiding in diagnosis and validating targeted molecular therapy in certain circumstances (7, 8).

The incidence of DFSP is approximately 1 case per 1,000,000 person-years of adults predominantly within the second to fifth decades, while even rare in children (9–12). Notably, to the best of our knowledge, previous reports are mostly sporadic or small series and there are only six large analyses involving pediatric DFSP, most of which are absent of detailed histological analysis or systematic molecular studies (11, 13–17). Therefore, we retrospectively evaluated a large series of 66 pediatric DFSPs at the largest institution in Southwest China and aimed to further investigate the clinicopathological features and molecular characteristics.

Materials and methods

Patient acquisition

This study was approved by the West China Hospital Institutional Review Board. A SNOMED search of the hospital surgical pathology and consultation files from January 2006 to May 2022 identified 926 DFSPs. All cases were independently reviewed by two pathologists (HZ and ZZ) who specialized in soft tissue tumors and two general surgical pathologists (XH and YL). The patients diagnosed with DFSP aged ≥ 19 years were considered adult DFSP and were excluded. Finally, 66 DFSP cases aged ≤ 18 years were confirmed as pediatric DFSP and included in this study.

Immunohistochemical staining

Immunohistochemical analysis was performed using the EnVision Plus detection system (DAKO, Carpinteria, CA, USA) with positive and negative controls. Antibodies for the experiments included CD34 (EP88, ready-to-use; ZSGB-Bio), SMA (UMAB237, ready-to-use; ZSGB-Bio), Ki-67 (clone MIB-1, 1:100; Dako), desmin (D33, 1:100; Dako), S-100 protein (4C49, 1:100; Dako), myogenin (F5D, 1:50; ZSGB-Bio), Bcl-2 (EP36, 1:200; ZSGB-Bio), CD99 (EP8, ready-to-use; ZSGB-Bio), p16 (16P04/IC2, ready-to-use; Dako), p63 (4A4, 1:400; Dako), cytokeratin (AE1/AE3, 1:100; Dako), and EMA (E29, 1:100; Dako).

Fluorescence *in situ* hybridization

FISH analyses were performed using commercially available ZytoLight® SPEC *PDGFB* Dual Color Break Apart Probe and ZytoLight® SPEC *COL1A1*/*PDGFB* Dual Color Dual Fusion Probe (ZytoVision, Bremerhaven, Germany). The tests were performed on 4-μm sections according to an established laboratory protocol, as previously described (18). Two investigators independently counted at least 100 nuclei on each slide. A case was considered positive for *PDGFB* rearrangement when at least ≥10% of the cells exhibited a split signal pattern which showed that the distance between the green and red signals was greater than the diameter of two signals. The *COL1A1-PDGFB* fusion was considered positive when at least 10% of the cells showed one separate red signal, one separate green signal, and two red/green fusion signals. The *COL1A1-PDGFB* copy gain was calculated according to the description of Abbott et al. (19).

Next-generation sequencing

Genomic profiling was performed on FFPE tissues with capture-based panel targeting 481 soft tissue tumor-relevant genes. Genomic

DNA was extracted from FFPE tissues using a QIAamp DNA FFPE Tissue Kit (Qiagen, Hilden, Germany) according to the manufacturer's protocol. The eligible DNA was hybridized with the capture probes, selected using magnetic beads, and polymerase chain reaction (PCR)-amplified. Then, library fragment size was determined by Bioanalyzer2100 (Agilent Technologies, Santa Clara, CA). The target-enriched library was sequenced on the Hiseq4000 platform (Illumina, Inc., San Diego, CA) following the manufacturer's instructions. The average sequencing depth was 1000× for all targeted regions.

Polymerase chain reaction and Sanger sequencing

The *COL3A1-PDGFB* fusion was analyzed by PCR using primers (COL3A1-F: 5'-CTTCAGGGTGAGACAGCCAA-3'; PDGFB-R: 5'-CATAAGCCCCCGGATTTGGT-3'). Sanger sequencing was performed at Tsingke Biological Technology Co., Ltd. (Chengdu, China).

Statistical analysis

Statistical analysis was performed using the GraphPad Prism version 5 (GraphPad Software, San Diego, CA). Comparisons between different groups were evaluated using Student's *t*-test and ANOVA for continuous variables. $p < 0.05$ indicates the statistical significance between different groups.

Results

Clinicopathological features of the study cohort

The relevant clinicopathologic data are summarized in Table 1. The study cohort comprised 32 male and 34 female patients (ratio, 1:1.1). The age of the patients ranged from 0.3 to 18 years (median, 13 years; mean, 11.38 years), including 2 infants (2/66, 3.0%; age ≤ 11 months) and 26 children aged less than 10 years (26/66, 39.4%). The tumor size ranged from 0.6 to 8 cm (median, 3 cm; mean, 2.9 cm). The majority of the tumors occurred on the trunk (38/66, 57.6%), followed by the extremities (20/66, 30.3%) and head/neck (8/66, 12.1%). The clinical manifestations commonly presented as nodular or multinodular masses (61/66, 92.4%) and much less in the plaque stage (5/66, 7.6%). The cut surfaces of DFSP were tan and yellow, with rubbery firm to soft gelatinous appearances. There were 15 cases (15/66, 22.7%) who underwent biopsies before treatment.

Histologic features

The tumors were classified according to histologic subtypes into classic DFSP (41/66, 62.1%), myxoid DFSP (4/66, 6.1%), pigmented DFSP (6/66, 9.1%), plaque-like DFSP (3/66, 4.5%), giant cell fibroblastoma (GCF; 6/66, 9.1%), and fibrosarcomatous DFSP (6/66, 9.1%).

Microscopically, the DFSPs diffusely infiltrated into the dermis and subcutis with ill-defined borders, which, with infiltration into the subcutaneous fat, could result in a honeycomb-like appearance. Typically, uniform wavy or spindle tumor cells were proliferative and arranged in a storiform or cartwheel pattern (Figure 1A). In the myxoid subtype (cases 10, 16, 23, and 40), the abundant myxoid stroma with low cellularity and numerous vessels occupied more than 50% of the tumor (Figure 1B). There were six pigmented-subtype tumors (including cases 14, 20, 41, 42, 51, and 58; case 58 was a recurrent lesion), all of which could find that the pigmented dendritic cells were scattered over fibroblastic tumor cells (Figure 1C). The three cases of plaque-like DFSP (cases 24, 61, and 64) were dermal-based lesions, composed of regular plump tumor cells presenting a horizontally oriented arrangement and a focal storiform structure (Figure 1D). In six GCF tumors, a varying number of pleomorphic mononucleated or multinucleated giant cells admixed with spindle cells in the loose myxoid matrix or abundant collagenous stroma. Among them, three were pure GCF (cases 19, 33, and 65) and three were hybrid lesions (cases 7, 57, and 63) that consisted of conventional DFSP and GCF components. Most differently, case 65 uniquely consisted of a higher proportion of neoplasms that were with larger and more atypical giant nuclei compared to that of the other five typical GCFs, which predominantly contained slender wavy spindled cells and sporadic giant cells. The floret-like giant cell-lined pseudovascular spaces and infiltrated subcutaneous fat mimicking liposarcoma were easy to find (Figure 1E). Most of the above variants of DFSP presented low mitotic activity (0–5/10 high-power fields), while one conventional DFSP showed mitotic activity with 11/10 high-power fields. FS-DFSP presented in four primary cases (cases 2, 15, 45, and 60) and two recurrent lesions (cases 1 and 3), whose primary tumors were both confirmed as a conventional DFSP. The fibrosarcomatous component was composed of neoplastic cells with increased cellularity and mitotic activity, arranging in a fascicular pattern with a herringbone appearance (Figure 1F). Necrosis was not identified.

Immunohistochemistry analysis

Immunohistochemical analysis revealed that most of the tumors (57/66, 86.3%) were diffusely positive for CD34, whereas the minority (9/66,13.6%) showed patchy or negative staining. The decreased or lost expression of CD34 was mainly observed in myxoid and fibrosarcomatous areas, originating from three conventional DFSPs, three myxoid DFSPs, two FS-DFSPs, and one GCF (Figure 2). Majority of tumors were negative for smooth muscle actin (SMA), while there were a few cases (9/46, 20%) exhibiting positivity or focal staining. All cases were negative for desmin, S-100 protein, myogenin, Bcl-2, CD99, p16, p63, cytokeratin, and EMA.

Molecular analysis

FISH analysis indicated that 46 cases (46/53, 86.8%) were positive for *PDGFB* in a split-signal pattern. There were four that showed

TABLE 1 Clinicopathological and cytogenetic features of 66 pediatric DFSPs.

No.	Age of operation (years)	Gender	Location	Size (cm)	Primary subtypes	Recurrent subtypes	CD34	SMA	PDGFB break signal	COLA1-PDGFB fusion signal	Surgery	Local recurrence (months)	Metastasis	Died	Follow-up (months)
1	16	F	Abdomen	3.0	Classic	FS	Negative	NA	Positive	Positive	E	40	No	No	NED/115
2	17	F	Shoulder	3.5	FS	FS	Positive	NA	Positive	Positive	E	20	NA	NA	NA
3	15	M	Chest	6.0	Classic	FS	Positive	NA	Positive	Positive	E	55	No	No	NED/114
4	6	M	Chest	2.0	Classic	NA	Positive	NA	Positive	Positive	WE	No	No	No	NED/94
5	16	F	Chest	2.2	Classic	Classic	Positive	NA	Failure	Positive	E	10	No	No	NED/149
6	17	M	Abdomen	2.5	Classic	NA	Positive	Negative	Positive	Positive	E	NA	NA	NA	NA
7	8	M	Shoulder	3.0	GCF	GCF	Positive	Negative	Positive	Positive	E	9, 34	No	No	NED/161
8	15	F	Chest	3.5	Classic	NA	Positive	NA	Positive	Positive	WE	No	No	No	NED/137
9	17	F	Abdomen	1.3	Classic	NA	Positive	NA	Positive	Positive	NA	No	No	No	NED/66
10	12	M	Chest	2.2	Myxoid	NA	Positive	NA	Positive	Positive	WE	No	No	No	NED/74
11	10	M	Chest	5.2	Classic	Classic	Positive	Negative	Positive	Positive	E	13	No	No	NED/81
12	15	F	Abdomen	3.5	Classic	Classic	Positive	Negative	Positive	Positive	E	22	No	No	NED/85
13	17	F	Chest	3.0	Classic	NA	Positive	NA	Failure	Positive	WE	NA	NA	NA	NA
14	4	F	Finger	2.5	Pigmented	Pigmented	Positive	Negative	Positive	Positive	E	5	No	No	NED/61
15	11	M	Forearm	0.7	FS	NA	Positive	Negative	Positive	Positive	WE	No	No	No	NED/60
16	0.3	F	Shoulder	2.8	Myxoid	NA	Patchy	Focal	Negative	Positive	E	No	No	No	NA
17	13	F	Chest	1.2	Classic	NA	Positive	Focal	Positive	Positive	WE	No	No	No	NED/101
18	6	M	Thigh	1.6	Classic	NA	patchy	Negative	Positive	Positive	WE	No	No	No	NED/100
19	3	M	Neck	4.0	GCF	NA	Positive	Negative	Positive	Positive	E	60	No	No	NED/89
20	11	M	Foot	2.0	Pigmented	NA	Positive	Negative	Positive	Positive	NA	No	No	No	NA
21	14	F	Scalp	2.5	Classic	NA	Positive	Negative	Positive	Positive	WE	No	No	No	NED/75
22	18	F	Back	1.8	Classic	NA	Positive	Negative	Positive	Positive	E	No	No	No	NA
23	16	M	Back	1.5	Myxoid	Myxoid	Patchy	Negative	Negative	Negative	E	10	No	No	NED/77
24	18	F	Face	3.0	Plaque-like	NA	Positive	Negative	Positive	Positive	E	No	No	No	NA
25	17	F	Upper arm	4.0	Classic	NA	Positive	Negative	Positive	Positive	WE	No	No	No	NA
26	17	F	Chest	1.0	Classic	NA	Positive	Negative	Positive	Positive	E	No	No	No	NA

(Continued)

10.3389/fonc.2023.1017154

TABLE 1 Continued

No.	Age of operation (years)	Gender	Location	Size (cm)	Primary subtypes	Recurrent subtypes	CD34	SMA	PDGFB break signal	COLA1-PDGFB fusion signal	Surgery	Local recurrence (months)	Metastasis	Died	Follow-up (months)
27	7	M	Leg	1.0	Classic	NA	Positive	Negative	NA	NA	E	No	No	No	NED/82
28	17	M	Back	5.0	Classic	NA	patchy	Negative	NA	NA	E	No	No	No	NED/79
29	18	M	Head	2.5	Classic	NA	Positive	Focal	NA	NA	E	No	No	No	NED/73
30	4	F	Back	3.0	Classic	NA	Positive	Negative	NA	NA	WE	No	No	No	NED/15
31	17	M	Thigh	NA	Classic	NA	Positive	Negative	Positive	Positive	WE	No	No	No	NED/14
32	17	M	Abdomen	3.5	Classic	NA	Positive	Focal	NA	NA	E	No	No	No	NED/69
33	0.9	M	Chest	4.0	GCF	NA	Positive	Negative	Positive	Positive	WE	No	No	No	NED/59
34	9	M	Thigh	NA	Classic	NA	Positive	Negative	NA	NA	E	No	No	No	NED/58
35	9	F	Waist	NA	Classic	NA	Positive	Negative	NA	NA	E	No	No	No	NED/29
36	8	F	Abdomen	NA	Classic	NA	Positive	Negative	NA	NA	E	No	No	No	NED/50
37	7	F	Abdomen	NA	Classic	NA	Positive	Negative	Positive	Positive	E	No	No	No	NED/26
38	6	M	Chest	NA	Classic	NA	Positive	Negative	Positive	Positive	WE	No	No	No	NED/9
39	5	M	Leg	NA	Classic	NA	Positive	Focal	Positive	Positive	WE	No	No	No	NA
40	4	M	Neck	2.8	Myxoid	NA	Patchy	NA	Positive	Positive	E	8	No	No	NED/27
41	4	F	Forearm	3.0	Pigmented	NA	Positive	Negative	Positive	Positive	E	16	No	No	NED/45
42	1	F	Hip	4.0	Pigmented	NA	Positive	Negative	Negative	Negative	E	No	No	No	NED/44
43	18	M	Abdomen	NA	Classic	NA	Positive	NA	Positive	Positive	E	No	No	No	NED/44
44	18	F	Abdomen	NA	Classic	NA	Positive	Negative	NA	NA	E	12, 12, 48	No	No	NED/66
45	18	F	Groin	NA	FS	NA	Patchy	Negative	NA	NA	WE	No	No	No	NED/48
46	15	M	Axilla	3.0	Classic	NA	Positive	Negative	Positive	Positive	WE	No	No	No	NED/26
47	14	F	Breast	NA	Classic	NA	Positive	NA	NA	NA	NA	No	No	No	NA
48	14	F	Neck	NA	Classic	NA	Positive	NA	Positive	Positive	WE	No	No	No	NED/54
49	13	F	Abdomen	NA	Classic	NA	Positive	Negative	NA	NA	WE	No	No	No	NED/26
50	13	M	Back	8.0	Classic	NA	Positive	NA	Positive	Positive	WE	No	No	No	NED/34
51	12	M	Shoulder	NA	Pigmented	NA	Positive	NA	NA	NA	E	No	No	No	NED/23
52	13	F	Forehead	NA	Classic	NA	Negative	NA	Negative	Negative	E	No	No	No	NA

(Continued)

10.3389/fonc.2023.1017154

TABLE 1 Continued

No.	Age of operation (years)	Gender	Location	Size (cm)	Primary subtypes	Recurrent subtypes	CD34	SMA	PDGFB break signal	COLA1-PDGFB fusion signal	Surgery	Local recurrence (months)	Metastasis	Died	Follow-up (months)
53	18	F	Breast	NA	Classic	NA	Positive	NA	Positive	Positive	WE	No	No	No	NED/61
54	3	M	Scalp	NA	Classic	NA	Positive	Negative	Positive	NA	E	No	No	No	NED/23
55	15	F	Shoulder	NA	Classic	NA	Positive	Negative	Positive	Positive	E	No	No	No	NED/22
56	6	M	Abdomen	NA	Classic	NA	Positive	Negative	Positive	Positive	WE	No	No	No	NED/21
57	5	F	Sacrococcygeal region	3.0	GCF	NA	Positive	Positive	Positive	Positive	E	No	No	No	NA
58	11	M	Forearm	3.0	NA	Pigmented	Positive	Focal	Positive	Positive	E	72	No	No	NED/84
59	18	F	Breast	0.6	Classic	NA	Positive	NA	Positive	Positive	E	No	No	No	NED/12
60	11	M	Thigh	NA	FS	NA	Positive	NA	Positive	Positive	E	72	No	No	NED/88
61	9	F	Breast	NA	Plaque-like	NA	Positive	Focal	Positive	Positive	E	No	No	No	NED/57
62	17	F	Abdomen	NA	Classic	NA	Positive	NA	Positive	Positive	WE	No	No	No	NED/12
63	2	M	Groin	3.0	GCF	NA	Positive	Negative	Positive	Positive	E	No	No	No	NED/25
64	10	M	Waist	NA	Plaque-like	NA	Positive	Negative	Positive	Positive	WE	No	No	No	NED/2
65	2	M	Forearm	NA	GCF	NA	Patchy	NA	Ambiguous	Negative	E	No	No	No	2
66	13	F	Groin	NA	Classic	NA	Positive	Negative	Positive	Positive	E	No	No	No	1

FS, fibrosarcomatous; GCF, giant cell fibroblastoma; NA, not available; E, excision; WE, wide excision; NED, no evidence of disease.

10.3389/fonc.2023.1017154

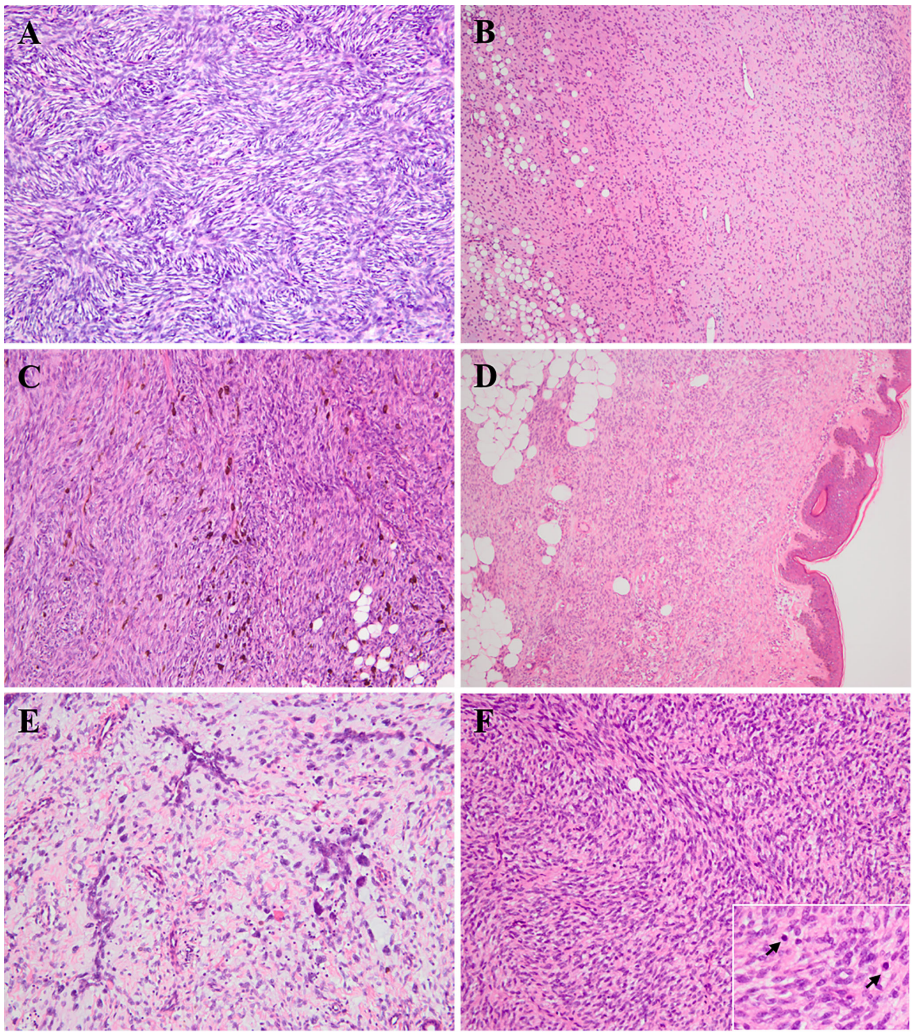

FIGURE 1
Histologic findings of various subtypes of pediatric DFSP. **(A)** Conventional DFSP. The lesion consisted of uniform bland spindled neoplastic cells arranged in a classic cartwheel pattern (H&E × 200). **(B)** Myxoid DFSP. The tumor had relatively low cellularity and consisted of pump spindle or stellated tumor cells diffusely distributed in prominent myxoid architecture with numerous vessels (H&E × 100). **(C)** Pigmented DFSP. The dendritic cells with melanin pigment punctuated within monotonous storiform area of conventional DFSP (H&E × 200). **(D)** Plaque-like DFSP. The dermal-based lesion composed of regular plump tumor cells presenting a horizontally oriented arrangement and a focal storiform structure (H&E × 100). **(E)** Giant cell fibroblastoma (case 65). High proportion of hyperchromatic multinucleated giant cells scattered in the loosely fibrous and myxoid stroma, and lined pseudovascular spaces (H&E × 200). **(F)** Fibrosarcomatous DFSP. The lesion was composed of high-grade fibrosarcoma-like component, showing a typical herringbone appearance with increasing mitoses (H&E × 200; insert × 400).

negative results of *PDGFB* rearrangement (cases 16, 23, 42, and 52), in one of which (case 16) *COL1A1-PDGFB* fusion was detected. One case exhibited an ambiguous result of *PDGFB* rearrangement (case 65). The last two cases failed the experiment (cases 5 and 13). The median *COL1A1-PDGFB* copy gain of pediatric DFSP was 0.7 (range 0–1.8; mean ± SD, 0.68 ± 0.46). Not much different from the classic DFSP, the median *COL1A1-PDGFB* copy gain in the FS subtype was 0.6 (range 0–1.1; mean ± SD, 0.58 ± 0.40) ($p = 0.64$), while in the GCF subtype, the median *COL1A1-PDGFB* copy gain was 0.45 (range 0–1.25; mean ± SD, 0.49 ± 0.50) ($p = 0.36$) (Figures 3A–C).

Moreover, 49 of 53 tested cases (92.5%) including all detected biopsy specimens (11/11, 100%) contained *COL1A1-PDGFB* fusion, while 4 cases were negative for *COL1A1-PDGFB* based on the routine FISH screening (cases 23, 42, 52, and 65). One case (case 65) with suspicious *PDGFB* split but *COL1A1-PDGFB* fusion negative was found to harbor a novel *COL3A1-PDGFB* fusion through NGS. The PCR and Sanger sequencing further confirmed the *COL3A1-PDGFB* fusion gene (Figure 3D).

Treatment and follow-up

The treatment and follow-up information is detailed in Table 1. Surgical strategies for 63 patients were composed of marginal excisions (40/63, 63.5%) and WLE (23/63, 36.5%). Eight cases (8/15, 53.3%) underwent WLE after biopsies. One (case 14) underwent finger amputation for recurrent tumor therapy. Targeted therapy with imatinib mesylate was administered to one patient (case 7) after tumor excision on the second relapse.

Follow-up information was available on 49 patients (49/66, 74.2%) with a duration from 12 to 161 months (median, 60 months). Fourteen patients (14/49, 28.5%) developed recurrence, all

10.3389/fonc.2023.1017154

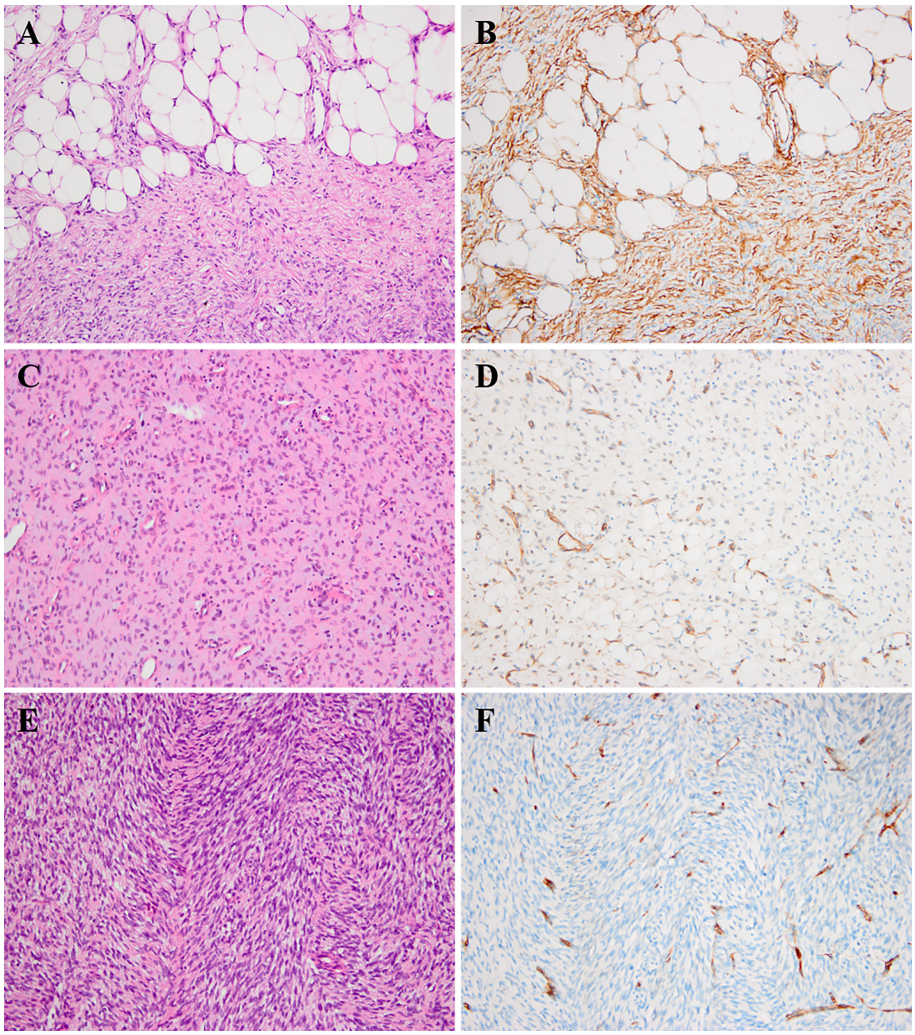

FIGURE 2
Histologic findings of DFSP and corresponding immunohistochemical images. **(A, B)** The neoplastic cells infiltrated into subcutaneous fat tissues forming a characteristic "honeycomb" pattern (**A,** H&E × 200). The corresponding component showed diffuse positivity for CD34 (**B,** × 200). **(C, D)** The myxoid component of DFSP (case 40) could show patchy or focal staining for CD34 (**C**, H&E × 200; **D**, × 200). **(E, F)** The fibrosarcomatous component of DFSP (case 1) could exhibit loss for CD34 staining (**E,** H&E × 200; **F,** × 200).

with marginal excisions with positive margins. The others survived with no evidence of disease.

Discussion

The occurrence of DFSP could involve people of all ages, from neonates to old adults (13, 20–22). Pediatric DFSPs were uncommon, which accounted for only 7.1% (66/926) of all DFSPs in our medical center. Among the DFSPs, the GCF subtype occurred mainly within 10 years old, which was consistent with previous observations as a pediatric-predominance subtype. The cohort of DFSP displayed a slight female predilection (M:F = 1:1.1), which was similar to the US pediatric population (11). Consistently, GCF occurred significantly in the male sex (M:F = 5:1) as the tendency of literature presenting male predominance in children diagnosed GCF (13, 14). The tumors in our cases were widespread and were predominantly distributed on the trunk (57.6%), followed by the extremities (30.3%) and head/neck (12.1%). Moreover, functional vitals or cosmetic positions including breast (4/66, 6%), groin (3/66, 4.5%), scalp (2/66, 3%), and face (1/66, 1.5%) could be involved and were rarely mentioned in children according to previous findings (12, 23, 24).

The distribution spectrum of the subtype exhibited some differences between pediatric and adult DFSPs. In the adult population, conventional DFSP was the most predominant subtype, which constituted approximately 61.3%–91% of DFSPs in previous studies, followed by FS-DFSP (10%–16%), myxoid DFSP (7.6%), pigmented DFSP (2.7%–5%), GCF (2.7%), and plaque-like DFSP (1.3%–1.7%) (3, 25–29). According to the results with detailed constitution of pediatric DFSP variants in this large cohort, the incidence of conventional DFSP (62.1%), FS-DFSP (9.1%), and myxoid DFSP (6.1%) was close to the lower limit of the adult counterparts, while pigmented DFSP (9.1%), GCF (9.1%), and plaque-like DFSP (4.5%) were higher than that of the adult.

CD34 is the most frequently used immunohistochemical marker for the diagnosis of DFSP. Typically, DFSP stains positive for CD34 in about 90% of tumors and mostly shows negativity for SMA (30, 31). In our series, 86.3% of cases were diffusely positive for CD34

10.3389/fonc.2023.1017154

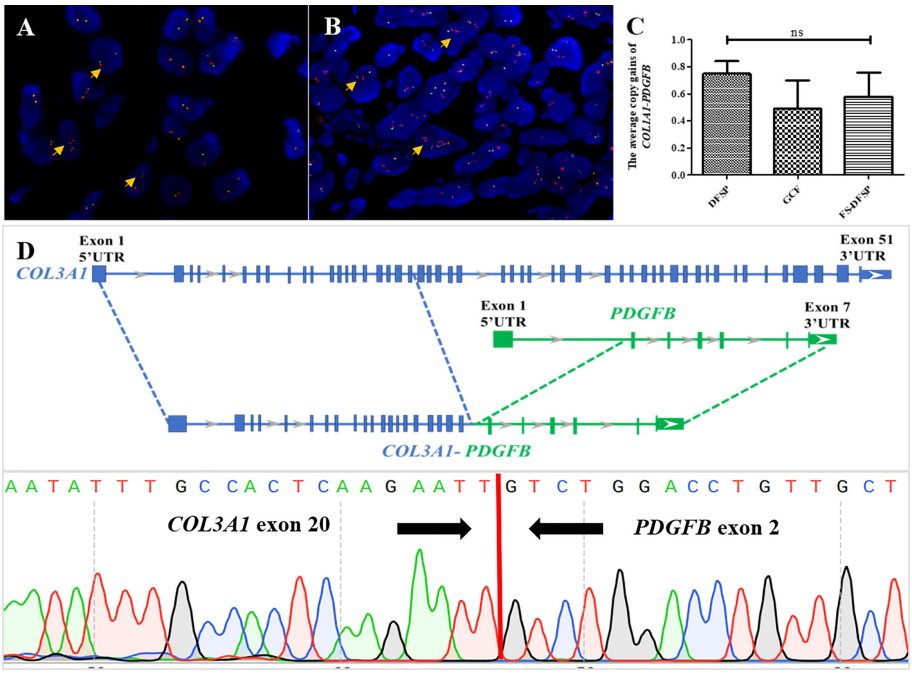

FIGURE 3
Molecular findings of pediatric DFSP. **(A)** FISH was performed on the DFSP component using a *PDGFB* break-apart probe to the locus on chromosome 22. The results showed several tumor cells with one red–green signal indicating a normal chromosome 22; one separate red and one separate green signal indicating a *COL1A1-PDGFB* fusion gene with no extra copies of red signal (orange arrows) (*PDGFB*, red signals and green signals). **(B)** FISH was performed on the DFSP component using a *PDGFB* break-apart probe to the locus on chromosome 22. The results showed several tumor cells with one red–green signal indicating a normal chromosome 22 and one to three extra copies of red signal (orange arrows) indicating a *COL1A1-PDGFB* fusion gene (*PDGFB*, red signals and green signals). **(C)** Comparison among DFSP (left column) and the GCF and the FS-DFSP (right two columns) indicated that there was not much difference in average *COL1A1-PDGFB* copy gains of pediatric DFSP. **(D)** Next-generation sequencing revealed case 65 with a novel *COL3A1* (e20)-*PDGFB* (e2) fusion (upper part); Sanger sequencing results demonstrated the presence of the *COL3A1-PDGFB* fusion gene (lower part).

expression, whereas diminished or absent staining presented in approximately 13.6% of pediatric DFSP cases. The decreased or lost expression of CD34 was mainly observed in myxoid and fibrosarcomatous areas, as published (3, 14, 32, 33). One case of classic DFSP showed a lack of CD34 expression (case 52), which two pathologists independently reviewed, arriving at a diagnosis of classic DFSP based on the typical histology. FISH utilizing the PDGFB break-apart probe revealed unbalanced translocation presenting additional 3'-red signals in 5% of these tumor cells, while the COL1A1-PDGFB fusion probe showed yellow signal denoting a fusion pattern in 2% of tumor cells. This case might show cryptic rearrangement associated with DFSP. Regretfully, the specimen could not be further investigated using NGS because of poor quality.

Evidence of *COL1A1-PDGFB* rearrangement is the key to the differential diagnosis of difficult cases and is inevitable for the effective application of targeted treatment. FISH has shown the validity for confirmation of the *COL1A1-PDGFB* fusion and it was widely applied to clinical detection. In our children's series, 92.5% of children's DFSPs were confirmed positive results by using the *PDGFB* break-apart probe and the *COL1A1-PDGFB* fusion probe as routine screening methods, similar to the previous FISH studies with detectable rate ranging from 86% to 96% (7, 8, 34). In addition, the fusion product *COL1A1-PDGFB* was amplified with low levels of the17q and 22q sequences (usually one to three copies), which could be detectable by either FISH or comparative genomic hybridization (GCH) (19, 35). In our study, we found that the average gains of the *COL1A1-PDGFB* fusion gene showed no statistical difference in ordinary DFSP, FS-DFSP, and GCF groups of children, among which the GCF cases presented the lowest average genomic gains. While correlated studies were scarce in children, more samples and deeper investigations are needed to further reveal the meaning of the molecular characters in pediatric patients.

Nevertheless, based on previous studies, a minority of DFSP cases with uncertain or negative results based on routine FISH assays are considered to be molecular unconfirmed DFSP and might result in inaccurate diagnosis (36). Application of supplementary NGS approaches would be of value to fusion detection (37). In our cohort, 7.5% (4/53) of pediatric DFSPs exhibited molecular unconfirmed characteristics. After carefully reviewing the published English articles, we included two studies and collected a total of seven pediatric DFSPs (including the four pediatric cases in our cohort) considered to be molecular unconfirmed based on routine FISH detection, the clinicopathological and molecular characteristics of which are summarized in Table 2. The clinicopathological features of most cases seem to not differ from the corresponding subtypes except one GCF (present case 65) with atypical morphology. Genetically important, NGS revealed the GCF containing a novel *COL3A1-PDGFB* fusion that was first presented in DFSP. *COL3A1*, located in 2q32.2, belongs to the collagen genes together with *COL1A1* and *COL1A2*, and encodes a structural protein of type III collagen, which is found in abundance in extensible connective tissues, such as skin, blood vessels, gastrointestinal tract, and the developing brain (38–41). The translocation of *COL3A1* had been reported as a rare partner fusing to *PLAG1*-rearranged neoplasms (including lipoblastoma and

TABLE 2 Clinicopathologic and molecular characteristics of 7 cytogenetically cryptic DFSPs in children.

No.	Gender/ Age	Location	Histologic findings	Diagnosis	CD34	FISH					RNA sequencing	PCR	Follow-up/ month
						COL1A1-PDGFB fusion	PDGFB break apart	PDGFD break apart	COL6A3 break apart	EMILIN2 break apart			
R1(48)	F/14	Neck	NA	DFSP	Positive	ND	Negative	Positive	Positive	NA	ND	NA	NA
R2(48)	F/15	Thigh	NA	FS-DFSP	Positive	NA	Negative	Positive	NA	Positive	ND	NA	NA
R3 (36)	M/4	Calf	Storiform pattern	Pigmented-DFSP	Positive	ND	Negative	Negative	Negative	Negative	No fusion transcript	NA	NED/17
Present case 23	M/16	Back	Myxoid matrix	Myxoid-DFSP	patchy	Negative	Negative	NA	NA	NA	NA	NA	R/10; NED/77
Present case 42	F/1	Hip	Pigmented cell, storiform pattern	Pigmented-DFSP	Positive	Negative	Negative	NA	NA	NA	NA	NA	NED/44
Present case 52	F/13	Forehead	Storiform pattern	Classic-DFSP	Negative	Negative	Negative	NA	NA	NA	NA	NA	NA
Present case 65	M/2	Forearm	Giant cell, myxoid matrix	GCF	partial	Negative	Ambiguous	NA	NA	NA	COL3A1(e20)-PDGFB(e2)	COL3A1(e20)-PDGFB(e2)	Recent case

ND, not detectable; NA, not available; R, relapse; NED, no evidence of disease.

10.3389/fonc.2023.1017154

unclassified spindle cell neoplasm) and *USP6*-rearranged neoplasms (including cranial fasciitis, cellular fibroma of the tendon sheath, and unclassified benign myofibroblastic tumor). The breakpoints seem to constantly occur at exon 1 of *COL3A1* in *COL3A1-PLAG1* and *COL3A1-USP6* cases, whereas they occurred at exon 20 of *COL3A1* in the present GCF case (40, 42–46). In addition, atypical variants of *COL3A1* were associated with Ehlers–Danlos syndrome (EDS) involving connective tissue disorders (39, 47). Furthermore, though without unique clinical presentation, some distinctive pathological morphology was observed that could be associated with the *COL3A1*-rearranged GCF, which contained a higher proportion of multinucleated giant cells with larger and more atypical nuclei than the *COL1A1*-rearranged GCFs. However, more studies are needed to confirm the relationship between the specific chimerism and morphology. In addition, there was one classic DFSP with *COL6A3-PDGFD* and one FS-DFSP with *EMILIN2-PDGFD* in children from the work of Lee et al. (48). Dadone-Montaudié et al. described one pediatric pigmented DFSP, which was not found to have suspicious transcript even after using RNA sequencing, indicating that a more complicated mechanism might exist (36). There were three cases (present cases 23, 42, and 52) of genetic aberrations in the current study that could not be further identified using NGS because of the poor quality of the specimens, which could be associated with alternative rearrangement (including *PDGFD* rearrangement and *PDGFB* rearrangement with novel partner genes), cryptic *COL1A1-PDGFB* fusion, and even other sophisticated chromosomal aberrations (36, 49–52). We still needed more specimens to reveal the genetic characteristics of cryptic pediatric DFSP. Altogether, NGS could be a helpful strategy to identify the molecular unconfirmed DFSP and provide detailed information about abnormal genes for further investigation.

The diagnosis of pediatric DFSP could be challenging, and it should be differentiated from not only benign mimics but also malignant neoplasms, similar to its subtypes in terms of the diversity of histological morphology in the pediatric tumor. Basically, the histologically and immunophenotypically (CD34 positive) overlapping pediatric lesions are often considered in the differential diagnoses, such as plaque-like CD34-positive dermal fibroma (lack of *COL1A1-PDGFB*), fibroblastic connective tissue nevus, fibrous hamartoma of infancy (EGFR exon 20 insertion/duplication mutations), pediatric NTRK-rearranged spindle cell neoplasm (co-expression of CD34 and S100, and NTRK-positive expression or rearrangement), lipofibromatosis, and plexiform myofibroblastoma. Although DFSPs are generally centered within the dermis or subcutis and characterized by spindle cells with a storiform to the whorled pattern, when these tumors have similar morphological features, the cytogenetic method can help with diagnosis, especially for small or superficial biopsy samples. In addition, there are a minority of DFSPs (especially myxoid DFSP and FS-DFSP) with patchy or negative staining for CD34 that are more likely to result in diagnostic pitfalls. The myxoid DFSP could be easily confused with other myxoid lesions such as superficial acral fibromyxoma, solitary fibrous tumor, and low-grade fibromyxoid sarcoma (LGFMS). Despite developing typically in old adults, pediatric liposarcoma should rarely be excluded, especially myxoid liposarcoma (ML) (53). FS-DFSP with atypical staining for CD34 could be confused with high-grade sarcomas, such as high-grade infantile fibrosarcoma (IFS) with *ETV6-NTRK3* fusion, especially dedifferentiated liposarcoma (DDL) without a well-differentiated liposarcoma (WDL) component. Notably, the situation we had reported could be extremely challenging due to the presence of *MDM2*/*FRS2* amplification and the lack of evidence for *COL1A1-PDGFB* fusion by routine FISH screening (54). Importantly, carefully looking for conventional components and searching for characteristics of fusion genes could be helpful for pathologists to confirm complicated cases.

Tissue biopsy, as one of the gold standard diagnostic examinations, could effectively assist in identifying uncertain lesions at an early stage. There were 15 (15/66, 22.7%) children who underwent biopsy, and 11 biopsy specimens detected by FISH all identified with *COL1A1-PDGFB* fusion, which reconfirmed the valuable function of FISH in biopsy samples as shown in our previous report (55). Therefore, it encouraged us to increase biopsy in children and boosted FISH application in pediatric specimens.

Accurate and early diagnosis is critical to guide an appropriate therapeutic scheme in children. Nowadays, the recommended treatment for DFSP is either WLE (2–4 cm) with tumor-negative margins or Mohs micrographic surgery (MMS) (56). In our group, 40 patients (63.5%) underwent marginal excisions, and the other 23 patients (36.5%) received WLE. The overall prognosis of pediatric DFSP was favorable, with all patients surviving without metastasis. However, 15 patients (15/49, 30.6%) developed tumor recurrence. It should be noted that there were 2 of 15 (13.3%) recurrent tumors transforming into fibrosarcomatous DFSP, which was more aggressive than the primary conventional types. Importantly, the recurrence of DFSP was closely related to surgical margin. A wide local excision (2–3 cm) with tumor-negative margins reduces the local recurrence of DFSP from 50%–75% to 0%–30% (24, 57). Moreover, MMS could further decrease the recurrence rate to 0.6%–6% (58). Noteworthy, a higher proportion of patients (8/15, 53.3%) were subjected to WLE, which was a benefit from early diagnosis through biopsy. It highlighted the pivotal role of biopsy in providing definitive evidence for patients to select an optimal therapeutic strategy. Moreover, 11 patients suffered defects from surgery involving anatomic critical regions including the breast, groin, finger, scalp, and face in this cohort. Actually, there are numerous issues arising from surgery for the special population: poor compliance of young patients, prolonged anesthesia duration, increasing surgical difficulty and risk, and unacceptable cosmetic and functional mutilation.

Another treatment opportunity that is typically reserved for adults in surgically unresectable, recurrent, or metastatic cases is targeted therapy (7). However, there is no standard clinical guidance about targeted therapy for pediatric patients. Hitherto, imatinib was applied on six child patients postoperatively for continuous remission and preoperatively for tumor reduction, all of whom achieved the desired effects (23, 59–62). In our study, we reported another patient (case 7) diagnosed with the GCF subtype who benefited from targeted therapy with imatinib after marginal excision in the second relapse, with no evidence of disease after 10 years. Therefore, using imatinib mesylate could act as a neoadjuvant or adjuvant therapy to help control tumor progression, in tandem with other treatments in children, but it still warrants further evaluation and large-scale investigation.

In conclusion, we present the largest series study of 66 cases of pediatric DFSP with genetic investigation. There are certain differences in clinicopathology between children and adults. Most pediatric DFSPs contain classical *COL1A1-PDGFB* fusion as compared with adults. The *COL3A1-PDGFB* chimerism might be associated with the special morphology of GCF, which needs further investigation. Furthermore, FISH screening, and even supplementary NGS detection, should be used in identifying pediatric lesions with typical or uncertain morphology involving dermis and subcutis. The overall prognosis would be favorable with appropriate treatment, while more attention should be paid to recurrence prevention and mutilation reduction in DFSP management in the special population.

Data availability statement

The data presented in the study are deposited in the NCBI repository (https://www.ncbi.nlm.nih.gov/), accession number OQ262947.

Author contributions

ZZ and YL analyzed the data and prepared the manuscript. CS collected the clinicopathological data of the patients. MC carried out the molecular studies. HZ, ZZ, XH and YL were responsible for diagnosis and review. HZ supervised and revised the manuscript. All authors contributed to the article and approved the submitted version.

Funding

This work was supported by the National Natural Science Foundation of China (No. 81972520), Sichuan Science and Technology Program (No. 2022YFS0376), and the 1·3·5 project for disciplines of excellence–Clinical Research Incubation Project, West China Hospital, Sichuan University (NO.2018HXFH011).

Conflict of interest

The authors declare that the research was conducted in the absence of any commercial or financial relationships that could be construed as a potential conflict of interest.

Publisher's note

References

1. Mentzel T, Pedeutour F. Dermatofibrosarcoma protuberans. In: *Who classification of tumours of soft tissue and bone, 5th Edition*. Lyon (France: International Agency for Research on Cancer (2020).

2. Abbott JJ, Oliveira AM, Nascimento AG. The prognostic significance of fibrosarcomatous transformation in dermatofibrosarcoma protuberans. *Am J Surg Pathol* (2006) 30(4):436–43. doi: 10.1097/00000478-200604000-00002

3. Llombart B, Monteagudo C, Sanmartín O, López-Guerrero JA, Serra-Guillén C, Poveda A, et al. Dermatofibrosarcoma protuberans: A clinicopathological, immunohistochemical, genetic (Col1a1-pdgfb), and therapeutic study of low-grade versus high-grade (Fibrosarcomatous) tumors. *J Am Acad Dermatol* (2011) 65(3):564–75. doi: 10.1016/j.jaad.2010.06.020

4. King L, López-Terrada D, Jakacky J, McCarville MB, Spunt SL, Bridge JA, et al. Primary intrathoracic dermatofibrosarcoma protuberans. *Am J Surg Pathol* (2012) 36 (12):1897–902. doi: 10.1097/PAS.0b013e31826b7919

5. Sirvent N, Maire G, Pedeutour F. Genetics of dermatofibrosarcoma protuberans family of tumors: From ring chromosomes to tyrosine kinase inhibitor treatment. *Genes Chromosomes Cancer* (2003) 37(1):1–19. doi: 10.1002/gcc.10202

6. Malhotra B, Schuetze SM. Dermatofibrosarcoma protruberans treatment with platelet-derived growth factor receptor inhibitor: A review of clinical trial results. *Curr Opin Oncol* (2012) 24(4):419–24. doi: 10.1097/CCO.0b013e328353d78d

7. Patel KU, Szabo SS, Hernandez VS, Prieto VG, Abruzzo LV, Lazar AJ, et al. Dermatofibrosarcoma protuberans Col1a1-pdgfb fusion is identified in virtually all dermatofibrosarcoma protuberans cases when investigated by newly developed multiplex reverse transcription polymerase chain reaction and fluorescence in situ hybridization assays. *Hum Pathol* (2008) 39(2):184–93. doi: 10.1016/j.humpath.2007.06.009

8. Karanian M, Pérot G, Coindre JM, Chibon F, Pedeutour F, Neuville A. Fluorescence in situ hybridization analysis is a helpful test for the diagnosis of dermatofibrosarcoma protuberans. *Mod Pathol* (2015) 28(2):230–7. doi: 10.1038/modpathol.2014.97

9. Jing C, Zhang H, Zhang X, Yu S. Dermatofibrosarcoma protuberans: A clinicopathologic and therapeutic analysis of 254 cases at a single institution. *Dermatol Surg* (2021) 47(2):e26–30. doi: 10.1097/dss.0000000000002578

10. Valdivielso-Ramos M, Torrelo A, Campos M, Feito M, Gamo R, Rodriguez-Peralto JL. Pediatric dermatofibrosarcoma protuberans in Madrid, Spain: Multi-institutional outcomes. *Pediatr Dermatol* (2014) 31(6):676–82. doi: 10.1111/pde.12371

11. Rubio GA, Alvarado A, Gerth DJ, Tashiro J, Thaller SR. Incidence and outcomes of dermatofibrosarcoma protuberans in the us pediatric population. *J Craniofac Surg* (2017) 28(1):182–4. doi: 10.1097/scs.0000000000003203

12. Sleiwah A, Wright TC, Chapman T, Dangoor A, Maggiani F, Clancy R. Dermatofibrosarcoma protuberans in children. *Curr Treat Options Oncol* (2022) 23 (6):843–54. doi: 10.1007/s11864-022-00979-9

13. Terrier-Lacombe MJ, Guillou L, Maire G, Terrier P, Vince DRde Saint Aubain Somerhausen N, et al. Dermatofibrosarcoma protuberans, giant cell fibroblastoma, and hybrid lesions in children: Clinicopathologic comparative analysis of 28 cases with molecular data–a study from the French federation of cancer centers sarcoma group. *Am J Surg Pathol* (2003) 27(1):27–39. doi: 10.1097/00000478-200301000-00004

14. Jha P, Moosavi C, Fanburg-Smith JC. Giant cell fibroblastoma: An update and addition of 86 new cases from the armed forces institute of pathology, in honor of dr. Franz m. enzinger. *Ann Diagn Pathol* (2007) 11(2):81–8. doi: 10.1016/j.anndiagpath.2006.12.010

15. Janz TA, Nagasubramanian R, Wei JL. Pediatric head and neck fibrosarcomas: A demographical, treatment, and survival analysis and review of a rare case. *Int J Pediatr Otorhinolaryngol* (2019) 116:92–6. doi: 10.1016/j.ijporl.2018.09.031

16. van Lee CB, Kan WC, Gran S, Mooyaart A, Mureau MAM, Williams HC, et al. Dermatofibrosarcoma protuberans re-excision and recurrence rates in the Netherlands between 1989 and 2016. *Acta Derm Venereol* (2019) 99(12):1160–5. doi: 10.2340/00015555-3287

17. Shmookler BM, Enzinger FM, Weiss SWJC. Giant cell fibroblastoma. *A Juvenile Form Dermatofibrosarcoma Protuberans* (1989) 64(10):2154. doi: 10.1002/1097-0142(19891115)64:10<2154::aidcncr2820641030>3.0.co;2-n

18. Zhang H, Erickson-Johnson M, Wang X, Oliveira JL, Nascimento AG, Sim FH, et al. Molecular testing for lipomatous tumors: Critical analysis and test recommendations based on the analysis of 405 extremity-based tumors. *Am J Surg Pathol* (2010) 34(9):1304–11. doi: 10.1097/PAS.0b013e3181e92d0b

19. Abbott JJ, Erickson-Johnson M, Wang X, Nascimento AG, Oliveira AM. Gains of Col1a1-pdgfb genomic copies occur in fibrosarcomatous transformation of dermatofibrosarcoma protuberans. *Mod Pathol* (2006) 19(11):1512–8. doi: 10.1038/modpathol.3800695

20. Weinstein JM, Drolet BA, Esterly NB, Rogers M, Bauer BS, Wagner AM, et al. Congenital dermatofibrosarcoma protuberans: Variability in presentation. *Arch Dermatol* (2003) 139(2):207–11. doi: 10.1001/archderm.139.2.207

21. Maire G, Fraitag S, Galmiche L, Keslair F, Ebran N, Terrier-Lacombe MJ, et al. A clinical, histologic, and molecular study of 9 cases of congenital dermatofibrosarcoma protuberans. *Arch Dermatol* (2007) 143(2):203–10. doi: 10.1001/archderm.143.2.203

22. Thway K, Noujaim J, Jones RL, Fisher C. Dermatofibrosarcoma protuberans: Pathology, genetics, and potential therapeutic strategies. *Ann Diagn Pathol* (2016) 25:64–71. doi: 10.1016/j.anndiagpath.2016.09.013

23. Posso-De Los Rios CJ, Lara-Corrales I, Ho N. Dermatofibrosarcoma protuberans in pediatric patients: A report of 17 cases. *J Cutan Med Surg* (2014) 18(3):180–5. doi: 10.2310/7750.2013.13099

24. Fezza R, Shahzeidi P, Downing C, Cognetta A. A rare presentation of dermatofibrosarcoma protuberans of the scalp treated with "Slow-mohs" micrographic surgery. *J Drugs Dermatol* (2022) 21(5):534–5. doi: 10.36849/jdd.6719

25. Zhou X, Sun D, Liu Y, Sun Q, Yuan Z, Luo X, et al. Dermatofibrosarcoma protuberans: Our 10-year experience on 80 patients. *J Dermatolog Treat* (2020) 31 (6):554–8. doi: 10.1080/09546634.2019.1622629

26. Fletcher CD, Theaker JM, Flanagan A, Krausz T. Pigmented dermatofibrosarcoma protuberans (Bednar tumour): Melanocytic colonization or neuroectodermal differentiation? a clinicopathological and immunohistochemical study. *Histopathology* (1988) 13(6):631–43. doi: 10.1111/j.1365-2559.1988.tb02094.x

27. Hoesly PM, Lowe GC, Lohse CM, Brewer JD, Lehman JS. Prognostic impact of fibrosarcomatous transformation in dermatofibrosarcoma protuberans: A cohort study. *J Am Acad Dermatol* (2015) 72(3):419–25. doi: 10.1016/j.jaad.2014.11.020

28. Xu S, Zhao L, Wang J. Atrophic dermatofibrosarcoma protuberans: A clinicopathological study of 16 cases. *Pathology* (2019) 51(6):615–20. doi: 10.1016/j.pathol.2019.06.002

29. Nishio J, Iwasaki H, Nabeshima K, Naito M. Cytogenetics and molecular genetics of myxoid soft-tissue sarcomas. *Genet Res Int* (2011) 2011:497148. doi: 10.4061/2011/497148

30. Llombart B, Sanmartín O, López-Guerrero JA, Monteagudo C, Serra C, Requena C, et al. Dermatofibrosarcoma protuberans: Clinical, pathological, and genetic (Col1a1-pdgfb) study with therapeutic implications. *Histopathology* (2009) 54(7):860–72. doi: 10.1111/j.1365-2559.2009.03310.x

31. Abenoza P, Lillemoe T. Cd34 and factor xiiia in the differential diagnosis of dermatofibroma and dermatofibrosarcoma protuberans. *Am J Dermatopathol* (1993) 15 (5):429–34. doi: 10.1097/00000372-199310000-00003

32. Lo CH, Tsang PM, Cheng SY. Myoid differentiation in dermatofibrosarcoma protuberans and its fibrosarcomatous variant: 10 years' experience in a tertiary hospital. *Autops Case Rep* (2022) 12:e2021368. doi: 10.4322/acr.2021.368

33. Reilly DJ, Loo YL, Alexander WM, Wilks DJ, MacGregor D, Coombs CJ. Diagnostic and management considerations in pediatric dermatofibrosarcoma protuberans. *Ann Plast Surg* (2022) 88(3):319–22. doi: 10.1097/sap.0000000000002970

34. Segura S, Salgado R, Toll A, Martín-Ezquerra G, Yébenes M, Sáez A, et al. Identification of T(17;22)(Q22;Q13) (Col1a1/Pdgfb) in dermatofibrosarcoma protuberans by fluorescence in situ hybridization in paraffin-embedded tissue microarrays. *Hum Pathol* (2011) 42(2):176–84. doi: 10.1016/j.humpath.2010.07.015

35. Kiuru-Kuhlefelt S, El-Rifai W, Fanburg-Smith J, Kere J, Miettinen M, Knuutila S. Concomitant DNA copy number amplification at 17q and 22q in dermatofibrosarcoma protuberans. *Cytogenet Cell Genet* (2001) 92(3-4):192–5. doi: 10.1159/000056901

36. Dadone-Montaudié B, Alberti L, Duc A, Delespaul L, Lesluyes T, Pérot G, et al. Alternative pdgfd rearrangements in dermatofibrosarcomas protuberans without pdgfb fusions. *Mod Pathol* (2018) 31(11):1683–93. doi: 10.1038/s41379-018-0089-4

37. Zhu R, Yan J, Li B, Tan F, Yan W, Shen J, et al. Determination of Col1a1-pdgfb breakpoints by next-generation sequencing in the molecular diagnosis of dermatofibrosarcoma protuberans. *Exp Mol Pathol* (2021) 122:104672. doi: 10.1016/j.yexmp.2021.104672

38. Ucaryilmaz Metin C, Ozcan G. Comprehensive bioinformatic analysis reveals a cancer-associated fibroblast gene signature as a poor prognostic factor and potential therapeutic target in gastric cancer. *BMC Cancer* (2022) 22(1):692. doi: 10.1186/s12885-022-09736-5

39. Sølyst S, Oksjoki R, Farholt S, Nielsen DG, Christensen AH, Fagerberg CR, et al. Carriers of Col3a1 pathogenic variants in Denmark: Interfamilial variability in severity and outcome of elective surgical procedures. *Clin Genet* (2022) 102(3):191–200. doi: 10.1111/cge.14176

40. Santisukwongchote S, Thorner PS, Desudchit T, Techavichit P, Jittapiromsak N, Amornfa J, et al. Pediatric fibromyxoid tumor with Plag1 fusion: An emerging entity with a novel intracranial location. *Neuropathology* (2022) 42(4):315–22. doi: 10.1111/neup.12837

41. Thiele BJ, Doller A, Kähne T, Pregla R, Hetzer R, Regitz-Zagrosek V. Rna-binding proteins heterogeneous nuclear ribonucleoprotein A1, E1, and K are involved in post-transcriptional control of collagen I and iii synthesis. *Circ Res* (2004) 95(11):1058–66. doi: 10.1161/01.Res.0000149166.33833.08

42. Fritchie K, Wang L, Yin Z, Nakitandwe J, Hedges D, Horvai A, et al. Lipoblastomas presenting in older children and adults: Analysis of 22 cases with identification of novel Plag1 fusion partners. *Mod Pathol* (2021) 34(3):584–91. doi: 10.1038/s41379-020-00696-4

43. Mantilla JG, Gross JM, Liu YJ, Hoch BL, Ricciotti RW. Characterization of novel Usp6 gene rearrangements in a subset of so-called cellular fibroma of tendon sheath. *Mod Pathol* (2021) 34(1):13–9. doi: 10.1038/s41379-020-0621-1

44. Malik F, Wang L, Yu Z, Edelman MC, Miles L, Clay MR, et al. Benign infiltrative myofibroblastic neoplasms of childhood with Usp6 gene rearrangement. *Histopathology* (2020) 77(5):760–8. doi: 10.1111/his.14182

45. Paulson VA, Stojanov IA, Wasman JK, Restrepo T, Cano S, Plunkitt J, et al. Recurrent and novel Usp6 fusions in cranial fasciitis identified by targeted rna sequencing. *Mod Pathol* (2020) 33(5):775–80. doi: 10.1038/s41379-019-0422-6

46. Logan SJ, Schieffer KM, Conces MR, Stonerock E, Miller AR, Fitch J, et al. Novel morphologic findings in Plag1-rearranged soft tissue tumors. *Genes Chromosomes Cancer* (2021) 60(8):577–85. doi: 10.1002/gcc.22953

47. Colman M, Castori M, Micale L, Ritelli M, Colombi M, Ghali N, et al. Atypical variants in Col1a1 and Col3a1 associated with classical and vascular ehlers-danlos syndrome overlap phenotypes: Expanding the clinical phenotype based on additional case reports. *Clin Exp Rheumatol* (2022) 40 Suppl 134(5):46–62. doi: 10.55563/clinexprheumatol/kzkq6y

48. Lee PH, Huang SC, Wu PS, Tai HC, Lee CH, Lee JC, et al. Molecular characterization of dermatofibrosarcoma protuberans: The clinicopathologic significance of uncommon fusion gene rearrangements and their diagnostic importance in the exclusively subcutaneous and circumscribed lesions. *Am J Surg Pathol* (2022) 46 (7):942–55. doi: 10.1097/pas.0000000000001866

49. Nakamura I, Kariya Y, Okada E, Yasuda M, Matori S, Ishikawa O, et al. A novel chromosomal translocation associated with Col1a2-pdgfb gene fusion in dermatofibrosarcoma protuberans: Pdgf expression as a new diagnostic tool. *JAMA Dermatol* (2015) 151(12):1330–7. doi: 10.1001/jamadermatol.2015.2389

50. Dickson BC, Hornick JL, Fletcher CDM, Demicco EG, Howarth DJ, Swanson D, et al. Dermatofibrosarcoma protuberans with a novel Col6a3-pdgfd fusion gene and apparent predilection for breast. *Genes Chromosomes Cancer* (2018) 57(9):437–45. doi: 10.1002/gcc.22663

51. Chen Y, Shi YZ, Feng XH, Wang XT, He XL, Zhao M. Novel tnc-pdgfd fusion in fibrosarcomatous dermatofibrosarcoma protuberans: A case report. *Diagn Pathol* (2021) 16(1):63. doi: 10.1186/s13000-021-01123-1

52. Bianchini L, Maire G, Guillot B, Joujoux JM, Follana P, Simon MP, et al. Complex T(5;8) involving the Cspg2 and Ptk2b genes in a case of dermatofibrosarcoma protuberans without the Col1a1-pdgfb fusion. *Virchows Arch* (2008) 452(6):689–96. doi: 10.1007/s00428-008-0580-2

53. Peng R, Li N, Lan T, Chen H, Du T, He X, et al. Liposarcoma in children and young adults: A clinicopathologic and molecular study of 23 cases in one of the largest institutions of China. *Virchows Arch* (2021) 479(3):537–49. doi: 10.1007/s00428-021-03076-8

54. Lu Y, Li T, Chen M, Peng H, Du T, Qiu Y, et al. Coamplification of 12q15 and 12p13 and homozygous Cdkn2a/2b deletion: Synergistic role of fibrosarcomatous transformation in dermatofibrosarcoma protuberans with a cryptic Col1a1-pdgfb fusion. *Virchows Arch* (2022) 481(2):313–9. doi: 10.1007/s00428-022-03297-5

55. Zhang Z, Chen H, Chen M, He X, Wang Y, Zhang H. Application of Col1a1-pdgfb fusion gene detection by fluorescence *In situ* hybridization in biopsy tissue of dermatofibrosarcoma protuberans. *J Dermatol* (2017) 44(7):798–802. doi: 10.1111/1346-8138.13767

56. Miller SJ, Alam M, Andersen JS, Berg D, Bichakjian CK, Bowen GM, et al. Dermatofibrosarcoma protuberans. *J Natl Compr Canc Netw* (2012) 10(3):312–8. doi: 10.6004/jnccn.2012.0032

57. Lemm D, Mügge LO, Mentzel T, Höffken K. Current treatment options in dermatofibrosarcoma protuberans. *J Cancer Res Clin Oncol* (2009) 135(5):653–65. doi: 10.1007/s00432-009-0550-3

58. Foroozan M, Sei JF, Amini M, Beauchet A, Saiag P. Efficacy of mohs micrographic surgery for the treatment of dermatofibrosarcoma protuberans: Systematic review. *Arch Dermatol* (2012) 148(9):1055–63. doi: 10.1001/archdermatol.2012.1440

59. Yen H, Pan SC, Huang CH, Wong TW. Complete remission of a periorbital dermatofibrosarcoma protuberans with adjuvant imatinib mesylate in a child. *JAAD Case Rep* (2015) 1(4):172–4. doi: 10.1016/j.jdcr.2015.04.003

60. Gooskens SL, Oranje AP, van Adrichem LN, de Waard-van der Spek FB, den Hollander JC, van de Ven CP, et al. Imatinib mesylate for children with dermatofibrosarcoma protuberans (Dfsp). *Pediatr Blood Cancer* (2010) 55(2):369–73. doi: 10.1002/pbc.22494

61. Suzuki D, Kobayashi R, Yasuda K, Yamamoto H, Morioka K, Mikawa M, et al. Congenital dermatofibrosarcoma protuberans in a newborn infant with a massive back tumor: Favorable effects of oral imatinib on the control of residual tumor growth. *J Pediatr Hematol Oncol* (2011) 33(7):e304–6. doi: 10.1097/MPH.0b013e31822d4d21

62. Price VE, Fletcher JA, Zielenska M, Cole W, Viero S, Manson DE, et al. Imatinib mesylate: An attractive alternative in young children with Large, surgically challenging dermatofibrosarcoma protuberans. *Pediatr Blood Cancer* (2005) 44(5):511–5. doi: 10.1002/pbc.20249

frontiers | Frontiers in Oncology

TYPE Original Research
PUBLISHED 30 January 2023
DOI 10.3389/fonc.2023.1013054

OPEN ACCESS

EDITED BY
Ming Zhao,
Zhejiang Provincial People's Hospital, China

REVIEWED BY
Mallikarjun Patil,
University of Alabama at Birmingham, United States
Yongfen Min,
National Institutes of Health (NIH), United States

*CORRESPONDENCE
Huiying He
huiyinghe@bjmu.edu.cn
Binbin Li
kqlibinbin@bjmu.edu.cn

SPECIALTY SECTION
This article was submitted to Surgical Oncology, a section of the journal Frontiers in Oncology

RECEIVED 06 August 2022
ACCEPTED 11 January 2023
PUBLISHED 30 January 2023

CITATION
Qin Z, Bai J, He H and Li B (2023) Expression and significance of m6A-RNA-methylation in oral cancer and precancerous lesion.
Front. Oncol. 13:1013054.
doi: 10.3389/fonc.2023.1013054

Expression and significance of m6A-RNA-methylation in oral cancer and precancerous lesion

Zhiming Qin[1,2], Jiaying Bai[1,2], Huiying He[3]* and Binbin Li[1,2]*

[1]Department of Oral Pathology, Peking University School and Hospital of Stomatology & National Center of Stomatology & National Clinical Research Center for Oral Diseases & National Engineering Research Center of Oral Biomaterials and Digital Medical Devices, Beijing, China, [2]Research Unit of Precision Pathologic Diagnosis in Tumors of the Oral and Maxillofacial Regions, Chinese Academy of Medical Sciences (2019RU034), Beijing, China, [3]Department of Pathology, School of Basic Medical Sciences, Third Hospital, Peking University Health Science Center, Beijing, China

Background: Oral potentially malignant disorders (OPMDs) and oral squamous cell carcinoma (OSCC) are a series of related pathologic and molecular events involving simple epithelial hyperplasia, mild to severe dysplasia and canceration. N6-methyladenosine RNA methylation, as the most common modification of both coding mRNA and non-coding ncRNA in eukaryotes, participates in the regulation of the occurrence and development of various malignant tumors in human. However, its role in oral epithelial dysplasia (OED) and OSCC remain unclear.

Materials and methods: In this study, multiple public databases were used for bioinformatics analysis of 23 common m6A methylation regulators in head and neck squamous cell carcinoma (HNSCC). Protein expressions of IGF2BP2 and IGF2BP3 were verified accordingly in clinical cohort samples of OED and OSCC.

Results: Patients with high expression of FTO、HNRNPC、HNRNPA2B1、LRPPRC、IGF2BP1、IGF2BP2、IGF2BP3 had a poor prognosis. IGF2BP2 had a relatively high mutation rate in HNSCC, and its expression was significantly positively correlated with tumor purity, and significantly negatively correlated with the infiltration level of B cells and CD8+T cells. The expression of IGF2BP3 was significantly positively correlated with tumor purity and CD4+T cells. Immunohistochemistrically, the expression of IGF2BP2 and IGF2BP3 in oral simple epithelial hyperplasia, OED and OSCC increased gradually. Both were strongly expressed in OSCC.

Conclusion: IGF2BP2 and IGF2BP3 were the potential biological prognostic indicators of OED and OSCC.

KEYWORDS

oral squamous cell carcinoma, oral epithelial dysplasia, N6-methyladenosine, IGF2BP2, IGF2BP3

Introduction

Oral squamous cell carcinoma (OSCC) is the most prevalent malignancy in oral and maxillofacial region, with approximately 350,000 newly diagnosed cases annually (1). A considerable number of patients with OSCC develop from oral epithelial dysplasia (OED). It is generally believed that the higher the degree of epithelial dysplasia, the higher the risk of malignant transformation. However, the pathological judgment is subjective to some extent, which may lead to discrepancy between different pathologists. In some cases, the pathologic predictions had no significant relation with clinical prognosis. Therefore, it is needed to discover more molecular markers for accurate assessment of cancer risk and further determine the specific biomarkers of OED and OSCC.

N6-methyladenosine (m6A), the methylation modification at the sixth N atom of adenine, is the most common post-transcriptional modification on mRNA, mediating >60% RNA methylation (2). Abnormal m6A methylation levels play an essential role in the progression of various cancers (3, 4). M6A methylation is dynamic and reversible in cells, and the levels of m6A methylation in tumors mainly depend on the expression of m6A methylation regulators. Regulators that interact with m6A methylation are mainly divided into three categories: Writers (methyltransferases), Erasers (demethylases), and Readers (reading proteins). Recently, new evidence has showed that m6A modification is associated with tumor proliferation, glycolysis, apoptosis, and metastasis. m6A modification could play either an oncogenetic or tumor-suppressive role in malignant tumors (5, 6). For example, METTL3, as one of the m6A-RNA-methylation regulators, is upregulated in OSCC tissues, and high levels of METTL3 expression in tumor tissues predict poor patient survival. METTL3 promotes the proliferation, invasion, and migration of OSCC cells *in vitro*, while METTL3-knockout inhibits tumor growth *in vivo*. METTL3 promotes the stabilization of c-Myc through YTHDF1-mediated m6A modification, leading to the occurrence of OSCC (7). In addition, OSCC patients with high FTO expression had larger tumor volume, higher tumor node metastasis (TNM) stage, worse differentiation, and shorter survival time. Stable knockout of FTO inhibited OSCC cell viability, colony formation, and tumor growth (8).

Abbreviations: OSCC, Oral squamous cell carcinoma; OED, Oral epithelial dysplasia; m6A, N6-methyladenosine; TNM, Tumor node metastasis; IGF2BP2, Insulin-like growth factor 2 mRA-binding Protein 2; IGF2BP3, Insulin Like Growth Factor 2 mNA Binding Protein 3; GEPIA, Gene expression profiling interactive analysis; RNA-Seq, RNA sequencing; GTEx, Genotype-Tissue Expression; OS, Overall survival; FP, First-progression survival; PPS, Post-progression survival; HNSCC, Head and neck squamous cell carcinoma; HR, Hazard ratio; CIs, Confidence intervals; CNAs, Copy number alterations; GISTIC, Genomic identification of significant targets in cancer; IHC, Immunohistochemistry; FFPE, Formalin-fixed, paraffin-embedded; HRP, Horse-radish peroxidase; DAB, 3, 3-diaminobenzidine; LSD, Least significant difference; HE, hematoxylin-eosin; TCGA, The cancer genome atlas; SCC, Squamous cell carcinoma; BMI1, B-cell-specific moloneymurine leukemia virus insertion site 1; LSCC, laryngeal squamous cell carcinoma; VEGF, vascular endothelial growth factor.

Thus, we utilized public databases to analyze the expression of 23 m6A methylation regulators and their relationships with clinicopathological characteristics, and to predict their potential functions. Further, clinical cohort cases with epithelial hyperplasia/dysplasia and OSCC were collected to verify the protein expression of Insulin-Like Growth Factor 2 mNA Binding Protein 2 (IGF2BP2) and Insulin-Like Growth Factor 2 mNA Binding Protein 3 (IGF2BP3), and their clinical associations in OSCC and OED cases.

Materials and methods

Oncomine analysis

Oncomine gene expression array datasets (https://www.oncomine.org/resource/login.html) were used to analyze the transcription levels of m6A regulators in cancers. The cutoffs of *P*-value and fold change were defined as 0.01 and 2 by Student's t-test, respectively.

Gene expression profiling interactive analysis dataset

GEPIA is a newly developed interactive web server for analyzing the RNA sequencing (RNA-Seq) expression data of 9,736 tumors and 8,587 normal samples from the Cancer Genome Atlas and the Genotype-Tissue Expression projects, using a standard processing pipeline. GEPIA provides customizable functions such as tumor/normal differential expression analysis, profiling according to cancer types or pathological stages, patient survival analysis, similar gene detection, correlation analysis, and dimensionality reduction analysis (9).

The Kaplan-Meier Plotter

Kaplan-Meier Plotter (www.kmplot.com) was used to analyze the overall survival (OS), first-progression survival (FP), and post-progression survival (PPS) of patients with head and neck squamous cell carcinoma (HNSCC), which contained gene expression data and survival information of HNSCC patients (10). Cases were divided into two groups by median expression (high vs low expression) and assessed by a Kaplan-Meier survival plot, with the hazard ratio (HR) with 95% confidence intervals (CIs) and log-rank p-value. Only the JetSet best probe set of m6A regulators was chosen to obtain Kaplan-Meier plots, in which the number-at-risk was indicated below the main plot.

The cBioPortal

The Cancer Genome Atlas have sequencing and pathological data of 30 different cancers. The HNSCC dataset, including data from 1,107 cases with pathology reports, was selected for further analyses of M6A regulators using cBioPortal (11). The genomic profiles included

mutations, putative copy number alterations (CNAs) from genomic identification of significant targets in cancer (GISTIC), mRNA expression Z scores (RNA-seq v.2 RSEM), and protein expression Z scores (reverse phase protein array).

The TIMER database analysis

The Timer database is a publicly available data platform for the systematic analysis of tumor immune infiltration (12). We used GENE modules to explore the correlation between the expression levels of m6A methylation regulators and immune cell infiltration in patients with HNSCC, including CD4+ T cells, CD8+ T cells, B cells, neutrophils, dendritic cells and macrophages.

Patient sections

The study samples were obtained from Peking University School and Hospital of Stomatology (Beijing, China) from January 2000 to June 2021. Inclusion criteria were as follows: the initial diagnosis was epithelial hyperplasia or epithelial dysplasia; there were complete medical records and clinical data; and there was no history of oral mucosal epithelial lesions or OSCC. Exclusion criteria were as follows: no pathological biopsy was performed; cancerous change was diagnosed by pathological biopsy at the first visit; and there was a history of radiotherapy and chemotherapy in the past. All study samples were further confirmed by two pathologists according to World Health Organization criteria (13). This study was in compliance with the Declaration of Helsinki. Data were collected after approval of the Biomedical Ethics Committee of Peking University School and Hospital of Stomatology (No. PKUSSIRB-201948111).

Immunohistochemistry

Formalin-fixed and paraffin-embedded (FFPE) tissues were chosen from above cases. Briefly, 3-mm sections were incubated with commercial rabbit poly-clonal antibodies against IGF2BP2 and IGF2BP3 (Abcam) at 1/200 dilution overnight at 4°C. Then, the sections were conjugated with horse-radish peroxidase (HRP) antibody (1:500 dilution; Gene Tech) at room temperature for 2 h, then covered by 3, 3-diaminobenzidine (DAB), and slides were mounted with mounting medium.

Statistical analysis

All analyses were performed with the SPSS 24.0 software (SPSS Inc., USA) and the data from these independent experiments were presented as mean ± SD. If the multi-sample comparisons were independent of each other and conform to the normal distribution and homogeneity of variance, a one-way analysis of variance would be applied. Differences between groups were compared using the least significant difference (LSD) test. If the heterogeneity between samples didn't conform to the normal distribution, the Nonparametric tests Mann-Whitney test, or Kruskal-Wallis H test would be used. Enumeration data were analyzed using Fisher's exact test of $\chi 2$ test. Correlation analysis was performed using Spearman correlation analysis. The test level $\alpha = 0.05$ and $P<0.05$ was considered statistically significant.

Results

Baseline characteristics of the patient sections

A total of 109 patients with OSCC or OED were enrolled. In this cohort, 28 patients relapsed after the initial biopsy and became cancer, and 81 patients underwent no recurrence within 5 years. Among them, 48 sections were assigned to the mild epithelial dysplasia group, 71 sections were assigned to the moderate epithelial dysplasia group, 57 sections were assigned to the severe epithelial dysplasia group, 63 sections were assigned to the OSCC group, and 37 sections were assigned to the epithelial hyperplasia group.

At the same time, 195 biopsy sections were collected from above 28 patients with malignant transformation, and only one section was selected for each biopsy, which were recorded as the progression group; 81 patients were pathologically diagnosed as epithelial dysplasia at the first visit, and there was no recurrence or malignant transformation during the follow-up period of at least 5 years, which were collected as the stable group (Tables 1, 2).

Bioinformatic analysis of m6A methylation regulators in HNSCC

A lot of evidence showed that m6A RNA methylation promotes tumor initiation and progression (14). However, there are few studies to explore the role of m6A methylation in OSCC and OED. To study the expression correlation of m6A methylation regulators in OSCC and OED, we reviewed relevant literature and selected a total of 23 m6A methylation regulators. We preliminarily analyzed the expression of these regulators in different cancer types through the Oncomine database compared with normal control. Figure 1A demonstrated that the m6A level upregulated in OSCC and OED tissues compared with normal control. It was found that m6A methylation regulators were expressed to different degrees in various cancer types, and the expressions of METTL3, WTAP, ZC3H13, KIAA1429, YTHDC, YTHDF2, YTHDF3, HNRNPA2B, HNRNPC, LRPPRC, IGF2BP2 and IGF2BP3 in HNSCC were higher, among which KIAA1429, YTHDF3, IGF2BP2, and IGF2BP3 had significant differences in the corresponding studies (Supplementary Material)

Figure 1B showed that the expression levels of RBM15, FTO, YTHDC1, YTHDC2, HNRNPC, HNRNPA2B1, LRPPRC, IGF2BP1, IGF2BP2, IGF2BP3 were significantly correlated with the overall survival of patients with HNSCC ($P<0.05$) through Kaplan-Meier curve and log-rank test analysis. Among them, the higher the expression of RBM15, YTHDC1, and YTHDC2, the better the prognosis of the patient; while the overall survival time of patients with high expressions of FTO, HNRNPC, HNRNPA2B1, LRPPRC,

10.3389/fonc.2023.1013054

TABLE 1 Baseline characteristics of the patients in advanced group.

Characteristic	Epithelial hyperplasia		Mild dysplasia		Moderate dysplasia		Severe dysplasia	
	Number	%	Number	%	Number	%	Number	%
Sex								
Female	6	85.71	4	80.00	8	61.54	3	100.00
Male	1	14.29	1	20.00	5	38.46	0	0.00
Age(years)								
≤40	0	0.00	1	20.00	1	7.69	0	0.00
40-60	5	71.43	1	20.00	7	53.85	0	0.00
≥60	2	28.57	3	60.00	5	38.46	3	100.00
Sites								
Tongue	2	28.57	3	60.00	6	46.15	1	33.33
Buccal	2	28.57	1	20.00	1	7.69	1	33.33
Gingiva	3	42.86	1	20.00	3	23.08	1	33.33
Other	0	0.00	0	0.00	3	23.08	0	0.00
Tobacco smoking								
Yes	0	0.00	0	0.00	2	15.38	0	0.00
No	7	100.00	5	100.00	11	84.62	3	100.00
Alcohol drinking								
Yes	0	0.00	0	0.00	1	7.69	0	0.00
No	7	100.00	5	100.00	12	92.31	3	100.00
Prognosis(relapse)								
Original sites	3	42.86	3	60.00	8	61.54	1	33.33
Multiple sites	4	57.14	2	40.00	5	38.46	2	66.67

TABLE 2 Baseline characteristics of the patients in stable group.

Characteristic	Epithelial hyperplasia		Mild dysplasia		Moderate dysplasia		Severe dysplasia	
	Number	%	Number	%	Number	%	Number	%
Sex								
Female	10	47.62	8	40.00	6	31.58	11	52.38
Male	11	52.38	12	60.00	13	68.42	10	47.62
Age(years)								
≤40	7	33.33	3	15.00	1	8.86	1	4.76
40-60	11	52.38	11	55.00	11	57.89	9	42.86
≥60	3	14.29	6	30.00	7	36.84	11	52.38
Sites								
Tongue	12	57.14	6	30.00	12	63.16	13	61.90
Buccal	6	28.57	10	50.00	3	15.79	0	0.00
Gingiva	3	14.29	3	15.00	2	10.53	3	14.29
Other	0	0.00	1	5.00	2	10.53	4	19.05
Tobacco smoking								
Yes	6	28.57	10	50.00	3	15.79	7	33.33
No	15	71.43	10	50.00	16	84.21		66.67
Alcohol drinking								
Yes	6	28.57	5	25.00	3	15.79	8	38.10
No	15	71.43	15	75.00	16	84.21	13	61.90

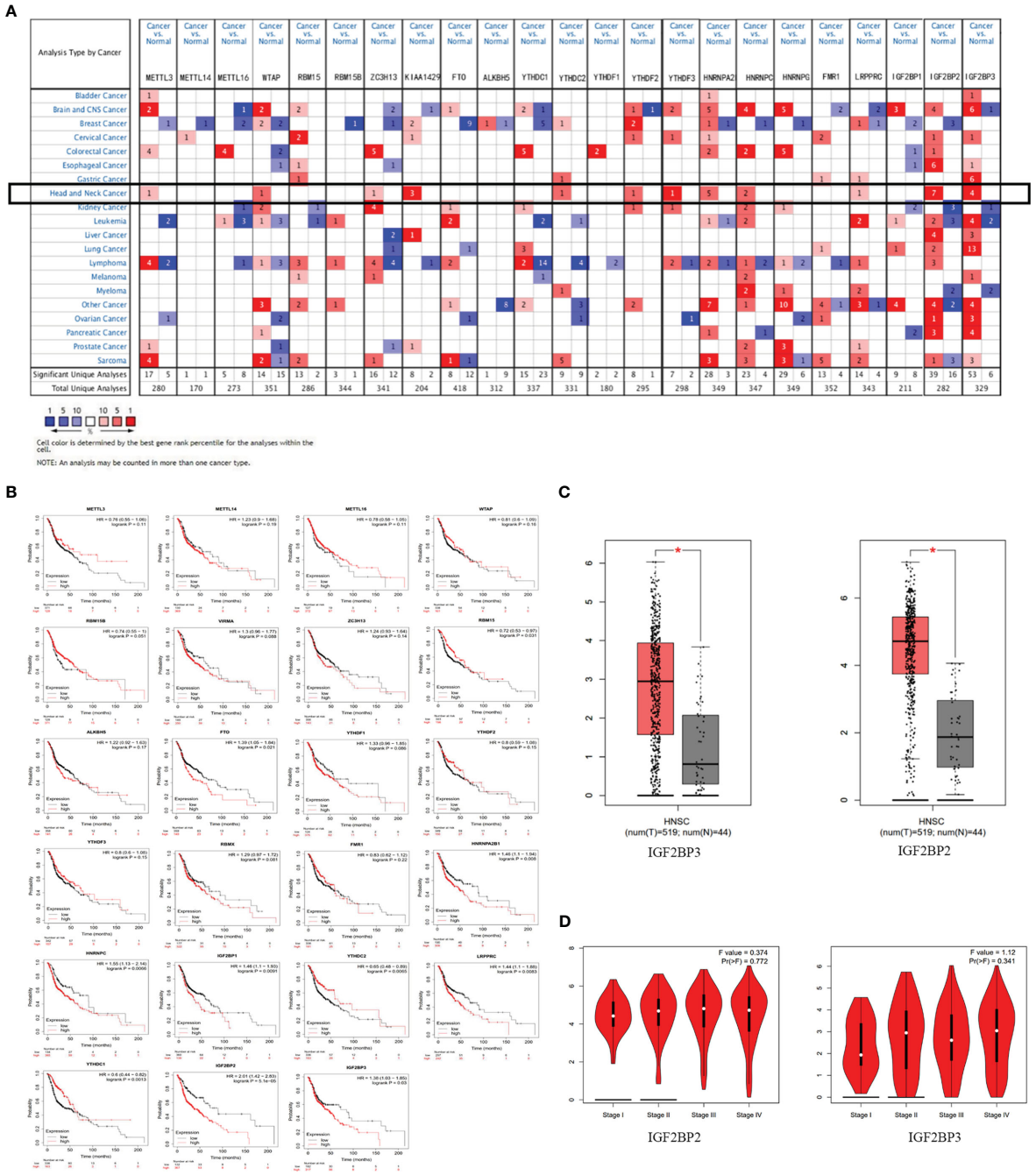

FIGURE 1
m6A and its regulatory genes abnormally expressed in head and neck squamous cell carcinoma (HNSCC). **(A)** An integrated analysis of 23 m6A methylation regulators by searching the Oncomine database. **(B)** The correlation between m6A methylation regulators and HNSCC prognosis supported by the data from Kaplan-Meier Plotter database. **(C)** The expressions of IGF2BP2 and IGF2BP3 were upregulated in HNSCC by searching the GEPIA database. **(D)** No significant difference between IGF2BP2 and IGF2BP3 in different stages of HNSCC (P>0.05) from the data of GEPIA database.

IGF2BP1, IGF2BP2, and IGF2BP3 were significantly shorter than those of patients with low expressions.

To analyze the expression of 23 methylation regulators in the cancer genome atlas (TCGA) in HNSCC and normal tissues, we searched the GEPIA database and found that only the m6A methylation regulators IGF2BP2 and IGF2BP3 had significant differences in expression in HNSCC than in normal tissues (P<0.05) (Figure 1C), which was consistent with the results from the Oncomine database. However, there was no significant difference between IGF2BP2 and IGF2BP3 in different stages of HNSCC (P>0.05) (Figure 1D). Infiltrating immune cells are an important part of the tumor microenvironment and are closely related to tumor progression. Furthermore, we explored the relationship between the expression of m6A methylation regulators and the level of immune infiltration. The results showed that the expression of IGF2BP2 was significantly positively correlated with tumor purity (cor=0.113, P=1.19e-02), and was significantly negatively correlated with the infiltration levels of B cells (cor=-0.249, P=3.89e-08) and CD8+ T

cells (cor=-0.225, *P*=1.91e-08). And the expression of IGF2BP3 was significantly correlated with tumor purity (cor=0.094, *P*=4.03e-02) and CD4+ T cells (cor=0.19, *P*=2.07e-05) (Figure 2A).

To obtain the mutation frequency of m6A methylation regulators in HNSCC, we analyzed and integrated the cBioPortal database. The m6A methylation regulators were found to have various degrees of genetic variation in HNSCC (Figure 2B), and the most common variation was amplification. Among them, IGF2BP2 had the highest genetic variation frequency (14%), followed by KIAA1429 (5%) and YTHDF3 (4%). The frequencies of other regulators were less than 3%, indicating that changes in the expression levels of these regulators were not caused by genetic alterations.

Immunohistochemical analysis of m6A methylation regulators IGF2BP2 and IGF2BP3

Combined with the m6A methylation regulator expression profile and prognosis of patients with HNSCC, we selected IGF2BP2 and IGF2BP3 to verify their expression in OSCC and OED. We examined

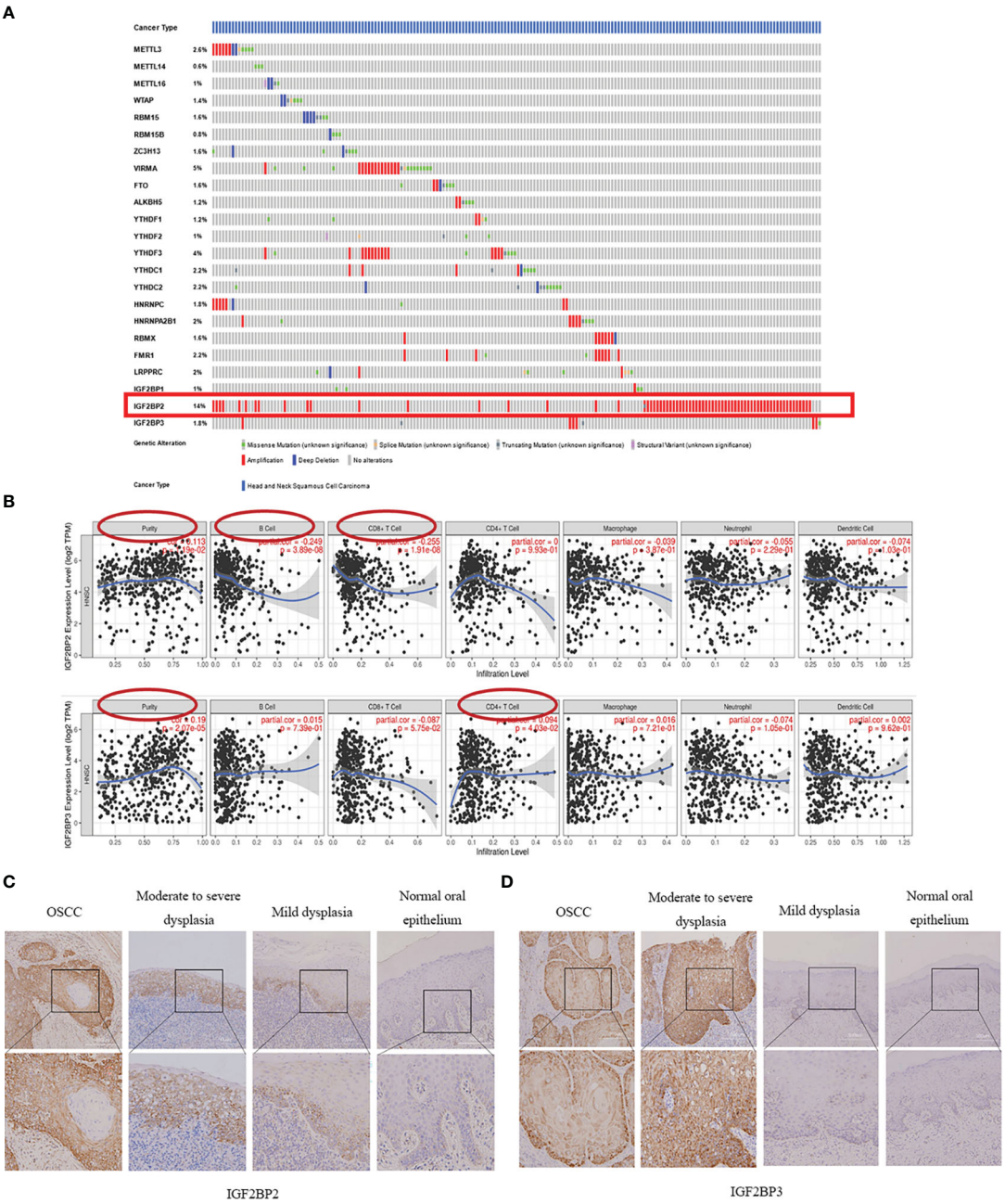

FIGURE 2
Mutation frequency of m6A methylation regulators in HNSCC and their association with IGF2BP2 and IGF2BP3. **(A)** The mutation frequency of m6A methylation regulators in HNSCC (The cBioPortal database). **(B)** The correlation of IGF2BP2 and IGF2BP3 expressions with immune cell infiltration in patients with HNSCC. **(C, D)** Protein expression of IGF2BP2 and IGF2BP3 in oral simple epithelial hyperplasia, OED and OSCC increased gradually.

IGF2BP2 and IGF2BP3 expression of 69 OSCC patients (A total of 236 tissue sections) from our department by IHC staining. The results showed that both IGF2BP2 and IGF2BP3 were expressed in the cytoplasm of squamous epithelial cells (Figures 2C, D).

According to the semi-quantitative results of IHC, we found that the expression of IGF2BP2 increased gradually in epithelial hyperplasia, epithelial dysplasia and squamous cell carcinoma (SCC) (all $P<0.01$) (Figure 3A, Table 3). And the expression of IGF2BP2 increased in epithelial hyperplasia, mild dysplasia, moderate dysplasia and severe dysplasia ($P<0.01$) (Figure 3C). Besides, the expression of IGF2BP3 was increased in epithelial hyperplasia, epithelial dysplasia and SCC (all $P<0.05$) (Figure 3B, Table 3). However, there was no statistical significance for IGF2BP3 between epithelial hyperplasia and mild dysplasia ($P>0.05$) (Figure 3D, Table 3).

There was no significant difference in immunohistochemical semiquantitative scores of IGF2BP2 and IGF2BP3 in the epithelial hyperplasia, mild dysplasia, moderate dysplasia and severe dysplasia groups ($P>0.05$). Moreover, the expression of IGF2BP2 and IGF2BP3 were shown moderate correlation ($r=0.490$, $P<0.001$).

The relationship between the expression of IGF2BP2 and IGF2BP3 in the initial biopsy samples of 69 patients and the clinicopathological characteristics of these patients was analyzed. The results showed that there was no significant difference in the expression of IGF2BP2 and IGF2BP3 among different genders, different ages or smoking/drinking ($P>0.05$). However, they were significantly correlated with pathological diagnosis in the initial biopsy ($P<0.05$) (Tables 4, 5).

Discussion

M6A methylation is one of the significant factors in the occurrence and development of tumors. Reported studies have shown that the m6A write protein METTL3 can recognize the m6A methylation site on the 3'-UTR of B-cell-specific Moloney murine leukemia virus insertion site 1 (BMI1), bind to the m6A read protein

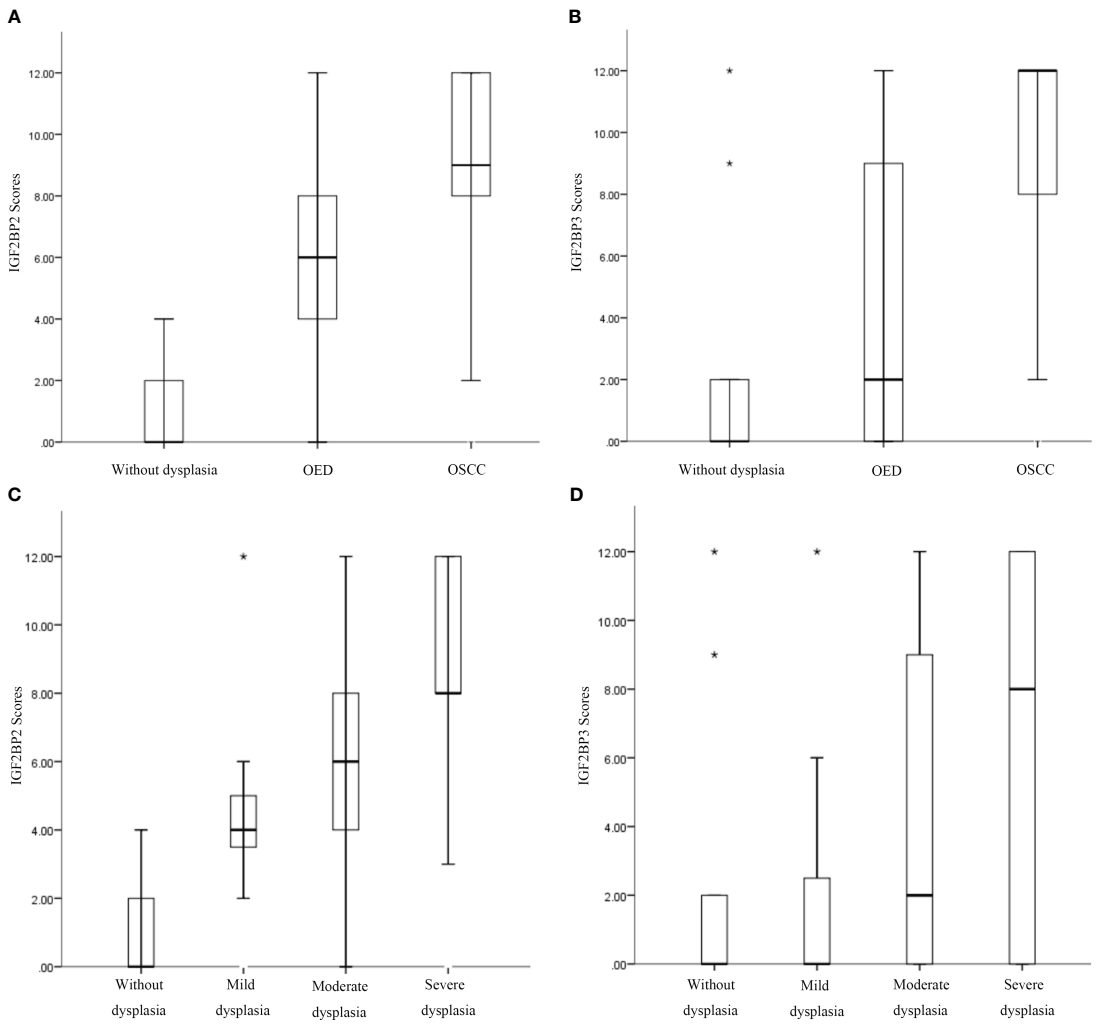

FIGURE 3
Increased expression of IGF2BP2 and IGF2BP3 was associated with the occurrence of oral squamous cell carcinoma (OSCC), oral epithelial dysplasia (OED), and progression of OED. **(A, B)** Immunohistochemical semiquantitative results of IGF2BP2 and IGF2BP3 expression in oral epithelial hyperplasia, OED, and OSCC. **(C, D)** Immunohistochemical semiquantitative results of IGF2BP2 and IGF2BP3 in epithelial hyperplasia, mild/moderate/severe epithelial dysplasia. *:extreme value.

TABLE 3 Differential expression of IGF2BP2 and IGF2BP3 in epithelial hyperplasia, dysplasia and SCC*.

Clinicopathological diagnosis	*p*	
	IGF2BP2	IGF2BP3
hyperplasia-dysplasia	0.000	0.000
Dysplasia-SCC	0.000	0.000
hyperplasia-mild dysplasia	0.000	0.511
mild dysplasia-moderate dysplasia	0.003	0.000
moderate dysplasia-severe dysplasia	0.000	0.018

SCC, squamous cell carcinoma.

TABLE 4 Association between the clinicopathological characteristics and IGF2BP2 expression in 109 cases of OSCC and OED.

Characteristic		IGF2BP2			*P**
	n	Negative	Weak Positive	Strong Positive	
Gender					
Female	62	22	18	22	0.490
Male	47	21	14	12	
Age(years)					
≤40	14	8	4	2	0.380
40-60	56	20	19	17	
≥60	39	15	9	15	
Locations					
Tongue	55	18	18	19	0.060
Buccal	23	14	4	5	
Gingiva	19	9	7	3	
Other	12	2	3	7	
Initial diagnosis					
Epithelial hyperplasia	28	27	1	0	0.000
Mild dysplasia	24	8	14	2	
Moderate dysplasia	33	8	11	14	
Severe dysplasia	24	0	6	18	
Smoking					
Yes	28	13	8	7	0.626
No	81	30	24	27	
Drinking					
Yes	23	11	5	7	0.577
No	86	32	27	27	

* $P < 0.05$ was considered statistically significant.

IGF2BP1, promote the translation of BMI1 and induce the proliferation and metastasis of OSCC thereby (15). However, at present, there is no comprehensive analysis of the relationship between m6A methylation regulators and tumor progression of HNSCC, especially its role in oral mucosal malignant transformation.

Differential expression analysis showed that there were differences between oral epithelial hyperplasia and epithelial dysplasia (16). The positive rate of P53 was gradually increasing also indicated that the degree of malignancy was increasing (17). Through bioinformatics analysis, we found that high expressions of 7 m6A methylation regulators including IGF2BP2 and IGF2BP3 were associated with poor prognosis. Therefore, IGF2BP2 and IGF2BP3 were selected to be explored in OSCC and OED tissues. It was found that both proteins were highly expressed in OSCC, and

10.3389/fonc.2023.1013054

TABLE 5 Association between the clinicopathological characteristics and IGF2BP3 expression in 109 cases of OSCC and OED.

Characteristic	IGF2BP3				P*
	n	Negative	Weak Positive	Strong Positive	
Sex					
Female	62	37	10	15	0.497
Male	47	31	4	12	
Age(years)					
≤40	14	10	2	2	0.895
40-60	56	35	7	14	
≥60	39	23	5	11	
Locations					
Tongue	55	32	10	13	0.119
Buccal	23	19	0	4	
Gingiva	19	12	1	6	
Other	12	5	3	4	
Initial diagnosis					
Epithelial hyperplasia	28	25	1	2	0.002
Mild dysplasia	24	18	3	3	
Moderate dysplasia	33	17	5	11	
Severe dysplasia	24	8	5	11	
Smoking					
Yes	28	19	0	9	0.054
No	81	49	14	18	
Drinking					
Yes	23	15	0	8	0.084
No	86	53	14	19	

* P < 0.05 was considered statistically significant.

their expression increased gradually in oral epithelial hyperplasia, OED, and OSCC.

The insulin-like growth factor 2 mRNA-binding proteins family consists of three restriction enzymes: IGF2BP1, IGF2BP2, and IGF2BP3, which are mainly responsible for regulating the localization, translation, and stability of m6A methylated mRNAs. IGF2BPs exert oncogenic effects by stabilizing m6A-modified mRNAs of oncogenic targets and promoting tumorigenesis (18, 19).

IGF2BP2 is located on chromosome 3q27.2, which binds to the 5' UTR of insulin-like growth factor 2 mRNA and regulates its translation (20). This study showed that the expression of IGF2BP2 increased in epithelial hyperplasia, OED, and OSCC, and gradually increased with the severity of dysplasia. However, there was no significant difference in expression between epithelial hyperplasia and mild epithelial dysplasia between the progressive and stable groups. Previous studies of IGF2BP2 mainly focused on its role as an RNA-binding protein regulating multiple biological processes. For instance, lncRNA HOTAIR inhibits IGF2BP2 and regulates the growth and invasion of colon cancer (21). In recent years, researchers are more tend to regard IGF2BP2 as a reading protein of m6A to regulate the occurrence and development of tumors. For instance, METTL3 stabilized the expression of SOX2 through an m6A-IGF2BP2-dependent mechanism in colon cancer (22). In a study on esophageal adenocarcinoma, IGF2BP2 was found to be more expressed in metastatic lesions than in primary tumors (23).

IGF2BP3 is located on chromosome 7p15.3 and is a carcinoembryonic protein, which is mainly expressed in the embryonic stage and has a lower expression in adult tissues (24). Most of the studies on IGF2BP3 were analyzed by immunohistochemical methods, and several studies in OSCC confirmed that the expression of IGF2BP3 was up-regulated in OSCC (25, 26). In this study, the expression of IGF2BP3 was positive in epithelial hyperplasia, OED, and OSCC. As an m6A methylation reader protein, IGF2BP3 is also involved in regulating the occurrence and development of tumors. In laryngeal carcinoma, RBM15 and IGF2BP3 are involved in m6A methylation modification of TMBIM6, thereby regulating the expression of TMBIM6 in laryngeal squamous cell carcinoma (LSCC) (27). And some studies have shown that the knockout of IGF2BP3 can inhibit DNA replication and angiogenesis in the S phase of the cell cycle by reading the m6A modification of CCND1 and vascular endothelial growth factor (VEGF) respectively in colon cancer (28).

Conclusion

We aimed to predict the cancer risk of OED from the perspective of epigenetics. This study suggested that m6A methylation regulators played an important role in head and neck tumor progression and demonstrates that IGF2BP2 and IGF2BP3 were prognostic indicators and potential biomarkers for immunotherapy in OSCC and OED. These findings may provide new strategies for the diagnosis and treatment of OSCC and OED.

Data availability statement

The raw data supporting the conclusions of this article will be made available by the authors, without undue reservation.

Ethics statement

The studies involving human participants were reviewed and approved by The Biomedical Ethics Committee of the Department of Peking University (No. PKUSSIRB-201948111).

Author contributions

All authors listed have made a substantial, direct, and intellectual contribution to the work and approved it for publication.

Funding

This work was supported by the CAMS Innovation Fund for Medical Sciences (2019-I2M-5-038) and the Fundamental Research Funds for the Central Universities: Special Projects for Strengthening Basic Research of Peking University (BMU2019JC001).

Conflict of interest

The authors declare that the research was conducted in the absence of any commercial or financial relationships that could be construed as a potential conflict of interest.

Publisher's note

Supplementary material

The Supplementary Material for this article can be found online at: https://www.frontiersin.org/articles/10.3389/fonc.2023.1013054/full#supplementary-material

References

1. Bray F, Ferlay J, Soerjomataram I, Siegel RL, Torre LA, Jemal A. Global cancer statistics 2018: GLOBOCAN estimates of incidence and mortality worldwide for 36 cancers in 185 countries. *CA Cancer J Clin* (2018) 68(6):394–424. doi: 10.3322/caac.21492

2. Jia G, Fu Y, He C. Reversible RNA adenosine methylation in biological regulation. *Trends Genet* (2013) 29(2):108–15. doi: 10.1016/j.tig.2012.11.003

3. Lipshitz HD, Claycomb JM, Smibert CA. Post-transcriptional regulation of gene expression. *Methods* (2017) 126:1–2. doi: 10.1016/j.ymeth.2017.08.007

4. Deng X, Su R, Feng X, Wei M, Chen J. Role of N6-methyladenosine modification in cancer. *Curr Opin Genet Dev* (2018) 48:1–7. doi: 10.1016/j.gde.2017.10.005

5. Dai D, Wang H, Zhu L, Jin H, Wang X. N6-methyladenosine links RNA metabolism to cancer progression. *Cell Death Dis* (2018) 9(2):124. doi: 10.1038/s41419-017-0129-x

6. Lan Q, Liu PY, Haase J, Bell JL, Hüttelmaier J, Liu T. The critical role of RNA mA methylation in cancer. *Cancer Res* (2019) 79(7):1285–92. doi: 10.1158/0008-5472.CAN-18-2965

7. Zhao W, Cui Y, Liu L, Ma X, Qi X, Wang Y, et al. METTL3 facilitates OSCC tumorigenesis by enhancing c-myc stability *via* YTHDF1-mediated mA modification. *Mol Ther Nucleic Acids* (2020) 20:1–12. doi: 10.1016/j.omtn.2020.01.033

8. Li D-Q, Huang C-C, Zhang G, Zhou L-L. FTO demethylates YAP mRNA promoting OSCC tumorigenesis. *Neoplasma* (2022) 69(1):71–9. doi: 10.4149/neo_2021_210716N967

9. Tang Z, Li C, Kang B, Gao G, Li C, Zhang Z. GEPIA: a web server for cancer and normal gene expression profiling and interactive analyses. *Nucleic Acids Res* (2017) 45 (W1):W98–W102. doi: 10.1093/nar/gkx247

10. Nagy Á, Munkácsy G, Győrffy B. Pancancer survival analysis of cancer hallmark genes. *Sci Rep* (2021) 11(1):6047. doi: 10.1038/s41598-021-84787-5

11. Gao J, Aksoy BA, Dogrusoz U, Dresdner G, Gross B, Sumer SO, et al. Integrative analysis of complex cancer genomics and clinical profiles using the cBioPortal. *Sci Signal* (2013) 6(269):pl1. doi: 10.1126/scisignal.2004088

12. Li T, Fan J, Wang B, Traugh N, Chen Q, Liu JS, et al. TIMER: A web server for comprehensive analysis of tumor-infiltrating immune cells. *Cancer Res* (2017) 77(21): e108–10. doi: 10.1158/1538-7445.AM2017-108

13. Maher SG, McDowell DT, Collins BC, Muldoon C, Gallagher WM, Reynolds JV. Serum proteomic profiling reveals that pretreatment complement protein levels are predictive of esophageal cancer patient response to neoadjuvant chemoradiation. *Ann Surg* (2011) 254(5):809–16. doi: 10.1097/SLA.0b013e31823699f2

14. Zhu F, Yang T, Yao M, Shen T, Fang C. HNRNPA2B1, as a m(6)a reader, promotes tumorigenesis and metastasis of oral squamous cell carcinoma. *Front Oncol* (2021) 11:716921. doi: 10.3389/fonc.2021.716921

15. Liu L, Wu Y, Li Q, Liang J, He Q, Zhao L, et al. METTL3 promotes tumorigenesis and metastasis through BMI1 mA methylation in oral squamous cell carcinoma. *Mol Ther* (2020) 28(10):2177–90. doi: 10.1016/j.ymthe.2020.06.024

16. Farah CS, Fox SA. Dysplastic oral leukoplakia is molecularly distinct from leukoplakia without dysplasia. *Oral Dis* (2019) 25(7):1715–23. doi: 10.1111/odi.13156

17. Kerdpon D, Rich AM, Reade PC. Expression of p53 in oral mucosal hyperplasia, dysplasia and squamous cell carcinoma. *Oral Dis* (1997) 3(2):86–92. doi: 10.1111/j.1601-0825.1997.tb00018.x

18. Huang H, Weng H, Sun W, Qin X, Shi H, Wu H, et al. Recognition of RNA n-methyladenosine by IGF2BP proteins enhances mRNA stability and translation. *Nat Cell Biol* (2018) 20(3):285–95. doi: 10.1038/s41556-018-0045-z

19. He L, Li H, Wu A, Peng Y, Shu G, Yin G. Functions of N6-methyladenosine and its role in cancer. *Mol Cancer* (2019) 18(1):176. doi: 10.1186/s12943-019-1109-9

20. Nielsen J, Christiansen J, Lykke-Andersen J, Johnsen AH, Wewer UM, Nielsen FC. A family of insulin-like growth factor II mRNA-binding proteins represses translation in late development. *Mol Cell Biol* (1999) 19(2):1262–70. doi: 10.1128/MCB.19.2.1262

21. Wu X-L, Lu R-Y, Wang L-K, Wang Y-Y, Dai Y-J, Wanget C-Y, et al. Long noncoding RNA HOTAIR silencing inhibits invasion and proliferation of human colon cancer LoVo cells via regulating IGF2BP2. *J Cell Biochem* (2019) 120(2):1229–31. doi: 10.1002/jcb.27079

22. Li T, Hu P-S, Zuo Z, Lin J-F, Li X, Wu Q-N, et al. METTL3 facilitates tumor progression *via* an mA-IGF2BP2-dependent mechanism in colorectal carcinoma. *Mol Cancer* (2019) 18(1):112. doi: 10.11861S12943-019-1038-7

23. Barghash A, Golob-Schwarzl N, Helms V, Haybaeck J, Kessler SM. Elevated expression of the IGF2 mRNA binding protein 2 (IGF2BP2/IMP2) is linked to short survival and metastasis in esophageal adenocarcinoma. *Oncotarget* (2016) 7(31):49743–50. doi: 10.18632/oncotarget.10439

24. Bell JL, Wächter K, Mühleck B, Pazaitis N, Köhn M, Lederer M, et al. Insulin-like growth factor 2 mRNA-binding proteins (IGF2BPs): post-transcriptional drivers of cancer progression? *Cell Mol Life Sci* (2013) 70(15):2657–75. doi: 10.1007/s00018-012-1186-z

25. Clauditz TS, Wang CJ, Gontarewicz A, Blessmann M, Tennstedt P, Borgmann K, et al. Expression of insulin-like growth factor II mRNA-binding protein 3 in squamous cell carcinomas of the head and neck. *J Oral Pathol Med* (2013) 42(2):125–32. doi: 10.1111/j.1600-0714.2012.01178.x

26. Hwang YS, Xianglan Z, Park K-K, Chung W-Y. Functional invadopodia formation through stabilization of the PDPN transcript by IMP-3 and cancer-stromal crosstalk for PDPN expression. *Carcinogenesis* (2012) 33(11):2135–46. doi: 10.1093/carcin/bgs258

27. Wang X, Tian L, Li Y, Wang J, Yan B, Yang L, et al. RBM15 facilitates laryngeal squamous cell carcinoma progression by regulating TMBIM6 stability through IGF2BP3 dependent. *J Exp Clin Cancer Res* (2021) 40(1):80. doi: 10.1186/s13046-021-01871-4

28. Yang Z, Wang T, Wu D, Min Z, Tan J, Yu B. RNA N6-methyladenosine reader IGF2BP3 regulates cell cycle and angiogenesis in colon cancer. *J Exp Clin Cancer Res* (2020) 39(1):203. doi: 10.1186/s13046-020-01714-8

frontiers | Frontiers in Oncology

TYPE Case Report
PUBLISHED 28 April 2023
DOI 10.3389/fonc.2023.1178945

OPEN ACCESS

EDITED BY
Jinping Lai,
Kaiser Permanente Sacramento Medical Center, United States

REVIEWED BY
Harold Bo Newton Lovvorn, III, Vanderbilt University Medical Center, United States
Alessandro De Vita,
Scientific Institute of Romagna for the Study and Treatment of Tumors (IRCCS), Italy

*CORRESPONDENCE
Xiao-Hong Li
li1989@csu.edu.cn

†The authors have contributed equally to this work

RECEIVED 03 March 2023
ACCEPTED 06 April 2023
PUBLISHED 28 April 2023

CITATION
Li N-M, Jiang S-H, Zhou P and Li X-H (2023) Case Report: An NTRK1 fusion-positive embryonal rhabdomyosarcoma: clinical presentations, pathological characteristics and genotypic analyses. *Front. Oncol.* 13:1178945. doi: 10.3389/fonc.2023.1178945

Case Report: An NTRK1 fusion-positive embryonal rhabdomyosarcoma: clinical presentations, pathological characteristics and genotypic analyses

Na-Mei Li†, Shi-He Jiang†, Peng Zhou and Xiao-Hong Li*

Department of Pathology, The Second Xiangya Hospital, Central South University, Changsha, China

Rhabdomyosarcoma (RMS) is a prevalent form of soft tissue sarcoma that primarily affects children. Pediatric RMS is characterized by two distinct histological variants: embryonal (ERMS) and alveolar (ARMS). ERMS is a malignant tumor with primitive characteristics resembling the phenotypic and biological features of embryonic skeletal muscles. With the widespread and growing application of advanced molecular biological technologies, such as next-generation sequencing (NGS), it has been possible to determine the oncogenic activation alterations of many tumors. Specifically for soft tissue sarcomas, the determination of tyrosine kinase gene and protein related changes can be used as diagnostic aids and may be used as predictive markers for targeted tyrosine kinase inhibition therapy. Our study reports a rare and exceptional case of an 11-year-old patient diagnosed with ERMS, who tested positive for MEF2D-NTRK1 fusion. The case report presents a comprehensive overview of the clinical, radiographic, histopathological, immunohistochemical, and genetic characteristics of a palpebral ERMS. Furthermore, this study sheds light on an uncommon occurrence of NTRK1 fusion-positive ERMS, which may provide theoretical basis for therapy and prognosis.

KEYWORDS

embryonal rhabdomyosarcoma, NTRK1 fusion, case report, pathological features, next generation sequencing (NGS)

Introduction

Rhabdomyosarcoma (RMS) is a common malignant tumor, accounting for 50% of all soft tissue sarcomas in children. It originates from the embryonic mesenchyme precursor of striated muscle and fails to undergo terminal differentiation (1). Based on the histopathologic and molecular features, RMS is categorized into four primary subtypes,

which are embryonal (ERMS), alveolar (ARMS), pleomorphic (PRMS), and spindle cell/sclerosing (SpRMS) (2). Currently, the diagnosis of RMS mainly relies on morphology (rhabdomyoblastic differentiation) and immunohistochemistry (IHC) (expression pattern of Myogenin and MYO-D1) (3). ERMS represents the most prevalent subtype of RMS and is imparted with a favorable prognosis; whereas, ARMS is known to exhibit a more aggressive clinical course and is often associated with a higher incidence of metastasis (2). The cornerstone of treatment comprises of multi-agent chemotherapy along with local intervention strategies, including surgery and/or radiotherapy, as required (3, 4).

With widespread applications of NGS, genetic testing in RMS diagnosis have delineated the mechanism of oncogenesis. The majority of ARMS harbor PAX-FOXO gene fusions owing to chromosomal translocations, mostly involving in PAX3-FOXO1 and PAX7-FOXO1 (5), and a small subset expressing PAX3-FOXO4 or PAX3-NOXA1 (6). As a transcription factor, the chimeric protein PAX-FOXO drives the expression of oncogenic genes. Molecular ancillary testing in ARMS even proposes a challenge for morphological classification: fusion-positive ARMS showing worse survival than fusion-negative subtype, irrespective of histopathologic features. Moreover, fusion-negative ARMS exhibits the molecular profile and clinical outcome that are analogous to the ERMS subtype (7). Application of ARMS fusion status in the risk stratification is popular in clinical trials (8, 9).

SpRMS was initially established as a distinct entity in the WHO 2013 classification of soft tissue and bone neoplasms (10). Morphologically, bland spindle cell and extensive hyalinized matrix are the outstanding features of spindle cell RMS and sclerosing RMS separately. The discovery of several significant genes associated with SpRMS has greatly deepened our comprehension of the biological processes underlying SpRMS, as well as indicated that it is a heterogeneous group of tumors, molecularly classifying it into four categories (1): infantile/congenital SpRMS harboring NCOA2 or VGLL2 gene fusions (11); (2) SpRMS occurring in the adult and pediatric which show MYOD1 gene mutations (12); (3) SpRMS with EWSR1/FUS–TFCP2 gene fusion, predilection for intraosseous locations (13, 14); (4) SpRMS with no known recurrent abnormalities. MYOD1 mutated SpRMS and SpRMS with EWSR1/FUS–TFCP2 gene fusion both behave aggressively and have a poor prognosis (15, 16). Molecular classification of SpRMS facilitates prognostic stratification.

Genetic analyses typically have indicated that ERMS is a biologically heterogeneous group of disorders, involving in aneuploidy and gene mutation including RAS genes (HRAS, KRAS, and NRAS) (17, 18), FGFR4 (19, 20), PIK3CA, NF1 and FBXW7 (21, 22). It has been observed in 1996 that ERMS exhibits the gain of multiple chromosomes, with notable instances on chromosomes 2, 7, 8, 12, 13, 17, 18, and 19, while concurrently demonstrating the loss of chromosomes 10, 14, 15, and 16 (23). In both fusion gene-negative ARMS and ERMS, frequent alterations can be observed in whole chromosome copy numbers, particularly, the amplification in chromosome 8 (24). At present, few literatures have reported that ERMS tumors harbor gene rearrangement. Here, we find a rare case of ERMS, harboring neurotrophic receptor tyrosine kinase 1 (NTRK1) gene rearrangement, which can broaden our understanding of ERMS genotype and maybe provide treatment options.

Case presentation

An 11-year-old male youngster reported a 20-day history of eyelid mass, which is painless and non-pruritic, as well as no skin ulceration. MRI scan revealed a subcutaneous mass (1.2 × 0.5 cm) in the left lower eyelid, which was well demarcated indicating a pre-operative clinical impression of skin benign tumor (Figures 1A, B). After surgical excision of subcutaneous tumor, samples were micro-evaluated in our department, and presented as monomorphous population of primitive cells with abundant mitosis and minimal cytoplasm (Figures 2A, C). The mass was surrounded by a continuous fibrous pseudocapsule (Figures 2A, B). Hyperendothelial vessels lied in maliglant tumor cells, with small lymphocytes surrounding these vessels (Figures 2B, D, F, G, H, K, L). Based on extensive H&E staining observation, there is no evidence of rhabdomyoblastic differentiation.

IHC demonstrated striated muscle differentiation (diffusely positive for DES, MYOD1 and Myogenin showing patchy staining) (Figures 2E–H), which led to reliable diagnosis of ERMS in the case. DNA-based NGS revealed MEF2D-NTRK1 (EX5:EX12)

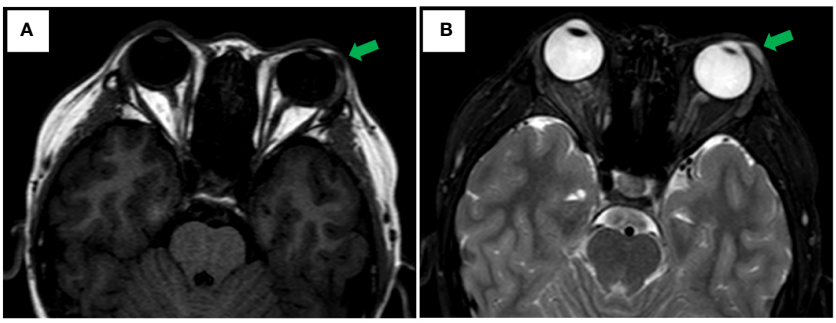

FIGURE 1
Axial MRI Imaging. **(A)** Well-circumscribed fusiformmass is noted in the left lower eyelid appearing hypointense on T1 weighted image with green arrowhead. **(B)** T2-weighted showing hyperintense with green arrowhead.

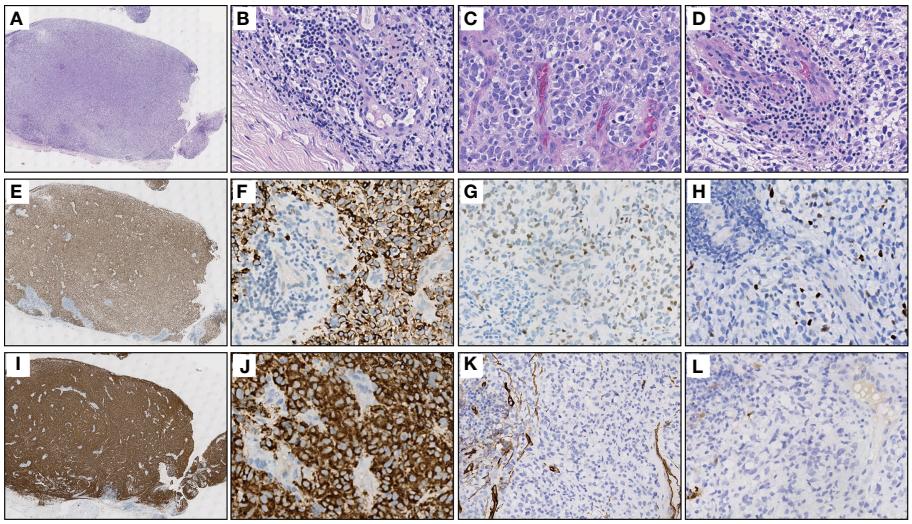

FIGURE 2
Representative H&E and IHC stainings of serial sections. **(A)** Extra-low power H&E image shows a well-demarcated mass entirely, surrounded by fibrous pseudocapsule. **(B)** High power view of A gets more detail about the pseudocapsule, simultaneously, demonstrates hyperendothelial vessels and lymphocytes that aggregated around these vessels. **(C)** The tumor is primarily composed of primitive round cells with scant cytoplasm and numerous mitosis. **(D)** Focally shows clear cytoplasm and lymphocytes aggregating around the hyperendothelial vessels. **(E)** Diffuse Desmin staining in the same power view of **(A, F)** A high power view of E showing cytoplasmic positive of Desmin, while the nonmuscular hyperendothelial vessels are negative for Desmin. **(G, H)** Focal positive immunohistochemical staining of tumor cells for MYOD1 and Myogenin respectively. **(I, J)** The immunohistochemical staining for TrkA/B/C expression was performed using pan-Trk (clone EPR17341, Roche/Ventana). There is a strong diffuse immunoreactivity for pan-Trk in cytoplasm of tumor cells. **(K, L)** Negative IHC reaction for CD34 and S100, respectively.

fusion (Figure 3A), and NTRK1 amplification, along with multiple genes amplifications (CDK6, PMS2, MET, EGFR, BRAF, MLL3, MYC, FGFR1, WRN, EXT1, NBN, RECQL4) and deletions (FLT4, MAP2K2, DOT1L, STK11, GNA11) (Table 1). These copy number variations involve chromosomes 7, 8 and 19. Next, RNA-based NGS also revealed MEF2D-NTRK1 (EX5:EX12) fusion (Figure 3B). IHC detection of Pan-Trk is a dependable and effective method for identifying NTRK fusions (25). In consideration of MEF2D-NTRK1 fusion detected by NGS, follow-up confirmatory IHC staining of pan-Trk was performed, as expected, it demonstrated diffusely strong positive in cytoplasm (Figures 2I, J). In terms of differential diagnosis in IHC, CD34 and S-100 were negative (Figures 2K, L). To sum up, the case is a rare ERMS with NTRK1 fusion positive, not an NTRK-rearranged spindle cell tumor.

Discussion

RMS is a frequently occurring soft tissue sarcoma in children, constituting over 50% of all cases (3). ERMS, the most common subtype, is an unsophisticated and malignant neoplasm of soft tissue that exhibits characteristics similar to those of embryonic skeletal muscle, both phenotypically and biologically (26). Histologically, ERMS features a proliferation of undifferentiated mesenchymal cells that exhibit round or spindle-shaped morphologies, mixed with a varying number of rhabdomyoblasts and interspersed with zones of stroma that are loose, myxoid, and paucicellular (27). ERMS is typified by the presence of oval to spindle-shaped primitive cells with minimal cytoplasm. These cells can be arranged in compact sheets or surrounded by a loose, myxoid background. Certain regions of ERMS display a small, blue, and round morphology. As these cells undergo differentiation, they gradually exhibit an increased eosinophilic cytoplasm and adopt elongated shapes that are described variously as “tadpole”, “strap”, and “spider” cells, indicating the presence of rhabdomyoblastic differentiation (28). Desmin is the leading diagnostic marker, commonly demonstrating diffuse staining. In general, ERMS features a patchy positivity for Myogenin and MYO-D1, and there are apparent divergences in Myogenin staining patterns between ERMS and ARMS. Specifically, ARMS usually displays a diffuse Myogenin staining, while in ERMS, the staining frequently appears patchy. Differences in Myogenin staining patterns have also been observed between ERMS and ARMS. ARMS tends to show diffuse staining for Myogenin, whereas the staining is often patchy in ERMS. In our report, IHC expression patterns of Desmin, Myogenin, and MYO-D1 were consistent with the immunological phenotype of ERMS.

Genotypic analyses of ERMS and fusion-negative ARMS typically reveal aneuploidy characterized by numerous copy number gains and losses (7). The ERMS tumors have been demonstrated the gain of whole or most of distinct chromosomes, particularly chromosomes 2, 13, 12, 8, 7, 17, 18, and 19, along with the loss of chromosomes 16, 10, 15, and 14 (23). ERMS is linked to distinct genetic changes, which encompass chromosomal gains and losses resulting in aneuploidy. Additionally, ERMS involves modifications in RAS family genes (HRAS, NRAS, KRAS), FGFR4, PIK3CA, NF1, and FBXW7 (28–30). In ARMS, identifying PAX3-FOXO1 and PAX7-FOXO1 gene fusions is an important feature for diagnosis (31, 32). The identification of gene fusions and the use of molecular ancillary testing have improved the

classification of RMS by grouping fusion-positive tumors into the alveolar subtype regardless of cytomorphology. However, no differences were observed between fusion-negative ARMS and ERMS (7). In this case, the patient harbors amplifications and losses of multiple genes, involving multiple chromosomes (1, 5, 7, 8, and 19).

Interestingly, the patient also has NTRK1 gene rearrangement. RNA-/DNA-based NGS testing confirms NTRK1 fusion with a partner gene MEF2D. Immunohistochemically, the case is also pan-TRK positive. Therefore, it is necessary to make differential diagnosis between this case and NTRK-rearranged spindle cell tumor. The NTRK-rearranged spindle cell tumor is a rare type of soft tissue tumor with NTRK gene rearrangement as the molecular feature, and is a group of soft tissue tumors defined by molecular genetic features (33). It has a wide spectrum of morphology and tissue classification. IHC often shows co-expression of S-100 and CD34, while lack of other definite differentiations. Its most common features are the phenotype of monomorphic spindle cells, interstitial transparency and infiltrating growth. In this case, IHC of S-100 and CD34 are both negative, moreover, Myogenin, MYO-D1 and Desmin reveal the skeletal muscle differentiation.

Tropomyosin receptor kinases (Trk) are encoded by the neurotrophic tyrosine/tropomyosin receptor kinase (NTRK) genes and belong to the family of tyrosine kinases (34). The Trk family comprises three isoforms, namely TrkA, TrkB, and TrkC, which are encoded by NTRK1, NTRK2, and NTRK3, respectively. In cancer, the most common mechanism of Trk activation involves fusion events that affect NTRK1/2/3. These fusions arise from chromosomal rearrangements between NTRK genes, which include the kinase domains, and various partner genes (35). Currently, there are two drugs approved for treating the NTRK fusion-positive cancers, irrespective of their type: larotrectinib (approved in 2018) and entrectinib (approved in 2019) (36). Involving rearrangements either within or between chromosomes, gene fusions that affect the Trk protein family typically entail the fusion of the 5' end of a partner gene that contains a dimerization/oligomerization domain with the 3' region of an NTRK gene that encodes the tyrosine kinase domain. The resulting chimeric gene gives rise to a protein that lacks the TRK ligand binding domain, but retains the tyrosine kinase domain. This fusion protein is associated with oncogenic and transforming potential, which arises from the overexpression and constitutive activation of the TRK kinase domain due to the presence of the dimerization domain derived from the partner gene (37).

In this case, DNA-based NGS results showed MEF2D-NTRK1 (EX5:EX12) gene fusion in tumor cells. Subsequently, we validated

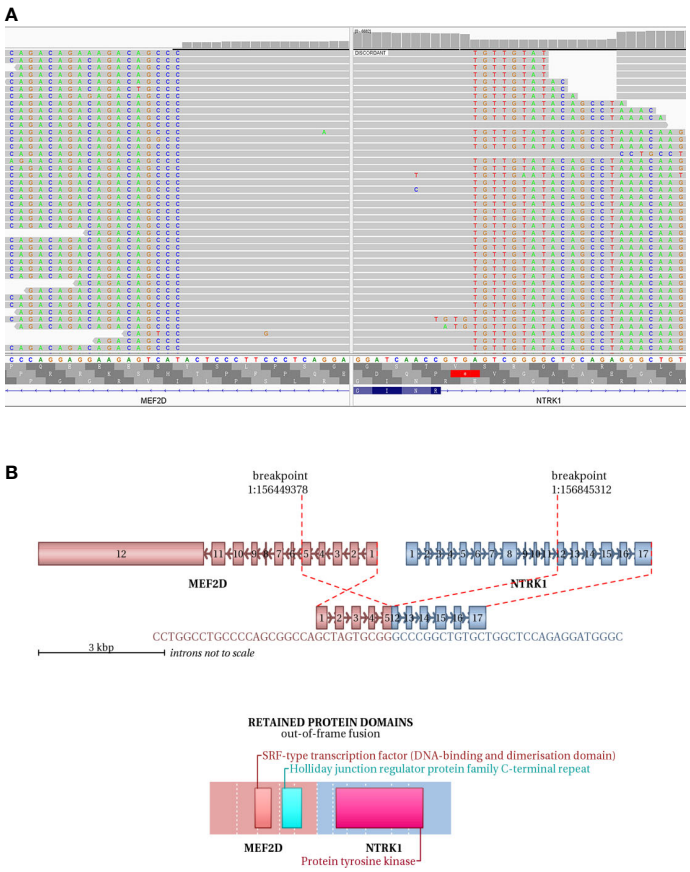

FIGURE 3
NGS testing of the tumor to validate NTRK1 fusion. **(A)** DNA-based NGS testing of the pan-tumor related 1021-Genes Panel is used to demonstrate the MEF2D-NTRK1 (EX5:EX12) fusion in formalin-fixed paraffin-embedded tissue sample. **(B)** Schematic representation of the predicted chimeric protein in RNA-based NGS assay with the 555-Genes Panel in formalin-fixed paraffin-embedded tissue sample.

NTRK1 gene fusion with RNA-based NGS, which also detected MEF2D-NTRK1 (EX5:EX12) fusion mutation, and the fusion breakpoint sequence was completely consistent with DNA-based NGS. In vertebrates, the myocyte enhancer factor 2 (MEF2) protein family is comprised of four members, MEF2A, B, C, and D, all of which contain a highly conserved MADS-box domain at their N-terminal regions. The MADS-box domain is composed of 55 amino acids and plays a crucial role in recognizing target sequences. The conserved residues within this domain are primarily responsible for binding to DNA sequences rich in A/T and mediating the dimerization of MADS-box proteins. NTRK1 protein is a transmembrane neurotrophic receptor that is found in neural cells and is triggered *via* the binding of its main ligand, nerve growth factor. The NTRK1 comprises an extracellular domain responsible for ligand binding, a transmembrane domain, and an intracellular region harboring the tyrosine kinase domain. Oncogenic activation of NTRK1 leads to autophosphorylation and activation of the MAP-kinase, PI3-kinase and PLC-γ pathways, mediating cell proliferation, survival and differentiation (38). After the rearrangement of MEF2D-NTRK1 (EX5:EX12), the 5' end of the resulting fusion gene retained the promoter of MEF2D gene to intron 5, and the 3' end retained the intron 11 of NTRK1 gene to the terminator. The fusion mutation occurs in the intra-codon reading frame, and the fusion protein will retain the tyrosine kinase domain of NTRK1. The protein formed by this fusion mutation retains the MADS-box domain of MEF2D gene at its 5' end, and the tyrosine kinase domain of NTRK1 at its 3' end (Figure 3B). Moreover, IHC staining of pan-Trk also demonstrated diffusely strong positive in cytoplasm (Figures 2I, J). Therefore, the resulting chimera protein is a Trk kinase that is activated in a constitutive manner, irrespective of ligand binding, and has biological functions.

Fusions of the NTRK1 gene are found in lung cancers, colorectal and thyroid cancers, and Glioma, etc (39). It has been reported that 3 cases of NTRK1 fusion were detected in 982 patients with glioma, and one patient had MEF2D-NTRK1 (EX9:EX12) fusion, and IHC detection of pan-Trk showed strong expression (40). Entrectinib (41) and larotrectinib (42) have demonstrated significant efficacy in NTRK fusion-positive tumors. Tadipatri et al. also demonstrated the administration of larotrectinib has resulted in the successful management for remission at 6 months in a high-grade glioneuronal tumor harboring the MEF2D-NTRK1 fusion (43). A patient newly diagnosed low-grade glioneuronal tumor with the BCAN-NTRK1 fusion was treated with entrectinib, 60% tumor reduction at 9 months, then progression at 11 months (44). A 26-

TABLE 1 Genetic mutations of DNA-based next generation sequencing (NGS) in the case.

Mutation Genes	Location	Transcript Version	Variant types	Copy number/ Mutation frequency
NTRK1	1q23.1	NM_002529.3	all exon, amplification	13.0
CDK6	7q21.2	NM_001145306.1	all exon, amplification	4.8
PMS2	7p22.1	NM_000535.5	all exon, amplification	4.0
MET	7p31.2	NM_000245.2	all exon, amplification	3.6
EGFR	7p11.2	NM_005228.3	all exon, amplification	3.6
BRAF	7q34	NM_004333.4	all exon, amplification	3.6
MLL3	7q36.1	NM_170606.2	all exon, amplification	3.6
MYC	8q24.21	NM_002467.4	all exon, amplification	8.2
FGFR1	8p11.23	NM_023110.2	all exon, amplification	7.0
WRN	8p12	NM_000553.4	all exon, amplification	6.8
EXT1	8q24.11	NM_000127.2	all exon, amplification	6.6
NBN	8q21.3	NM_002485.4	all exon, amplification	6.0
RECQL4	8q24.3	NM_004260.3	all exon, amplification	5.4
FLT4	5q35.3	NM_182925.4	all exon, deletion	1.2
MAP2K2	19p13.3	NM_030662.3	all exon, deletion	1.2
DOT1L	19p13.3	NM_032482.2	all exon, deletion	1.0
STK11	19p13.3	NM_000455.4	all exon, deletion	1.0
GNA11	19p13.3	NM_002067.2	all exon, deletion	1.0
MEF2D-NTRK1	1q22; 1q23.1	NM_005920.2; NM_002529.3	Fusion (EX5:EX12)	49.7%

year-old male with advanced TPM4-NTRK1 rearranged spindle cell neoplasm and liver, lung and bone metastases, treated with larotrectinib on a continuous 28-day schedule, and showed tumor shrinkage in both visceral and bone lesions after 7 days of treatment (45). ERMS is usually treated primarily by the surgical resection in clinical practice, with adjuvant comprehensive treatment such as radiotherapy, chemotherapy, or targeted drug therapy when necessary to improve patient survival. For this case, the current treatment of this patient is systemic chemotherapy and local radiotherapy after the surgical resection, without the use of NTRK inhibitors. This treatment regimen is currently effective. Targeted drug therapy with NTRK1 fusion will be a very good option if disease progression occurs in the future. NGS assay also identified the NTRK1, EGFR, MET, BRAF and FGFR1 amplifications in this patient. Interestingly, the targeted systemic therapy with larotrectinib was efficacious in a clinical case study, an individual with metastatic esophageal carcinoma was observed NTRK1 amplification (46). The amplification of MET and FGFR, and the activation of bypass signaling molecules including RAS-MAPK/ERK and PI3K-AKT pathways (such as BRAF) are important mechanisms of resistance to tyrosine kinase inhibitors (TKIs) (47). Considering that the patient has a variety of sensitive and drug-resistant mutations involving targeted drugs, whether and how to use targeted drugs in the future need to be further discussed.

Here, we find a rare case of NTRK1 fusion-positive ERMS, which is the first report in literature. In the case, we believe that MEF2D-NTRK1 fusion is a driving mutation and harbors oncogenic and transforming potentials, which is one of the potential pathogeneses. The patient has not been treated with NTRK inhibitors, which is the limitation of the study. Approaches for the identification of cancers driven by NTRK fusions encompass the following tactics: IHC staining of pan-Trk, but NTRK fusion detection by NGS remains the most reliable tool. With NGS application in rare tumors, more NTRK fusion-driven RMS may be found, providing theoretical basis for the follow-up targeted therapy. Therefore, we recommend that all ERMS should undergo the NGS detection with large panel, which can enrich the gene mutation spectrum of ERMS and promote the molecular typing and diagnosis of ERMS. If gene mutation with targeted drug is detected, it will also provide patients with more treatment options.

Conclusion

Based on the results of morphology, immunology, and genotype analysis, we present a rare ERMS with NTRK1 fusion. With the growing accessibility of NGS analysis, rare tumors are now amenable to management through identifying the targetable molecular markers. Importantly, the oncogenic receptor tyrosine kinase that is abnormally expressed in NTRK-rearranged sarcoma has been proved to have therapeutic targeting, which may improve the prognosis of patients.

Data availability statement

The original contributions presented in the study are included in the article. Further inquiries can be directed to the corresponding author.

Ethics statement

The studies involving human participants were reviewed and approved by the Ethics Committee of the Second Xiangya Hospital of Central South University. Written informed consent to participate in this study was provided by the participants' legal guardian/next of kin. Written informed consent was obtained from the individual(s), and minor(s)' legal guardian/next of kin, for the publication of any potentially identifiable images or data included in this article.

Author contributions

X-HL and PZ designed the study. N-ML and S-HJ participated in patient treatment and analyzed clinical data. N-ML and X-HL performed molecular testing and analyzed the data. N-ML and S-HJ drafted the manuscript. X-HL supervised the work and revised the manuscript. All authors contributed to the article and approved the submitted version.

Funding

This work was supported by the National Natural Science Foundations of China (No. 81900070 for X-HL) and the Natural Science Foundation of Hunan Province (No. 2020JJ5813 for X-HL). The funder has roles in the design and conduct of the study, the analysis and interpretation of the data, and preparation of the manuscript.

Conflict of interest

The authors declared that the research was conducted in the absence of any commercial or financial relationships that could be construed as a potential conflict of interest.

Publisher's note

References

1. Anderson WJ, Doyle LA. Updates from the 2020 world health organization classification of soft tissue and bone tumours. *Histopathology* (2021) 78(5):644–57. doi: 10.1111/his.14265

2. Agaram NP. Evolving classification of rhabdomyosarcoma. *Histopathology* (2022) 80(1):98–108. doi: 10.1111/his.14449

3. Chen C, Dorado Garcia H, Scheer M, Henssen AG. Current and future treatment strategies for rhabdomyosarcoma. *Front Oncol* (2019) 9:1458. doi: 10.3389/fonc.2019.01458

4. Makimoto A. Optimizing rhabdomyosarcoma treatment in adolescents and young adults. *Cancers (Basel)* (2022) 14(9):2270. doi: 10.3390/cancers14092270

5. Barr FG, Qualman SJ, Macris MH, Melnyk N, Lawlor ER, Strzelecki DM, et al. Genetic heterogeneity in the alveolar rhabdomyosarcoma subset without typical gene fusions. *Cancer Res* (2002) 62(16):4704–10. Available at: https://pubmed.ncbi.nlm.nih.gov/12183429/.

6. Wachtel M, Dettling M, Koscielniak E, Stegmaier S, Treuner J, Simon-Klingenstein K, et al. Gene expression signatures identify rhabdomyosarcoma subtypes and detect a novel T(2;2)(Q35;P23) translocation fusing Pax3 to Ncoa1. *Cancer Res* (2004) 64(16):5539–45. doi: 10.1158/0008-5472.CAN-04-0844

7. Williamson D, Missiaglia E, de Reynies A, Pierron G, Thuille B, Palenzuela G, et al. Fusion gene-negative alveolar rhabdomyosarcoma is clinically and molecularly indistinguishable from embryonal rhabdomyosarcoma. *J Clin Oncol* (2010) 28 (13):2151–8. doi: 10.1200/JCO.2009.26.3814

8. Mascarenhas L, Chi YY, Hingorani P, Anderson JR, Lyden ER, Rodeberg DA, et al. Randomized phase ii trial of bevacizumab or temsirolimus in combination with chemotherapy for first relapse rhabdomyosarcoma: a report from the children's oncology group. *J Clin Oncol* (2019) 37(31):2866–74. doi: 10.1200/JCO.19.00576

9. Gallego S, Zanetti I, Orbach D, Ranchere D, Shipley J, Zin A, et al. Fusion status in patients with lymph node-positive (N1) alveolar rhabdomyosarcoma is a powerful predictor of prognosis: experience of the European paediatric soft tissue sarcoma study group (Epssg). *Cancer* (2018) 124(15):3201–9. doi: 10.1002/cncr.31553

10. Zambo I, Vesely K. [Who classification of tumours of soft tissue and bone 2013: the main changes compared to the 3rd edition]. *Cesk Patol* (2014) 50(2):64–70. Available at: https://www.ncbi.nlm.nih.gov/pubmed/24758500.

11. Alaggio R, Zhang L, Sung YS, Huang SC, Chen CL, Bisogno G, et al. A molecular study of pediatric spindle and sclerosing rhabdomyosarcoma: identification of novel and recurrent Vgll2-related fusions in infantile cases. *Am J Surg Pathol* (2016) 40 (2):224–35. doi: 10.1097/PAS.0000000000000538

12. Szuhai K, de Jong D, Leung WY, Fletcher CD, Hogendoorn PC. Transactivating mutation of the Myod1 gene is a frequent event in adult spindle cell rhabdomyosarcoma. *J Pathol* (2014) 232(3):300–7. doi: 10.1002/path.4307

13. Watson S, Perrin V, Guillemot D, Reynaud S, Coindre JM, Karanian M, et al. Transcriptomic definition of molecular subgroups of small round cell sarcomas. *J Pathol* (2018) 245(1):29–40. doi: 10.1002/path.5053

14. Agaram NP, Zhang L, Sung YS, Cavalcanti MS, Torrence D, Wexler L, et al. Expanding the spectrum of intraosseous rhabdomyosarcoma: correlation between 2 distinct gene fusions and phenotype. *Am J Surg Pathol* (2019) 43(5):695–702. doi: 10.1097/PAS.0000000000001227

15. Agaram NP, Chen CL, Zhang L, LaQuaglia MP, Wexler L, Antonescu CR. Recurrent Myod1 mutations in pediatric and adult sclerosing and spindle cell rhabdomyosarcomas: evidence for a common pathogenesis. *Genes Chromosomes Cancer* (2014) 53(9):779–87. doi: 10.1002/gcc.22187

16. Le Loarer F, Cleven AHG, Bouvier C, Castex MP, Romagosa C, Moreau A, et al. A subset of epithelioid and spindle cell rhabdomyosarcomas is associated with Tfcp2 fusions and common alk upregulation. *Mod Pathol* (2020) 33(3):404–19. doi: 10.1038/s41379-019-0323-8

17. Bauer J, Cuvelier N, Ragab N, Simon-Keller K, Nitzki F, Geyer N, et al. Context-dependent modulation of aggressiveness of pediatric tumors by individual oncogenic ras isoforms. *Oncogene* (2021) 40(31):4955–66. doi: 10.1038/s41388-021-01904-4

18. Agaram NP, Huang SC, Tap WD, Wexler LH, Antonescu CR. Clinicopathologic and survival correlates of embryonal rhabdomyosarcoma driven by Ras/Raf mutations. *Genes Chromosomes Cancer* (2022) 61(3):131–7. doi: 10.1002/gcc.23010

19. De Vita A, Vanni S, Fausti V, Cocchi C, Recine F, Miserocchi G, et al. Deciphering the genomic landscape and pharmacological profile of uncommon entities of adult rhabdomyosarcomas. *Int J Mol Sci* (2021) 22(21):11564. doi: 10.3390/ijms222111564

20. De Vita A, Ferrari A, Miserocchi G, Vanni S, Domizio C, Fonzi E, et al. Identification of a novel Rab3ip-Hmga2 fusion transcript in an adult head and neck rhabdomyosarcoma. *Oral Dis* (2022) 28(7):2052–4. doi: 10.1111/odi.14036

21. Kim J, Light N, Subasri V, Young EL, Wegman-Ostrosky T, Barkauskas DA, et al. Pathogenic germline variants in cancer susceptibility genes in children and young adults with rhabdomyosarcoma. *JCO Precis Oncol* (2021) 5:PO.20.00218. doi: 10.1200/PO.20.00218

22. Bennett JA, Ordulu Z, Young RH, Pinto A, Van de Vijver K, Burandt E, et al. Embryonal rhabdomyosarcoma of the uterine corpus: a clinicopathological and molecular analysis of 21 cases highlighting a frequent association with Dicer1 mutations. *Mod Pathol* (2021) 34(9):1750–62. doi: 10.1038/s41379-021-00821-x

23. Weber-Hall S, Anderson J, McManus A, Abe S, Nojima T, Pinkerton R, et al. Gains, losses, and amplification of genomic material in rhabdomyosarcoma analyzed by comparative genomic hybridization. *Cancer Res* (1996) 56(14):3220–4. Available at: https://pubmed.ncbi.nlm.nih.gov/8764111/.

24. Wexler LH, Ladanyi M. Diagnosing alveolar rhabdomyosarcoma: morphology must be coupled with fusion confirmation. *J Clin Oncol* (2010) 28(13):2126–2128. doi: 10.1200/JCO.2009.27.5339

25. Hechtman JF, Benayed R, Hyman DM, Drilon A, Zehir A, Frosina D, et al. Pan-trk immunohistochemistry is an efficient and reliable screen for the detection of ntrk fusions. *Am J Surg Pathol* (2017) 41(11):1547–51. doi: 10.1097/PAS.0000000000000911

26. Patil G, Halawar S, Sagari S, Babannavar R, Purohit S. Embryonal rhabdomyosarcoma occurring on mandibular gingiva in an adult. *J Clin Diagn Res* (2013) 7(9):2088–9. doi: 10.7860/JCDR/2013/6008.3415

27. Angelico G, Piombino E, Broggi G, Motta F, Spadola S eds. Rhabdomyoblasts in pediatric tumors: a review with emphasis on their diagnostic utility. *J Stem Cell Ther Transplant* (2017) 1:008-016. doi: 10.29328/journal.jsctt.1001002

28. Agaram NP. Update on myogenic sarcomas. *Surg Pathol Clin* (2019) 12(1):51–62. doi: 10.1016/j.path.2018.10.003

29. Paulson V, Chandler G, Rakheja D, Galindo RL, Wilson K, Amatruda JF, et al. High-resolution array cgh identifies common mechanisms that drive embryonal rhabdomyosarcoma pathogenesis. *Genes Chromosomes Cancer* (2011) 50(6):397–408. doi: 10.1002/gcc.20864

30. Shern JF, Chen L, Chmielecki J, Wei JS, Patidar R, Rosenberg M, et al. Comprehensive genomic analysis of rhabdomyosarcoma reveals a landscape of alterations affecting a common genetic axis in fusion-positive and fusion-negative tumors. *Cancer Discovery* (2014) 4(2):216–31. doi: 10.1158/2159-8290.CD-13-0639

31. Davis RJ, D'Cruz CM, Lovell MA, Biegel JA, Barr FG. Fusion of Pax7 to fkhr by the variant T(1;13)(P36;Q14) translocation in alveolar rhabdomyosarcoma. *Cancer Res* (1994) 54(11):2869–72. Available at: https://pubmed.ncbi.nlm.nih.gov/8187070/.

32. Barr FG, Galili N, Holick J, Biegel JA, Rovera G, Emanuel BS. Rearrangement of the Pax3 paired box gene in the paediatric solid tumour alveolar rhabdomyosarcoma. *Nat Genet* (1993) 3(2):113–7. doi: 10.1038/ng0293-113

33. Yin L, Shi C, He X, Qiu Y, Chen H, Chen M, et al. Ntrk-rearranged spindle cell neoplasms: a clinicopathological and molecular study of 13 cases with peculiar characteristics at one of the largest institutions in China. *Pathology* (2022) 55 (3):362–374. doi: 10.1016/j.pathol.2022.10.003

34. Cocco E, Scaltriti M, Drilon A. Ntrk fusion-positive cancers and trk inhibitor therapy. *Nat Rev Clin Oncol* (2018) 15(12):731–47. doi: 10.1038/s41571-018-0113-0

35. Vaishnavi A, Le AT, Doebele RC. Trking down an old oncogene in a new era of targeted therapy. *Cancer Discovery* (2015) 5(1):25–34. doi: 10.1158/2159-8290.CD-14-0765

36. Han SY. Trk inhibitors: tissue-agnostic anti-cancer drugs. *Pharm (Basel)* (2021) 14(7). doi: 10.3390/ph14070632

37. Wong D, Yip S, Sorensen PH. Methods for identifying patients with tropomyosin receptor kinase (Trk) fusion cancer. *Pathol Oncol Res* (2020) 26 (3):1385–99. doi: 10.1007/s12253-019-00685-2

38. Alberti L, Carniti C, Miranda C, Roccato E, Pierotti MA. Ret and Ntrk1 proto-oncogenes in human diseases. *J Cell Physiol* (2003) 195(2):168–86. doi: 10.1002/jcp.10252

39. Manea CA, Badiu DC, Ploscaru IC, Zgura A, Bacinschi X, Smarandache CG, et al. A review of ntrk fusions in cancer. *Ann Med Surg (Lond)* (2022) 79:103893. doi: 10.1016/j.amsu.2022.103893

40. Gatalica Z, Xiu J, Swensen J, Vranic S. Molecular characterization of cancers with ntrk gene fusions. *Mod Pathol* (2019) 32(1):147–53. doi: 10.1038/s41379-018-0118-3

41. Doebele RC, Drilon A, Paz-Ares L, Siena S, Shaw AT, Farago AF, et al. Entrectinib in patients with advanced or metastatic ntrk fusion-positive solid tumours: integrated analysis of three phase 1-2 trials. *Lancet Oncol* (2020) 21 (2):271–82. doi: 10.1016/S1470-2045(19)30691-6

42. Drilon A, Laetsch TW, Kummar S, DuBois SG, Lassen UN, Demetri GD, et al. Efficacy of larotrectinib in trk fusion-positive cancers in adults and children. *N Engl J Med* (2018) 378(8):731–9. doi: 10.1056/NEJMoa1714448

43. Tadipatri R, Eschbacher J, Fonkem E, Kresl J, Azadi A. Larotrectinib in ntrk fusion-positive high-grade glioneuronal tumor: a case report. *Cureus* (2022) 14(11): e31449. doi: 10.7759/cureus.31449

44. Alvarez-Breckenridge C, Miller JJ, Nayyar N, Gill CM, Kaneb A, D'Andrea M, et al. Clinical and radiographic response following targeting of bcan-Ntrk1 fusion in glioneuronal tumor. *NPJ Precis Oncol* (2017) 1(1):5. doi: 10.1038/s41698-017-0009-y

45. Recine F, De Vita A, Fausti V, Pieri F, Bongiovanni A, Franchini E, et al. Case report: adult ntrk-rearranged spindle cell neoplasm: early tumor shrinkage in a case with bone and visceral metastases treated with targeted therapy. *Front Oncol* (2021) 11:740676. doi: 10.3389/fonc.2021.740676

46. Hempel D, Wieland T, Solfrank B, Grossmann V, Steinhard J, Frick A, et al. Antitumor activity of larotrectinib in esophageal carcinoma with ntrk gene amplification. *Oncologist* (2020) 25(6):e881–e6. doi: 10.1634/theoncologist.2019-0641

47. Johnson M, Garassino MC, Mok T, Mitsudomi T. Treatment strategies and outcomes for patients with egfr-mutant non-small cell lung cancer resistant to egfr tyrosine kinase inhibitors: focus on novel therapies. *Lung Cancer* (2022) 170:41–51. doi: 10.1016/j.lungcan.2022.05.011

frontiers | Frontiers in Oncology

TYPE Case Report
PUBLISHED 17 May 2023
DOI 10.3389/fonc.2023.1175279

OPEN ACCESS

EDITED BY
Ming Zhao,
Zhejiang Provincial People's Hospital, China

REVIEWED BY
Shih-Sung Chuang,
Chi Mei Medical Center, Taiwan
Aruna Nambirajan,
All India Institute of Medical Sciences, India

*CORRESPONDENCE
Guang-Jie Duan
gjduan@163.com

RECEIVED 27 February 2023
ACCEPTED 02 May 2023
PUBLISHED 17 May 2023

CITATION
Wu Y-L, Wu F, Cao M-F, Lan Y, Du M-S, Yu S-T, Wang Y, Yan X-C, Bian X-W and Duan G-J (2023) Primary pulmonary hyalinizing clear cell carcinoma with fusions of both EWSR1::CREM and IRF2::NTRK3: report of a case with an aggressive behavior.
Front. Oncol. 13:1175279.
doi: 10.3389/fonc.2023.1175279

Primary pulmonary hyalinizing clear cell carcinoma with fusions of both EWSR1::CREM and IRF2::NTRK3: report of a case with an aggressive behavior

You-Li Wu[1], Feng Wu[1], Mian-Fu Cao[1], Yang Lan[1], Ming-Shan Du[2], Song-Tao Yu[3], Yan Wang[1], Xiao-Chu Yan[1], Xiu-Wu Bian[1] and Guang-Jie Duan[1]*

[1]Institute of Pathology and Southwest Cancer Center, Southwest Hospital, Third Military Medical University (Army Medical University), Chongqing, China, [2]Department of Radiology, Southwest Hospital, Third Military Medical University (Army Medical University), Chongqing, China, [3]Department of Oncology, Southwest Hospital, Third Military Medical University (Army Medical University), Chongqing, China

Primary pulmonary hyalinizing clear cell carcinoma (HCCC) is a rare salivary gland-type tumor newly recognized in recent years, with approximately 21 cases reported to date in the English literature, which constitutes a challenge in pathology diagnosis, particularly in small biopsy specimens. Here, we present a case of pulmonary HCCC diagnosed by computed tomography-guided percutaneous lung biopsy in a 70-year-old man's right lower lung. Although the morphology and immunophenotype of the tumor suggested the diagnosis of mucoepidermoid carcinoma, fluorescence *in situ* hybridization failed to reveal the rearrangement of MAML2 gene, which is characteristic of mucoepidermoid carcinoma. Instead, further molecular genetic testing showed that the tumor harbored a rare EWSR1::CREM fusion combined with a previously unreported IRF2::NTRK3 fusion. Pulmonary HCCC is commonly regarded as a low-grade malignant tumor with an indolent course, but this case has a different biological behavior, presenting extensive dissemination and metastases at the time of diagnosis, which expands our understanding of the prognosis of this tumor. The patient has had five cycles of combination chemotherapy and has been alive with the tumor for eight months.

KEYWORDS

hyalinizing clear cell carcinoma, lung biopsy, EWSR1::CREM fusion, next-generation sequencing, prognosis

Abbreviations: CT, computed tomography; FISH, fluorescence *in situ* hybridization; HCCC, hyalinizing clear cell carcinoma; MEC, mucoepidermoid carcinoma; NGS, next-generation sequencing; RNA-Seq, ribonucleic acid sequencing; SCC, squamous cell carcinoma.

Introduction

Primary pulmonary hyalinizing clear cell carcinoma (HCCC) is a rare new entity listed in the 2021 World Health Organization classification of thoracic tumors, which was first described by García et al. in 2015 (1), and only 21 cases have been reported in English publications to date (2–13). The typical histopathologic features of pulmonary HCCC are similar to those of the salivary gland counterparts, mainly composed of clear cells arranged in nests, cords, and trabecular patterns with hyalinization of the stroma. However, because of small tissue samples often with artificial extrusion in the preoperative biopsy, the morphology of pulmonary HCCC is variable and usually not typical, and the diagnosis of which remains very challenging.

We herein report a case of pulmonary HCCC diagnosed by computed tomography (CT)-guided percutaneous lung biopsy, the morphology and immunophenotype of which were similar to those of mucoepidermoid carcinoma. However the molecular genetic testing revealed that the tumor harbored a rare EWSR1::CREM fusion combined with an IRF2::NTRK3 fusion, rather than the rearrangement of MAML2 gene, which is characteristic of mucoepidermoid carcinoma (14). Meanwhile, we reviewed 21 cases reported previously (Table 1) to explore their clinicopathologic and imaging features, so as to strengthen our understandings of this rare tumor and, to improve diagnostic accuracy.

Case presentation

A 70-year-old male patient suffered from persistent dull pain in the right chest for two months, which was exacerbating at night. He presented neither symptoms of fever, cough, sputum, hemoptysis and dyspnea, nor history of chronic disease, infection, trauma, smoking and drinking. Chest CT revealed a lobulated mass with a diameter of approximately 5.3 cm in the right lower lobe of the lung close to the bronchus (Figure 1A), which was heterogeneously enhanced (Figure 1B). Multiple nodules were found in the middle and lower lobes of the right lung and the right interlobular fissure. CT also demonstrated multiple enlarged lymph nodes in the right subphrenic and anterior supradiaphragmatic spaces (Figure 1C), nodular thickening of the right pleura and the diaphragm around the liver (Figure 1D), and bone destruction in the right third, fourth, seventh, and eighth ribs (Figure 1E). All the findings suggested a lung cancer with metastases to intrapulmonary, pleural, diaphragm, right ribs and multiple lymph nodes. Subsequently, a CT-guided percutaneous lung biopsy was performed for pathological diagnosis (Figure 1F).

Microscopically, the epithelioid tumor cells were arranged in nests (Figure 2A), cords, and trabeculae (Figure 2B), with moderate cytologic atypia. Most atypical cells had eosinophilic cytoplasm, except for some scattered tumor cells containing clear cytoplasm. Focally, the tumor showed cyst formation. The nuclei were round or oval with fine chromatin and small nucleoli. Neither significant mitotic activity nor necrosis was observed. Loose myxoid stroma and scattered mucus-secreting cells (mucocytes) were observed in focal areas (Figure 2C). The mucinous differentiation was demonstrated *via* Alcian blue staining (Figure 2D). Cord-like collagen fibers were observed only in focal areas (Figure 2E). Immunohistochemical staining showed that the tumor cells were positive for CK5/6 (Figure 2F), CK7 (Figure 2G), p40 (Figure 2H) and p63, but negative for S-100, SOX10, SMA, Calponin, and TTF1. The Ki-67 proliferation index was approximately 20% (Figure 2I).

Although the morphology and the immunophenotype suggested the diagnosis of mucoepidermoid carcinoma (MEC), fluorescence *in situ* hybridization (FISH) failed to disclose the rearrangement of MAML2 gene (Figure 3A), a typical genetic alteration in MEC, which casted doubt on the initial diagnosis of MEC. It has been found in pathological practice that the pathological features of MEC resemble those of hyalinizing clear cell carcinoma (HCCC) or myoepithelial carcinoma. However, HCCC and myoepithelial carcinoma are featured with the rearrangement of EWSR1 gene, whereas MEC is not. Therefore, we performed FISH for the EWSR1 gene. Interestingly, we found the rearrangement of EWSR1 gene (Figure 3B), implying the nature of HCCC or myoepithelial carcinoma. Subsequently, next-generation sequencing (NGS) with a 425-gene panel was conducted, which revealed EWSR1::CREM fusion (Figure 3C) and IRF2::NTRK3 fusion (Figure 3D) at the DNA level. To determine whether there were potential targets of the NTRK inhibitor, newly approved by National Medical Products Administration (NMPA), the tissue sample was subjected to RNA sequencing (RNA-Seq). Unexpectedly, only EWSR1::CREM fusion was found at the RNA level (Figures 3E, F). The molecular profiling data indicated that the NTRK3 fusion gene encoded no protein product, and thus the patient could not receive the NTRK-targeted therapy. Surgery was not possible because the patient had substantial metastases and dissemination at the time of diagnosis. As a result, five cycles of combination chemotherapy were administered, and the patient has been alive with the tumor for eight months.

Discussion

Primary pulmonary HCCC is a very rare salivary gland-type tumor recognized in recent years, with approximately 21 cases so far reported in the English literature (1–13). Together with our newly identified HCCC case, the 22-case cohort (Table 1) demonstrates that it mainly occurred in middle-aged and older adults, with ages ranging from 32 to 75 years (median, 55 years; average, 53 years). The ratio of male to female patients was 9:13. Most patients lacked specific clinical manifestations and apparent symptoms. The tumor masses in the lung were often observed during regular physical examinations. A few patients presented back pain, chest pain, cough, hemoptysis, and dyspnea. Some patients had a history of smoking. The maximal diameter of the tumor ranged from 0.9 cm to 5.3 cm, and our case was the largest one reported so far.

Imaging presents that most HCCCs are well-demarcated, and destruction of the surrounding bronchus is recognized in some cases. Unlike common lung cancers, primary pulmonary HCCC is often close to and grows along the bronchus. These imaging features of HCCC may be related to its origin from the bronchial

10.3389/fonc.2023.1175279

TABLE 1 Summaries of 22 cases of primary pulmonary hyalinizing clear cell carcinoma.

Case No.	Age (y)/ Sex	Maximal Tumor Diameter (cm)	Location	Gross pathological features	Initial diagnoses	Molecular results	Treatment	Follow-up (mo)
1 (1)	38/M	2.6	Bronchus	Clear boundary	HCCC	EWSR1::ATF1 gene fusion	Surg	NED (10)
2 (2)	32/M	1.8	Segmental bronchus	Clear boundary, protrusion into the bronchi	SCC or low-grade MEC	EWSR1 gene rearrangement	Surg	NED (18)
3 (2)	39/M	2.6	Right lower lobe	Clear boundary	SCC or low-grade MEC	EWSR1 gene rearrangement	Surg	NED (18)
4 (3)	69/M	NA	Right upper lobe	NA	Lung cancer	EWSR1::ATF1 gene fusion	Surg + LND	AWD, with multiple pulmonary and lymph node metastases (192)
5 (4)	54/F	3.2	Left upper lobe	Clear boundary	SCC	EWSR1::ATF1 gene fusion	Surg	NED (16)
6 (5)	55/M	2.5	Right intermedius bronchus	Clear boundary, protrusion into the bronchi	NSCLC	EWSR1 gene rearrangement	Surg	NED (20)
7 (6)	75/F	0.9	Lower lobe	Clear boundary	MEC	EWSR1:: CREM gene fusion	Surg	NED (8)
8 (7)	52/F	3.3	Segmental bronchus	Clear boundary, protrusion into the bronchi	HCCC	EWSR1::ATF1 gene fusion	Surg	NED (181)
9 (7)	35/F	2.8	secondary bronchus	Clear boundary, protrusion into the bronchi	HCCC	EWSR1::ATF1 gene fusion	Surg	NED (79)
10 (7)	56/F	3.3	secondary bronchus	Clear boundary, protrusion into the bronchi	HCCC	EWSR1::ATF1 gene fusion	Surg	NED (12)
11 (8)	66/F	1.3	Trachea	Polypoid mass	HCCC	EWSR1 gene rearrangement	Transbronchial laser resection	NA
12 (9)	55/F	2.5	Distal tracheal	Polypoid mass	HCCC	EWSR1 gene rearrangement	Surg + LND + RT	NED (72)
13 (10)	46/F	NA	Trachea	NA	SCC	EWSR1::ATF1 gene fusion	Surg + LND + ChT + RT	Recurrences (24), STD (72)
14 (11)	57/F	2.8	Right lower lobe	Clear boundary	MEC	EWSR1::ATF1 gene fusion	Surg + LND	AWD, with lymph node metastasis at diagnosis (3)
15 (12)	58/M	4.3	Right upper lobe	Clear boundary	Squamous papillary neoplasm	EWSR1::ATF1 gene fusion	Surg + ChT	NED (10)
16 (12)	60/F	2.0	Left lower lobe	Polypoid mass	HCCC	EWSR1::ATF1 gene fusion	Surg	NED (10)
17 (13)	44/M	3.5	Left lower lobar bronchus	NA	HCCC	EWSR1 gene rearrangement	Surg	NED (48)
18 (13)	56/F	1.6	Left upper lobar bronchus	NA	HCCC	EWSR1 gene rearrangement	Surg	NA
19 (13)	44/F	1.3	Right upper lobar bronchus	NA	HCCC	EWSR1 gene rearrangement	Surg	NA
20 (13)	33/F	4.9	Right middle lobar bronchus	NA	HCCC	EWSR1 gene rearrangement	Surg	NA

(Continued)

TABLE 1 Continued

Case No.	Age (y)/ Sex	Maximal Tumor Diameter (cm)	Location	Gross pathological features	Initial diagnoses	Molecular results	Treatment	Follow-up (mo)
21 (13)	64/M	4.9	Left upper lobe hilum	NA	HCCC	EWSR1 gene rearrangement	Surg	NED (9)
22	70/M	5.3	Right lower lobe	Clear boundary	MEC	EWSR1:: CREM gene fusion	ChT	AWD, with intrapulmonary, pleural, multiple bone and lymph node metastases (8)

22, Present case; M, male; F, female; NA, not available; HCCC, hyalinizing clear cell carcinoma; SCC, squamous cell carcinoma; MEC, mucoepidermoid carcinoma; NSCLC, non-small-cell lung carcinoma; Surg, surgery; LND, lymph node dissection; RT, radiotherapy; ChT, chemotherapy; NED, no evidence of disease; AWD, alive with disease; STD, succumbed to disease.

submucosal glands (7). CT and fiberoptic bronchoscopy also find some polypoid masses in the bronchial lumen, which may lead to airway obstruction. Icard et al. reported a case of HCCC undergoing emergency admission due to progressive dyspnea. Fiberoptic bronchoscopy unveiled a polypoid mass blocking 60% of the tracheal lumen, and emergency endobronchial laser resection was performed to relieve the obstruction (8). Therefore, clinicians should pay attention to the acute airway events in this disease.

The patient herein is the first case of HCCC diagnosed by CT-guided percutaneous lung biopsy. In the previously described cases, 20 of 21 (95%) were diagnosed after surgical resection, and only one was diagnosed by bronchoscopic biopsy (11). Jeffus et al. reported a case initially misdiagnosed as moderately to poorly differentiated squamous cell carcinoma (SCC) with a biopsy specimen (4). Based on the bronchoscopic biopsy specimen, two cases were misdiagnosed as non-small cell lung cancer and squamous papillary neoplasm, respectively (5, 12). The postoperative cases were also often diagnosed as other common tumors, such as MEC (1 case), SCC (2 cases), SCC/MEC (2 cases), and lung cancer (1 case) (2–4, 6, 10), which indicates a high misdiagnosis rate of pulmonary HCCC.

Together, the diagnostic difficulty might be attributed to the followings: (a) The morphology of HCCC is variable. The tumor cells might contain clear or eosinophilic cytoplasm, and the hyalinizing stroma might not be apparent. Additionally, the tumor cells might present with squamous and mucinous cell differentiation, pathologically resembling MEC, SCC, and myoepithelial carcinoma; (b) HCCC lacks specific immunohistochemical markers, and its immunophenotype overlaps with MEC, SCC, and myoepithelial carcinoma; and (c) Most importantly, primary pulmonary HCCC is so scarce that both clinicians and pathologists do not have enough awareness and understanding of this new entity.

It is challenging to distinguish HCCC from MEC because both show epidermoid and mucinous differentiation. Among the 22 cases, 5 (23%) were initially diagnosed as MEC (2, 6, 11). MEC is the most common malignant salivary gland-type lung tumor, and is more aggressive than HCCC. Our case had been initially diagnosed as a stage IV lung cancer with high invasiveness,

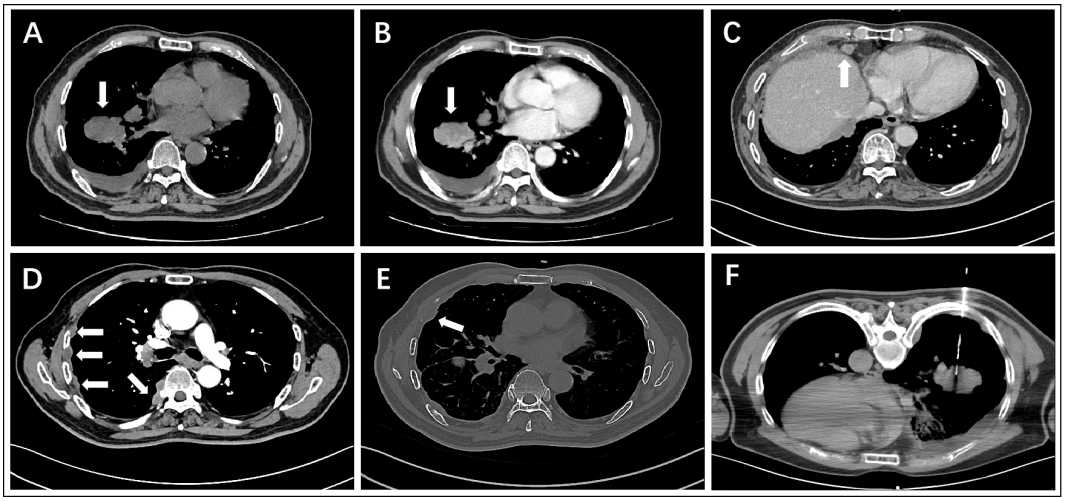

FIGURE 1
CT images show a lobulated mass in the right lower lobe of the lung **(A)** non-contrast, **(B)** contrast-enhanced), enlarged anterior supradiaphragmatic lymph nodes **(C)**, multiple thickening nodules in the right pleura **(D)**, bone destruction in the right fourth rib **(E)**, and CT-guided percutaneous lung biopsy **(F)**.

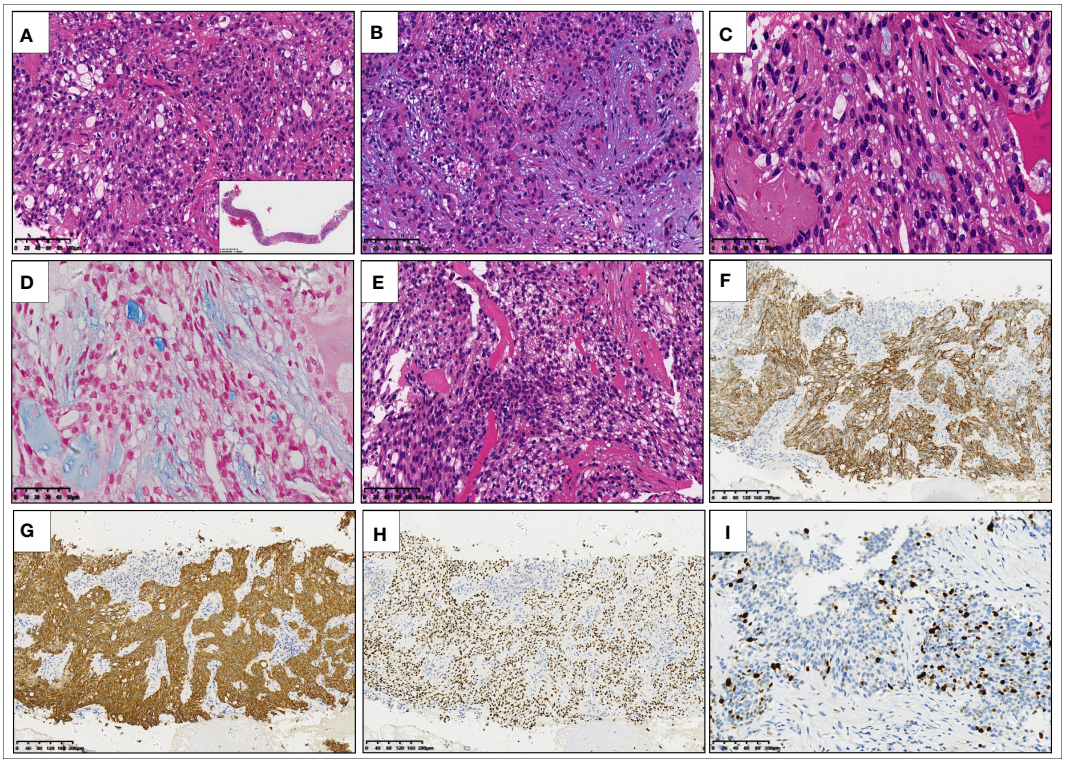

FIGURE 2
Hematoxylin and eosin staining of the core needle biopsy specimen reveals that epithelioid tumor cells with eosinophilic cytoplasm are arranged in nests **(A)** inset: low-power view of needle biopsy), cords, and trabeculae **(B)**. There are scattered mucocytes among the tumor cell nests **(C)**. Alcian blue staining highlights the mucocytes and loose myxoid stroma **(D)**. Cord-like collagen fibers are seen only in focal areas **(E)**. Immunohistochemical staining shows that the tumor cells are positive for CK5/6 **(F)**, CK7 **(G)**, and p40 **(H)**, the Ki-67 proliferation index of which is about 20% **(I)**.

which prompted us to consider this case as MEC. However, the lack of MAML2 gene rearrangement and the acquisition of EWSR1 gene rearrangement argued against the diagnosis of high-grade MEC. Therefore, the characteristic molecular changes are crucial in the differential diagnosis. Pulmonary HCCC should also be distinguished from SCC. Among 22 cases, 4 cases (18%) were initially considered as SCC (2, 4, 10). Compared with HCCC, SCC has remarkable cellular atypia with prominent nucleoli and obvious mitotic figures. Although both HCCC and SCC consistently express CK5/6, CK7, and p40, the Ki-67 proliferation index of HCCC is usually lower than that of SCC. Therefore, if the Ki-67 proliferation index is relatively low, the possibility of HCCC should be considered.

Pulmonary HCCC has characteristic molecular changes, including EWSR1::ATF1 fusion (10 of 11 cases) and EWSR1::CREM fusion (1 of 11 cases) (1–13). In our case, NGS revealed a rare EWSR1::CREM fusion and an unreported IRF2::NTRK3 fusion at the DNA level. Although the gene rearrangement of EWSR1 can occur in both HCCC and myoepithelial carcinoma, the fusion partners are different. Myoepithelial carcinoma often presents with EWSR1::PBX1 fusion, EWSR1::ZNF444 fusion, or FUS::KLF17 fusion. Therefore, NGS, RNA-seq, or other methods of fusion gene detection could be used for differential diagnosis.

Complete resection of the mass is the first choice for treating pulmonary HCCC (21/22 cases). It remains unclear whether regional lymph node dissection or postoperative chemo radiotherapy is necessary. In our case, the patient received five cycles of combined chemotherapy (paclitaxel plus nedaplatin). However, the CT showed that the primary tumor and metastatic lesions had no response after chemotherapy. The chemotherapy will be continued, and the therapeutic effect will be further followed up.

Primary pulmonary HCCC is commonly considered a low-grade malignant tumor with an indolent clinical course. Analysis of 18 patients with an average follow-up of 44 months revealed that 14 (78%) survived without tumors, four experienced disease relapses or metastases, and only one died. However, in our case, the patient had active disease progression with extensive dissemination and metastases at the time of diagnosis, which is different from those reported in the literature and expands our understanding of the biological behavior of the pulmonary HCCC. Specifically, the case had unusual genetic changes including EWSR1::CREM fusion and IRF2::NTRK3 fusion, and the largest tumor diameter of 5.3 cm,

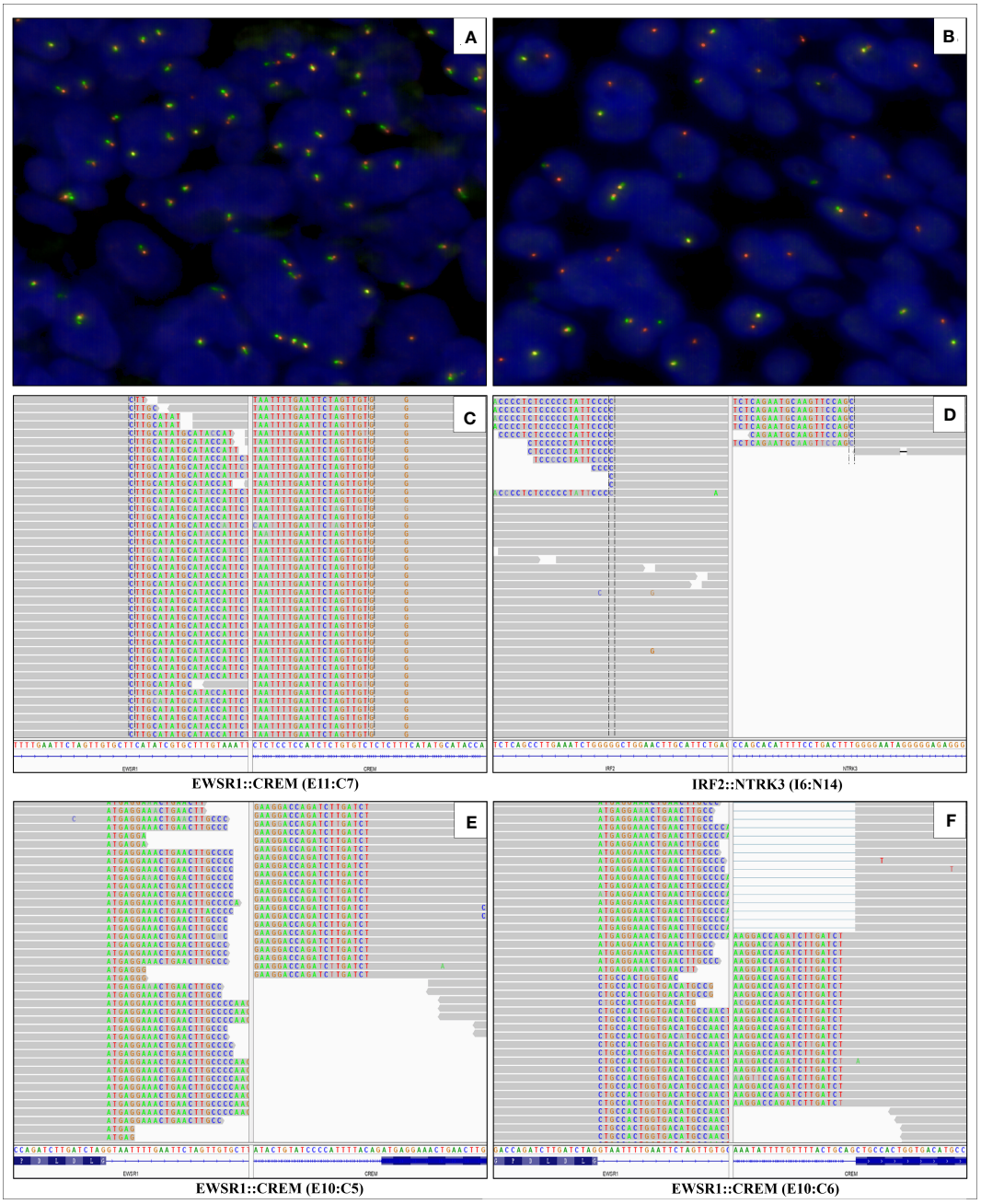

FIGURE 3
Fluorescence *in situ* hybridization is negative for MAML2 gene rearrangement **(A)** and positive for EWSR1 gene rearrangement **(B)**. Next-generation sequencing with a 425-gene panel reveals the EWSR1::CREM fusion (fusion of EWSR1 exon 11 to CREM exon 7) and IRF2::NTRK3 fusion (fusion of IRF2 intron 6 to NTRK3 intron 14) at DNA level **(C, D)**. RNA sequencing detects the EWSR1::CREM fusion transcript in which exon 10 of EWSR1 is fused to exon 5 and 6 of CREM **(E, F)**, respectively.

whether these phenotypes were associated with poor prognosis of the patient remained to be investigated.

Conclusion

The diagnosis of primary pulmonary HCCC is very challenging because of its rarity, particularly in small biopsy specimens. This paper reports an unusual pulmonary HCCC diagnosed by CT-guided percutaneous lung biopsy. Further understanding of this enigmatic tumor is essential to augment its diagnostic accuracy.

Data availability statement

The original contributions presented in the study are included in the article/supplementary material. Further inquiries can be directed to the corresponding author.

Ethics statement

Written informed consent was obtained from the individual(s) for the publication of any potentially identifiable images or data included in this article.

Author contributions

Material preparation, data collection and analysis were performed by Y-LW, YL, M-SD, and S-TY. The first draft of the manuscript was written by Y-LW, FW, and M-FC. The manuscript was revised and reviewed by G-JD, X-WB, X-CY, and YW. All authors contributed to the article and approved the submitted version.

Funding

This work was supported by a China National Science and Technology Major Project (2021YFF1201005) to X-WB.

Acknowledgments

The authors are grateful to Prof. Xin-Dong Liu and Xia Zhang of their institute, for their thoughtful reviews and comments on the format and language of the manuscript.

Conflict of interest

The authors declare that the research was conducted in the absence of any commercial or financial relationships that could be construed as a potential conflict of interest.

Publisher's note

References

1. García JJ, Jin L, Jackson SB, Larsen BT, Lewis JE, Sukov WR, et al. Primary pulmonary hyalinizing clear cell carcinoma of bronchial submucosal gland origin. *Hum Pathol* (2015) 46(3):471–5. doi: 10.1016/j.humpath.2014.11.010

2. Shah AA, Mehrad M, Kelting SM, Lewis JSJr, Stelow EB. An uncommon primary lung tumour: hyalinizing clear cell carcinoma, salivary gland-type. *Histopathology* (2015) 67(2):274–6. doi: 10.1111/his.12636

3. Wang H, Li WY, Kuo YJ, Yeh YC, Hsieh MS. Primary pulmonary hyalinising clear cell carcinoma with mucin production and delayed metastases after 16 years. *Pathology* (2016) 48(5):518–21. doi: 10.1016/j.pathol.2016.04.011

4. Jeffus SK, Gardner JM, Steliga MA, Shah AA, Stelow EB, Arnaoutakis K. Hyalinizing clear cell carcinoma of the lung: case report and review of the literature. *Am J ClinPathol* (2017) 148(1):73–80. doi: 10.1093/ajcp/aqx048

5. Shahi M, Dolan M, Murugan P. Hyalinizing clear cell carcinoma of the bronchus. *Head Neck Pathol* (2017) 11(4):575–9. doi: 10.1007/s12105-017-0820-3

6. Chapman E, Skalova A, Ptakova N, Martinek P, Goytain A, Tucker T, et al. Molecular profiling of hyalinizing clear cell carcinomas revealed a subset of tumors harboring a novel EWSR1-CREM fusion: report of 3 cases. *Am J SurgPathol* (2018) 42 (9):1182–9. doi: 10.1097/PAS.0000000000001114

7. Takamatsu M, Sato Y, Muto M, Nagano H, Ninomiya H, Sakakibara R, et al. Hyalinizing clear cell carcinoma of the bronchial glands: presentation of three cases and pathological comparisons with salivary gland counterparts and bronchial mucoepidermoid carcinomas. *Mod Pathol* (2018) 31(6):923–33. doi: 10.1038/s41379-018-0025-7

8. Icard B, Grider DJ, Aziz S, Rubio E. Primary tracheal hyalinizing clear cell carcinoma. *Lung Cancer* (2018) 125:100–2. doi: 10.1016/j.lungcan.2018.09.009

9. Doxtader EE, Shah AA, Zhang Y, Wang H, Dyhdalo KS, Farver C. Primary salivary gland-type tumors of the tracheobronchial tree diagnosed by transbronchial fine needle aspiration: clinical and cytomorphologic features with histopathologic correlation. *DiagnCytopathol* (2019) 47(11):1168–76. doi: 10.1002/dc.24285

10. Gubbiotti MA, Montone K, Zhang P, Livolsi V, Baloch Z. A contemporary update on hyalinizing clear cell carcinoma: compilation of all in-house cases at our institution and a literature review spanning 2015-2020. *Hum Pathol* (2021) 111:45–51. doi: 10.1016/j.humpath.2021.01.007

11. Zhang Y, Han W, Zhou J, Yong X. Primary lung hyalinizing clear cell carcinoma: a diagnostic challenge in biopsy. *DiagnPathol* (2022) 17(1):35. doi: 10.1186/s13000-022-01216-5

12. Feng L, Han Y, Wang Y, Zhang Y, Li J, Liang J, et al. Primary pulmonary hyalinizing clear cell carcinoma with pseudopapillary structures and abundant cysts filled with mucus. *Pathol Res Pract* (2023) 241:154237. doi: 10.1016/j.prp.2022.154237

13. Thakur S, Nambirajan A, Larsen BT, Butt YM, Roden AC, Kumar S, et al. Primary pulmonary hyalinizing clear cell carcinoma: case series with review of literature [published online ahead of print, 2022 Dec 13]. *Int J SurgPathol* (2022), 10668969221137516. doi: 10.1177/10668969221137516

14. Bishop JA, Cowan ML, Shum CH, Westra WH. MAML2 rearrangements in variant forms of mucoepidermoid carcinoma: ancillary diagnostic testing for the ciliated and warthin-like variants. *Am J Surg Pathol* (2018) 42(1):130–6. doi: 10.1097/PAS.0000000000000932

Frontiers in Oncology

Advances knowledge of carcinogenesis and tumor progression for better treatment and management

The third most-cited oncology journal, which highlights research in carcinogenesis and tumor progression, bridging the gap between basic research and applications to imrpove diagnosis, therapeutics and management strategies.

Discover the latest Research Topics

See more →

Frontiers

Avenue du Tribunal-Fédéral 34
1005 Lausanne, Switzerland
frontiersin.org

Contact us

+41 (0)21 510 17 00
frontiersin.org/about/contact